A Critical Assessment of Ages Derived Using Pre-Main-Sequence Isochrones in Colour-Magnitude Diagrams

Cameron Pearce MacDonald Bell

I certify that all material in this thesis which is not my own work has been identified and that no material has previously been submitted and approved for the award of a degree by this or any other University.

Signed: . . . .
Cameron P. M. Bell

Date: 26th November 2012

Abstract

In this thesis a critical assessment of the ages derived using theoretical pre-main-sequence (pre-MS) stellar evolutionary models is presented by comparing the predictions to the low-mass pre-MS population of 14 young star-forming regions (SFRs) in colour-magnitude diagrams (CMDs).

Deriving pre-MS ages requires precise distances and estimates of the reddening. Therefore, the main-sequence (MS) members of the SFRs have been used to derive a self-consistent set of statistically robust ages, distances and reddenings with associated uncertainties using a maximum-likelihood fitting statistic and MS evolutionary models. A photometric method for de-reddening individual stars – known as the Q-method – in regions where the extinction is spatially variable has been updated and is presented. The effects of both the model dependency and the SFR composition on these derived parameters are also discussed.

The problem of calibrating photometric observations of red pre-MS stars is examined and it is shown that using observations of MS stars to transform the data into a standard photometric system can introduce significant errors in the position of the pre-MS locus in CMD space. Hence, it is crucial that precise photometric studies – especially of pre-MS objects – be carried out in the natural photometric system of the observations. This therefore requires a robust model of the system responses for the instrument used, and thus the calculated responses for the Wide-Field Camera on the *Isaac Newton* Telescope are presented. These system responses have been tested using standard star observations and have been shown to be a good representation of the photometric system.

A benchmark test for the pre-MS evolutionary models is performed by comparing them to a set of well-calibrated CMDs of the Pleiades in the wavelength regime $0.4-2.5\,\mu\text{m}$. The masses predicted by these models are also tested against dynamical masses using a sample of MS binaries by calculating the system magnitude in a given photometric band-pass. This analysis shows that for $T_{\text{eff}} \lesssim 4000\,\text{K}$ the models systematically overestimate the flux by a factor of 2 at $0.5\,\mu\text{m}$, though this decreases with wavelength, becoming negligible at $2.2\,\mu\text{m}$. Thus before the pre-MS models are used to derive ages, a recalibration of the models is performed by incorporating an empirical colour-T_{eff} relation and bolometric corrections based on the K_{s}-band luminosity of Pleiades members, with theoretical corrections for the dependence on the surface gravity ($\log g$).

The recalibrated pre-MS model isochrones are used to derive ages from the pre-MS populations of the SFRs. These ages are then compared with the MS derivations, thus providing a powerful diagnostic tool with which to discriminate between the different pre-MS age scales that arise from a much stronger model dependency in the pre-MS regime. The revised ages assigned to each of the 14 SFRs are up to a factor two older than previous derivations, a result with wide-ranging implications, including that circumstellar discs survive longer and that the average Class II lifetime is greater than currently believed.

Contents

List of Figures

List of Tables

Declaration

The work presented in Chapters 3 and 4 was taken from a paper published in the Monthly Notices of the Royal Astronomical Society by Cameron P. M. Bell, Tim Naylor, N. J. Mayne, R. D. Jeffries, and S. P. Littlefair entitled Pre-main-sequence isochrones – I. The Pleiades benchmark (MNRAS, 424, 3178).

Chapters 2, 5, and 6 contain work that will be published in the near future and represent the second instalment of the saga.

The photometric observations taken with the Wide-Field Camera on the *Isaac Newton* Telescope were obtained by Tim Naylor and myself. The *Isaac Newton* Telescope is operated on the island of La Palma by the *Isaac Newton* Group (ING) in the Spanish Observatorio del Roque de los Muchachos of the Institutio de Astrofisica de Canarias.

Near-IR photometric data for the sample of main-sequence binaries were obtained from the Two-Micron All-Sky Survey (2MASS), which is a joint project of the University of Massachusetts and the Infrared Processing and Analysis Center, funded by the National Aeronautics and Space Administration (NASA) and the National Science Foundation.

The final reduction of the *Isaac Newton* Telescope data and the calculation of the *Isaac Newton* Telescope bandpasses were performed by Tim Naylor.

The τ^2 fitting statistic used for fitting the models to the data is the brainchild of Tim Naylor and R. D. Jeffries.

The rest of the work presented in this thesis is my own.

Acknowledgements

It was never my intention to leave it until the very last month of my Ph.D. before submitting, however in the end.....I did it?! There are a host of people who deserve credit for their guidance and patience over these past years, and for helping me limp across the finishing line.

Naturally, a huge thanks goes out to my supervisor Tim who not only set me on my way with a very interesting project but then proceeded to show remarkable patience despite my fully unintentional, yet at times perceivably persistent, stubbornness at not seeing the bloody obvious on more than the odd occasion. Tim has been consistently enthusiastic throughout my Ph.D. and I hope at times it appeared as though some of it rubbed off on me?! I think he fully deserves his sabbatical year and I look forward to hearing what science comes of it.

A big cheers also to my fellow grad students, past and present, who have no doubt enjoyed the ups and downs as have I – although I suspect their ride has not been as long as mine. In particular, I would like to acknowledge the existence of Ben, Cátia, Dave, Nathan, and Rob who not only ensured that my work environment was enjoyable, but also helped me out in one way or another.

On a more personal level, I would like to extend my gratitude to the members of the Bell clan and to my partner Tina, who is a much cherished by-product of my Ph.D. relocation. Thanks for all the support in my choice of academic pursuits and I someday hope to to repay you all for the time – and money – sacrificed.

Lastly, it is my fondest wish that my mother could have witnessed the final culmination(?) of my education. I therefore dedicate this thesis to the memory of Barbara Ann Bell.

<div align="right">

Cameron Bell

September 2012

</div>

P.S. Time to get yourselves another tea-b*tch!

Chapter 1

Introduction

1.1 Historical Prelude

Philosophical debate concerning the creation and subsequent evolution of the stars, and in particular that of the Sun, date back to antiquity. Heliocentrism, a model by which the Sun is placed at the centre of the Solar System with the Earth orbiting, was proposed as early as the 3rd century BC by Aristarchus of Samos (Draper 1874). This was generally overlooked, however, in favour of the geocentric models, advanced by more influential figures such as Aristotle and Ptolemy, wherein the Earth is the focal point of the entire Universe with all other objects orbiting around it. It was not until the 16th century and the instrumental work of Copernicus, later expanded upon by Johannes Kepler and Isaac Newton, that the heliocentric model was once more embraced and the foundation of a theory of Solar System formation laid.

The first records of a modern theory that suggests the planets were formed from matter cast off from the Sun, is a revised heliocentric model termed the Nebular Hypothesis and was proposed by Emanuel Swedenborg in *Opera Philosophica et Mineralia* published in 1734. Later, Immanuel Kant expanded this and hypothesised, in his 1755 work *Allgemeine Naturgeschichte und Theorie des Himmels*, that the Solar System was formed from a nebulous cloud of gas and dust. Kant further theorised that large-scale structures, such as the Milky Way, were themselves formed from much larger condensates of gas and dust. Pierre-Simon Laplace introduced his own version of the Nebular Hypothesis – independently of Kant – in his work entitled *Exposition du Système du Monde* in 1796. In the Laplacian model, the nebula is considered as an isolated, rotating dusty cloud. As the nebula begins to cool and collapse its rotational velocity increases due to the conservation of angular momentum and thus begins to flatten along the rotational axis. Further collapse results in the orbital motion of material at the equator, and as the collapse proceeds, annuli of material would form in circular Keplerian orbits about the central mass. These annuli, orbiting at different velocities, would then condense over time to form planets.

The Laplacian nebular model prevailed throughout the 19th century, despite the fact that several problems remained unresolved by the current formulation – chiefly the

distribution of mass and angular momentum between the Sun and the planets. This inconsistency led to a host of alternative theories on the formation of Solar Systems, which are simply listed for brevity – the planetesimal theory (Chamberlin 1901; Moulton 1905); the tidal theory (Jeans 1917, 1919); the accretion model (Schmidt 1944; Lyttleton 1961); the protoplanet theory (McCrea 1960); the capture theory (Woolfson 1964; Dormand & Woolfson 1989); and even a revised version of the Laplacian model (Prentice 1978).

Over the last few decades a modified theory for the formation of the Solar System has arisen known as the Solar Nebula Disc Model. The foundations of this theory can be found in Safronov (1972) where many of the principal physical problems concerning the formation of the Solar System were posed, including the effects of magnetic fields and turbulence, the distribution of dust necessary for planetesimal growth, and the subsequent formation of both the terrestrial and giant planets. This was built upon by works such as Wetherill (1989) in which the idea of 'runaway accretion' – the process by which protoplanetary embryos grow in a protoplanetary disc – was discussed. This paradigm, originally designed for the formation of the Solar System, is believed to be the default mechanism of star and planet formation throughout the Universe. A comprehensive discussion on the various theories proposed in explaining the formation of the Solar System along with their respective successes and shortcomings in answering the key problems can be found in Woolfson (1993).

Whilst the theoretical discussions concerning star formation have been argued for centuries, it was not until the identification of the class of T-Tauri stars (Joy 1945), observed to reside within dark clouds, that the empirical study of star formation commenced. With the realisation that these objects represent an early evolutionary phase of a star's life came a considerable effort into studying both the physical processes within the stellar interior and the impact of environmental effects. During the 1950s and 60s evolutionary models of the pre-main-sequence (pre-MS) phase of a star's life were developed using numerical models (see for instance Henyey et al. 1955 and Hayashi 1961). Instrumental advancements headed this progress by enabling the comparison of observational stellar properties with theoretical predictions. Fainter stars within clusters were uncovered due to the advent of larger telescopes, however interstellar extinction towards specific clusters (e.g. Trumpler 1930) limited the number of new discoveries. The arrival of infrared (IR) astronomy heralded the study of more embedded and younger objects known as protostars, with X-ray telescopes offering insights into the magnetic properties of these objects. The study of the earliest phases of star formation have been permitted via millimetre dishes that reveal the processes occurring within the optically obscure cold, molecular clouds in which stars are formed.

1.2 An Overview of Low-Mass Star Formation

Star formation is a ubiquitous process and one that touches almost every area of astrophysics, from galaxy formation to the origin of the Solar System. In this section a brief

Table 1.1: Observed temperature (T) and number densities (n) for the various phases of the ISM (Ferrière 2001).

Component	State of hydrogen	T (K)	n (cm^{-3})
Molecular clouds	Molecular (H$_2$)	$10 - 20$	$10^2 - 10^6$
Cold neutral medium	Neutral atomic (H I)	$50 - 100$	$20 - 50$
Warm neutral medium	Neutral atomic (H I)	few $10^3 - 10^4$	$0.2 - 0.5$
Warm ionised medium	Ionised (H II)	few 10^3	$0.2 - 0.5$
H II regions	Ionised (H II)	few 10^3	$10^2 - 10^4$
Hot ionised medium	Ionised (H II)	10^6	$10^{-4} - 10^{-2}$

overview of the current understanding of star formation based on observational evidence as well as the underlying theoretical framework is described. For a more comprehensive discussion on this topic, the recent review by McKee & Ostriker (2007) is an excellent source.

1.2.1 The Interstellar Medium and Molecular Clouds

Any theory of star formation must include a description of the the material from which the stars are formed. This rarified material pervades the Galaxy and is known as the interstellar medium (ISM). It is a heterogeneous mixture of gas and dust of varying thermal and chemical phases. The main components are detailed in Table 1.1.

The most important of these, in terms of star formation, is molecular hydrogen. Star formation can only occur in the over-dense regions of the ISM. These over-dense regions can vary widely in both size and mass from giant molecular clouds (GMCs), such as Orion, with masses $\sim 10^5 \, \mathrm{M_\odot}$ and covering a region $\sim 100 \, \mathrm{pc}$ (Genzel & Stutzki 1989) to dense cores/Bok globules of masses $< 10 \, \mathrm{M_\odot}$ and size $< 1 \, \mathrm{pc}$ (Bok & Reilly 1947; Clemens et al. 1991). The distribution of GMCs within the Milky Way is not random, instead they are found to group about the Galactic plane (Wood & Churchwell 1989; Hartmann 1998). The mechanisms responsible for the formation and physical properties of molecular clouds are still the topic of debate, but it is likely that their formation is due to large-scale compression of material in the ISM, possibly as a result of nearby supernovae or large-scale gravitational perturbations within the ISM (Ballesteros-Paredes et al. 2007). Observations of the Milky Way have shown that molecular clouds tend to be concentrated towards the spiral arms (Georgelin & Georgelin 1976; Dame et al. 1986; Lee et al. 2001) which are manifestations of gravitational instability within the ISM.

GMCs are believed to be highly dynamic, filamentary entities (McCray & Snow 1979) with gravitational energies that far exceed their thermal energies (Zuckerman & Palmer 1974), but comparable to both the magnetic (Crutcher 1999) and turbulent energies (Larson 1981). The traditional picture of GMCs is that this near equipartition of energies is indicative of the cloud existing in an almost virial equilibrium state and hence one of general longevity (McKee et al. 1993). The dominant gravitational energy was interpreted as evidence that these objects are strongly self-gravitating (McKee 1995),

whereas the magnetic and turbulent energies provided support against gravity. The resulting turbulence within a given molecular cloud scales with its size and there are a host of potential driving mechanisms (Mac Low & Klessen 2004) including gravitational collapse, differential rotation of Galactic discs (Fleck 1981), ionising radiation from local massive star formation leading to increased levels of ultraviolet (UV) flux (McKee 1989; Vázquez-Semadeni et al. 1995), and finally jets and outflows from the more prolific low-mass protostars (Norman & Silk 1980; Franco & Cox 1983). Note, however, that stellar feedback induced turbulence will act on local scales and only become a dominant feature after the first generation of stars have formed.

The formation of stars hinges on whether the attractive force of gravity can overcome the resistive thermal pressure, turbulent motions and magnetic forces within a given region. Thus it is not surprising that stars form in dense, cold ($\sim 10\,\mathrm{K}$) molecular clouds (Bergin & Tafalla 2007). The high dust extinction of molecular clouds (Cernicharo 1991) may act to assist star formation by essentially shielding the gas from the heating effects of nearby luminous stars, and therefore maintain low internal temperatures (McKee 1989; Myers & Khersonsky 1995). External photoionising radiation can be absorbed by the molecular dust, thereby reducing the ionisation levels within the cloud. This enables gas to diffuse across the magnetic field lines, effectively decreasing the magnetic forces opposing gravity, in a process known as ambipolar diffusion (Shu et al. 1987).

1.2.2 Models of Star Formation

Over the past decade there has been a paradigm shift in the mode of star formation from one which occurs in a quasi-static medium to one in a supersonic turbulent medium. Both modes will briefly be discussed as well as the observational evidence that has led to this shift.

1.2.2.1 The Standard 'Slow' Model

The standard model of star formation considers an isolated pre-stellar core (Ebert 1955; Bonnor 1956) in which gravity overcomes the thermal pressure to form a single star. Jeans (1902) considered the process of gravitational instability and demonstrated that a cloud could become unstable and begin to collapse if there was insufficient thermal pressure to counter the effects of gravity. This can easily be derived for a spherical cloud of mass M_{cl} and radius R_{cl}. Starting from the virial theorem, which balances the kinetic and gravitational energies

$$2K + U = 0, \tag{1.1}$$

where K is the kinetic energy and U the gravitational energy of the cloud. The kinetic energy is given by

$$K = \frac{3M_{\mathrm{cl}}k_{\mathrm{B}}T_{\mathrm{cl}}}{2\mu m_{\mathrm{H}}}, \tag{1.2}$$

where k_B is the Boltzmann constant, T_{cl} the temperature of the cloud, μ the mean molecular weight and m_H the mass of molecular hydrogen. The gravitational energy of a spherical cloud of uniform density is

$$U = -\frac{3GM_{cl}^2}{5R_{cl}}, \tag{1.3}$$

where G is the gravitational constant. The Jeans length, which is defined as the length below which a cloud is unstable to collapse, can be determined by substituting Eqns. 1.2 and 1.3 into Eqn. 1.1 so that

$$R_J = \left(\frac{15k_B T_{cl}}{4\pi m_H \mu G \rho}\right)^{1/2}, \tag{1.4}$$

where ρ is the density, and this then provides the Jeans mass, given by

$$M_J = \left(\frac{3}{4\pi\rho}\right)^{1/2} \left(\frac{5k_B T_{cl}}{m_H \mu G}\right)^{3/2}. \tag{1.5}$$

Adopting typical GMC parameters ($T_{cl} \sim 10\,\mathrm{K}$, $n_{H_2} \simeq 10^3\,\mathrm{cm^{-3}}$; Blitz 1993) the Jeans mass is usually a few solar masses.

The typical timescale for such a process in which gravity alone is acting, neglecting all other resistive forces, is known as the free-fall timescale (t_{ff}; Hunter 1962), where

$$t_{ff} = \left(\frac{3\pi}{32G\rho}\right)^{1/2}. \tag{1.6}$$

For typical pre-stellar cores densities ($n_{H_2} \simeq 10^4 - 10^5\,\mathrm{cm^{-3}}$) these free-fall timescales are $\sim 0.5\,\mathrm{Myr}$. Note however that these timescales will inevitably be too short as the resistive effects of both magnetic and turbulent pressures have not been incorporated.

The standard model of star formation is based on works by Shu (1977) and Shu et al. (1987) in which the pre-stellar core is magnetically dominated (or subcritical). Here subcritical is defined as the ratio of mass-to-magnetic flux ratios $(M/\Phi)/(M/\Phi)_{crit} \leq 1$ where $(M/\Phi)_{crit}$ is the critical value necessary for support against gravitational collapse. Subcritical cores collapse and form stars only after ambipolar diffusion has extracted excess magnetic flux, leading to cloud collapse timescales of order $10\,\mathrm{Myr}$ (Mouschovias 1976; Shu 1977; Tassis & Mouschovias 2004; Tan et al. 2006). Tassis & Mouschovias (2004) argue that the subcritical cores in molecular clouds can last $\sim 10-15\,\mathrm{Myr}$ before becoming supercritical in the final few million years and subsequently collapsing. This collapse produces a centrally condensed core in which gravity is able to overcome the thermal pressure on free-fall timescales.

1.2.2.2 The Revised 'Rapid' Model

The standard model of star formation implies molecular cloud lifetimes of order $10-20$ free-fall times (Solomon et al. 1979; Blitz & Shu 1980; Ciolek & Mouschovias 1995). If molecular clouds survive for long durations prior to the onset of star formation, then one

would naturally expect to find a host of starless dark clouds. Observational evidence, however, points to the contrary and shows that almost all cloud complexes within $\simeq$ 500 pc exhibit on-going star formation, containing stellar populations with ages $1 - 10$ Myr (Hartmann et al. 2001; Briceño et al. 2007; Hartmann et al. 2012). A further consequence of the standard model is that of age spreads in star-forming regions (SFRs). If a molecular cloud lasts for tens of Myr, an older pre-MS population with similar ages should be present – the 'post T-Tauri problem' (Herbig 1978; Jensen 2001). Several surveys have found no evidence for a significant population of pre-MS stars older than $\simeq$ 5 Myr in nearby molecular complexes (Herbig et al. 1986; Gauvin & Strom 1992; Gomez et al. 1992). X-ray surveys of the same regions claim to have identified these older stars (Alcalá et al. 1995; Sterzik et al. 1995; Wichmann et al. 1996; Neuhäuser 1997), however Briceño et al. (1997) showed that these samples contain a mixture of young, X-ray active zero-age main-sequence (ZAMS) field stars and some bonafide pre-MS members of the SFR. There is currently sparse evidence for a significant number of older pre-MS stars in and around molecular clouds (see for example Mamajek et al. 2002).

Recent observational evidence, combined with theoretical predictions, suggest that the average lifetime of molecular clouds cluster at around $2 - 3$ Myr (Elmegreen 2000; Hartmann et al. 2001; Hartmann 2003; Clark et al. 2005; Ballesteros-Paredes & Hartmann 2007). In this revised picture, molecular clouds are no longer envisaged as well-defined quasi-static entities, but instead as magnetically supercritical transient objects (Hunter et al. 1986; Elmegreen 1993; Nakano 1998; Ballesteros-Paredes et al. 1999a,b) whose production is linked to large-scale turbulent flows of atomic hydrogen. Pringle et al. (2001) have further suggested that molecular clouds may in fact be just visible regions, heated by nearby sources, of a much larger structure of molecular gas that is distributed throughout the atomic component of the ISM.

Magnetohydrodynamic (MHD) simulations (e.g. Dobbs et al. 2006; Dobbs & Bonnell 2007) and numerical analyses (e.g. Heitsch et al. 2005, 2006) have demonstrated mechanisms which result in the creation of such atomic flows. The colliding flows would accumulate atomic gas that might eventually reach column densities high enough for molecular hydrogen formation. The point at which molecular hydrogen begins to form essentially defines the point at which the 'lifetime' of the molecular cloud would start i.e. the accumulation timescale could be much larger. Numerical simulations have shown that at such densities turbulence dissipates rapidly, thus permitting gravitational collapse, at least in restricted regions, on timescales of a few Myr or less (Ballesteros-Paredes et al. 1999a; Pringle et al. 2001; Hartmann 2003). The large-scale flows are driven by large-scale compression within the ISM via supernovae, Galactic shear or even through galaxy interactions (Looney et al. 2006; Ballesteros-Paredes et al. 2007). Such a swift collapse time invariably leads to stellar feedback that disperses the remaining material, hence the lack of SFRs embedded in dense molecular clouds (Hartmann et al. 2001). Observations have further shown that the transient morphology of the large-scale turbulent flows is mirrored on smaller scales. Embedded clusters within molecular clouds (Elmegreen 2007) and pre-

stellar cores within these clusters (Bacmann et al. 2000) demonstrate non-regular structures as opposed to the regular shape one might expect in a quasi-equilibrium paradigm, and lends further support to the idea that the observed structure in molecular clouds is simply a consequence of the collisional processes that formed them.

1.2.2.3 Molecular Cloud Core Lifetimes

Molecular cloud core lifetimes have been investigated on both a statistical and chemical basis. The statistical method is based on the observed number ratio of starless to stellar cores in surveys to determine the time spent in the pre-stellar and protostellar stages respectively (Beichman et al. 1986; Ward-Thompson et al. 1994). Observed chemical abundances in cores can also be compared with time-dependent evolutionary models to derive ages (Langer et al. 2000; Jørgensen et al. 2005b). Although both methods tend to agree on the duration of the pre-stellar stage $(0.1 - 1\,\mathrm{Myr})$, these methods are subject to biases, be it detection limits when looking at supposedly starless cores (Young et al. 2004) or the model dependency when using evolutionary models. For a comprehensive discussion on the observational perspective concerning low-mass pre-stellar cores see Ward-Thompson et al. (2007). MHD simulations of molecular clouds incorporating magnetic and turbulent effects have found that the median lifetime of cloud cores is $2 - 3\,t_{\mathrm{ff}}$ (Nakamura & Li 2005; Vázquez-Semadeni et al. 2005).

1.2.3 From Pre-Stellar Cores to Stars

Despite the difference in opinion concerning the exact processes involved in the creation of a self-gravitating molecular cloud core (in addition as to whether these objects are long-lived and magnetically subcritical or short-lived transient objects), the discussion will move onto the subsequent evolutionary stages taken by such a core through the pre-MS phase and onto the ZAMS (see Fig. 1.1).

1.2.3.1 Protostellar Stages

Supercritical regions within these molecular clouds collapse, thereby producing a centrally condensed clump. The initial clump is both massive and centrally condensed enough for gravity to overcome the thermal energy produced during contraction in order to maintain an enhanced density. Gas and dust fall towards the core of the clump and the liberated gravitational potential energy can be radiated away due to the optically thin nature of the clump. The influx of material causes the core density and temperature to increase eventually becoming optically thick $(n_{\mathrm{H_2}} \sim 10^{10}\,\mathrm{cm^{-3}})$, thereby trapping radiation previously able to escape. The increase in core temperature causes a temporary cessation of the collapse, and the formation of the so-called first core (Larson 1969). Material is still being accreted from the surrounding cloud causing further compression and an increase in core temperature. At a temperature of $\simeq 2000\,\mathrm{K}$ molecular hydrogen dissociates via collisional processes (Larson 1969) and leads to a levelling off in the central temperature
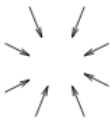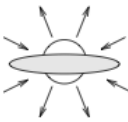
Properties	Infalling Protostar	Evolved Protostar	Classical T Tauri Star	Weak-lined T Tauri Star	Main Sequence Star
Age (years)	10^4	10^5	$10^6 - 10^7$	$10^6 - 10^7$	$> 10^7$
mm/Infrared Class	Class 0	Class I	Class II	Class III	(Class III)
Infall and Mass loss	Infall + Collimated Outflow	Infall + Open Outflow	Strong Wind	Weak Wind	Very Weak Wind
Disk	Yes	Thick	Thick	Thin or Non-existent	Possible Planetary System
X-ray	Not Detected	Yes	Strong	Strong	Weak
Radio	Thermal	Thermal + Non-thermal	Thermal	Non-thermal	Non-thermal

Figure 1.1: Schematic evolution of a protostar. From the initial molecular cloud core which will collapse and subsequently form a protostar (Class 0); to an evolved protostar accreting from the molecular envelope (Class I); to a CTTS with a thick disc (Class II); and then to a WTTS with an optically thin disc (Class III); finally evolving into a MS star with no disc but a possible planetary system. Credit: Carkner (1998).

and eventually a lack of support and the core begins to collapse once more. Once all the molecular hydrogen is dissociated, the temperature is able to increase dramatically and the gas pressure prohibits further gravitational collapse, leading to the formation of a protostar.

Successive stages of protostellar evolution towards the ZAMS are generally separated into four distinct classes of young stellar object (YSO) – termed Class 0, I, II, and III. These latter three are classified on the basis of their spectral energy distribution (SED) and spectral index (α_{IR}; Lada & Wilking 1984; Lada 1987), defined as

$$\alpha_{\mathrm{IR}} = \frac{d\log(\lambda F_\lambda)}{d\log(\lambda)}, \tag{1.7}$$

where λ is the wavelength of the radiation and F_λ is the flux at this given wavelength. This spectral index is commonly derived using an objects SED, specifically in the region between 2.2 and $10 - 25\,\mu$m (see Fig. 1.2). André et al. (2000) have summarised the classification scheme as follows. Class I objects have $\alpha_{\mathrm{IR}} > 0$ with the associated SED rising in the wavelength regime stated, indicating an SED with stronger emission at longer wavelengths. Class II objects have $-1.5 \leq \alpha_{\mathrm{IR}} \leq 0$ with either a near flat or slightly falling SED, suggesting an object associated with a dusty circumstellar disc and hence a strong IR emitter. Class III objects have $\alpha_{\mathrm{IR}} < -1.5$ with a falling SED, implying a lack/absence of circumstellar material and is responsible for the little/no IR excess. Each YSO class will be discussed briefly, starting with Class 0.

Class 0 (André et al. 1993; age $\sim 10^4$ years) defines the creation of a protostar. YSOs in this evolutionary stage are still embedded in their parent molecular cloud and as such are extremely faint in the optical and near-IR – being undetectable at $\lambda < 10\,\mu$m – but with a significant sub-mm luminosity. Hence the above definition of the spectral index is not applicable to this evolutionary state. Initial rotation of the molecular cloud core ensures that as the protostar rotates so does the dust and gas in the immediate vicinity of the core. The motion of material as it falls towards the protostar is slowed perpendicular to the rotational axis, resulting in a material density increase along this axis and subsequent formation of a disc (Terebey et al. 1984; Yorke et al. 1993). Material continually collects in the disc from the pre-natal stellar envelope, where the disc can act to remove momentum from the protostar and transport mass towards it through viscous interactions. If momentum was not removed from the protostar, the build up of mass would lead to resulting angular velocities large enough to inhibit the further collapse of the core. Protostars are believed to acquire a significant fraction of their total mass in this phase. Powerful collimated jets have been observed (Snell et al. 1980; Bachiller 1996) that may be an additional mechanism for removing this momentum, as noted in MHD simulations of collapsing, rotating, magnetised cloud cores (Banerjee & Pudritz 2006), as well as acting to disperse the residual envelope. As this natal envelope clears, the protostar and its accretion disc become visible in the mid- and far-IR. This heralds the transition into a Class I object. Typical Class I SEDs show that the peak of emission still lies in the far-IR ($\simeq 100\,\mu$m), although a larger fraction of emission lies at shorter wavelengths. Such emission at longer
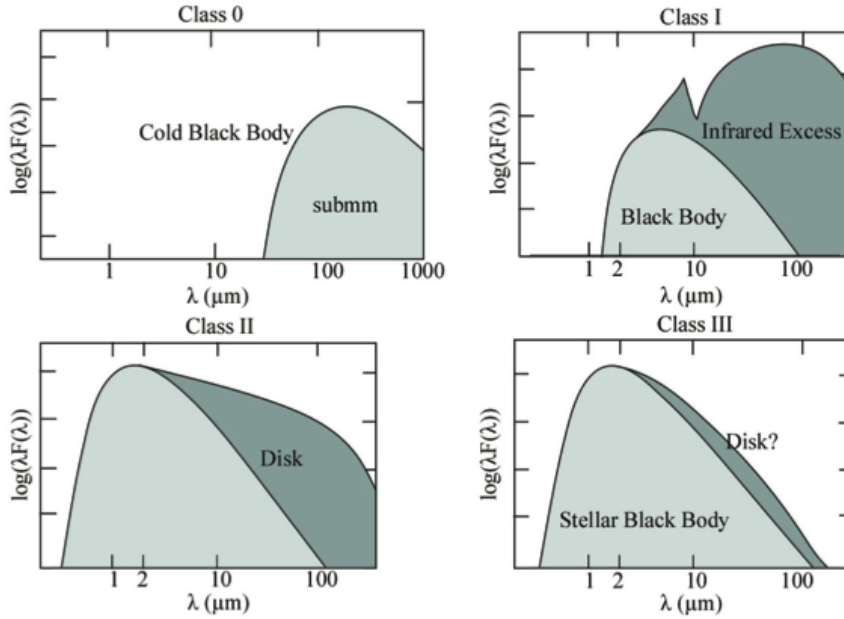
Figure 1.2: Schematic evolution of a typical SED during the pre-MS phase. The initial stage is a cold core ($T_{eff} \sim 20 - 30$ K) with emission peaking in the sub-mm (Class 0). A strong IR excess, peaking in the far-IR, represents a protostar (Class I) with strong accretion luminosity as it accretes from the surrounding molecular envelope. The peak of the emission moves to the mid- and near-IR as an optically thick disc forms around the protostar (Class II; CTTS). The shape of the SED at this stage is dependent upon whether the disc is passive (simply re-radiating photons from the parent star) or active (heating maintained through on-going accretion). The disc dissipates, with only an optically thin component remaining (Class III; WTTS). Reproduced with permission from the ASA. Credit: Burton et al. (2005).

wavelengths likely arises from the infall of dusty material from the surrounding envelope. Such sources are believed to be relatively evolved protostars with both circumstellar discs and envelopes. As the surrounding envelope dissipates due to accretion onto the protostar and the dispersing effects of the bipolar jets, the YSO moves into the Class II phase. Typical SEDs at this phase demonstrate a near blackbody curve at optical wavelengths – indicative of photospheric emission – in addition to strong IR emission associated with a dusty circumstellar disc. As the envelope has dissipated, accretion can only now proceed through the circumstellar disc. As this disc is accreted onto the protostar it will become more tenuous and eventually optically thin. The YSO has now entered the Class III phase. Associated SEDs are almost entirely dominated by photospheric emission, with the remnant disc providing little/no IR excess. The evolutionary timescales associated with Class I, Class II and Class III objects are ~ 0.1, 1 and 10 Myr respectively for a typical mass of $\simeq 1\,M_{\odot}$ (Feigelson & Montmerle 1999).

The class assigned to a particular object depends entirely on its observable properties. During each phase of YSO evolution observables are subject to geometrical effects which may lead to the misclassification of sources (Masunaga & Inutsuka 2000). In the earliest Class 0 phase, a flattened protostellar envelope (Looney et al. 2007), which may

result from large-scale magnetic field structures that act to influence the infall of material from an initially spherical cloud (Galli & Shu 1993a,b) or arising from powerful bipolar jets, may make the source instead appear as a Class I object. Similarly, for more evolved YSOs, the inclination at which it is observed may influence classification, such that at small inclinations a source may appear as a Class II object (with a visible central star) and at larger inclinations may instead seem to be a Class I object (where the central star is obscured by the disc). Further support for the misclassification of sources is presented in White et al. (2007) who summarise that the observable properties of both Class I and Class II objects are similar.

Due to the large photospheric component in the SEDs of Class II and Class III objects, these stages of YSO evolution are generally associated with pre-MS stars (André & Montmerle 1994). Pre-MS stars are currently undergoing gravitational contraction towards the ZAMS, defined as the point at which hydrogen fusion can occur within the stellar core resulting in a state of hydrostatic equilibrium. The evolutionary timescales involved before arriving on the ZAMS are a function of stellar mass. This thesis is predominantly concerned with low-mass pre-MS stars and as such the discussions that follows will focus predominantly on such masses.

1.2.3.2 T-Tauri Stars

The low-mass ($\lesssim 2\,\mathrm{M_\odot}$) end of the pre-MS regime is associated with the class of highly variable objects called T-Tauri stars (TTS). These objects are generally clustered around reflection nebulae and dark clouds (Joy 1945, 1949; Jones & Herbig 1979) or sites of high-mass star formation (Ambartsumian 1947) and therefore presumably young. Spectroscopic measurements further indicated pre-MS evolutionary status, with high lithium abundances in their atmospheres (Bonsack & Greenstein 1960; Strom et al. 1989b). TTS are extremely young objects $\sim 0.1 - 1\,\mathrm{Myr}$ with spectral types ranging from late-G to mid-M (Covino et al. 1997).

The most striking observational property is their variability in all wavelengths and over all timescales (Carpenter et al. 2001; Herbst 2001; Eiroa et al. 2002; Forbrich et al. 2007). Studies have demonstrated a wealth of observational properties including both UV and IR excesses (Mendoza V. 1966; Rydgren et al. 1976; Rucinski 1985), X-rays (Feigelson & Decampli 1981; Walter et al. 1988), blueshifted forbidden line emission (Appenzeller et al. 1984; Edwards et al. 1987) and starspot-modulated lightcurves (Vrba et al. 1986). For a comprehensive discussion of the observational properties of TTS see Appenzeller & Mundt (1989). The general belief is that these properties arise from the existence of a circumstellar disc which remains around the star after the main accretion phase has ceased (Adams et al. 1987; Bertout et al. 1988) or from an active stellar chromosphere (Dumont et al. 1973; Calvet et al. 1984).

TTS have been classified into two distinct groups based on the equivalent width (W_λ) of the Hα emission line – classical T-Tauri stars (CTTS) and weak-lined T-Tauri stars (WTTS). The classification criterion is that TTS with $W_\lambda(\mathrm{H}\alpha) \leq 10\,\mathrm{\AA}$ are deemed
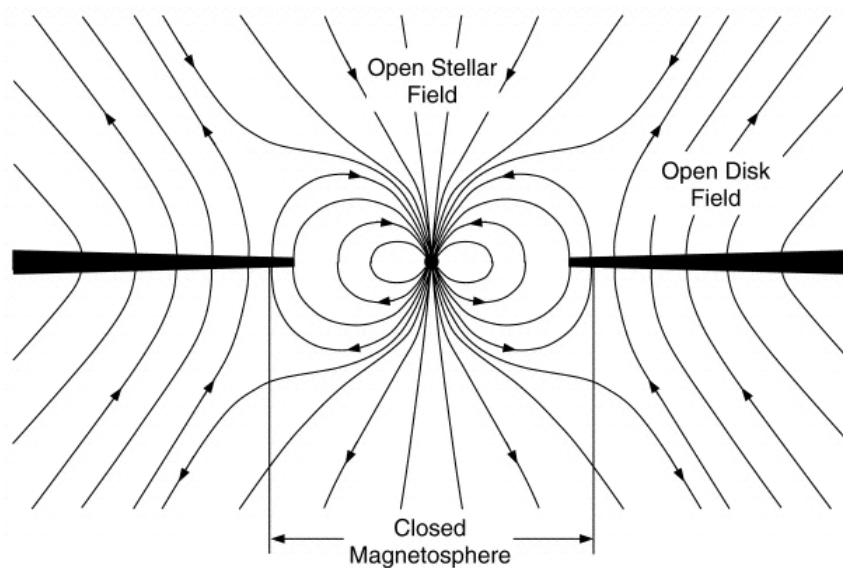
Figure 1.3: An idealised representation of the magnetic field structure of a CTTS. There are three discrete regions of field – i) closed field lines close to the stellar surface that contain the coronal plasma, ii) closed field lines that thread the circumstellar disc and permit accretion flows onto the stellar surface, and iii) open field lines which support outflows. Reproduced with permission from the AAS. Credit: Goodson et al. (1997).

to be WTTS (Herbig & Bell 1988), however this is a somewhat arbitrary choice and has been shown to vary with spectral type (Stahler & Palla 2005).

Classical T-Tauri Stars

CTTS are low-mass pre-MS stars that are actively accreting from a circumstellar disc, which will eventually disperse prior to arrival on the ZAMS. The strong surface magnetic field (typically $2 - 3$ kG; Johns-Krull et al. 1999) disrupts the disc and leads to accretion (see Fig. 1.3). Gas and dust are stripped from the disc and transported along the field lines in the stellar magnetosphere leading to the formation of accretion columns. This material travels along the field lines at near free-fall velocities, as indicated by inverse P-Cygni profiles (Walker 1972; Edwards 1997), and impacts upon discrete regions on the stellar surface. These impacts produce shocks with the excess energy radiated away in the optical, UV and X-ray. Open field lines can carry away material in the form of stellar winds or collimated jets. CTTS are observed to be strong Hα emitters, possibly due to either material within the accretion columns or from chromospheric activity. Observed IR excesses can be attributed to both the reprocessing of photospheric radiation by the dusty circumstellar disc and the heating of gas and dust in the accretion process (Lynden-Bell & Pringle 1974; Kenyon & Hartmann 1987; Beckwith et al. 1990). Robust evidence for this accretion driven production of multi-wavelength excess is the observed strong correlation between the UV and IR excess emission (Hartigan et al. 1990; Edwards 1995).

Weak-lined T-Tauri Stars

WTTS are believed to be a stage of pre-MS evolution following the CTTS stage and the dispersal of the circumstellar disc. Weak Hα emission suggests that it is primarily produced through chromospheric activity with a distinct lack of magnetically channelled accretion columns, as noted by the absence of UV excess in WTTS (Montmerle et al. 1993). High chromospheric magnetic activity is observed on WTTS (Bouvier 1990), leading to enhanced levels of X-ray emission. Measured IR excesses are smaller for WTTS, suggesting either depletion of or a smaller circumstellar disc component. WTTS that exhibit no IR excess are believed to harbour no disc and as such are termed naked T-Tauri stars (NTTS; Walter 1986). Whereas Walter (1986) defined NTTS on a multi-wavelength basis (i.e. lack of accretion and disc signatures in the optical and IR), Herbig & Bell (1988) defined WTTS as pre-MS stars with $W_\lambda(\mathrm{H}\alpha) \leq 10\,\text{Å}$, hence while all NTTS are WTTS the converse is not true. Some stars traditionally classified as WTTS based on Hα emission in fact have mass accretion rates comparable to that of CTTS (Littlefair et al. 2004). Hence the classification scheme based solely on Hα can lead to misclassification, however CTTS have other observational characteristics such as excess continuum emission in the UV, optical and IR which should aid classification.

Post T-Tauri Stars

A further category of TTS are the post T-Tauri stars (PTTS). PTTS are low-mass pre-MS stars with properties between those of TTS – either CTTS with an associated disc or WTTS without any such structure – with ages of less than a few Myr and ZAMS stars with ages exceeding tens of Myr, depending on spectral type (Bubar et al. 2007). No strict observational criteria exist with which to define a PTTS however it is assumed that such stars are Li rich compared to their ZAMS counterparts in moderately aged clusters (e.g. the Pleiades) and whose position in either a Hertzsprung-Russell (H-R) diagram or colour-magnitude diagram (CMD) is above the main-sequence (MS). Some PTTS show evidence of disc material (Rucinski & Krautter 1983; Brandner et al. 2000), however at the age of the Pleiades ($\sim 100\,\text{Myr}$) very few stars show IR excess (Meyer & Beckwith 2000). Strong Hα emission has also been observed on some PTTS (Henize 1976), however comparisons of median X-ray luminosity in clusters with different ages suggest a steady decline between 1 and 100 Myr, although the spread of X-ray luminosities at a given age makes differentiation between possible older pre-MS and ZAMS stars difficult (Briceño et al. 1997). It is clear that the observable properties of PTTS are complex and manifold and that any secure classification must be made on the basis of several criteria (Mamajek et al. 2002; Montes et al. 2009).

Adams et al. (1987) suggested that the classification of YSOs based on their spectral index can be interpreted in terms of an evolutionary sequence from Class 0 to Class III objects, however as discussed in Herbig (1978) and Jensen (2001), the lack of observed PTTS coupled with similar age estimates for both CTTS and WTTS suggests that the evolutionary sequence of YSOs – evolving from Class 0 objects to Class III – may not be

unambiguous. It seems reasonable that Class 0 objects evolve into Class I, however the evolutionary progression from Class II to Class III objects may not be as definitive. Observational evidence that shows the coevality and different spatial distributions of CTTS and WTTS with respect to their associated molecular cloud (Neuhäuser et al. 1995; Feigelson 1996) may indicate that CTTS and WTTS are not evolutionary stages of similar mass objects, but instead different evolutionary tracts dependent upon the star-disc interaction. Conversely, observations have also shown significant deviations in the ages between CTTS and WTTS (Wichmann et al. 1997). Differences in both the age and mass between the samples of CTTS and WTTS – where the WTTS are in general older and predominantly more massive than the CTTS – can be explained by a disc evolution model in which CTTS evolve into WTTS after the disc is completely accreted by the star (Bertout et al. 2007). These studies highlight the importance of the star-disc interaction during early pre-MS stellar evolution.

1.2.4 Rotational Evolution

The evolution of pre-MS stars is dominated by both the gravitational contraction and accretion from the disc/envelope. One would thus expect that as material, and hence angular momentum, is accreted onto the protostar it continually spins-up during this contraction towards the ZAMS. The star-disc interaction involves both mass and angular momentum transfer. Accretion onto the star and the presence of jets/outflows are obvious manifestations of mass transfer, whilst angular momentum transfer is believed to be the dominant factor in dictating the rotational evolution of young stars. A study of stellar rotation from young pre-MS objects to those on the ZAMS yields clues to the solution of the angular momentum problem, which is that a star has significantly less angular momentum than an equivalent mass in the ISM. The specific angular momentum of a molecular cloud core is $\sim 10^{21}\,\mathrm{cm^2\,s^{-1}}$ (Goodman et al. 1993; Caselli et al. 2002), while protostars have specific angular momentum of order $\sim 10^{16}\,\mathrm{cm^2\,s^{-1}}$ (Bouvier et al. 1993; Herbst et al. 2007, see also Bodenheimer 1995). The distribution of angular momentum in the orbital motions of protostars within such clouds may partially explain this dilemma, however an additional reduction of $1-2$ orders of magnitude in specific angular momentum is still required to account for the rotation rates of solar-type stars at $100\,\mathrm{Myr}$ and the rotation of the Sun at $4.5\,\mathrm{Gyr}$ (Mathieu 2004). Angular momentum loss during the earliest stages of protostellar formation can be attributed to magnetic torques between the collapsing cloud core and the surrounding interstellar material (Larson 1973; Fleck & Hunter 1976). During the later stages of protostar evolution TTS jets and outflows can remove angular momentum from the star-disc system (Blandford & Payne 1982; Dopita et al. 1982) with strong observational evidence that outflow activity is tightly correlated to the presence of discs and accretion activity (Strom et al. 1988; Königl & Pudritz 2000). The rotational nature of these jets and the derived rotational velocities suggest that the amounts of angular momentum loss may be large (Bacciotti et al. 2002). A complete solution to the complexities of angular momentum loss will no doubt be a multifaceted affair combining

several mechanisms over the course of the formation of the star (Bodenheimer 1995).

Prior to the intense photometric monitoring campaigns of SFRs over the past couple of decades, very few young $(5-30\,\mathrm{Myr})$ low-mass stars were known and as such the theory of rotational evolution in the pre-MS phase was primarily based on the interpolation between the youngest regions $(< 5\,\mathrm{Myr};$ the Orion Nebula Cluster [ONC], IC 348 and NGC 2264) and ZAMS clusters $(30-100\,\mathrm{Myr};$ the Pleiades and α Per). This in-depth monitoring has provided robust rotation period distributions in this critical age range. Photometric variability studies are now able to constrain rotation rates of pre-MS stars to high precision. This photometric variability is primarily due to high surface magnetic activity producing cool spots in the stellar chromosphere. Rotation of these spots with the star will cause luminosity fluctuations. Spot patterns are sufficiently asymmetric and stable enough to allow observers to photometrically determine rotation rates (e.g. Herbst et al. 1994). Studying the luminosity variations at given wavelengths allows information concerning the spots – such as temperature, size and areal coverage – to be extracted. Using these rotation rates in conjunction with observing SFRs at different evolutionary stages allows the effects of stellar age on rotation rates to be investigated (Terndrup et al. 2000; Herbst et al. 2002a; Lamm et al. 2004; Rebull et al. 2004; Littlefair et al. 2005, 2010). The advantage of using photometric variability studies over spectroscopic ($v \sin i$) studies is that the photometrically derived rotation rates are independent of stellar inclination and can be used to derive rates of slowly rotating stars. There are still issues that need to be addressed when treating photometric studies, such as integrating the effects of differential rotation which has both been observed (Collier Cameron et al. 2002; Donati et al. 2010) and predicted theoretically (Smith 1994; Browning 2011), although others have questioned this insisting instead that TTS essentially rotate as rigid bodies across their surface (Bouvier et al. 1995; Kuker & Rudiger 1997; Cohen et al. 2004). A further complication in the determination of photometric rotation rates is one of bias concerning the study of TTS in SFRs. This bias is towards detections of periods among WTTS, whereas the irregular variations in CTTS may mask underlying rotational periods, hence more detections are likely to be found for WTTS.

A compilation of literature rotation periods for stars with masses $< 1.2\,\mathrm{M}_\odot$ in young $(< 1\,\mathrm{Gyr})$ open clusters has been collated by Irwin & Bouvier (2009) (see Fig. 1.4), which when combined with several more recent studies (Collier Cameron et al. 2009; Hartman et al. 2009; Sukhbold & Howell 2009; Hartman et al. 2010; Meibom et al. 2011a,b) that further increase the available data in the $125\,\mathrm{Myr}-1\,\mathrm{Gyr}$ range, make it possible to draw conclusions on rotational evolution in two separate mass regimes.

1.2.4.1 Solar Mass

Solar mass stars $(0.9 \lesssim M_\star \lesssim 1.1\,\mathrm{M}_\odot)$ will remain in the pre-MS phase for approximately $30\,\mathrm{Myr}$. The slowest rotators have periods $\sim 10\,\mathrm{days}$ at ages of $\sim 1\,\mathrm{Myr}$. The rotation period remains almost constant to an age of $\sim 5\,\mathrm{Myr}$, eventually spinning-up to $\sim 8\,\mathrm{days}$ by $\sim 40\,\mathrm{Myr}$, at which point gravitational contraction has ceased. The most rapidly rotating
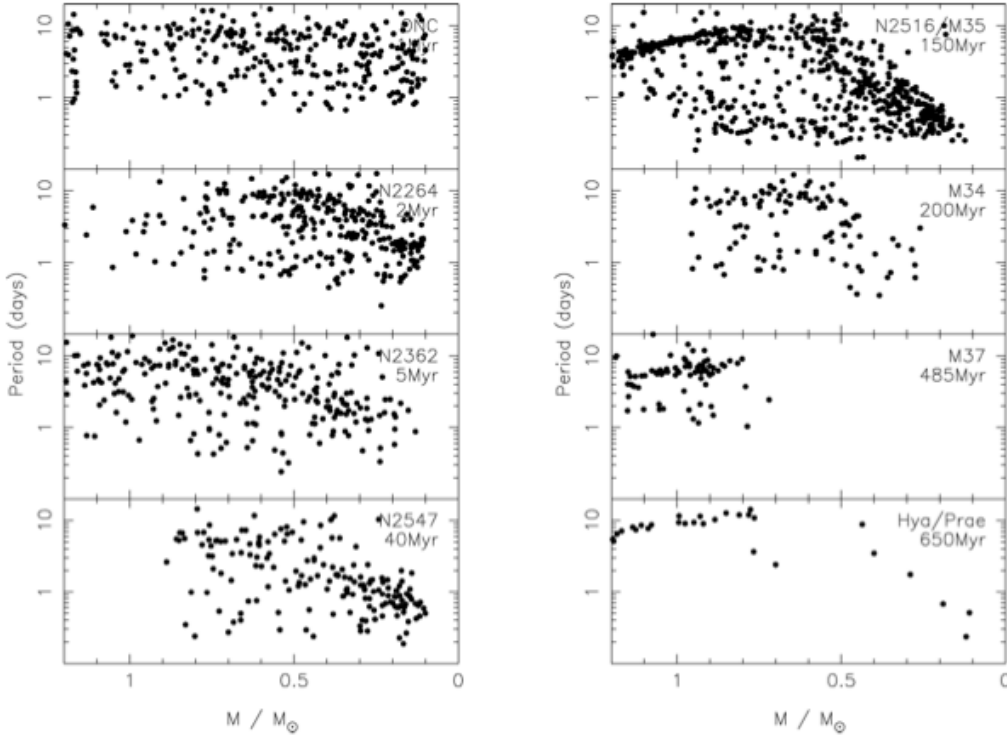
Figure 1.4: Rotation periods for stars with masses $\lesssim 1.2\,\mathrm{M_\odot}$ in young ($\lesssim 1\,\mathrm{Gyr}$) open clusters from the available literature. Each panel plots the rotational periods as a function of stellar mass for a particular cluster. Note that NGC 2516 and M 35 have been combined as they have essentially identical ages, as have the Hyades and Praesepe. Stellar masses are based on the *I*-band magnitude of the sources in conjunction with the evolutionary models of Baraffe et al. (1998) assuming literature values of the age, distance modulus and reddening for each cluster. Reproduced with permission from the IAU. Credit: Irwin & Bouvier (2009).

objects with periods $\sim 1\,\mathrm{day}$ at $\sim 1\,\mathrm{Myr}$ spin-up to $\sim 0.6\,\mathrm{days}$ at $\sim 5\,\mathrm{Myr}$ and $\sim 0.2\,\mathrm{days}$ at $\sim 40\,\mathrm{Myr}$ (consistent with predictions from stellar contraction). This behaviour suggests the presence of a mechanism acting to remove angular momentum from the slow rotators only up to an age of $\sim 5\,\mathrm{Myr}$ with further angular momentum losses ceasing soon after, hence leaving the star free to spin-up towards the ZAMS. This results in a range of rotation rates in early MS clusters with ages $\sim 100-150\,\mathrm{Myr}$. In more evolved clusters such as the Hyades and Praesepe (age $\sim 650\,\mathrm{Myr}$) this range of rotation rates is no longer observed, instead, for a star of given mass the rotation rate is well defined (allowing for the paucity of data in this domain). Hence indicating that another rotation rate dependent angular momentum loss mechanism operates in the early MS phase, with the more rapid rotators losing more angular momentum than more slowly rotating stars.

1.2.4.2 Fully Convective

The behaviour of the fully convective stars is rather different from the solar mass objects. The most massive of the low-mass fully convective objects ($M_\star \simeq 0.4\,\mathrm{M_\odot}$) will reach

the ZAMS at approximately $\sim 150\,\text{Myr}$. Over this timescale, all these stars appear to continually spin-up onto the ZAMS, and the maximum rotation rate observed is clearly a function of mass. This suggests that there is little rotation rate dependence in this mass domain, and further, that these stars lose little angular momentum during pre-MS contraction. Also in contrast to the solar mass stars, is that between ~ 150 and $\sim 650\,\text{Myr}$ there appears to be no evolution of rotation periods, indicating that little angular momentum is lost in the early MS phase.

1.2.4.3 Models of Rotational Evolution

These results indicate that some efficient braking mechanism is present during the early stages ($\sim 5-10\,\text{Myr}$) of low-mass pre-MS evolution (Scholz et al. 2007). Angular momentum evolution for MS stars is primarily based upon the loss via magnetised stellar winds (Skumanich 1972), although alternative theories exist proclaiming the importance of the presence/depth of convective zones in regulating the angular momentum loss (Barnes 2003b). It is strongly believed that the angular momentum evolution of young pre-MS stars is greatly influenced by the interaction between the star and its circumstellar disc. This star-disc interaction is significant in the transfer of both mass and angular momentum and is believed to be responsible for the observed slow rotation of young stars.

Models of angular momentum evolution during the pre-MS phase and the contraction onto the ZAMS have been developed over the past couple of decades and rely on two basic mechanisms for the removal of angular momentum from the star. Primarily there is the disc-locking process in which angular momentum is efficiently removed from the star as long as it is magnetically interacting with the circumstellar disc thus forcing the star to evolve at a constant angular velocity despite gravitationally contracting during this time (Königl 1991; Collier Cameron & Campbell 1993; Collier Cameron et al. 1995; Bouvier et al. 1997). Disc-braking operates on only short timescales i.e. comparable with the disc lifetime of $1-10\,\text{Myr}$ (see Section 1.2.5). The other mechanism is a magnetised solar-type stellar wind extracting angular momentum from the star and working in unison with disc-locking, although the wind is less efficient at removing angular momentum and saturates at high velocities (Kawaler 1988; Keppens et al. 1995; Matt & Pudritz 2005a). Angular momentum loss by magnetised winds is still likely in young pre-MS stars, with the chance that these winds are stronger than MS counterparts due to enhanced levels of magnetic activity (Walter et al. 1988). The timescales on which this type of braking occurs are greater than the Kelvin-Helmholtz timescale and is thus unable to prevent the star from spinning-up during contraction (Matt & Pudritz 2007) and regulates the stellar spin-down on timescales of hundreds of Myr. Naturally, one would expect a range of disc lifetimes and thus stars will be released from the disc-locking process at various times resulting in a distribution in rotation rates during the pre-MS and onto the ZAMS.

Despite the fact that these mechanisms lack a complete theory of the processes by which angular momentum is removed and instead rely on semi-empirical parameterised braking laws, they have been shown to reproduce reasonably successfully the overall trends

observed in the rotational evolution of young low-mass stars (Yi 1994; Armitage & Clarke 1996; Bouvier et al. 1997; Allain 1998; Sills et al. 2000). More recent models (Matt & Pudritz 2005b; Matt et al. 2010) also include the opening of magnetic field lines connected to the star due to differential rotation between the star and circumstellar disc. This opening of magnetic field lines acts to reduce the spin-down torque on the star.

From the available rotation rate information it is clear that some mechanism is responsible for the regulation of the angular velocity during the initial several Myr of pre-MS evolution (see also Scholz 2009). Although the exact processes underpinning this regulation, or which component is the most dominant, remain unclear it has been shown that when the ambiguities concerning near-IR excesses and observational biases are removed there is a clear correlation between rotation rate and the presence of a circumstellar disc (e.g. Cieza & Baliber 2007). Thus it is suggestive that whichever mechanism is responsible, it is intimately linked to the interaction between the parent star and circumstellar disc.

1.2.5 Circumstellar Discs and Magnetospheric Accretion

Circumstellar discs are a ubiquitous by-product of the star formation process (see Section 1.2.3.1). High-resolution sub-mm continuum observations indicate that average disc sizes around TTS are of order $\sim 200\,\mathrm{AU}$ (Andrews & Williams 2005) with similar estimates derived on the basis of millimeter interferometry (Dutrey et al. 1996; Kitamura et al. 2002). The initial dimensions of circumstellar discs are non-trivial to assess as, prior to the TTS stage of protostellar evolution, such objects are heavily embedded in envelopes that emit at wavelengths similar to the disc itself, however estimates for even these youngest objects are akin to those for more evolved objects (Jørgensen et al. 2005a).

To explain the observed slow rotation of accreting CTTS, a magnetised braking theory – originally developed for accreting neutron stars (Ghosh & Lamb 1978, 1979) – was modified for accreting CTTS and suggests that the magnetic star-disc interaction could regulate the angular momentum of the star via magnetic coupling of the star to a disc truncated at a distance of a few stellar radii (Camenzind 1990; Königl 1991). To produce a situation in which accreting CTTS are rotating slowly, it is necessary that some magnetic field lines thread the disc outside of the co-rotation radius – the radius at which the Keplerian angular velocity of the disc matches the rotation angular velocity of the star – while at the same time material is accreted onto the star through field lines that intersect the disc inside of co-rotation. The details of how the field lines bisect the circumstellar disc and the processes occurring in this interaction region remain unclear, and although the field lines are believed to be confined to a region close to co-rotation (Wang 1995), if the field lines are attached to a region that rotates with a slightly different velocity to that of the star this will lead to stretching and warping of the field lines. As a way of side-stepping this inevitability, Shu et al. (1994) suggested that the field lines interact with the disc within a confined region at the co-rotation radius only, hence the star and field lines rotate synchronously, however this assumes that stellar magnetic fields

are both axisymmetric and steady. Observed line profiles indicate that the magnetosphere of accreting CTTS may not be axisymmetric (Giampapa et al. 1993; Johns & Basri 1995b) and that accretion from the disc is non-steady (Herbst et al. 1994; Johns & Basri 1995a). With this in mind, a more complex picture of time-variable magnetospheric accretion (van Ballegooijen 1994) appears more plausible with excess magnetic energy arising from differential rotation between the star and disc released via reconnection events (Aly & Kuijpers 1990). MHD simulations have shown that angular momentum can be extracted from the star by the magnetic field and transported away by the disc or by accretion driven winds (Romanova et al. 2002). Hence as long as the star is accreting material from the disc, it will experience magnetic braking (Ferreira et al. 2000; Matt & Pudritz 2005a).

Magnetospheric accretion makes clear predictions regarding the existence of certain phenomena for which the observational evidence is robust (Muzerolle et al. 1998; Bouvier et al. 2007). The theory suggests that the disc is truncated by the magnetosphere at a few stellar radii and that material can then be channelled via magnetic field lines to impact upon the stellar surface. Given typical mass accretion rates ($10^{-9} - 10^{-7}\,\mathrm{M_\odot\,yr^{-1}}$; Gullbring et al. 1998a) and magnetic field strengths (typically $2-3\,\mathrm{kG}$; Valenti & Johns-Krull 2004), circumstellar cavities of $\sim 3 - 8$ stellar radii are required to explain the near-IR SEDs of CTTS (Bertout et al. 1988; Meyer et al. 1997) and the line widths of CO emission, likely arising from the gas within the circumstellar disc (Najita et al. 2003, 2007). Shapes of SEDs have been observed which are consistent with inner disc cavities (D'Alessio et al. 2005; Dutrey et al. 2008). However, whether this is as a result of the magnetospheric accretion process or instead evidence of disc clearing due to, for example, binary or planet formation, photoevaporation or photoionisation of the disc, or dust grain growth (see Mayne & Harries 2010) is still debatable. Evidence for accretion columns comes in the form of observed inverse P-Cygni profiles with redshifted line widths reaching several hundred $\mathrm{km\,s^{-1}}$, indicating that material is accreting onto the star from a distance of a few stellar radii (Walker 1972; Edwards 1997). Accretion shocks are inferred from rotational modulation of bright surface spots (Simon et al. 1990; Kenyon et al. 1994; Bouvier et al. 1995). The prediction of these hot spots and associated excess emission is supported by accretion models representing observed SEDs of optical and UV excess (Calvet & Gullbring 1998; Ardila & Basri 2000; Gullbring et al. 2000). Recent evidence suggests that accreting systems show large veiling variability in the near-IR (Eiroa et al. 2002; Barsony et al. 2005) indicating that time variable accretion is present within such systems. In conjunction with the fact that measured near-IR veiling measurements in CTTS are often greater than the values predicted by standard disc models (Folha & Emerson 1999) suggests that the inner disc topology is markedly modified by the star-disc interaction (Bouvier et al. 2003). So-called veiling is a confusing term as it refers to two distinct phenomena that are not easily disentangled – i) the filling-in of spectral lines and ii) an overlying continuous emission, where the net effect of either process is to decrease the absorption line equivalent width of given spectral lines with respect to a standard star.

An easy assumption to make on the basis of the above evidence is that any accretion-

rotation connection should manifest itself as accreting objects rotating, on average, slower than non-accreting objects. Such correlations have been noted among TTS in young SFRs (Edwards et al. 1993; Herbst et al. 2002a; Dahm & Simon 2005; Lamm et al. 2005; Cieza & Baliber 2007), although non-correlations have also been detected (Stassun et al. 1999; Rebull 2001; Makidon et al. 2004; Cieza & Baliber 2006). Reasons for this ambiguity are highlighted in Rebull et al. (2006a) and may be attributed to; i) inaccuracies in the near-IR excesses and ii) the effects of sample size (e.g. age mixing). Addressing the former issue, it is typically the K-band that is used to calculate the near-IR excess however there are several effects which may interfere with robust measurements including geometrical effects, for instance, the size of the inner disc wall or cavities within the disc (Natta et al. 2001; Isella & Natta 2005). Projection effects (Hillenbrand et al. 1998) and contrast between the photosphere and disc may also hamper determinations. Rotation rates among young pre-MS stars cover a broad distribution and so a large sample is needed before one can, with any degree of certainty, testify to an observable signature between stars with associated circumstellar discs and stars that lack such structures, and hence further differentiate those that are 'locked' to those that are freely rotating. To fully investigate the accretion-rotation paradigm, a robust method is needed to differentiate between accreting and non-accreting objects. Commonly used near/mid-IR excesses or colour indices only prove the presence of a circumstellar disc, not that the star is actively accreting (Rebull et al. 2006a). UV continuum excesses (Johns-Krull et al. 2000; Herczeg & Hillenbrand 2008) and Hα line emission (Edwards et al. 1987; Kurosawa et al. 2006) are more thorough determinants for accretion onto the star, however Hα emission is also produced via chromospheric emission, hence the emission flux/width must exceed this component.

One crucial factor in the efficiency of the star-disc interaction in regulating stellar rotation rates during the pre-MS contraction is the disc lifetime itself. Herbst & Mundt (2005) and Herbst et al. (2007) suggest that the disc locking mechanism is only effective in removing significant amounts of angular momentum for the first $5 - 6$ Myr of pre-MS evolution which is consistent with observations indicating no significant angular momentum loss after ~ 5 Myr (Scholz et al. 2007; Irwin & Bouvier 2009). These timescales may be linked to the presence of a disc and hence a representation of typical disc lifetimes.

1.2.5.1 Disc Lifetimes

Observations of the ONC have shown that the local environment has a marked effect on the evolution and subsequent lifetime of circumstellar discs (O'Dell et al. 1993; McCaughrean & O'Dell 1996). Recent evidence also suggests erosion by massive neighbours (Adams et al. 2004) and the parent star (Alexander et al. 2006a,b; Gorti & Hollenbach 2009). The erosion of circumstellar discs is a consequence of the UV and X-ray flux generated by the more massive stars that act to photoevaporate disc material, culminating in material streams from the disc (Hollenbach & Adams 2004). Disc erosion not only depends on the proximity to massive stars, but also on the number density of massive stars in the surrounding region. As this increases so does the levels of UV/X-ray flux in the region, hence one would

expect areas containing more massive stars, or where stars are more densely clustered, to erode circumstellar discs on much shorter timescales than more quiescent regions (Haisch et al. 2001a; Lyo et al. 2003; Mayne et al. 2007). Recent observations have highlighted discrepancies as to whether the effect of massive neighbouring stars is pronounced (Stolte et al. 2004; Guarcello et al. 2009; Roccatagliata et al. 2011) or not (Balog et al. 2007; Hernández et al. 2007). Comparisons between models (Sills et al. 2000) and observations suggest that rotational velocities of low-mass pre-MS stars are regulated on timescales of $2 - 10\,\mathrm{Myr}$. As the star-disc interaction governs the braking during the pre-MS evolution, it is reasonable to suggest that active accretion occurs over these timescales.

Circumstellar disc lifetimes around young, low-mass stars have been the topic of investigation of several recent observational studies (Hernández et al. 2007; Sicilia-Aguilar et al. 2008; Currie & Kenyon 2009; Luhman et al. 2010). Current disc lifetimes are inferred from a combination of stellar ages and other diagnostics including near/mid-IR excesses and Hα emission line widths. As mentioned previously, near/mid-IR excesses only reveal the presence of a disc, whereas Hα can directly track active accretion. Estimates based solely on IR excesses demonstrate disc fractions of $40 - 60\,\%$ for stellar ages $\simeq 1\,\mathrm{Myr}$, with no evidence of prevailing discs past $5 - 6\,\mathrm{Myr}$ (Haisch et al. 2001b; Hillenbrand 2005). Estimates incorporating Hα line profiles plus IR excesses suggest longer disc survival times with a disc fraction of $40 - 60\,\%$ at ages $\simeq 2\,\mathrm{Myr}$ (Damjanov et al. 2007) with accretion ceasing on timescales $\simeq 10\,\mathrm{Myr}$ (Jayawardhana et al. 2006). Despite the lack of accretion based indicators, IR disc signatures are still observed at this stage (Sicilia-Aguilar et al. 2006a) with indications that disc survival times are inversely correlated with stellar mass (Carpenter et al. 2006; Lada et al. 2006; Hernández et al. 2007; Currie et al. 2009b). The effects of binarity on disc lifetimes has been investigated by Bouwman et al. (2006). They looked at the η Cha cluster (age $\simeq 8\,\mathrm{Myr}$) and found that the presence of a circumstellar disc was anti-correlated with binarity and derived a mean disc lifetime of 9 and $5\,\mathrm{Myr}$ for low-mass single and binary stars respectively. Studies investigating whether warm circumstellar dust discs survive in older open clusters (Mamajek et al. 2004; Gorlova et al. 2007) have found that the fraction of stars with excess emission in the mid-IR ($3-8\,\mu\mathrm{m}$) is less than $1\,\%$, in contrast to the fraction that demonstrate excesses at longer wavelengths (tens of $\%$) that are indicative of a large debris disc population. These results, combined with surveys of younger clusters, suggest that circumstellar discs become so optically thin as to be undetectable in the mid-IR on timescales of $\sim 20\,\mathrm{Myr}$.

1.3 Comparing Theory and Observations

It is clear that any comprehensive theory of star formation hinges on the adopted timescales for specific phenomena – be it the timescale required for a protostar to evolve through the pre-MS phase and onto the MS; the timescale on which the rotational evolution of a star is regulated, and by extension the lifetime of circumstellar discs; or differentiating between competing theories of star formation (see Section 1.2.2). Key to the derivation

of such timescales, is the ability to compare theoretical predictions with observable stellar properties. By studying regions of current/recent star formation the importance of these physical processes can be determined. Furthermore, by deriving mean ages and age distributions the timescales over which certain processes occur can be understood, and then, once a general theory is in place, further investigation as to how variations in environmental conditions affect this theory can be assessed.

1.3.1 OB Associations

Observable groups of stars such as OB associations are relatively rare, however such aggregates are almost always young, based either on their photospheric properties or by their association with nearby gas. Near-IR studies of close SFRs have concluded that clustering is an important feature in the early stages of stellar evolution (Lada 1991; Lada & Lada 2003; Porras et al. 2003), further suggesting that most, if not all stars, form in clusters and associations. Recent *Spitzer* data analysis of the YSO surface densities (Σ) in nearby (< 500 pc) SFRs by Bressert et al. (2010) shows that the spatial distribution is smooth and continuous with little evidence for discrete modes of star formation. Bressert et al. (2010) argue that only a small fraction of stars form in dense clusters and that the very definition of a 'cluster' has a major influence on the reported fractions of stars believed to form in aggregates in the solar neighbourhood. N-body simulations of static and dynamically evolving star clusters by Parker & Meyer (2012), however, have shown that the distribution of Σ is degenerate i.e. many different cluster morphologies – smooth or sub-structured – produce similar cumulative distributions. Gieles et al. (2012) suggest that the observed Σ is exactly what one would expect if the majority of stars are born in clusters, however due to the degeneracy of Σ, it is not possible to use it alone to place constraints on the initial conditions of star formation and should therefore be combined with other metrics (see also Parker & Meyer 2012).

Star formation occurs within the cold, deeply embedded cores of molecular clouds known as infrared dark clouds (IRDCs), the presence of which is revealed in the absorption of the diffuse background mid-IR emission from the Galactic plane (Egan et al. 1998). The fate of such embedded cores depends primarily on the local environment, but a typical molecular cloud may spawn one or more complexes known as OB associations which further contain clusters, groups and subgroups (Kholopov 1959; Herbig 1962; Strom et al. 1975). It was noted from the earliest reliable spectral typing for bright stars that O and B-type stars are not distributed randomly across the sky but instead tend to congregate in loose associations. The term 'association' was introduced by Ambartsumian (1947) to describe these groups of OB stars which have a typical stellar mass density of less than $0.1 \, \mathrm{M_\odot \, pc^{-3}}$. Stellar groups of such low-density will disperse with time due to a combination of large internal velocities ($\sim$ few $\mathrm{km \, s^{-1}}$) and Galactic tidal effects (Bok 1934; Blaauw 1952), meaning that OB associations do not survive as coherent entities for much longer than $10 - 30 \, \mathrm{Myr}$, and as a result it can become difficult to differentiate the low-mass population from the background field stars. Hence it was proposed that OB associations are young

($\sim 10\,\mathrm{Myr}$; Ambartsumian 1949), a claim later supported by the ages derived from CMDs (Lohmann 1957; von Hoerner 1957). OB associations are generally located in or near SFRs, tracing the spiral structure of the Galaxy (Morgan et al. 1953; Walborn 1971), due largely to the fact that such stars are too young to have moved far from their places of birth, and are thus prime sites in which to study recent and on-going star formation (Blaauw 1964, 1991).

Studies of the observable properties of OB associations (Blaauw 1964; Garmany & Stencel 1992; de Zeeuw et al. 1999) indicate a large range in both size and number of OB stars, ranging from the most compact ($\sim$ few parsecs) to the most extended ($\sim$ several hundred parsecs) and harbouring anything from a single to over a hundred OB stars. The majority of OB associations are comprised of a number of smaller subgroups that reflect various epochs of star formation within the region and as such will be at various evolutionary stages – see for instance the Orion OB1 and Cep OB2 associations. Age estimates for associations can be derived from a CMD using theoretical evolutionary models or from kinematic datasets – assuming that all O and B-type stars have a common origin – with current estimates placing an upper limit of $\sim 10\,\mathrm{Myr}$, although older populations of low-mass pre-MS stars have been identified in both the Lower Centaurus-Crux and Upper Centaurus-Lupus subgroups of the nearest OB association Scorpius-Centaurus (Mamajek et al. 2002).

Until recently, it was believed that only high-mass stars form in OB associations and low-mass stars in so-called T associations (Larson 1986). T associations are similar to OB associations, but lack the distinguishing OB stars. Large-scale surveys of OB associations, however, have found that OB associations not only produce high-mass stars but also hundreds of low-mass members (Walter et al. 1998; Naylor & Fabian 1999; Pozzo et al. 2000; Preibisch et al. 2002; Pozzo et al. 2003). The dispersed nature of such associations is not due to rapid dispersal of material, but instead reflects the topology of the parent cloud (Palla & Stahler 2002) and, when combined with current age estimates for low-mass stars, suggest that the parent molecular clouds are transient structures with lifetimes of $\lesssim 10\,\mathrm{Myr}$ and that star formation is a rapid and triggered process (Briceño et al. 2007; Briceño 2009).

1.3.2 Hertzsprung-Russell Diagram

The H-R diagram is arguably the most powerful conceptual tool in stellar astrophysics. The H-R diagram is a plot that relates the luminosity of stars to their effective temperature – or spectral type – and represents the combined efforts of a number of astronomers, in particular Enjar Hertzsprung and Henry Russell. A star's effective temperature is related to its bolometric luminosity by

$$L_{\mathrm{bol}} = 4\pi R_\star^2 \sigma T_{\mathrm{eff}}^4, \tag{1.8}$$

where L_{bol} is the bolometric luminosity, $R_\star$ is the stellar radius, σ is the Stefan-Boltzmann
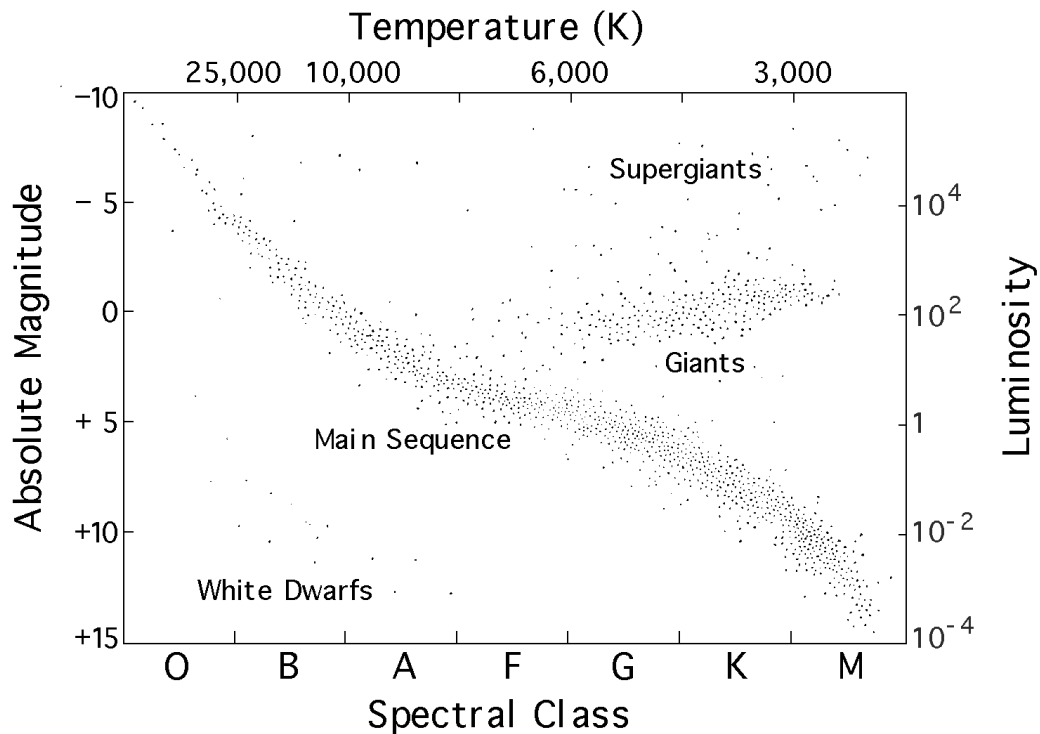
Figure 1.5: A Hertzsprung-Russell diagram illustrating the three main population regions – i) MS (dwarf) stars, ii) the giant stars, and iii) the white dwarf stars. Credit: Phil Newman, `http://heasarc.gsfc.nasa.gov/docs/RXTE_Live/class.html`.

constant and T_{eff} is the effective temperature. The observational equivalent of the H-R diagram is the CMD which plots stellar colours against magnitudes. Hertzsprung (1911) published the first diagrams depicting colour against luminosity for stellar clusters, whilst at a similar time Russell (1910) was studying the relationship between stellar spectral classification and their absolute magnitude using reliable parallax measurements of stars in the solar neighbourhood, publishing his first CMD in Russell (1913).

The diagrams of Hertzsprung (1911) and Russell (1913) highlighted two distinct groups of late-type stars, one of which is the MS – termed MS or dwarf stars – and the other was a group of stars known as giants (see Fig. 1.5). The majority of stars, including the Sun, lie along a diagonal band (in $\log L_{\text{bol}} - \log T_{\text{eff}}$ space) of the MS. The MS represents the stage in a star's life when the interior reaches sufficient temperature and density that hydrogen begins fusing to form helium. This thermonuclear energy release halts any further contraction and the star is defined as being on the ZAMS and in a state of hydrostatic equilibrium. Stellar MS lifetimes are dependent upon mass, with lower mass stars spending more time on the MS. The process by which hydrogen is converted into helium in the stellar core is directly related to the temperature of the core and therefore the mass of the star. Lower mass stars ($\lesssim 1\,\text{M}_\odot$) follow the proton-proton (p-p) chain reaction (e.g. Eddington 1917, 1926), whereas in higher mass objects ($\gtrsim 1.3\,\text{M}_\odot$) the dominant source of energy in MS stars is the CNO-cycle of nuclear reactions (von Weizsäcker 1938;

Bethe 1939). Once core hydrogen burning has ceased the star will evolve away from the MS, where hydrogen burning continues in a shell around the core and eventually the core becomes hot enough to fuse helium. Depending on the stellar mass, the star will evolve into a red giant or supergiant. These giants are located to the right and above the MS and represent stars that are brighter than their MS counterparts of same $T_{\rm eff}$, or of lower $T_{\rm eff}$ for a similar $L_{\rm bol}$, hence a spectral shift towards the red. From Eqn. 1.8, a higher $L_{\rm bol}$ and lower $T_{\rm eff}$ implies a larger radius, hence the term giant. Another region that is relatively well populated resides in the lower left corner of the H-R diagram, and represents populations of stars that have small radii and a bluish-white colour, these are called white dwarfs. It is quite clear from observing any H-R diagram that a given stars location is not random and that the distribution of a number of stars is restricted to a few well-defined regions. Stars within the same region share common characteristics and as these physical characteristics of a star change over its lifetime, its position within the H-R diagram will change accordingly, hence the H-R diagram can be thought of as a visual representation of stellar evolution and, more importantly, can be used to test and constrain theoretical models of stellar evolution (Gamow 1939; Schönberg & Chandrasekhar 1942; Henyey et al. 1955; Hoyle & Schwarzschild 1955; Hayashi 1961, 1966).

1.3.3 Pre-Main-Sequence Evolution in the Hertzsprung-Russell Diagram

The protostellar phase, as described in Section 1.2.3.1, is a very brief one, after which, the pre-MS star emerges from its natal envelope and contracts towards the MS. Whilst accretion from the circumstellar disc is still on-going, ground-based spectroscopic observations of nearby young SFRs suggest that the mass accretion rate appears to decrease steadily with time, from $\lesssim 10^{-5}\,{\rm M_\odot\,yr^{-1}}$ during the protostellar regime (Hartmann 1998; Ceccarelli et al. 2000; White et al. 2007) to $\lesssim 10^{-9}\,{\rm M_\odot\,yr^{-1}}$ at ages of $\sim 10\,{\rm Myr}$ (Muzerolle et al. 2000; Sicilia-Aguilar et al. 2005, 2006b), indicating that the main source of energy during the pre-MS phase is not from accretion but from gravitational contraction.

After the cessation of the main accretion phase, protostars become optically visible having shed their natal envelopes and lie along the so-called birthline in the H-R diagram (Stahler 1983). The location of this birthline is a function of mass. TTS represent the low-mass regime ($\lesssim 2\,{\rm M_\odot}$) of the pre-MS while Herbig Ae/Be stars (Herbig 1960b) denote the intermediate mass range ($2-10\,{\rm M_\odot}$). The rapidity with which higher mass stars evolve makes the pre-MS study of such objects difficult. Herbig Ae/Be stars are typically located near the ZAMS (Hillenbrand et al. 1992), whereas for high-mass stars ($\gtrsim 10\,{\rm M_\odot}$) the birthline is coincident with the ZAMS (Palla & Stahler 1990) and hence there is no optical pre-MS phase for such objects. The rapid gravitational contraction of massive protostellar cores causes hydrogen fusion whilst the main accretion phase is still on-going. As the main work in this thesis is concerned with low-mass pre-MS objects, the remainder of this section will focus on that particular mass regime.

Fig. 1.6 shows a series of theoretical evolutionary tracks from D'Antona & Mazzitelli (1994). These tracks span the entire pre-MS phase from the emergence on the birthline to
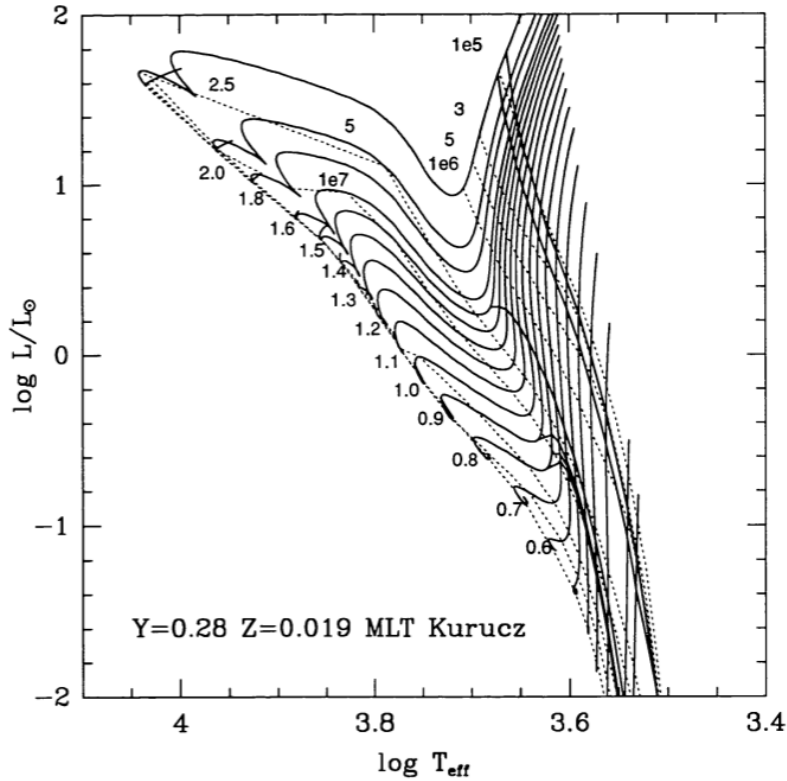
Figure 1.6: Schematic of theoretical evolutionary mass tracks in the H-R diagram for low-mass pre-MS stars. Solid lines are evolutionary tracks for masses $0.3 - 2.5\,\mathrm{M_\odot}$. Dotted lines represent isochrones ranging in age from $10^5 - 10^7$ years. The upper continual line illustrates the average sequence of deuterium burning. The point at which the evolutionary tracks cease (note the numerals on the left-hand side of each track) denotes the point at which said star has reached the ZAMS. These models are based on solar abundances. Reproduced with permission from the AAS. Credit: D'Antona & Mazzitelli (1994).

its termination on the ZAMS. Pre-MS stars are fully convective and experiencing gravitational contraction towards the ZAMS (Hayashi 1961, 1966). Their fully convective nature implies that T_{eff} remains essentially constant during contraction, hence their luminosity will decrease with time. The rate of contraction is regulated on the Kelvin-Helmholtz timescale, t_{KH}, which defines the timescale over which an appreciable portion of the gravitational potential energy of a star (absolute value $GM_\star^2/R_\star$) is radiated away. Thus for an object of luminosity $L_\star$, this timescale becomes

$$t_{\mathrm{KH}} = \frac{GM_\star^2}{R_\star L_\star}, \tag{1.9}$$

and thus implies that more massive pre-MS stars contract towards the ZAMS faster than lower mass stars. In the H-R diagram, fully convective stars will move approximately vertically downwards along Hayashi tracks, maintaining convective equilibrium. As stellar contraction continues the interior opacity increases, thereby forcing the star out of convective equilibrium and generating a radiative core. For stars with masses $\gtrsim 0.4\,\mathrm{M_\odot}$, the radiative core precedes arrival onto the ZAMS (Henyey et al. 1955). Further increases in

core temperature provide an outward pressure that prohibits further gravitational contraction and the star moves horizontally leftwards along Henyey tracks. Stars below this mass threshold are believed to remain fully convective until their arrival on the ZAMS (Chabrier & Baraffe 2000).

One way to compare observations of pre-MS stars with evolutionary models is to plot them in H-R space and thus in the same plane as the models themselves (Cohen & Kuhi 1979; Kenyon & Hartmann 1995; Hillenbrand 1997; Luhman 1999). Unlike the temporally near-stationary nature of MS evolution in the H-R diagram, the rapid descent during pre-MS evolution allows the H-R diagram to be used as a tool for ageing stars and in particular stellar populations such as clusters/associations. This, however, begs the question of how does one place observations of pre-MS stars in H-R space, given that neither luminosity nor effective temperature are directly observable quantities. A stellar spectral type is generally determined from spectroscopic measurements of optical ($BVRI$) or infrared ($YJHK$) absorption line strengths in conjunction with a spectral type-T_{eff} conversion to calculate an effective temperature. Stellar luminosities are provided using optical or infrared photometry, with the spectral type used to account for the effects of interstellar reddening. Finally, a bolometric correction appropriate to the spectral type is applied to calculate the bolometric luminosity.

This may seem like a straightforward process, however there are caveats when comparing observational data of pre-MS stars with theoretical models in the H-R plane. For the study of young pre-MS stars an inherent complication in this procedure arises when one considers the effects that the circumstellar disc may have during this phase (see Section 1.2.3). Excess emission in both the UV – due to the accretion shocks on the stellar surface (Basri & Batalha 1990; Hartigan et al. 1991) – and IR – due to the disc itself (Strom et al. 1989a) – can lead to overestimated magnitudes in particular bandpasses (Gullbring et al. 1998b; Hartmann 1998). These may have a significant effect when it comes to de-reddening the source and it may in fact be difficult to find a bona fide photospheric bandpass at which to apply a given bolometric correction (Preibisch & Zinnecker 1999), or alternatively calculate the bolometric luminosity via the integration of flux across the bandpasses. Further to the bolometric correction difficulty is the fact that standard bolometric corrections are derived from MS dwarfs of the same spectral type (Hartigan et al. 1994; Kenyon & Hartmann 1995).

Pre-MS stars have a lower surface gravity than a MS counterpart of the same spectral type and as such the spectroscopic temperature measured for both will not be the same i.e. the MS bolometric correction scale is dissimilar to the pre-MS bolometric correction scale and should therefore not be applied in this regime. Furthermore, some sources may actually be viewed through the obscuring medium of its circumstellar disc or envelope leading to underestimated luminosities, not to mention the random and systematic errors inherent in spectral typing, measured photometric uncertainties and unresolved multiplicity (Simon et al. 1993; Hillenbrand 2009). Finally, the T_{eff} scale in the cool MS domain is highly uncertain (Casagrande et al. 2006, 2010) and is even worse for cool pre-MS stars.

It is unclear whether the $T_{\rm eff}$ scale is more akin to that of dwarf or giant stars. The typical scale is assumed to be dwarf-like in nature (Leggett et al. 1996), however for M-type pre-MS stars a slightly hotter temperature scale has been proposed to account for the lower surface gravities (White et al. 1999; Luhman et al. 2003) leading to a 400 K increase in $T_{\rm eff}$ by a spectral type of M7. Hence even with accurate spectral types it is difficult to place pre-MS stars on an H-R diagram for comparison with evolutionary models, especially for mid to late M-type pre-MS stars where the $T_{\rm eff}$ scale differences can lead to age discrepancies by factors of a few.

1.3.4   The Colour-Magnitude Diagram

The CMD is the observational equivalent of the H-R diagram, plotting stellar colours against magnitudes, and can be used to infer ages from stellar populations in much the same way. Unlike the H-R diagram in which the data is transformed into the theoretical plane, for a comparison in CMD space it is the outputs of the models – namely $L_{\rm bol}$ and $T_{\rm eff}$ – that must be transformed into observable colours and magnitudes. These transformations are provided via the use of bolometric corrections to $L_{\rm bol}$ which defines the magnitude in a given bandpass and a colour-$T_{\rm eff}$ relation that sets the colour scale. The effects of distance and interstellar reddening will act to make stars appear fainter in magnitude and redder in colour – termed apparent magnitudes and colours – than their intrinsic values and so these must be accounted for when deriving ages.

The derivation of ages from young ($\leq 10\,{\rm Myr}$) pre-MS populations is made more difficult by the large luminosity spreads observed in the sequences of pre-MS stars in CMDs of such regions ($\sim 2-3\,{\rm mag}$ at a given colour). This spread is often interpreted as evidence for a prolonged period ($\geq 10\,{\rm Myr}$) of star formation within a given cluster. Such spreads have important implications for theories of star formation and the constraints placed upon them (see Section 1.2.2). Spreads of the order of $10\,{\rm Myr}$ would imply a 'slow' star formation process, whereby the collapse of material within a molecular cloud is impeded by the presence of, for instance, the magnetic field (e.g. Tassis & Mouschovias 2004). Conversely, a lack of a luminosity spread favours the 'rapid' process (e.g. Elmegreen 2000; Hartmann 2001) in which the star formation process is driven by the rapid dissipation of turbulence, and collapse of molecular material on timescales of a few Myr or less. The existence of these spreads will inevitably have implications for derived ages and it is therefore imperative to understand the physical processes that contribute to these features.

Various sources of observational and astrophysical scatter have been identified by Hartmann (2001) that could contribute to an *apparent* luminosity spread. Such factors include the unresolved multiplicity of stars; highly variable extinction and reddening for a given region; the intrinsic variability of pre-MS stars; variable accretion luminosities; and that stars (at least in nearby SFRs) are at a range of distances. Burningham et al. (2005a) incorporated astrophysical sources of scatter – such as photometric variability and the effects of binarity – in addition to observational uncertainties into simulated pre-MS populations and showed that these effects do not account for the magnitude of the spread

at a given colour, suggesting that the remaining spread reflects either a true age spread or longer term variability due to accretion. A more recent study by Da Rio et al. (2010a) also included these longer term effects due to accretion – as well as rotational variability and differential extinction – and conclude that the spread in the CMD is still too large to be accounted for by the various sources of astrophysical scatter and thus the residual spread represents a true age spread with FWHM $2.8 - 4.4$ Myr.

A possible explanation for the observed spreads in CMDs of young SFRs could be brief phases of intense accretion during the early Class I phase of a YSO. Investigations into the effects that early phases of accretion could have on the position of pre-MS stars in the H-R diagram (e.g. Mercer-Smith et al. 1984; Hartmann et al. 1997; Tout et al. 1999) have shown that stars having undergone such accretion events appear older than those without such accretion histories. So-called 'episodic accretion' has been modelled for the early Class I T-Tauri phase by Vorobyov & Basu (2006) in which a prolonged quiescent period of low accretion ($\leq 10^{-7}$ M$_\odot$ yr^{-1}) is punctuated by intense bursts of high accretion ($\sim 10^{-4}$ M$_\odot$ yr^{-1} over timescales of ≤ 100 years; see for example Enoch et al. 2009) in which the majority of the protostellar mass is accumulated. Baraffe et al. (2009) have investigated what effects such bursts of accretion would have on pre-MS stars in the H-R diagram. If the accreted energy is efficiently radiated away – so-called 'cold accretion' – such high accretion rates compress the pre-MS star, leading to a smaller radius and lower luminosity. The pre-MS stars will relax back to the structure predicted by the non-accreting models on the Kelvin-Helmholtz timescale (~ 20 Myr) and thus determining ages from these objects using standard non-accreting models will result in erroneously large ages. For a given coeval stellar population one would naturally expect a range of accretion rates as protostars evolve through the early YSO phases, thereby resulting in the observed luminosity spreads in CMDs of young SFRs.

Recently, Hartmann et al. (2011) have discussed how rapid disc accretion is unlikely to be 'cold', based on observations of well-studied FU Ori objects, and advocate two possible reasons why this may be the case. First, SEDs of FU Ori objects imply large, not small, stellar radii. Second, theoretical models predict that at such high accretion rates protostellar discs become internally heated and geometrically thick, making it more likely that the material transferred onto the protostar is hot. In addition, they argue that the high luminosity of the accretion disc may act to irradiate the central protostar, thereby heating the outer layers and possibly expanding them. Furthermore, Hartmann et al. (2011) show that both the protostellar and post-protostellar H-R diagram positions of the 'cold accretion' models of Baraffe et al. (2009) lie well below observations of young stars in molecular clouds (e.g. Doppmann et al. 2005; Rebull et al. 2006b) and assert that the current observational constraints suggest that the age uncertainties due to rapid accretion are considerably less than the upper limit of ~ 10 Myr as discussed in Baraffe et al. (2009). More recent calculations (Baraffe et al. 2012) show that both the observed spread in the H-R diagram and the inferred properties of FU Ori-type objects can be explained assuming that; i) there is a variation in the fraction of the accretion energy
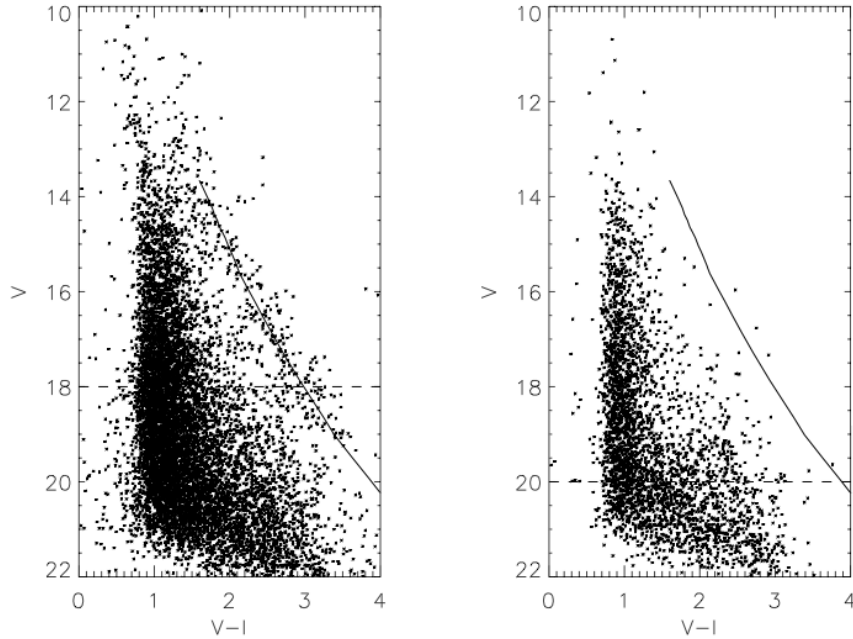
Figure 1.7: Left: The $V, (V - I_c)$ CMD of the central $0.89 \deg^2$ of the σ Ori association. The solid line is a $2.5\,$Myr isochrone (Baraffe et al. 1998, 2001) at a distance of $440\,$pc (Brown et al. 1994). The isochrone denotes the expected location of the pre-MS population of the Orion OB1b association. **Right:** The same CMD but for a control field with a smaller $(0.29 \deg^2)$ field-of-view. The isochrone is the same as in the left panel. The dashed line in both cases represents the completeness limit of the data. Reproduced with permission from the AAS. Credit: Sherry et al. (2004).

absorbed by the protostar during the accretion process and ii) the range of this variation should increase with increasing accretion burst intensity and thus with the initial core mass.

1.4 Identifying Low-Mass Pre-Main-Sequence Stars

The vast number of low-mass pre-MS stars known to reside in OB associations are in general – except for the most embedded populations and clusters of high number density – widely spread over tens or even hundreds of square degrees on the sky. Furthermore, as a given population ages the remaining molecular material slowly dissipates thus making differentiation between them and the older field stars more problematic. Pre-MS stars exhibit several characteristics that highlight their youth which can be used to discriminate between these and the field stars. These characteristics can only differentiate between different types of stellar populations, not between distinct young populations.

Before discussing the specific indicators that are commonly used to confirm pre-MS status, it is instructive to know how pre-MS stars appear in a CMD. Large-scale surveys have permitted photometric studies of expansive OB associations and clusters to become more widely available. As noted in Section 1.3.3, pre-MS stars are more luminous than a ZAMS counterpart of similar $T_{\rm eff}$ or spectral type. Residual molecular

material associated with sites of recent star formation acts to absorb stellar radiation and re-emit at longer wavelengths, leading to such stars appearing redder than the Galactic foreground/background population in a CMD (Pozzo et al. 2000; Dolan & Mathieu 2002; Sherry et al. 2004; Dahm & Simon 2005; see Fig. 1.7). Selection of low-mass pre-MS stars via photometric selections in CMD space have been previously employed (Béjar et al. 1999; Kenyon et al. 2005; Jeffries et al. 2007), with evidence that such selections do not include/exclude a significant number of non-members/members (Burningham et al. 2005b). The main advantage of photometric selection is that for a given amount of telescope time, a region of sky can be surveyed to a fainter limiting magnitude than either a variability study or spectroscopic survey. Furthermore, photometric selections can also identify low-mass stars with very low levels of variability. The main disadvantage with photometric selection is that they inherently contain some contamination from foreground/background field stars. Typically, an initial photometric selection of targets is made in CMD space to identify a list of candidate objects on which spectroscopic follow-up observations are made. Final memberships are then assigned based on the following diagnostics.

1.4.1 Infrared Excess

The first detections of IR excess from young TTS were made by Mendoza V. (1966, 1968). These observations showed that the IR fluxes were well above those expected from reddened stellar photospheres and instead originated from dusty circumstellar material in the discs and envelopes surrounding the stars. This IR excess is a result of stellar radiation being absorbed and re-processed by the dust grains around the star (Bertout et al. 1988). As discussed in Allen et al. (2004), for these reasons IR colour-colour diagrams have become widely used tools in the identification and classification of YSOs. IR colour-colour diagrams can differentiate between stars with IR excess as a result of interstellar extinction from those with intrinsic IR excess due to circumstellar material and can furthermore discriminate between different types of YSOs which occupy distinct regions within these diagrams (e.g. Lada & Adams 1992; Rebull et al. 2002; Gutermuth et al. 2008).

1.4.2 X-ray Emission

Pre-MS stars in all stages of evolution, from Class I protostars to their arrival on the ZAMS, exhibit increased levels of X-ray activity that far exceed those associated with MS stars (Montmerle et al. 1983; Basri et al. 1992; Strom & Strom 1994; Gagné et al. 1995). These enhanced levels of X-ray activity are believed to be a direct consequence of the elevated levels of magnetic activity in TTS and is primarily chromospheric in nature, although X-ray flaring has also been observed (Feigelson & Decampli 1981; Walter & Kuhi 1981; Preibisch et al. 1993). Enhanced levels of solar-type magnetic activity is not surprising in rapidly rotating cool stars with deep convection zones. In the solar dynamo ($\alpha\omega$) model, the magnetic field is believed to be generated at the boundary between the radiative core and convection zone, known as the tachocline, however this model breaks down in fully convective TTS where the highest levels of X-ray emission are observed (Feigelson et al.

2003). Although the exact processes underpinning these enhanced levels remain unclear (Stassun et al. 2004a), it is currently believed that the dynamos in fully convective pre-MS stars may be different in nature than those in solar-type stars (e.g. Saunders et al. 2009; Gregory et al. 2012), consisting instead of a dynamo powered primarily by turbulence distributed throughout the convective interior (Mullan & MacDonald 2001; Barnes 2003a; Preibisch & Feigelson 2005).

X-ray observations are a well established tool for identifying young low-mass pre-MS stars in associations and clusters (Naylor & Fabian 1999; Preibisch & Zinnecker 2002; Getman et al. 2005; Wang et al. 2008). As the X-ray luminosities of young stars – for a given mass, age and bolometric luminosity – can vary by several orders of magnitude, it is appropriate to ask whether all young stars are highly X-ray active or whether there is a population that exhibit suppressed magnetic activity, and furthermore, whether this introduces a source of bias in the X-ray selection of stars. The *Chandra* Orion Ultradeep Project (COUP; Getman et al. 2005) is the most intensive observation ever made in the X-ray regime spanning 10 days and represents the most comprehensive dataset on the X-ray emission of pre-MS stars. The study found no evidence for suppressed magnetic activity in TTS, with more than 97 % of optically visible late-type stars exhibiting X-ray emission. Recently, Feigelson et al. (2003) demonstrated that the presence, or lack thereof, of a circumstellar disc has little effect on the X-ray emission of pre-MS stars, however more recently, Preibisch et al. (2005a) found evidence that accreting pre-MS stars are less X-ray active – by a factor of $\sim 2 - 3$ on average – than non-accreting stars, suggesting that the accretion process may act to distort the large-scale stellar magnetic field (Miller & Stone 1997) or even alter the internal stellar structure and differential rotation patterns (Siess et al. 1999). Hence, whilst X-ray selection of pre-MS stars is very efficient, it tends to be biased toward the selection of non-accreting objects.

1.4.3 Lithium Absorption

As mentioned in Section 1.4, spectroscopic follow-up observations are essential to categorically assign pre-MS status to an object. Whilst the telescope time required to observe a widespread low-mass pre-MS population interspersed among field stars in extended clusters and especially OB associations is vast, the advent of powerful multi-fibre spectrographs such as the AF2/WYFFOS on the 4.2-m *William Herschel* Telescope and FLAMES on the 8-m Very Large Telescope mean that large-scale spectroscopic surveys are now feasible.

Arguably the most powerful pre-MS indicator is the presence of strong Li I absorption at 6708 Å (Preibisch et al. 1998; Dolan & Mathieu 1999; Randich et al. 2001). ^{7}Li is converted to He through nuclear reactions along the p-p chain. This occurs at relatively low temperatures ($2.5 - 3.0 \times 10^6$ K; Bodenheimer 1965) with a reaction rate that is heavily dependent upon the core temperature. ^{6}Li also exists however this is very rare as it has a lower critical temperature and faster reaction rate, hence it is depleted more rapidly (Hayashi 1965). Due to the dependence on the stellar core temperature, Li I depletion is therefore also dependent upon stellar mass (Randich et al. 1997). For fully convective
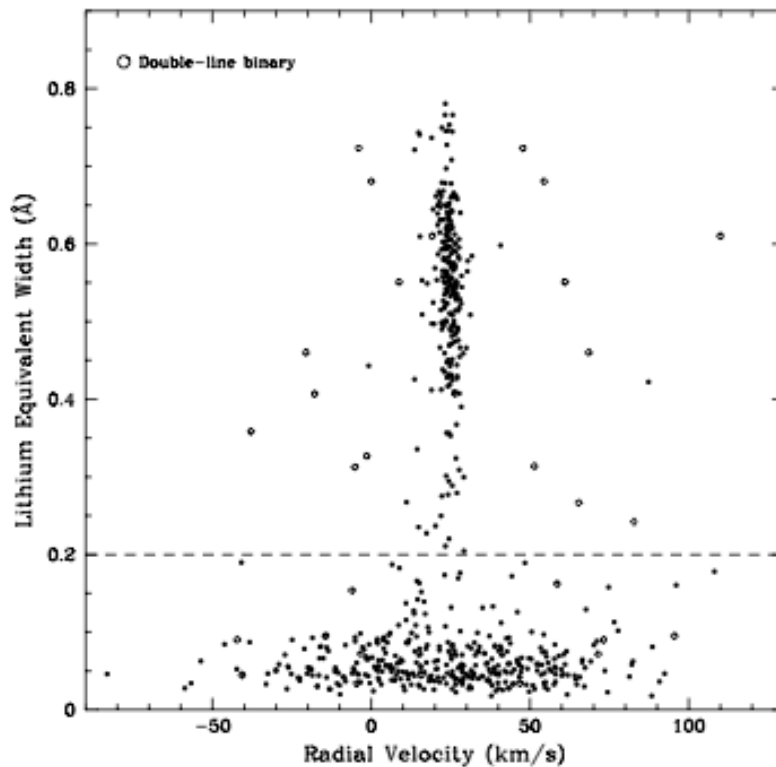
Figure 1.8: Equivalent width of Li I against radial velocity for stars around the λ Ori association. Those with $W_\lambda(\mathrm{Li\,I}) > 0.2\,$Å and clustered about the mean radial velocity are taken to be pre-MS members. Reproduced with permission from the AAS. Credit: Dolan & Mathieu (2001).

very-low-mass stars ($< 0.35\,\mathrm{M_\odot}$) the material in the stellar interior can mix convectively in a fraction of the Kelvin-Helmholtz timescale, thereby rapidly exhausting Li I. The core temperature for stars with masses $< 0.06\,\mathrm{M_\odot}$ never reaches critical values from Li I depletion to occur (Martín et al. 1994). More massive stars ($0.35 - 1.2\,\mathrm{M_\odot}$) develop a radiative core prior to arrival on the ZAMS. The efficiency of material mixing in the stellar interior decreases, thus halting further Li I depletion. Hence the presence of strong Li I absorption in the spectra of stars and brown dwarfs with masses $0.06 - 1.2\,\mathrm{M_\odot}$ is a robust indicator of stellar youth and pre-MS status (Herbig 1962; D'Antona & Mazzitelli 1994; Jeffries 2004, see Fig. 1.8). Li I depletion, as well as being a function of stellar age, is also dependent upon stellar mass (Wallerstein et al. 1965; Zappala 1972; Duncan 1981) and some believe even a function of additional factors including stellar rotation (Pinsonneault et al. 1992; Soderblom 1996).

1.4.4 Hα Emission

As discussed in Section 1.2.3.2, TTS were identified as young objects which displayed high levels of variability and strong emission lines, especially Hα. The distinction between WTTS and CTTS is based on an $W_\lambda(\mathrm{H}\alpha) = 10\,$Å (see Herbig & Bell 1988), however a recent revision of the WTTS/CTTS transition by White & Basri (2003) suggested a

modified criterion that takes into account the contrast effect of Hα as a function of spectral type for stars later than K-type. It is believed that the excess Hα emission in WTTS likely stems from chromospheric activity as a result of intense magnetic fields at the stellar surface (Walter et al. 1988), whereas the broader emission observed in CTTS arises from a combination of enhanced chromospheric activity and emission from accretion shocks. The strong magnetic field disrupts the disc and the magnetically channeled accretion columns transport material from the disc which essentially free-falls towards the stellar surface with velocities ∼ few hundred km s^{-1}. Stellar rotation with respect to the line-of-sight, when accounting for the accretion columns, leads to broader and shallower Hα emission lines observed in CTTS due to blue and red-shifted Balmer lines (Muzerolle et al. 1998). Given the generally held opinion that CTTS are associated with Class II objects – optically thick circumstellar disc at $\lambda < 10 \, \mu$m – and WTTS are Class III objects – optically thin circumstellar disc at $\lambda < 10 \, \mu$m – it was assumed that the observational bias related to the use of Hα emission as a pre-MS indicator was towards stars with circumstellar discs (see the correlation between Hα emission and IR excess by Cabrit et al. 1990). A study of TTS by Littlefair et al. (2004) identified previously classified WTTS with possible high accretion rates, suggesting that TTS may switch between WTTS and CTTS states, depending on a variable accretion rate. This combined with previous studies of WTTS (see Bary et al. 2002; Gregorio-Hetem & Hetem 2002; Herbst et al. 2002b) suggests that the bias may no longer apply to just stars with circumstellar discs, but more specifically stars with active accretion.

1.4.5 Photometric Variability

Variability has been intensively studied in TTS over the past couple of decades (Rydgren & Vrba 1983; Bouvier et al. 1993; Choi & Herbst 1996; Stassun et al. 1999; Littlefair et al. 2005). The advent of multi-CCD cameras mounted on wide-field telescopes have allowed multi-epoch photometric surveys to utilise variability as a means of identifying possible TTS candidates. Herbst et al. (2007) indicate the sources of common stellar variability in pre-MS stars compiled using large-scale surveys based on TTS and periodic variability (Herbst et al. 1994; Bouvier et al. 1995).

Periodic rotational modulation of the stellar flux caused by an asymmetric distribution of cool spots on the stellar surface is more commonly observed on WTTS but also seen on CTTS. High surface magnetic fields can create concentrations of field lines that inhibit convective motions through the stellar chromosphere producing cooler regions similar to solar sunspots (Strassmeier et al. 1994). Typical amplitudes for this type of variation can range from $0.03 - 0.3$ mag, with extremes of ∼ 1 mag, in the *V*-band. These amplitudes can then be used to calculate spot sizes and temperatures. Unlike the relatively small areal coverage of solar sunspots (typically ∼ few %; Baliunas & Vaughan 1985), the derived spot coverage factors for TTS range from a few percent up to ∼ 30 % (Bouvier et al. 1995). The determination of robust rotation periods can be linked to the longevity of these cool spots, which have been observed to survive over thousands of stellar rotations

(Cohen et al. 2004; Lamm et al. 2005). Rotational studies of pre-MS periods based on photometric monitoring may be heavily biased against actively accreting CTTS (Cohen et al. 2004), however such effects can be negated with a sufficiently high temporal density of observations (Littlefair et al. 2005).

Enhanced levels of magnetic activity can result in the disruption of the circumstellar disc leading to aperiodic variations caused by magnetically channeled accretion from the disc onto the star. The complex interaction between the stellar magnetosphere and inner disc is highly dynamic. Accretion columns are variable both temporally – on timescales of hours to years (Bouvier et al. 2004; Grankin et al. 2007) – and spatially – non-uniform distribution of channels across the stellar surface (Petrov et al. 2001). Typical aperiodic variation amplitudes are generally factors of $2-5$ times larger than those generated by the periodic rotational modulation of cool spots. Another source of accretion-based variation is periodic hot spots – observed only on CTTS – created at the base of magnetically channeled accretion columns as it impacts upon the stellar surface (Kenyon et al. 1994; Eaton et al. 1995). Magnetic field configurations can be very complex and temporally variable (e.g. Gregory et al. 2008), and hence the configuration of the accretion columns can change on the order of a few rotation periods. This can result in changes to both the size and location of the hot spots and thus the shape of the modulation will also vary on such timescales.

Flare-like variations have also been noted on both WTTS and CTTS, a further indication of the enhanced levels of magnetic activity omnipresent in TTS, with typical timescales of less than a few hours (Guenther & Ball 1999). Indications show that flare activity decreases with age and suggest that the TTS phase of stellar evolution could be the main flaring stage in the life of a star (Guenther & Ball 1998). Despite the frequency of flares on both types of TTS, the origins of these may be qualitatively different on WTTS than for those on CTTS. Flares on WTTS are believed to originate from the stellar surface, whereas it is suggested that such events on CTTS could emanate from the circumstellar environment such as the accretion columns or the circumstellar disc itself (Gahm 1990). Large-scale aperiodic variability on CTTS may make the differentiation of flare signatures hard to determine.

1.4.6 Kinematic Methods

The final method of assigning pre-MS membership is by demonstrating common motion through space with a young cluster/association. The motion of a given star can be measured in two distinct and orthogonal directions, namely proper motion and radial velocity. A star's proper motion is its motion on the plane of the sky relative to background stellar or extragalactic objects, whereas its radial velocity is along the line-of-sight of the star. By identifying a cluster, one can measure either the proper motion or radial velocity of stars in the vicinity and determine whether the values group around a common value, after allowing for the internal velocity dispersion, observational uncertainties and the possibility of close binaries. Despite OB associations being gravitationally unbound, a combination

of low velocity dispersions (few $km\,s^{-1}$; Mathieu 1986; Tian et al. 1996) and youth mean that they form coherent structures in velocity space and as such share a common motion.

The advent of deep, all-sky missions, such as *Hipparcos* (Perryman et al. 1997) and combinations of all-sky catalogues (e.g. PPMXL; Roeser et al. 2010), have facilitated the use of proper motions as membership indicators, especially in the nearest OB associations. An alternative method is to use photographic plates with a significantly long baseline to derive proper motions of individual objects (Gould & Kollmeier 2004; Deacon et al. 2009). One of the most extensive studies of memberships of OB associations within $1\,kpc$ of the Sun based on proper motions was performed by de Zeeuw et al. (1999). This comprehensive census found a clear kinematic signature of a moving group in several OB associations as well as discovering a new group in Cepheus. Despite confirming kinematic members in many of these groups to fainter magnitudes than previous studies, the limiting magnitude of the *Hipparcos* mission means that the confirmation of low-mass stars is confined to only the closest OB associations e.g. Sco-Cen (Mamajek et al. 2002). Preibisch et al. (1998) performed a spectroscopic study in the Upper Sco OB association to identify pre-MS stars, based on follow-up X-ray observations. They further investigated the completeness of the X-ray selected sample by observing 115 stars that were not detected as X-ray sources, but had proper motions consistent with Upper Sco membership and found that none of these objects were pre-MS stars. Thus, the use of proper motions alone is insufficient to confidently identify low-mass pre-MS objects in nearby OB associations and should therefore be used in conjunction with ancillary data, such as X-ray or spectroscopic.

In contrast to proper motions, radial velocities of low-mass pre-MS stars are routinely available from single spectroscopic observations and have thus been used in the identification of such stars in young open clusters/OB associations (Jeffries et al. 1998; Dolan & Mathieu 1999; Nordhagen et al. 2006). The radial velocity of a given star is generally determined through cross-correlation of its spectra against that of a radial velocity standard with a similar spectral type. As with calculated proper motions, radial velocity measurements alone are not enough to identify bonafide pre-MS objects (see Dolan & Mathieu 1999; Jeffries et al. 2009). In these studies, the $W_\lambda(\mathrm{Li})$ was plotted against the radial velocity and highlighted that although a number of stars showed a common velocity, there was a fraction that further demonstrated depleted Li and therefore were unlikely to be true cluster members. Hence whilst kinematic velocity measurements are a robust indicator, they should be complimented with ancillary data before categorically assigning pre-MS status to a given object.

1.5 Summary

In this introductory chapter the current theoretical models of star formation have been discussed and the two main theories which suggest different regulating phenomena, and therefore timescales for star formation within a molecular cloud, briefly highlighted. The regulation by quasi-static ambipolar diffusion acts on timescales of $\sim 3 - 10\,\mathrm{Myr}$, whereas

regulation by dissipation of turbulence in large-scale flows of atomic hydrogen occurs on dynamical timescales of $\sim 0.5 - 3\,\mathrm{Myr}$. The subsequent evolution of protostars is driven by gravitational contraction. Wide-field photometric surveys of young pre-MS populations have highlighted the importance of the star-disc interaction in regulating the rotational evolution and, furthermore, the need for precise absolute ages for these populations.

The early evolution of low-mass objects in the H-R diagram, and CMD, has been discussed and specifically how the comparison of observations of pre-MS objects with theoretical evolutionary models can be used to determine ages for young stellar populations. These ages can further be used to constrain the associated timescales of star formation and in particular the loss of angular momentum, magnetic field changes and the lifetimes of circumstellar discs, which have far reaching implications for subsequent planet formation.

Currently the ages for a given region can vary by up to a factor of ~ 3 depending on the colours adopted and the region of the sequence that is fitted. Hence absolute ages would allow the relative importance of the physical processes occurring within stellar clusters to be probed and therefore pave the way for a general theory of star formation to be created. Furthermore, absolute ages for the youngest SFRs would allow for the discrimination between the dominant mechanisms that drive the star formation process, and moreover place strong constraints on the timescales over which the various phases of YSO evolution occur. In addition, robust ages can then allow the empirical study of circumstellar discs as a function of time, which is vital to fully understand the importance of the disc-locking mechanism and over what timescales the rotational evolution of stars is regulated, as well as the time available in which to form planets. Additional studies can then investigate what effects differences in cluster-to-cluster environments might have on this generalised theory.

The remainder of this thesis will concentrate on the derivation of ages, distances and reddenings for a sample of young pre-MS SFRs. In Chapter 2 the sample of young SFRs will be introduced, as will the techniques that can be used to derive such parameters from photometric data of MS stars. The MS evolutionary models are discussed as are the atmospheric models required to transform these models into observable CMD space. A maximun-likelihood fitting statistic is then used to derive a self-consistent set of best-fit ages, distances and reddenings for the sample of SFRs. Additionally, the effects of model dependency and assumed composition are discussed in terms of how these can affect the derived parameters. Chapter 3 describes the photometric observations of the SFRs and the subsequent data reduction. In this chapter the main problems related to the calibration of photometric observations of pre-MS stars into a standard photometric system are discussed. As a result the characterisation and calibration of the *Isaac Newton* Telescope Wide-Field Camera photometric system is described. In Chapter 4 the pre-MS evolutionary models are introduced and a brief discussion of the basic physics included in these models presented. A critical assessment of these models is performed by comparing their predictions to a set of well-calibrated CMDs of the Pleiades and testing the mass scales using dynamical masses from a sample of MS binaries. This analysis shows that models

tend to overestimate the flux in the optical colours for $T_{\mathrm{eff}} \lesssim 4000\,\mathrm{K}$. This discrepancy is quantified and the effects on derived pre-MS ages discussed. Chapter 5 describes the process of isolating pre-MS stars in a CMD and the creation of recalibrated semi-empirical pre-MS model isochrones which are subsequently used to derive pre-MS ages for the sample of SFRs. In Chapter 6 the MS and pre-MS age estimates are brought together, and a final revised age is assigned to each SFR in the sample. The implications of these revised ages are then discussed in terms of circumstellar disc lifetimes and evolutionary timescales for YSOs. Finally, Chapter 7 concludes by summarising the main findings presented in this thesis and ends with some thoughts concerning complementary future work.

Chapter 2

Fitting the Main-Sequence Population of Young Star-Forming Regions

2.1 Motivation

In a series of papers the Cluster Collaboration[1] have highlighted the problems with pre-MS evolutionary models and attempted to provide consistent pre-MS ages. In Mayne et al. (2007), pre-MS stars in a series of young SFRs were used to create a set of empirical isochrones. When plotted in absolute magnitude-intrinsic colour space these isochrones placed the clusters on a relative age ladder independent of theoretical assumptions (fiducial ages were assigned to a subset of these SFRs). The main problem with this work is that it suffered from a lack of self-consistent distance measurements, relying instead on heterogeneously derived literature estimates. To rectify this Mayne & Naylor (2008) used MS model isochrones to fit the young MS population of many of the clusters studied in Mayne et al. (2007) and derived self-consistent distances and extinctions. These revised distances led to a subtle modification of the Mayne et al. (2007) pre-MS age scale. Although self-consistent, the Mayne et al. (2007) and Mayne & Naylor (2008) pre-MS age scale only provided relative ages. In an effort to create an absolute age scale, Naylor (2009) used only stars between the ZAMS and terminal-age main-sequence (TAMS), in conjunction with the τ^2 fitting statistic, to derive absolute ages. These MS ages were found to be a factor $1.5 - 2$ times older than the pre-MS ages based on the Mayne et al. (2007) and Mayne & Naylor (2008) pre-MS age scale.

In contrast to pre-MS evolutionary models, MS models are built upon well tested physics and provide more reliable predictions of stellar properties, as well as showing high levels of consistency between models from different groups (Mayne & Naylor 2008). Ideally, one would like to use the accuracy of cluster parameters derived using MS models

---

[1]The Cluster Collaboration consists of teams within the Exeter Astrophysics Group led by Tim Naylor and the Keele Astrophysics Group led by R. D. Jeffries. The homepage is available at `http://www.astro.ex.ac.uk/people/timn/Catalogues/`

to explore the dramatic evolution in the pre-MS regime, and hence by creating an absolute age scale thereby place stronger constraints on future models of star and planet formation. The drawback with using MS ages alone is twofold. First, the rate of change of the slope of the isochrone for a given age increment is subtle (i.e. $\Delta(B-V)/\sigma_{(B-V)}$ is small, despite the precision in $B-V$). Second, MS ages suffer from small number statistics as only the most massive stars in young SFRs have evolved sufficiently so as to be on the MS. Therefore, the only practical way to proceed is to use age diagnostics based on the more populous pre-MS. If the pre-MS is to be used, then it must be demonstrated that the ages derived from the MS and pre-MS populations agree. This has so far been hampered by uncertainties in the pre-MS regime, with only tentative evidence for agreement between MS and pre-MS age derivations for stellar populations older than 50 Myr (Lyra et al. 2006), whereas for younger clusters there is an increased disparity between the two ages (Piskunov et al. 2004; Naylor 2009).

In this chapter literature Johnson UBV photometry is used in conjunction with MS stellar evolutionary models to derive a homogeneous set of reddenings, distances, and ages for a sample of young SFRs. In Section 2.2 the sample of young SFRs is described. Section 2.3 discusses how reddenings, distances, and ages can be calculated from photometric observations of MS stars. Section 2.4 details the photometric datasets for the sample of SFRs. In Section 2.5 the MS interior evolutionary models are introduced, as are the processes required to transform the models into CMD space and the theoretical stellar atmospheric models. Section 2.6 introduces the fitting statistic used to derive the reddenings, distances, and ages from the photometric datasets. Section 2.7 discusses the effects of interstellar reddening and extinction on deriving parameters from photometric observations. Revised colour- and extinction-dependent reddening vectors and a method to de-redden stars individually based on photometric observations alone are introduced. Section 2.8 describes the fitting process by way of two examples and presents the results for the full sample of SFRs. The derived parameters are then discussed in Section 2.9. Section 2.10 discusses the effects of the model dependency on the derived parameters and Section 2.11 discusses the assumption of a fixed metallicity for different SFRs. Finally, Section 2.12 summarises this chapter and presents the MS parameters that will be used for the remainder of this thesis.

2.2 Sample of Young Star-Forming Regions

The sample of 14 SFRs studied were chosen based primarily on the fact that these populations constitute young (< 30 Myr) SFRs that have been well studied in the literature. For this analysis it is imperative that all SFRs have a sufficiently well-populated MS so that, at least, the distance and reddening, but hopefully also an age, can be determined in a homogeneous way. Furthermore, a populated pre-MS is required so that pre-MS ages can be derived and hence compared to the MS derivations. As all the SFRs have been the focus of previous investigations, they benefit from membership diagnostics in both the

high-mass and low-mass regime. In addition, high-quality UBV photometric data is available for the SFRs (see Section 2.4) which is essential for deriving parameters from the MS population. Finally, the wide-field instrument used to observe the low-mass populations of these SFRs is situated on the island of La Palma, and therefore a further constraint on the SFRs studied was that they must be observable from La Palma in the autumn.

As the SFRs in the sample cover different evolutionary stages, and are at a range of distances, the mass range sampled across the SFRs varies. For close SFRs (e.g. the λ Ori association) the mass range sampled stretches from late O-type stars to the brown dwarf limit, whereas for the most distant SFRs (e.g. NGC 6611) the highest mass stars have spectral types of early/mid O-type stars and the lowest mass objects observed are late K-/early M-type stars. Furthermore, the SFRs range from dense areas of massive star formation (e.g. χ Per) to more quiescent regions that lack a large high-mass population (e.g. IC 348). By deriving self-consistent parameters for SFRs that span a range of ages, and hence stellar populations in different stages of evolution, as well as various environments, the theoretical framework discussed in Chapter 1 can be used to infer how various phenomena evolve in time and ultimately map star formation as a function of time and space within the local Galaxy.

2.2.1 Cep OB3b

Cep OB3b is a subgroup of the Cep OB3 association (Blaauw 1964) and lies at the centre of an expanding H I shell (Simonson & van Someren Greve 1976). The first detailed photoelectric photometric study of the Cep OB3 region was performed by Blaauw et al. (1959), who discovered 40 early-type stars and derived a distance of 725 pc. Since this initial study, additional photometric surveys have refined the Blaauw et al. (1959) membership list, extending it to lower masses as well as deriving an age of ~ 5.5 Myr and revising the earlier distance estimate to ~ 850 pc (Moreno-Corral et al. 1993; Jordi et al. 1996). The central coordinates of the subgroup are $\alpha_{\mathrm{J2000.0}} = 22^{\mathrm{h}} 55^{\mathrm{m}} 43.3^{\mathrm{s}}$, $\delta_{\mathrm{J2000.0}} = +62° 40' 13.0''$ (Littlefair et al. 2010).

Evidence of a rich pre-MS population in Cep OB3b was provided by Naylor & Fabian (1999) who discovered over 50 X-ray sources using the *ROSAT* PSPC and HRI. A *UBVI* photometric follow up by Pozzo et al. (2003), with supplementary multi-fibre spectroscopy, identified additional TTS with evidence of a possible age spread ($\sim 1 - 10$ Myr). More recent *Chandra*-ACIS observations of Cep OB3b have increased the number of X-ray sources dramatically (> 300 point sources; Getman et al. 2006).

2.2.2 χ Per

χ Per (or NGC 884) represents one half of the famous Double Cluster which forms the nucleus of the Per OB1 association. Struve (1927), discussing the Henry Draper Catalogue of stars type B3 and earlier, emphasised a clustering of B-type stars in Perseus and suggested that this might in fact represent a physical grouping in space. The first

CMD of the region was by Oosterhoff (1937) using photographic photometric observations. Subsequent photometric studies (Johnson & Morgan 1955; Wildey 1964; Crawford et al. 1970) constrained the distance to χ Per to $\sim 2.0 - 2.4$ kpc with an age of between 7 and 20 Myr. The study of Wildey (1964) is of particular interest, as he suggested several distinct episodes of star formation, with a spread of $\simeq 50$ Myr in the formation times of OB stars in a single cluster. Furthermore, the photographic measurements clearly show a discrete stellar population that has yet to contract onto the MS. The central coordinates of the cluster are $\alpha_{J2000.0} = 02^h 22^m 04.3^s$, $\delta_{J2000.0} = +57° 08' 35.0''$ (Currie et al. 2010).

More recent CMDs of χ Per (e.g. Mayne et al. 2007; Currie et al. 2010) show that a rich pre-MS population is obvious, however the number of members identified other than photometrically is sparse. Whilst pre-MS members have been identified in h Per via photometric variability and X-ray studies (Saunders et al. 2009 and Currie et al. 2009a respectively), such observations are lacking for χ Per. The first extensive spectroscopic survey of χ Per was performed by Currie et al. (2010) who identify approximately 750 cluster members down to early/mid M-type stars (note however that these 'spectroscopically confirmed' members in fact represent a locus defined by a combined 14 Myr MS and pre-MS isochrone in the de-reddened V-band magnitude versus spectral type diagram and are not based on spectral features such as Li I or Hα). Near-IR JHK_s and *Spitzer* IRAC observations (Currie et al. 2007) show that less than 5% of low-mass cluster members show signs of excess emission due to warm circumstellar material, whereas far-IR MIPS observations suggest a population of stars with excess emission most likely caused by debris from the planet formation process (Currie et al. 2008).

2.2.3   IC 348

IC 348 is a small young cluster associated with the Per OB2 complex and is approximately 300 pc from the Sun (Herbig 1998). It was first recognised and catalogued as a reflection nebula by Dreyer (1895). Photoelectric photometric and spectroscopic measurements of twelve bright sources in IC 348 were taken by Harris et al. (1954) and demonstrated that the cluster contained no O-type stars, the earliest being B5. In the same year, Herbig (1954) performed an Hα survey and discovered several late-type emission line stars in the periphery of the cluster, thus suggesting that IC 348 might be a site of recent/current star formation. The central coordinates of the cluster are $\alpha_{J2000.0} = 03^h 44^m 31.3^s$, $\delta_{J2000.0} = +32° 08' 13.0''$ (Luhman et al. 2003).

IC 348 has been intensively studied at a variety of wavelengths. Deep $UBVRI$ photometric and spectroscopic Hα surveys have been carried out identifying significant numbers of pre-MS objects (Trullols & Jordi 1997; Herbig 1998) with the latter assigning a mean age of 1.3 Myr but also finding evidence for a significant range of ages from 0.7 to 12 Myr. Near- and mid-IR surveys have found evidence of a large disc fraction population in IC 348 ($\sim 65\%$) with this fraction dependent upon stellar mass (Haisch et al. 2001a), and by combining optical and IR data Lada et al. (2006) have created SEDs for approximately 300 cluster members. X-ray observations have identified approximately 200 members

(Preibisch et al. 1996; Preibisch & Zinnecker 2004). Photometric variability studies have also been used to identify additional cluster members (Cohen et al. 2004; Littlefair et al. 2005), but also to probe the rotational evolution of stars in an attempt to compare the period distribution to similarly aged clusters such as NGC 2264 and the ONC.

2.2.4 IC 5146

IC 5146 (or the Cocoon Nebula) is a transitionary object that is both a reflection nebula and an H II region surrounding the B0 star BD+46° 3474 in the region of Cygnus (Wolf 1904; Hubble 1922; Minkowski 1947). Walker (1959) used a combination of photoelectric and photographic photometry to study the stellar population of IC 5146 and discovered a small MS population consisting of 5 B-type stars. The remaining objects (> 50) comprised fainter variable and non-variable stars that lay above the MS, suggesting a probable pre-MS population. The MS population has been used to derive a distance of $0.9 - 1.4 \, \mathrm{kpc}$ (Elias 1978; Herbig & Dahm 2002). The central coordinates of the cluster are $\alpha_{\mathrm{J2000.0}} \simeq 21^{\mathrm{h}} 53^{\mathrm{m}} 24.0^{\mathrm{s}}$, $\delta_{\mathrm{J2000.0}} \simeq +47° 16' 00.0''$ (Herbig & Dahm 2002).

Herbig (1960a) carried out an objective-prism survey and identified approximately 20 Hα emission stars. The number of known Hα emitters was increased markedly by the $BVRI$ photometric and spectroscopic Hα study of Herbig & Dahm (2002). This work found a total of over 100 Hα emitters and derived a median age of $\sim 1 \, \mathrm{Myr}$, with a significant dispersion. Far-IR maps of the IC 5146 region (Sargent et al. 1981; Wilking et al. 1984) found no evidence of embedded massive stars, suggesting that the observed dust luminosity is supplied solely by the illuminating source BD+46° 3474. Recent *Spitzer* IRAC and MIPS observations have identified more than 200 YSO candidates based on CMD and colour-colour diagram positions (Harvey et al. 2008).

2.2.5 λ Ori

λ Ori is an extensively studied SFR with the O8III visual binary λ Ori at its centre. The region contains hundreds of stars as well as numerous dark clouds that are actively forming stars concentrated in a dense ring of molecular gas and dust around λ Ori (Barnard 1927; Lynds 1962). The first photoelectric photometric survey of early-type members was performed by Murdin & Penston (1977) and initially constrained the age to $\sim 4 \, \mathrm{Myr}$ and distance to $\sim 400 \, \mathrm{pc}$. The central coordinates of the cluster are $\alpha_{\mathrm{J2000.0}} = 05^{\mathrm{h}} 35^{\mathrm{m}} 06.5^{\mathrm{s}}$, $\delta_{\mathrm{J2000.0}} = +09° 54' 00.0''$ (Sacco et al. 2008).

λ Ori has an abundant pre-MS population which has been observed in a variety of wavelengths. The initial surveys to identify pre-MS stars were Hα objective-prism surveys (Haro et al. 1953; Manova 1959; Duerr et al. 1982), which when combined, discovered approximately 100 Hα emitters. Over the past decade additional spectroscopic (Dolan & Mathieu 1999, 2001; Sacco et al. 2008), optical VRI photometric (Dolan & Mathieu 2002; Barrado y Navascués et al. 2004a), near- to far-IR (Barrado y Navascués et al. 2007; Hernández et al. 2009, 2010), and X-ray surveys (Barrado et al. 2011) have identified approximately 300 low-mass pre-MS members. In addition to the rich low-mass pre-MS

population, the more massive clouds surrounding λ Ori harbour embedded sources, several of which have associated Herbig-Haro flows (Reipurth 1999; Magakian et al. 2004).

2.2.6 NGC 1960

NGC 1960 (or M 36) is a young open cluster that apparently forms the centre of the Aur OB1 association. Despite early photographic photometric studies of the cluster (Hopmann 1924; Boden 1951), it was not until the first photoelectric study of Johnson & Morgan (1953), and later Barkhatova et al. (1985), that derivations of the age and distance to the cluster were published ($\sim 30\,\text{Myr}$ and $1200\,\text{pc}$ respectively). The first detailed spectroscopic observations classified most of the brightest stars in NGC 1960 as B2V (Harris 1976). The lack of evidence for a more evolved stellar population has contributed to the large range of derived ages (e.g. Sanner et al. 2000; Hasan et al. 2008). The central coordinates of the cluster are $\alpha_{\text{J2000.0}} = 05^{\text{h}}\,36^{\text{m}}\,06.0^{\text{s}}$, $\delta_{\text{J2000.0}} = +34°\,08'\,00.0''$ (Sanner et al. 2000). Memberships have been assigned on the basis of proper motions (Chian & Zhu 1966; Sanner et al. 2000) and despite the deep BV and JHK photometric surveys of Sanner et al. (2000) and Hasan et al. (2008) respectively, there is little published evidence of a large pre-MS population.

2.2.7 NGC 2169

NGC 2169 is a sparsely populated young open cluster in the constellation of Orion (Ruprecht 1966). Early photometric studies (Cuffey & McCuskey 1956; Grubissich 1959; Sagar 1976) derived a distance of $\sim 830\,\text{pc}$ and an age of $\sim 9\,\text{Myr}$. The high-mass population consists of approximately 15 stars with spectral types earlier than A0, the most evolved is a B2III binary star (Abt 1977). The central coordinates of the cluster are $\alpha_{\text{J2000.0}} = 06^{\text{h}}\,08^{\text{m}}\,24.0^{\text{s}}$, $\delta_{\text{J2000.0}} = +13°\,57'\,54.0''$ (Jeffries et al. 2007).

The pre-MS population of NGC 2169 was discovered by Jeffries et al. (2007) through a combined RI photometric and intermediate-resolution spectroscopic survey. Pre-MS cluster members were classified on the basis of strong Li I absorption. Combining Hα emission strength and width with K-band data, Jeffries et al. (2007) found no evidence of either accretion activity or warm circumstellar material in the spectroscopically confirmed members.

2.2.8 NGC 2244

NGC 2244 (or the Rosette Nebula) is in the Mon OB2 association and part of a larger structure known as the Rosette Complex. The large high-mass population of NGC 2244 – approximately 30 stars with spectral types earlier than B3 – have given rise to a large expanding H II region (Flynn 1965; Smith 1968) that is in the process of interacting with a GMC, leading to the formation of new star clusters along the interface (Schneps et al. 1980; White et al. 1997). Initial photoelectric photometric observations (Johnson 1962; Ogura & Ishida 1981) were able to constrain the distance to NGC 2244 to $\sim 1700\,\text{pc}$ and the age

to ~ 4 Myr. The central coordinates of the cluster are $\alpha_{\text{J2000.0}} = 06^{\text{h}}\,32^{\text{m}}\,02.1^{\text{s}}$, $\delta_{\text{J2000.0}} = +04°\,56'\,30.0''$ (Park & Sung 2002).

A combined *UBVRI* photometric and spectrophotometric study by Pérez et al. (1987) showed that some members of NGC 2244 provided evidence of anomalous extinction values, suggesting that this could be due to a combination of MS and pre-MS objects. A *ubvyβ* follow-up analysis (Pérez et al. 1989) confirmed that several objects were indeed TTS based on levels of excess emission, whilst also providing evidence of a significant age spread within the cluster and hypothesising that this can only be due to continuous star formation. The number of pre-MS objects was increased to over 20 by the *UBVI* and Hα photometric study of Park & Sung (2002). Various X-ray surveys have detected point sources that coincided with previously confirmed members (Berghöfer & Christian 2002; Chen et al. 2004), however the most sensitive X-ray survey to date is that of Wang et al. (2008) (see also the study by Townsley et al. 2003). Of the point sources discovered, 77 % were found to have optical or near-IR counterparts based on comparisons with previous optical (Berghöfer & Christian 2002; Park & Sung 2002) and near-IR (2MASS; Cutri et al. 2003 and FLAMINGOS; Román-Zúñiga et al. 2008) surveys. Based on their relative positions in near-IR colour-colour diagrams it was found that the majority of these sources were WTTS, with a less, but significant, number of CTTS.

2.2.9   NGC 2362

NGC 2362, in Canis Majoris, is a well-populated cluster and dominated by the O9Ib multiple star τ CMa as well as several dozen B-type stars (McSwain & Gies 2005). Distance measurements to NGC 2362 are highly variable, from ~ 900 pc based on the position of τ CMa on the H-R diagram (Humphreys 1978) to ~ 2100 pc based on photoelectric observations (Johnson & Morgan 1953). Due to the large number of unevolved B-type stars the age of NGC 2362 has been assumed to be quite young, with current estimates based on post-MS isochrones suggesting $\sim 4-5$ Myr (Balona & Laney 1996; Moitinho et al. 2001). The central coordinates of the cluster are $\alpha_{\text{J2000.0}} = 07^{\text{h}}\,18^{\text{m}}\,46.3^{\text{s}}$, $\delta_{\text{J2000.0}} = -24°\,57'\,22.0''$ (Moitinho et al. 2001).

The deep *UBVRI* photometric survey by Moitinho et al. (2001) highlighted the pre-MS in NGC 2362. The combined *VRI* photometric and spectroscopic Hα observations of Dahm (2005) not only extended the pre-MS further towards the substellar limit, but also detected ~ 130 Hα emitters. Comparison of the bona fide pre-MS objects, on the basis of strong Hα emission, with the full optical CMD of the region, shows that a possible $200-300$ additional low-mass objects might be associated with NGC 2362. Early X-ray surveys (Berghöfer & Schmitt 1998) were hampered by poor spatial sensitivity, but with the *Chandra* ACIS observations by Damiani et al. (2006a) 308 star-like objects were discovered. Approximately 90 % of these sources were identified as probable cluster members based on the comparison with optical surveys. The spatial distributions of the low-mass and high-mass populations suggest that mass segregation might be occurring within the cluster. Dahm & Hillenbrand (2007) used *Spitzer* IRAC observations to probe the disc

harbouring population of NGC 2362 and found that only $\sim 7\%$ have optically thick circumstellar discs, whereas the fraction with associated optically thin discs is slightly higher ($\sim 12\%$).

2.2.10   NGC 6530

NGC 6530 is the oldest component of the large H II region known as the Lagoon Nebula and forms the nucleus of the Sgr OB1 association. The MS population of NGC 6530 is rich, containing several O stars and dozens of B stars (Walker 1957; Kilambi 1977) however due to its location – close to the Galactic plane and projected on top of the Galactic bulge – it can be difficult to differentiate its stellar population from foreground and background stars. The earliest photometric study of the core of NGC 6530 was performed by Walker (1957) who discovered a MS extending to spectral types of approximately A0 below which the stars lie systematically above the empirically defined MS and determined a distance in the region of $1400 - 2000$ pc. NGC 6530 is a very young SFR with most estimates – based on MS fitting of the high-mass OB population – suggesting an age in the range of $1.5 - 3.0$ Myr (Sagar & Joshi 1978; Sung et al. 2000). The central coordinates of the cluster are $\alpha_{\text{J2000.0}} = 18^{\text{h}} 04^{\text{m}} 31.0^{\text{s}}$, $\delta_{\text{J2000.0}} = -24° 21' 30.0''$ (Chen et al. 2007).

The initial evidence of a well-populated pre-MS was the photoelectric study of Walker (1957) that showed late-type stars lying above the ZAMS. Although the pre-MS nature of these objects was disputed (Thé 1960), later studies confirmed the findings of Walker (1957) (van Altena & Jones 1972; Kilambi 1977). A deep $UBVRI$ and Hα survey by Sung et al. (2000) found several dozen pre-MS objects on the basis of excess Hα emission (see also the earlier study of Herbig 1957). Several X-ray surveys (Rauw et al. 2002; Damiani et al. 2004) have identified 884 point sources, and although only 220 of these have optical counterparts (see for instance the BVI study of Prisinzano et al. 2005), it is believed that at least 90% of these are low-mass pre-MS stars. Damiani et al. (2006b) combined previous X-ray data with near-IR 2MASS data to study the low-mass disc bearing population of NGC 6530. They discovered 120 additional pre-MS candidates on the basis of near-IR excesses indicative of warm circumstellar material that were not present in the X-ray catalogue and also interpreted a small subset of objects with more extreme IR excesses as possible Class I objects.

2.2.11   NGC 6611

NGC 6611 (or the Eagle Nebula) is a vast SFR in the constellation Serpens Cauda. It is somewhat similar in nature to NGC 2244, in that there is a massive star population that is photoionising the surrounding region giving rise to a complex morphology of gas and dust as the H II region expands into the surrounding molecular cloud (Gum 1955; Sharpless 1959), creating such structures as the famous elephant trunks (Duncan 1920; Hester et al. 1996). The first detailed photometric study of the region was performed by Walker (1961) who discovered a well populated MS – consisting primarily of OB-type stars – as well as a population of stars that lay above the MS. From this sample, Walker

(1961) calculated a distance of $\sim 3.2\,\mathrm{kpc}$ and an age of $1.8\,\mathrm{Myr}$. Further photometric studies (Hiltner & Morgan 1969; Sagar & Joshi 1979; Thé et al. 1990) have increased the known high-mass population of NGC 6611, whilst also providing evidence of a rich pre-MS population. Surveys studying the extinction properties in the direction of NGC 6611 (e.g. Hillenbrand et al. 1993; Belikov et al. 1999) have not only found that it is highly variable, but also that the ratio of total-to-selective extinction (R_V) estimated on a star-by-star basis appears to be larger than the normal interstellar medium value (see also the polarimetric observations of Orsatti et al. 2000, 2006). The central coordinates of the cluster are $\alpha_{\mathrm{J2000.0}} = 18^{\mathrm{h}}\,18^{\mathrm{m}}\,40.0^{\mathrm{s}}$, $\delta_{\mathrm{J2000.0}} = -14° \, 47' \, 06.0''$ (Belikov et al. 1999).

A large Herbig Ae/Be star population has been discovered from photometric (Hillenbrand et al. 1993; de Winter et al. 1997) and spectroscopic Hα surveys (Herbig & Dahm 2001; Ogura et al. 2002). The low-mass pre-MS population has only recently been investigated by the deep IZ photometric survey of Oliveira et al. (2005). Follow-up optical and near-IR *Hubble* Space Telescope observations (Oliveira et al. 2009) extended the low-mass pre-MS census well into the substellar regime. *Chandra*-ACIS observations of the central region (Guarcello et al. 2007) and the more recent survey of Guarcello et al. (2009) that combined optical BVI, near-IR JHK, *Spitzer* mid-IR and X-ray surveys found a total of 458 candidate members with associated circumstellar discs and provided evidence that the UV radiation from high-mass stars affects the evolution of nearby circumstellar discs.

2.2.12   NGC 7160

NGC 7160 is a young SFR and forms the nucleus of the Cep OB2 association (Markarian 1952). Around NGC 7160 is a bubble of atomic and molecular gas (Simonson & van Someren Greve 1976) that is possibly driven by the stellar winds produced by the several B-type stars (Daflon et al. 1999) and triggering star formation along the edge of the bubble (Duvert et al. 1990; Patel et al. 1998). Early UBV photoelectric photometric studies of the region (Conti & van den Heuvel 1970; Janes & Adler 1982) constrained the age to $10 - 18\,\mathrm{Myr}$ and distance to $\sim 830 - 1300\,\mathrm{pc}$. The central coordinates of the cluster are $\alpha_{\mathrm{J2000.0}} \simeq 21^{\mathrm{h}}\,53^{\mathrm{m}}\,40.0^{\mathrm{s}}$, $\delta_{\mathrm{J2000.0}} \simeq +62° \, 36' \, 12.0''$ (Sicilia-Aguilar et al. 2004).

Although embedded YSOs were discovered by IRAS observations of the region (Balazs & Kun 1989; Schwartz et al. 1991), the first identification of unobscured low-mass pre-MS objects was the photometric and spectroscopic study of Sicilia-Aguilar et al. (2004). This study was expanded upon in a series of papers (Sicilia-Aguilar et al. 2005, 2006a) supplementing the visual photometry with far-IR observations from *Spitzer*. Approximately 30 low-mass pre-MS members were discovered in NGC 7160, with the IR observations finding that only $4\,\%$ of stars showed excess emission due to circumstellar material.

2.2.13   Orion Nebula Cluster

The ONC is part of the northern Orion A molecular which in turn forms part of the Orion Complex. This is a vast complex of bright nebulae, dark clouds, and young stars that stretches several degrees from Orion's Belt to the Upper Sword (see the various subgroups

in Blaauw 1964). Due to a combination of its richness (> 2000 members) and relative proximity ($\sim 400\,\mathrm{pc}$), the ONC is arguably the most frequently observed nearby SFR, hence the properties of the stellar population – such as masses, rotational distributions, circumstellar disc fractions, etc. – provide crucial constraints on theoretical models of molecular cloud evolution and star formation. Early photoelectric photometric observations (Sharpless 1952, 1954; Johnson 1957b) provided evidence of a densely populated MS and a lower mass population that lay well above the empirically derived MS. The central coordinates of the cluster are $\alpha_{\mathrm{J2000.0}} = 05^{\mathrm{h}}\,35^{\mathrm{m}}\,16.0^{\mathrm{s}}$, $\delta_{\mathrm{J2000.0}} = -05°\,23'\,22.40''$ (Rebull 2001).

The ONC has been studied at almost every wavelength regime from X-rays to radio waves (see O'Dell et al. 2008 for a more comprehensive discussion). Early Hα surveys (Haro 1953; Parsamian & Chavira 1982; Herbig & Bell 1988) documented hundreds of stars within a 3.5 degree region around the Trapezium, whilst later photometric studies (Prosser et al. 1994; Hillenbrand 1997) extended the pre-MS population towards the substellar limit. Disc fractions in the ONC are of the order of $60 - 90\,\%$ (Hillenbrand et al. 1998) with the mid-IR $3.8\,\mu m$ survey of (Lada et al. 2004) extending measurements well into the substellar regime. The deepest X-ray survey to date is the COUP (Getman et al. 2005) which identified ~ 1400 YSOs. Later studies of the COUP dataset provided evidence of X-ray emission from spectroscopically identified brown dwarfs (Preibisch et al. 2005b). Using a combination of ground based CTIO near-IR and *Spitzer* mid-IR data, Prisinzano et al. (2008) established a list of 45 protostellar candidates (Class $0 - I$) within the COUP field-of-view.

2.2.14 σ Ori

σ Ori is a cluster of stars around the multiple high-mass system σ Ori and is associated with, but kinematically distinct from, the Ori OB1 association (Blaauw 1964). Garrison (1967) first identified the clustering of stars around σ Ori and derived a distance of $\sim 440\,\mathrm{pc}$. Initial age estimates were based on the MS turn-off of the more massive stars. Blaauw (1964) derived an age of 8 Myr based on high-mass stars in the Ori OB1b subgroup. A more recent age of $4-5\,\mathrm{Myr}$ was derived by Voss et al. (2010) based on the comparison of MS evolutionary models to the massive star population in the H-R diagram. The central coordinates of the cluster are $\alpha_{\mathrm{J2000.0}} = 05^{\mathrm{h}}\,38^{\mathrm{m}}\,48.9^{\mathrm{s}}$, $\delta_{\mathrm{J2000.0}} = -02°\,34'\,22.0''$ (Sacco et al. 2008).

A handful of X-ray sources were detected in the vicinity of σ Ori with the *Einstein* Observatory. Spectroscopic follow-up (Wolk 1996; Walter et al. 1998) identified over 100 pre-MS objects within 30 arcmin of σ Ori based on the strengths of Li I and Hα. Since these initial surveys σ Ori has been intensively studied. Deep optical and near-IR photometric surveys (Béjar et al. 2001, 2004; Sherry et al. 2004) have increased the number of low-mass pre-MS dramatically, with follow-up spectroscopic observations corroborating many of these objects (Kenyon et al. 2005; Maxted et al. 2008). *Spitzer* IRAC observations (Caballero et al. 2007; Hernández et al. 2007) discovered over 1000 point sources and

considered 336 to be members based on positions in the optical and near-IR CMDs in conjunction with ancillary data such as variability (e.g. Bailer-Jones & Mundt 2001) and X-ray observations (e.g. Franciosini et al. 2006). A precise radial velocity study of σ Ori members (Jeffries et al. 2006) showed that the cluster is actually comprised of two kinematically distinct groups, comprising bona fide σ Ori members, but also a number of objects associated with the Ori OB1a, concluding that within 10 arcmin of σ Ori the contamination by the Ori OB1a subgroup is $\sim 10\%$.

2.3 Deriving Parameters from Main-Sequence Fitting

So far in the discussion of comparing observations of stellar populations with theoretical evolutionary models the focus has been on the pre-MS regime only (see Section 1.3.3). The high-mass population of young SFRs are sparse and hence it can be difficult to derive robust ages from these stars, therefore for young SFRs, ages are typically derived using the more numerous pre-MS population. The age determinations from both MS and pre-MS populations rely on different aspects of stellar physics and hence any disagreement between these ages (e.g. Naylor 2009) will hamper the study, for instance, of circumstellar disc fractions in young SFRS in an effort to empirically constrain the rotational evolution of stellar populations or planet formation.

As discussed in Section 1.3.3, there are two ways in which one can compare observations of stars with theoretical evolutionary models – in the theoretical (H-R diagram) or the observational plane (CMD). Both of these comparisons require either the model or the data to be transformed into the other plane for direct comparison. Several problems have been highlighted with converting stars, and especially pre-MS objects, into the H-R plane (see Section 1.3.3). Therefore from a purists perspective, it is preferable to leave the data in its natural plane and instead transform the theoretical model. In the following sections the method of transforming the evolutionary models into the CMD plane and the statistical fitting technique used to fit a stellar population using these transformed models will be discussed. Before deriving an age, however, the subtle degeneracies that are introduced due to the effects of both distance and interstellar reddening are described.

2.3.1 Distance Fitting

The conversion of stellar luminosities into magnitudes allows the effects of distance on these magnitudes to be assessed. The apparent magnitude in a given bandpass with response function R_λ of a star at an arbitrary distance d is given by

$$m_{R_\lambda} = -2.5 \log I(f_\lambda, R_\lambda) + C. \tag{2.1}$$

By comparing the difference in magnitude between the apparent magnitude at a distance d with its absolute magnitude M_{R_λ} at a distance of 10 pc the distance modulus dm can be defined as
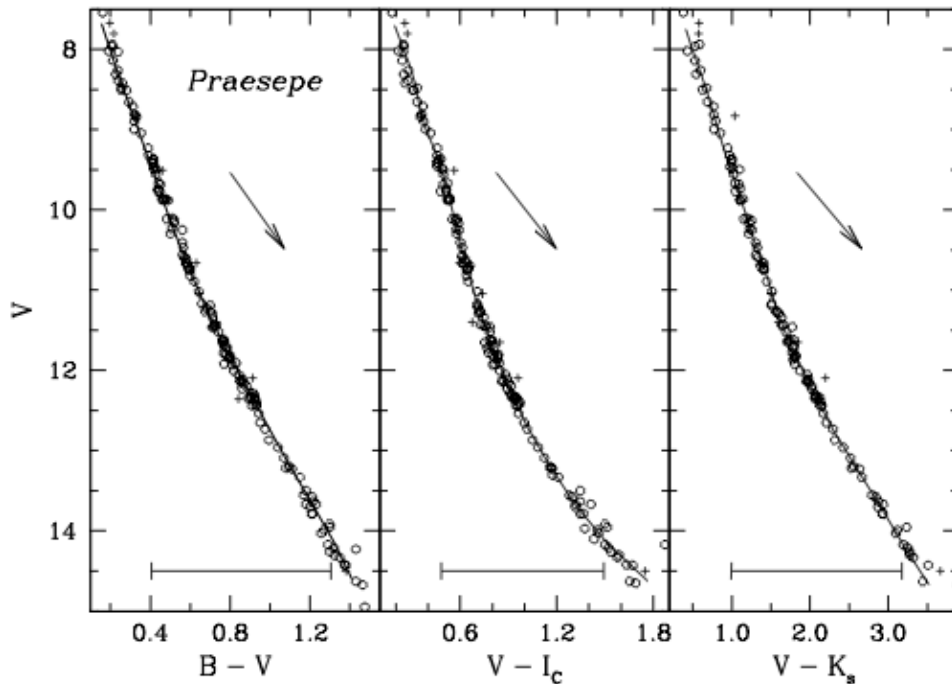
Figure 2.1: Main-sequence distance fitting for the Praesepe open cluster. The solid lines are empirically calibrated MS isochrones with a metallicity based on spectroscopic measurements and a reddening based on literature values. The horizontal bars denote the fitting range and arrows show the direction of the reddening vector in each CMD. **Left panel:** $V, B - V$ CMD. **Middle panel:** $V, V - I_c$ CMD. **Right panel:** $V, V - K_s$ CMD. Reproduced with permission from the AAS. Credit: An et al. (2007).

$$dm \equiv m - M = -5 + 5\log(d). \tag{2.2}$$

The effect of distance is the same for each bandpass and hence its effect cancels entirely when magnitudes in two bandpasses are subtracted to calculate the colour of a star. Therefore, adjusting the distance of a given star, or population thereof, only shifts the star in magnitude and not colour.

Stars that have contracted onto the MS are in a state of hydrostatic equilibrium and as such are temporally static compared with the rapid evolution in the pre-MS regime (see Section 1.3.3). By concentrating on this near stationary region of the CMD, accurate distance determinations based on photometric observations of MS stars alone is possible (Becker & Stock 1954; Johnson 1957a; Mitchell & Johnson 1957). In practice, this involves fitting a theoretical isochrone to the single-star sequence (e.g. An et al. 2007; Sherry et al. 2008, see Fig. 2.1). The isochrone is shifted vertically until a best-fit is achieved (generally by-eye), however care must be taken as unresolved binary stars create a spread in CMD space of $\simeq 0.75$ mag between the single-star lower envelope and the equal-mass binary upper envelope. If the MS is not sufficiently populated, the pre-MS population may be used to derive an age and distance simultaneously. Note, however, that in this regime age and distance are heavily degenerate with one another (see Fig. 1.6).
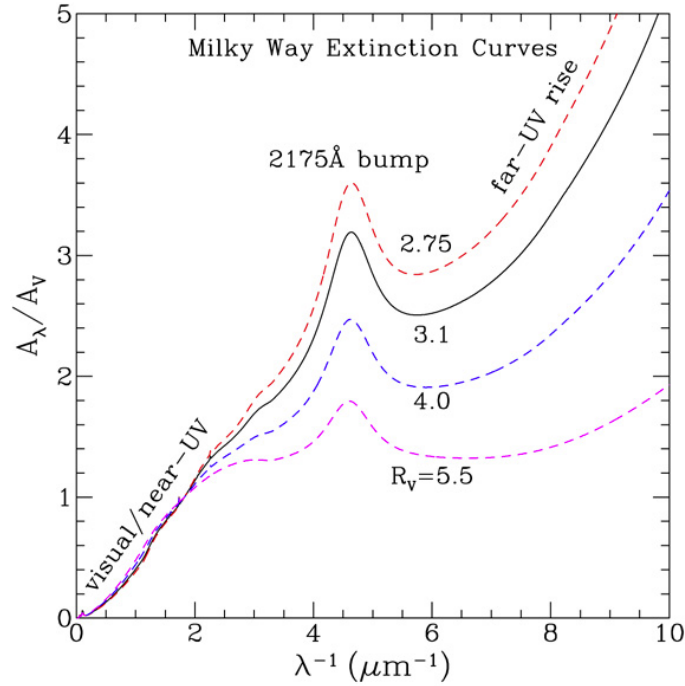
Figure 2.2: Interstellar extinction curves for the Milky Way ($R_V = 2.75, 3.1, 4.5$ and 5.5). The optical/UV extinction curves highlight considerable regional differences depending on the local environment and indicate different dust grain size distributions. Credit: NASA/IPAC Extragalactic Database (NED), `http://ned.ipac.caltech.edu/level5/ Sept07/Li2/Li2.html`.

2.3.2 Interstellar Extinction and Reddening

The radiation emitted from stars is attenuated by dust in the ISM which absorbs a fraction of the stellar light and re-radiates it, altering the intensity, in a process that is strongly dependent upon the incident wavelength (see Fig. 2.2). To incorporate and quantify the wavelength dependence of the interstellar extinction, Eqn. 2.1 must be modified so that Eqn. 2.2 becomes

$$dm \equiv m - M = -5 + 5\log(d) + A_{R_\lambda}, \tag{2.3}$$

where A_{R_λ} is the extinction measured in magnitudes in a given bandpass with response function R_λ. As a result of the interstellar extinction's dependence on wavelength – and therefore bandpass – it will not act, as in the case of distance, in only one direction in CMD space, but will have distinct magnitude and colour components. The component in the magnitude direction is termed the extinction, whereas the colour component is called the reddening. Note that the reddening is also known as the colour excess and is the difference between the intrinsic and apparent colour i.e. $A_B - A_V \equiv E(B-V) \equiv (B-V) - (B-V)_\circ$. To derive accurate distances based on MS fitting, one must first calculate and account for the effects of interstellar extinction. The determination of cluster reddening depends upon the identification of particular stellar types within the cluster and the comparison of these stars with unreddened stars of the same types (see for instance the spectral type analysis

in Sharpless 1952). Alternative methods include using three-colour UBV photometry to create colour-colour diagrams, thereby removing the effects of distance, and fitting MS isochrones to determine a mean cluster reddening (e.g. Sagar 1976). For very young SFRs, the reddening may be variable across the cluster and in such cases individual stellar reddenings can be derived using the Q-method (Johnson & Morgan 1953; discussed further in Section 2.7.2).

2.3.3 Main-Sequence Ages

Whilst the MS represents a stellar population with which to derive robust distance measurements, its temporally static nature makes it less well suited for age estimates. Although most stars in young SFRs are still in the pre-MS contraction phase, the most massive stars may have evolved onto, and even away from, the MS. As discussed in Naylor (2009), this offers two possible age diagnostics for young SFRs – namely an age derived using stars that have evolved past the TAMS and an age derived using stars between the ZAMS and TAMS. Stars that have reached the ZAMS will begin converting hydrogen in their cores into helium. As the helium content of the core of MS stars increases with time the star will move redward and to higher luminosities, away from the ZAMS. This movement continues until core hydrogen burning has ceased and the star has reached the TAMS. The star will then evolve away from the MS, eventually fusing helium in the core after a phase of hydrogen shell burning, and evolve into either a red giant or supergiant depending on the stellar mass. This evolution between the ZAMS and TAMS means that in a CMD the MS, which normally has a positive gradient, can near the high-mass terminus, become vertical or even negative. For young SFRs, the number of stars that have evolved past the TAMS is smaller than those evolving towards the TAMS and as such, deriving ages using stars between the ZAMS and TAMS is statistically more robust. In CMD space, this evolution is very subtle and the typical approach of simply fitting model isochrones by-eye raises questions of objectivity and can result in large uncertainties on the derived age.

The position of the TAMS is dependent upon physical processes that affect the MS lifetime such as the mass-loss rate (particularly important for massive stars), stellar rotation and the degree of convective core overshoot (see Demarque et al. 2004; Ekström et al. 2012). Significant effort has been undertaken in attempting to constrain each of these (see for example Vink et al. 2001; Huang et al. 2010; Vink et al. 2010) with the results subsequently being incorporated into successive generations of MS evolutionary models. Hence depending on the initial choice one assumes for a given physical input, the position of the TAMS for a star of given mass may vary. In Section 2.10 a discussion is presented that compares the derived parameters based on different combinations of both MS interior and atmospheric models, the conclusion of which is that the parameters may vary on the order of $5-10\%$ depending on the initial choice.

Table 2.1: Literature sources for the Johnson UBV photoelectric photometric data.

SFR	Source
Cep OB3b	Blaauw et al. (1959)
χ Per	Johnson & Morgan (1955)
IC 348	Harris et al. (1954)
IC 5146	Walker (1959)
λ Ori	Murdin & Penston (1977)
NGC 1960	Johnson & Morgan (1953)
NGC 2169	Hoag et al. (1961)
NGC 2244	Johnson (1962)
NGC 2362	Johnson & Morgan (1953)
NGC 6530	Walker (1957)
NGC 6611	Walker (1961)
NGC 7160	Hoag et al. (1961)
ONC	Walker (1969)
σ Ori	Hardie et al. (1964)

2.4 Main-Sequence Data

Observations of the SFRs were taken in the $(UgriZ)_{\mathrm{WFC}}$ bandpasses with the Wide-Field Camera (WFC) on the 2.5-m *Isaac Newton* Telescope (INT) on La Palma (see Section 3.2 and Appendix A), however the WFC saturates at magnitudes $g_{\mathrm{WFC}} \lesssim 10\,\mathrm{mag}$ thus additional literature data was included so that the MS population could be fitted. To derive statistically meaningful parameters from these objects a significant mass range is required to display measurable evolution between the ZAMS and TAMS. Furthermore, robust reddening and distance measurements are required which can then be applied to the low-mass regime when fitting the pre-MS isochrones. Using UBV photometry, reddenings can be calculated from fitting data in the $U - B, B - V$ colour-colour diagram and distances can be derived through the traditional MS fitting technique. Additionally, the upper region of the $V, B - V$ CMD is age sensitive, tracing out the evolution between the ZAMS and TAMS.

To maintain consistency within the UBV photometric data, whenever possible, the UBV photoelectric photometry of Johnson and collaborators was used. These pioneering works defined and characterised the UBV photometric system, and provide the high levels of calibration and consistency required. Table 2.1 details the literature source for the UBV photoelectric photometry of the sample of SFRs. MS memberships were generally published alongside the photometry and have been adopted unless stated.

2.5 Main-Sequence Models

The Geneva interior models of Lejeune & Schaerer (2001), specifically the basic model set 'c' (Schaller et al. 1992), covering the mass range $0.8 - 120\,\mathrm{M_\odot}$ were adopted. The rate of change of L_{bol} and T_{eff} with time changes discontinuously at the TAMS, and

as the grid of interior models was much coarser than that required, intermediate age models were created by temporally interpolating between existing calculations. For this the interpolation routine provided by the Geneva group was used to create a grid with spacing $\Delta \log(\text{age}) = 0.02$.

For a given mass the interior models predict the bolometric luminosity (L_{bol}), effective temperature (T_{eff}) and surface gravity ($\log g$). These must then be transformed into colours and magnitudes in the required photometric system to allow the fitting and hence derivation of parameters such as age and distance from photometric data. Colours are calculated through a colour-T_{eff} relation and magnitudes via bolometric corrections to L_{bol}. Both relations can be derived via the convolution of atmospheric model flux distributions through the appropriate photometric filter responses. The colours and magnitudes must then be calibrated to a standard scale. Note that the commonly referred to colour-T_{eff} relation is a misnomer for the bolometric correction relation as it is the difference in bolometric corrections at a specific T_{eff} that explicitly defines the colour of the star i.e.

$$B(T_{\text{eff}}) - V(T_{\text{eff}}) = BC_V(T_{\text{eff}}) - BC_B(T_{\text{eff}}), \qquad (2.4)$$

and so from now on the transformation from H-R to CMD space will be discussed in terms of the bolometric correction (BC-T_{eff}) relation. Note that due to the definition of the bolometric correction the colour index, as defined by the difference in two photometric bandpasses, is equal to the inverse difference of the bolometric corrections in the two bandpasses. The formalism of Bessell et al. (1998) was adopted to create the BC-T_{eff} relation and transform the MS isochrones into the Johnson UBV photometric system.

2.5.1 Creating the Bolometric Correction-T_{eff} Relation

The definition for the apparent magnitude of a star in a given bandpass with response function R_λ is

$$m_{R_\lambda} = -2.5 \log I(f_\lambda, R_\lambda) + C, \qquad (2.5)$$

where

$$I(f_\lambda, R_\lambda) = \frac{\int_\lambda f_\lambda R_\lambda \, d\lambda}{\int_\lambda R_\lambda \, d\lambda}, \qquad (2.6)$$

where f_λ is the stellar flux as observed at Earth and the response function R_λ includes the cumulative effects of the transmission of the Earth's atmosphere and the telescope optics. Note that as the Johnson UBV photometric system was defined using energy amplifier devices such as photomultiplier tubes it is necessary to reflect this in the integrand of Eqn. 2.6 by convolving the stellar flux in units of energy with the response function, and therefore one is measuring the energy across a given bandpass. By setting $m_{R_\lambda} = m^\circ_{R_\lambda}$ and $f_\lambda = f^\circ_\lambda$ where f°_λ denotes a reference spectrum which produces a known apparent magnitude $m^\circ_{R_\lambda}$, the constant C then becomes

$$C = m^{\circ}_{R_\lambda} + 2.5 \log I(f^{\circ}_\lambda, R_\lambda), \tag{2.7}$$

and the initial definition becomes

$$m_{R_\lambda} = -2.5 \log I(f_\lambda, R_\lambda) + 2.5 \log I(f^{\circ}_\lambda, R_\lambda) + m^{\circ}_{R_\lambda}. \tag{2.8}$$

The relation between the flux received at Earth, f_λ, compared to that at the stellar surface, F_λ, is simply

$$f_\lambda = 10^{-0.4A_\lambda} \left(\frac{R}{d}\right)^2 F_\lambda, \tag{2.9}$$

where R is the stellar radius, d its distance and A_λ is the extinction measured in magnitudes at a given wavelength λ. As fluxes from atmospheric models represent the flux at the stellar surface, Eqn. 2.8 becomes

$$m_{R_\lambda} = -2.5 \log \left[\left(\frac{R}{d}\right)^2 \frac{I(f_\lambda, R_\lambda)}{I(f^{\circ}_\lambda, R_\lambda)} \right] + m^{\circ}_{R_\lambda}. \tag{2.10}$$

By setting $d = 10\,\mathrm{pc}$ so as to calculate the absolute magnitude M_{R_λ} and using $L = 4\pi R^2 \sigma T^4_{\mathrm{eff}}$, the radial dependence – which the atmospheric models are unable to specify – can be removed, so that

$$M_{R_\lambda} = -2.5 \log \left[\frac{L}{(10\,\mathrm{pc}^2)4\pi\sigma T^4_{\mathrm{eff}}} \frac{I(f_\lambda, R_\lambda)}{I(f^{\circ}_\lambda, R_\lambda)} \right] + m^{\circ}_{R_\lambda}. \tag{2.11}$$

The definition of the bolometric magnitude is

$$M_{\mathrm{bol}} - M_{\mathrm{bol},\odot} = -2.5 \log \left(\frac{L}{L_\odot}\right), \tag{2.12}$$

and so combining Eqn. 2.10 with the definition of the bolometric correction, this becomes

$$BC_{R_\lambda} = M_{\mathrm{bol}} - M_{R_\lambda}, \tag{2.13}$$

which can be generalised to

$$BC_{R_\lambda} = M_{\mathrm{bol},\odot} - 2.5 \log \left(\frac{4\pi(10\,\mathrm{pc}^2)F_{\mathrm{bol}}}{L_\odot}\right) + 2.5 \log \left(\frac{\int_\lambda F_\lambda 10^{-0.4A_\lambda} R_\lambda \, d\lambda}{\int_\lambda f^{\circ}_\lambda R_\lambda \, d\lambda}\right) - m^{\circ}_{R_\lambda}, \tag{2.14}$$

thus allowing bolometric corrections to be derived based solely on information provided by the atmospheric models. Here $F_{\mathrm{bol}} = \sigma T^4_{\mathrm{eff}}$ is the total flux emergent at the stellar surface and all other symbols retain their usual definitions. For the solar values, $M_{\mathrm{bol},\odot} = 4.74$ and $L_\odot = 3.855 \times 10^{33}\,\mathrm{erg\,s}^{-1}$ (Bessell et al. 1998) are adopted. The interstellar extinction is assumed to be zero ($A_\lambda = 0$) for the calculation of the bolometric corrections, however a re-evaluation of the interstellar reddening will be addressed later (see Sections 2.7.1 and 5.5) when it is necessary to account for its effects when fitting the photometric data with

model isochrones.

To calibrate the bolometric corrections to a standard scale f_λ° and $m_{R_\lambda}^\circ$ in Eqn. 2.14 must first be defined. As explained in Johnson & Morgan (1953), the original zero-point of the International System was set by the condition that the colour index equal zero for A0 stars near the sixth magnitude[2]. In accordance, the Johnson UBV photometric system zero-point was set by the mean value of six stars of class A0 on the MK spectral type system. The six stars were α Lyr (Vega), γ UMa, 109 Vir, α CrB, γ Oph and HR 3314, with a mean colour of $U-B = B-V = 0.0$. Subsequent surveys (e.g. Johnson 1965, 1966) used only the colours and magnitudes of Vega to calibrate photometric observations. In the visible regime, Vega is a reliable standard as it is a single-star with a magnitude of 0.03 mag in all bandpasses. Furthermore, it is relatively unaffected by the interstellar extinction and shows minimal levels of variability. Hence the measured magnitude of $V = 0.03$ mag was adopted and all colours assumed to be zero. Finally, to derive bolometric corrections in all bandpasses, a Vega reference spectrum is required. For this, the empirical CALSPEC alpha_lyr_stis_005[3] spectrum was used.

In the MS interior models, some of the most luminous stars have associated $\log g$ values that lie just below the range provided by the ATLAS9 atmospheric models. In such cases, it was necessary to extrapolate the models by setting the colour equal to that of the nearest $\log g$. As the $\log g$ dependence is very small at such $T_{\rm eff}$, this extrapolation affects the model isochrone at $\ll 0.01$ mag level (see Naylor 2009).

2.5.2 Atmospheric Models

To calculate the BC-$T_{\rm eff}$ relation, a grid of theoretical stellar atmospheric models that covers a wide range of $T_{\rm eff} - \log g$ parameter space is required. The full spectral library consists of PHOENIX BT-Settl model atmospheres for $400 \leq T_{\rm eff} \leq 7800$ K and the Kurucz ATLAS9 models with newly updated opacity distribution functions (ODFs) for $8000 \leq T_{\rm eff} \leq 50\,000$ K. Despite the differences in microphysics between the two sets of models, at the transitional $T_{\rm eff} = 8000$ K derived colours from both sets agree to within 0.02 mag in all colours.

2.5.2.1 The ATLAS9 ODFnew Models

The ATLAS9 models are based on the assumption of steady-state plane-parallel layers under the influence of local thermodynamic equilibrium (LTE). The original grid of atmospheric models (Kurucz 1992) showed evidence of some discontinuities in the computed colours of stars which were attributed to the initial treatment of convection. Instead of a pure mixing length theory (MLT; Böhm-Vitense 1958) treatment, Kurucz (1992) adopted a modification of this theory, termed 'approximate overshooting' in the computation of these original models (see Castelli et al. 1997 and Bessell et al. 1998).

---

[2]Trans. I.A.U., 1922, 1, 79
[3]`http://www.stsci.edu/hst/observatory/cdbs/calspec.html`

The ATLAS9 atmospheric models adopted here are those of Castelli & Kurucz (2004)[4] with newly updated ODFs (hereafter ATLAS9/ODFnew). These models include the updated solar abundances of Grevesse & Sauval (1998), the revised TiO line list of Schwenke (1998), the addition of H_2O lines from Partridge & Schwenke (1997), and the inclusion of quasi-molecular absorptions in the UV by Allard et al. (1998). Line-blanketing effects are computed statistically via the use of ODFs which average the contribution of the various atomic and molecular species as described in Kurucz (1979). A pure MLT is used in the computation of these models and those termed 'no-overshoot' were used on the basis that these better recreate the observed spectra of stars with $T_{\rm eff}$ greater than the Sun (Castelli et al. 1997). The mixing length parameter is set to $\alpha = 1.25$, with the convective flux decreasing as an increasing function of $T_{\rm eff}$, ceasing at $T_{\rm eff} \sim 9000\,{\rm K}$. The models are computed with a microturbulent velocity $\xi = 2\,{\rm km\,s^{-1}}$.

2.5.2.2 The PHOENIX BT-Settl Models

The initial NextGen atmospheric models were first introduced to the community by Allard & Hauschildt (1995) and Hauschildt et al. (1996) using the multi-purpose atmospheric code PHOENIX. Akin to the ATLAS9 models, they were computed adopting plane-parallel geometry under LTE. More contemporary computations of the PHOENIX/NextGen atmospheres however (Hauschildt et al. 1999b; Allard et al. 2000) have seen the introduction of spherical symmetry i.e. a spherical radiative transfer as opposed to the plane-parallel approach in the low gravity regime ($\log g \leq 3.5$) for giant and pre-MS stars. In contrast to the treatment of line-blanketing as in the ATLAS9 models through the use of ODFs, the PHOENIX/NextGen models directly sample the opacity utilising a library of over 700 million lines including atomic and molecular species along the spectrum.

The PHOENIX models used here are the most recent BT-Settl models of Allard et al. (2011)[5]. These models have been computed using an updated version of the PHOENIX atmospheric code (cf. Allard et al. 2001) to include the updated BT2 H_2O (Barber et al. 2006) and extended methane (Homeier et al. 2003) line lists, the revised solar abundances of Asplund et al. (2009), and a sophisticated cloud model that accounts for the formation and settling of dust condensates under steady-state conditions (Allard et al. 2003). The effects of turbulent mixing in the atmosphere are calculated by interpolating from two- and three-dimensional radiation hydrodynamic models (Ludwig et al. 2006), with the treatment of dust for cooler models ($T_{\rm eff} < 2600\,{\rm K}$) based on the dust formation models of Freytag et al. (2010). A mixing length parameter of $\alpha = 2.0$ and microturbulent velocity of $\xi = 2\,{\rm km\,s^{-1}}$ are used.

---

[4] `ftp://ftp.stsci.edu/cdbs/grid/ck04models`
[5] `http://phoenix.ens-lyon.fr/Grids/BT-Settl/`

2.6 A Maximum-Likelihood Fitting Statistic

With the formula for deriving bolometric corrections (Eqn. 2.14), the atmospheric models can be folded through the appropriate filter responses to calculate bolometric corrections in the Johnson UBV system. These can then be used to transform MS isochrones into observable CMD space with which to fit photometric data. To fit the young MS populations of the SFRs, a statistically robust and objective method is required – this technique is called the τ^2 fitting statistic.

2.6.1 Definition of the τ^2 Fitting Statistic

The τ^2 fitting statistic was introduced in Naylor & Jeffries (2006) as a solution to fitting model isochrones to photometric data in CMDs. It is a maximum-likelihood fitting technique that can be viewed as an extension of the χ^2 fitting statistic on the basis that both the isochrone and data are two-dimensional distributions – uncertainties in colour and magnitude for the data and the widening of the model isochrone due to the effects of binarity. This technique has been employed in several studies to derive ages and distances for young SFRs (e.g. Jeffries et al. 2007; Mayne & Naylor 2008; Jeffries et al. 2009; Naylor 2009; Cargile & James 2010).

As described in Naylor & Jeffries (2006), imagine a datapoint i with an observed position in CMD space (x_i, y_i). This datapoint will have a two-dimensional probability distribution, which is later assumed to be Gaussian. Thus, for a given datapoint, the probability can be calculated that the true value lies within an elemental box of area $dx\,dy$ about a point (x, y) as $U_i(x - x_i, y - y_i)\,dx\,dy$, where U_i is the two-dimensional uncertainty function. Assuming that a model $\rho(x, y)$ represents a probability distribution of the expected model in CMD space, the probability density that the model produces a star at the point (x_i, y_i) is

$$P_i = \iint U_i(x - x_i, y - y_i)\,\rho(x, y)\,dx\,dy. \tag{2.15}$$

If there are N datapoints, the probability that the datapoints originate from the model then becomes

$$D = \prod_{i=1,\,N} P_i = \prod_{i=1,\,N} \iint U_i(x - x_i, y - y_i)\,\rho(x, y)\,dx\,dy, \tag{2.16}$$

and by defining $\tau^2 \equiv -2\ln D$, the expression for τ^2 is then

$$\tau^2 = -2 \sum_{i=1,\,N} \ln \iint U_i(x - x_i, y - y_i)\,\rho(x, y)\,dx\,dy. \tag{2.17}$$

The best-fitting model is found by minimising τ^2.

2.6.2 Limiting Cases

The original formulation of τ^2 reduces to that of χ^2 for fitting a curve to data with uncertainties in one dimension. When attempting, however, to fit sequences where the gradient becomes vertical this definition is impractical (see Naylor 2009). Thus the normalisation now ensures that the integral of the model distribution ρ from the faintest to the brightest datapoint is unity. Similarly, the integral of the uncertainty function U is unity over the entire CMD i.e.

$$\int \rho(x, y) \, dx \, dy = 1, \qquad (2.18)$$

$$\int U_i(x - x_i, y - y_i) \, dx \, dy = 1. \qquad (2.19)$$

Thus, from Eqn. 2.17, for a single point

$$\tau_i^2 = -2 \ln \iint U_i(x - x_i, y - y_i) \, \rho(x, y) \, dx \, dy. \qquad (2.20)$$

If the two-dimensional model distribution $\rho(x, y)$ is retained, but only datapoints with one-dimensional uncertainties (in the y-direction) are considered, the uncertainty function then becomes

$$U(y - y_i) = U_{\mathrm{L}}(y - y_i) \, \delta(x - x_i), \qquad (2.21)$$

where U_{L} is the linear uncertainty function and δ is a delta function. By substituting Eqn. 2.21 into Eqn. 2.20 the definition of τ^2 becomes

$$\tau_i^2 = -2 \ln \int U_{\mathrm{L}}(y - y_i) \, \rho(x_i, y) \, dy. \qquad (2.22)$$

If, in addition to datapoints with only one-dimensional uncertainties, the model distribution is now simply a curve of the form $y = f(x)$, then the model distribution takes the form

$$\rho(x, y) = \rho_{\mathrm{L}}(x) \, \delta(y - f(x)). \qquad (2.23)$$

Hence the expression for τ^2 further reduces to

$$\tau_i^2 = -2 \ln \left[U_{\mathrm{L}}(f(x_i) - y_i) \, \rho_{\mathrm{L}}(x_i) \right], \qquad (2.24)$$

and thus for N datapoints

$$\tau^2 = -2 \sum_{i=1, N} \ln \left[U_{\mathrm{L}}(f(x_i) - y_i) \, \rho_{\mathrm{L}}(x_i) \right]. \qquad (2.25)$$

Eqn. 2.25 highlights the subtle difference between τ^2 and χ^2. Assuming that the uncertainty function takes the form of a one-dimensional Gaussian i.e.

$$U_{\mathrm{L}}(y - y_i) = A e^{-\frac{(y - y_i)^2}{2\sigma_{y_i}^2}}, \tag{2.26}$$

then Eqn. 2.19 implies that

$$A = \frac{1}{\sigma_{y_i} \sqrt{2\pi}}, \tag{2.27}$$

and furthermore, if the model distribution ρ_{L} is a constant and independent of position in (x, y), then

$$\tau^2 = \sum_{i=1, N} \left(\frac{f(x_i) - y_i}{\sigma_{y_i}} \right)^2 - \sum_{i=1, N} 2 \ln A. \tag{2.28}$$

Hence whereas the χ^2 statistic does not include the density distribution of the model in the (x, y) plane, this is implicitly expressed in the τ^2 statistic, however in this limiting case, minimising τ^2 is the same as minimising χ^2.

2.6.3 The Model Colour-Magnitude Diagram

The model CMD is created by simulating 10^6 stars over a given mass range using a Monte-Carlo method. There is strong evidence that the binary fraction amongst O-type stars in clusters is higher than for later spectral types (Mason et al. 1998; Sana et al. 2008, 2009; Chini et al. 2012) and that the mass-ratio distribution is non-uniform (e.g. Lucy 2006 and references therein). Hence, as described in Naylor & Mayne (2010), an O-star binary fraction of 75 % is assumed. Of these, 25 % are evenly distributed over $0.95 < q < 1.0$, 75 % are evenly distributed over $0.2 < q < 0.95$, and a lower restriction of $q > 0.2$ is adopted. For later spectral types, a binary fraction of 50 % and a uniform secondary distribution ranging from zero to the mass of the primary is assumed. For each star, a mass is drawn from a Salpeter initial mass function (IMF) and if it happens to be a binary the companion mass is assigned as described above. For each star, the interior model assigns an L_{bol}, T_{eff} and $\log g$ which can then be converted into CMD space using the appropriate BC-T_{eff} relation. Binary companions that lie below the lower mass limit of the interior models are assumed to have a flux equal to zero and thus provide no contribution to the overall luminosity of the binary system.

The recent work of Weidner & Vink (2010) highlights the so-called 'mass discrepancy' (see also Herrero et al. 1992; Hohle et al. 2010) where O-star masses derived from evolutionary models are found to be systematically higher than those derived from stellar atmospheric analyses by up to a factor of two. The CMD fitting routine does not measure the MS lifetime of a given mass, but instead how far from the ZAMS a star at a given luminosity has moved. Hence possible inconsistencies in the mass scale of the MS evolutionary models does not introduce any systematic biases into the derived parameters.

2.7 Reddening and Extinction for UBV data

In broadband photometry the effective wavelength of a given bandpass shifts depending on the incident stellar flux distribution and hence the colour – and gravity – of the star (see Bessell et al. 1998). This dependence results in a non-linear reddening trajectory in the $U - B, B - V$ colour-colour diagram, which further depends, albeit to a lesser extent, on the intrinsic reddening of the observed object (Hiltner & Johnson 1956; Wildey 1963). Hence these dependencies must be accounted for when calculating a mean reddening for a given SFR in the $U - B, B - V$ colour-colour diagram. In some cases there is significant scatter around the isochrone in the $U - B, B - V$ colour-colour diagram. The reason for such dispersion is the remnant gas and dust from the star formation process around young SFRs which can result in highly variable reddening across the SFR. In such cases, stars are individually de-reddened using a revised Q-method (Johnson & Morgan 1953).

2.7.1 Colour- and Extinction-Dependent Reddening Vectors

To determine reddenings – be it the mean of a cluster or individual stellar values – it is imperative to understand how stars of varying colour move as a function of reddening in the $U - B, B - V$ colour-colour diagram. These reddenings can be quantitatively determined using the stellar atmospheric models discussed in Section 2.5.2, the standard $UBVRI$ responses of Bessell (1990) and the parameterised interstellar extinction law of Cardelli et al. (1989). Note that only atmospheric models with intrinsic colours $(B - V)_\circ \leq 0.05$ were used to derive the reddening vectors. The parameterised extinction law can be visualised in terms of a nominal $E(B - V)$ which represents the amount of intervening interstellar material between an observer and the object, but does not necessarily correspond to the observationally measured $E(B - V)$ value since this value will vary with the colour of the star.

To determine the relationship between the nominal and measured $E(B - V)$ values, atmospheric models with intrinsic colours $(B-V)_\circ \leq 0.05$ were reddened using the Cardelli et al. (1989) extinction curve of $R_V = A_V/E(B - V)$. The total-to-selective extinction ratio $R_V = 3.2$ was taken to be appropriate for the diffuse ISM (Savage & Mathis 1979). The atmospheric models were reddened in steps of 0.2 from $E(B - V) = 0.0$ to 2.0. Measured $E(B - V)$ values were inferred from the reddened atmospheric models at an intrinsic colour $(B - V)_\circ = -0.15$. Fig. 2.3 shows the difference between the nominal and measured $E(B-V)$ as a function of nominal $E(B-V)$ and highlights the non-linear relation between what is inferred from the atmospheric models and what is predicted by the parameterised extinction law. The modified U_x and B_x responses of Bessell (1990) for the $U - B$ colour were used to derive the updated reddening vectors, which are

$$\frac{A_V}{E(B - V)} = 3.264 + 0.088E(B - V) + 0.018E(B - V)^2 \qquad (2.29)$$
$$+ \; 0.450(B - V)_\circ + 0.333(B - V)_\circ^2,$$
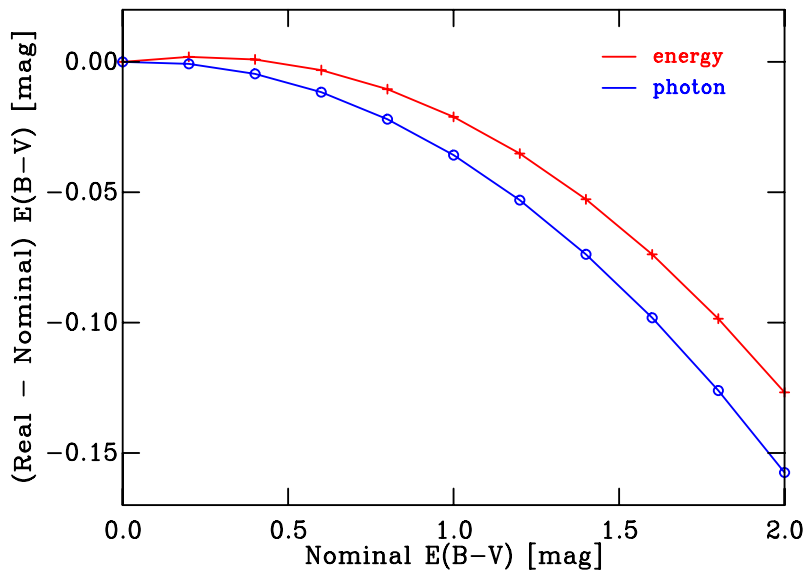
Figure 2.3: The difference between the nominal $E(B - V)$ as predicted by the parameterised extinction law of Cardelli et al. (1989) and that derived from the reddened atmospheric models at an intrinsic colour of $(B - V)_\circ = -0.15$ using energy integration (red) and photon counting (blue) flux measurements as a function of nominal $E(B - V)$.

and

$$
\begin{aligned}
\frac{E(U - B)}{E(B - V)} &= 0.687 + 0.061E(B - V) \\
&+ 0.013E(B - V)^2 - 0.064(B - V)_\circ,
\end{aligned} \tag{2.30}
$$

where the dependence on both the colour of the star and the intrinsic reddening of the object are explicitly incorporated. These reddening vectors are applicable to measured $E(B - V)$ values up to $\simeq 1.9$ and are accurate to within $0.03\,\mathrm{mag}$.

2.7.1.1 Anomalous Line-of-Sight Extinction

There have been numerous investigations in the literature concerning the universality of the reddening law, however there have been suggestions that the law towards extremely young and dense SFRs may differ from that characteristic of the normal ISM (e.g. Thé et al. 1990; Nishiyama et al. 2006; Stead & Hoare 2009). Anomalous extinction may be caused by the photoevaporation of small dust grains by nearby massive stars or grain growth in circumstellar environments resulting in large values of R_V (Cardelli & Clayton 1988; van den Ancker et al. 1997). Of the SFRs in the sample, there is evidence that towards both the ONC and NGC 6611 the reddening law is significantly different with $R_V \simeq 5.5$ and 3.75 respectively (see Costero & Peimbert 1970 and Hillenbrand et al. 1993).

In the case of the ONC, it is possible that the reported anomalous reddening law might be caused by not accounting for near-IR excesses arising from circumstellar material

(Penston et al. 1975; Hillenbrand 1997). The Johnson UBV photometric study of Walker (1969) obtained photometry for as many stars as possible in the vicinity of the ONC that lay within the outline of the dark cloud. The later study of Penston et al. (1975) concentrated on stars within the ONC itself. These studies showed that stars both within the ONC and in the immediate vicinity follow the standard reddening law of $R_V \simeq 3.1$ and that whereas the reddening in the vicinity of the cluster is low and uniform, that within the ONC itself is high and patchy.

Several investigations have studied the extinction properties of members of NGC 6611 (e.g. Chini & Kruegel 1983; Thé et al. 1990; Hillenbrand et al. 1993; de Winter et al. 1997) and all come to the conclusion that not only is the reddening very patchy, but also that the values of R_V, estimated on an individual stellar basis, seem to be larger than the normal ISM value. Polarimetric observations by Orsatti et al. (2000, 2006) suggest that silicate and graphite grains in the vicinity of NGC 6611 are larger than grains in the diffuse ISM. Values of R_V range from $3.5 - 4.8$, with a typical value of $\simeq 3.75$ (Hillenbrand et al. 1993).

Hence, for the ONC, the derived reddening vectors (Eqns. 2.29 and 2.30) using $R_V = 3.2$ may be appropriate. For NGC 6611, on the other hand, the reddening vectors were recalculated adopting the typical value of $R_V = 3.75$, and the MS age, distance and reddening derived under this assumption.

2.7.2 Q-Method

The Q-method is a mechanism used to de-redden stars individually using the $U-B, B-V$ colour-colour diagram and was first introduced by Johnson & Morgan (1953). The method as shown in Johnson & Morgan (1953) was developed empirically using photometry of unreddened MS stars in NGC 2362, the Pleiades and Praesepe. Assuming that $E(U-B)/E(B-V) = 0.72$ (see later), the photometry of these stars was adjusted to absolute magnitude-intrinsic colour space by fitting against a sequence defined by nearby bright stars. This process defined a set of empirical MSs in the absolute magnitude-intrinsic colour $M_V, (B-V)_\circ$ and $M_V, (U-B)_\circ$ CMDs. The unreddened stars in NGC 2362 and Praesepe were used to create an empirical MS in the intrinsic $(U-B)_\circ, (B-V)_\circ$ colour-colour diagram. Note that the Pleiades members were not used for this due to the variable reddening associated with the cluster. Thus reddened stars can be de-reddened based on the relative positions of similar spectral types. Johnson & Morgan (1953) noted that the reddening vectors connecting reddened and unreddened stars of the same spectral type were essentially constant. This was the initial derivation of, what subsequently became the canonical extinction vector, $E(U-B)/E(B-V) = 0.72 \pm 0.03$. Thus the interstellar reddening independent quantity Q was defined as

$$Q \equiv (U-B) - (E(U-B)/E(B-V)) \times (B-V), \qquad (2.31)$$

and can be visualised as the value of $U-B$ at $B-V = 0$ along the extinction vector. Using photometry of NGC 2362, M 36 and nearby bright stars, Johnson & Morgan (1953)

plotted the value of Q for B-type stars against apparent $B - V$ colour and derived the following linear relation for unreddened stars

$$(B - V)_\circ = -0.009 + 0.337Q. \tag{2.32}$$

Since the colour excess is defined as the difference between the intrinsic and apparent colour, then for reddened stars

$$E(B - V) = (B - V) - (B - V)_\circ = (B - V) - 0.337Q + 0.009. \tag{2.33}$$

The quantity Q can thus be viewed as a parameterisation of the intersection of a linear MS and linear reddening vector. Hence stars can be de-reddened by moving reddened stars along this reddening vector until they lie on the MS.

This monotonic relation between Q and spectral type for OB MS stars was later modified (see Johnson 1958; Heintze 1973) as subsequent, more extensive studies found that not only was the reddening vector non-linear due to a subtle dependence on the intrinsic reddening of the object (Blanco 1956; Hiltner & Johnson 1956), but also that the slope of the reddening vector was dependent upon the spectral type of the source (Lindholm 1957).

2.7.3   Revised Q-Method

The foundation of the original Q-method is that a section of the MS in the $U - B, B - V$ colour-colour diagram is a straight line. With the advent of MS stellar evolutionary models, it has become apparent that this straight line is unphysical and not representative of the observed sequence in the $U - B, B - V$ colour-colour diagram. The revised Q-method builds upon the previous revision of Mayne & Naylor (2008). It involves fitting a straight line to a section of the Geneva-Bessell $(U - B)_\circ, (B - V)_\circ$ isochrone computed using the ATLAS9/ODFnew atmospheric models and incorporates the newly derived colour- and extinction-dependent reddening vector. Fitting a line of the form $y = mx + c$ to a 5 Myr Geneva-Bessell isochrone gives

$$(U - B)_\circ = 4.138(B - V)_\circ - 0.006, \tag{2.34}$$

where this line lies within 0.01 mag in colour of the Geneva-Bessell isochrone up to colours of $(U - B)_\circ = -0.14$ and $(B - V)_\circ = -0.04$. Substituting Eqns. 2.30 and 2.34 into the definition of Q, this becomes

$$\begin{aligned} Q &= (0.064 \times (B - V)^2) - (B - V)\{(0.013 \times E(B - V)^2) \\ &+ (0.061 \times E(B - V)) - 3.451\} - 0.006, \end{aligned} \tag{2.35}$$

hence Q is now no longer a reddening independent quantity, but a function of the colour and intrinsic reddening of the object.
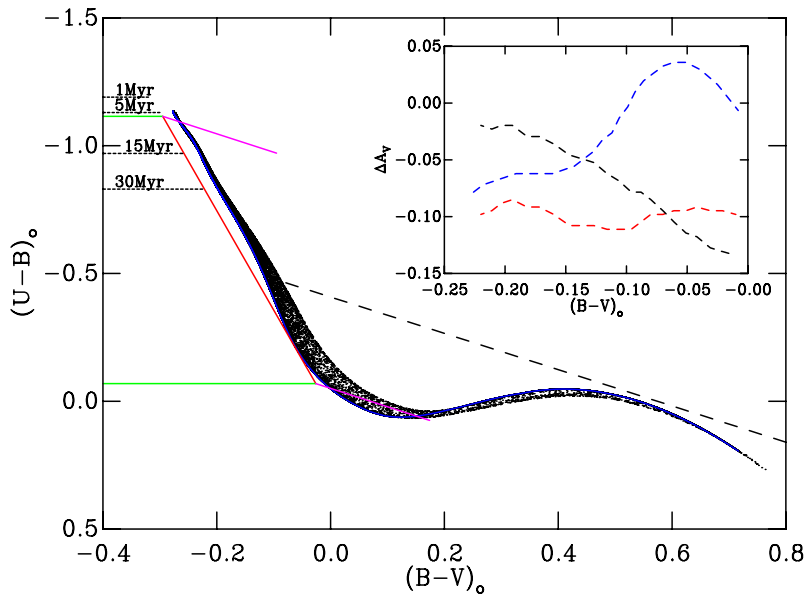
Figure 2.4: Adapted from Mayne & Naylor (2008). A 5 Myr Geneva-Bessell isochrone with a 50 % binary fraction (as described in Section 2.6.3) where the blue line indicates the position of single-stars and equal-mass binaries. Plotted is the original Q-method MS straight line as derived in Johnson & Morgan (1953) (red line) and the range of colours that the original Q-method was valid over (green lines). Horizontal dashed lines are the approximate TAMS for the Geneva-Bessell isochrone of the stated age. The magenta lines show the updated reddening vectors derived in Section 2.7.1. The large dashed line indicates the portion of the $U - B, B - V$ colour-colour diagram below which the reddening solution for a given star can be multi-valued. The inset shows the approximate difference in the calculated extinction A_V. The blue dashed line is the revised Q-method single-star sequence minus the original Q-method, the red dashed line is the revised Q-method outer binary envelope minus the original Q-method, and finally the black dashed line is the revised Q-method outer binary envelope minus the revised Q-method single-star sequence.

Fig. 2.4 illustrates the difference in the calculated extinction A_V between the original and revised Q-methods. This difference can be as large as $\simeq 0.1$mag for the single-star and equal-mass binary case. Within the red limits defined above and the TAMS (see Section 2.7.3.1) the expression for Q in Eqn. 2.35 differs by less than 0.01 mag from interpolating stars onto the updated Geneva-Bessell intrinsic $(U - B)_\circ, (B - V)_\circ$ isochrone. In practice the updated expression shown in Eqn. 2.35 is not used to de-redden stars individually. Instead, an isochrone of a given age is used and the reddened stars are interpolated onto the unreddened isochrone using the derived colour- and extinction-dependent reddening vectors derived in Section 2.7.1.

2.7.3.1 Assumptions

By replacing the original Q-method MS straight line with a line fitted to a section of a Geneva-Bessell isochrone, it was necessary to assign a given age. Unlike the evolution of the MS in the $V, B - V$ CMD, the MS in the $U - B, B - V$ colour-colour diagram moves very little with age (see Fig. 2.5). As a given sequence ages, stars of increasingly lower
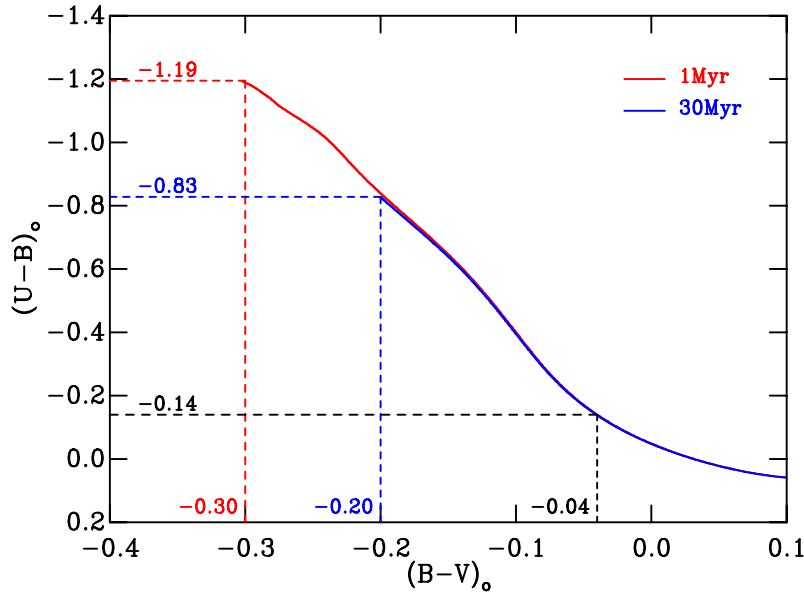
Figure 2.5: Geneva-Bessell isochrones – restricted to stars that have not yet reached the TAMS – in the $(U-B)_\circ, (B-V)_\circ$ colour-colour diagram. Two isochrones at ages of 1 Myr (red) and 30 Myr (blue) show that the MS is essentially insensitive to the adopted age. The approximate position of the TAMS at both ages are indicated by the coloured dashed lines. The black dashed lines indicate the adopted red limit in the fitting of the 5 Myr Geneva-Bessell isochrone to create the revised Q parameter shown in Eqn. 2.35.

mass evolve away from the MS. Fig. 2.5 shows the approximate TAMS $(U-B)_\circ, (B-V)_\circ$ positions for a 1 and 30 Myr isochrone. Hence when using the revised Q-method to de-redden stars on an individual basis, it is important to ensure that any post-MS objects are excluded as these will be incorrectly de-reddened and therefore occupy the wrong position in both the $(U-B)_\circ, (B-V)_\circ$ colour-colour diagram and $V_\circ, (B-V)_\circ$ CMD.

Interpolating reddened stars onto a $U-B, B-V$ isochrone implicitly assumes that all objects are either single-stars or equal-mass binaries. Hence there is a fundamental caveat that the Q-method is unable to account for the observed spread in colour-colour space as a result of binarity. Fig. 2.4 clearly shows that unequal-mass binaries do not lie on the same sequence as single-stars and equal-mass binaries in the $U-B, B-V$ colour-colour diagram. With only photometric data and no ancillary information, it is not clear whether a given star should lie on the single-star/equal-mass binary sequence or somewhere within the region occupied by the unequal-mass binaries. Fig. 2.4 shows an unreddened 5 Myr updated Geneva-Bessell isochrone with a binary fraction of 50 %. The effects of the assumption that all stars are single-stars or equal-mass binaries is quantified. Differences in the derived extinction A_V values have been calculated for three cases – i) the difference between the single-star sequence and the original Q-method straight line MS, ii) the difference between the outer envelope of the unequal-mass binary region and the original Q-method straight line MS, and iii) the difference between the outer envelope of the unequal-mass binaries and the single-star sequence. The effects of binarity are clearly non-negligible, affecting the calculated A_V on the $\simeq 0.15$ mag level. This effect becomes

more marked as one moves to lower masses (redder colours) along the MS isochrone.

Due to the problems arising from not being able to model the scatter in the colour-colour diagram as a result of binarity, the revised Q-method was only used to calculate individual stellar reddenings when there was strong evidence of highly variable reddening across a given SFR. Hence a two-step approach, as described in Mayne & Naylor (2008), was followed. Firstly, a mean extinction for a SFR is assumed and the $U - B, B - V$ colour-colour diagram fitted using the τ^2 fitting statistic allowing the extinction to float as a free parameter. This was then tested to ensure that the model was a good fit to the data. If the fit to the data was not good, reddenings were derived on a star-by-star basis using the revised Q-method, whereby the stars were moved along the colour- and extinction-dependent reddening vector shown in Eqn. 2.30 until they lay on the intrinsic single-star or equal-mass binary $(U - B)_\circ, (B - V)_\circ$ isochrone.

2.8 Fitting the Data

MS memberships were generally published alongside the photometry (listed in Table 2.1) and have been adopted unless otherwise stated. The Geneva-Bessell models (described in Section 2.5) were used to fit the MS populations of the sample of young SFRs for reddening in the $U - B, B - V$ colour-colour diagram and then for distance and age in the $V, B - V$ CMD. As a way of demonstrating the fitting technique, two examples of the procedure are now described – one for which a mean reddening was derived using the τ^2 fitting statistic (NGC 1960) and another for which individual stellar reddenings have been calculated using the revised Q-method (the λ Ori association).

The figures showing fitted data have several elements that require explanation. Taking Fig. 2.7 as an example, the shaded area shows the probability density of finding a star at a given colour and magnitude (or colour and colour when fitting data in the $U - B, B - V$ colour-colour diagram). This density ρ is that of Eqn. 2.15 generated for a specific isochrone. The circles are the photometric data, with the uncertainties in colour and magnitude represented by the bars. In all figures showing fitted data – unless otherwise stated as in the case of data de-reddened on an individual star-by-star basis – the models have been adjusted to apparent colour-magnitude space using the derived reddening $E(B - V)$ and the derived reddening vectors in Section 2.7.1.

2.8.1 Isolating the Main-Sequence

Stars in both the pre- and post-MS phases evolve on much shorter timescales than stars on the MS and hence the inclusion of these stars could introduce an unwanted age dependency into the derived MS distance. When necessary, stars that have evolved past the TAMS in the $U - B, B - V$ colour-colour diagram and $V, B - V$ CMD have been clipped. Stars that are evolving between the ZAMS and the TAMS have been retained as these have little effect on the derived MS distance, but provide extremely useful age diagnostics (see Section 2.3.3). Stars with very red colours may still be in the pre-MS regime (this is of
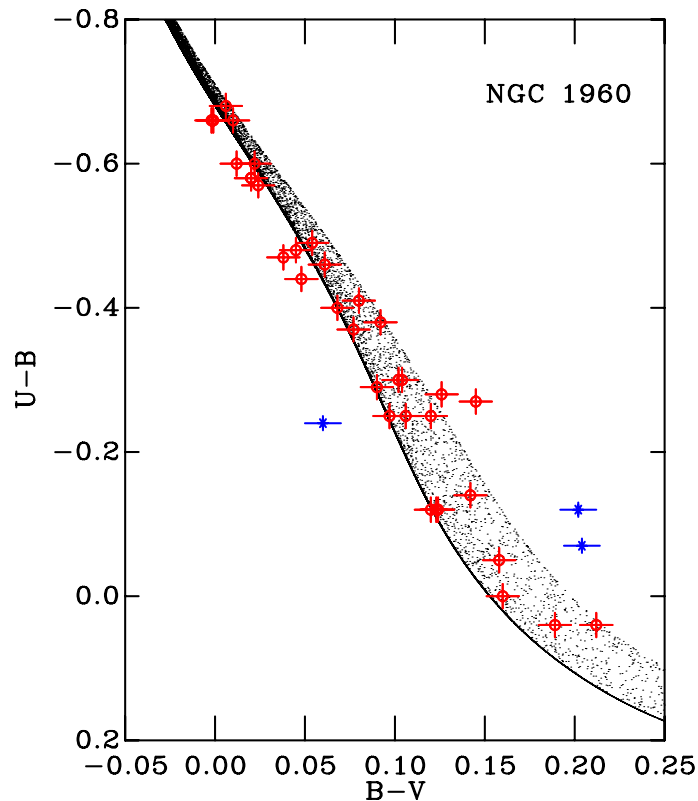
Figure 2.6: The best-fitting $U - B, B - V$ colour-colour diagram for NGC 1960 with a reddening $E(B-V) = 0.20$. The probability density ρ is shown as the greyscale isochrone. Circles represent the photometric data of Johnson & Morgan (1953) with the associated uncertainties shown as the bars. Asterisks represent stars that were clipped before deriving the best-fit (see text).

course exacerbated by sometimes high and variable interstellar extinction). In the pre-MS regime age and distance are highly degenerate. The MS data was plotted in the $V, B - V$ CMD and a judgement made as to whether some of the reddest stars have yet to reach the ZAMS. As noted in Mayne & Naylor (2008), adopting empirical colour cuts based on the data in CMD space – as opposed to theoretical intrinsic colours based on pre-MS stellar evolutionary models – can result in more precise distance estimates. Comparing the theoretical cuts with the de-reddened data in the $V, B - V$ CMD showed that the theoretical cuts were often too blue, and hence if these cuts were adopted stars that trace the curve of the isochrone as it moves to fainter magnitudes would be excluded.

2.8.2 Example 1: NGC 1960 – Uniform Reddening

The photoelectric data and associated uncertainties from Johnson & Morgan (1953) were used, taken as part of a large observing programme that eventually defined the UBV photometric system. Only stars blueward of $B - V = 0.25$ and those marked as members by Johnson & Morgan (1953) were retained. Three stars – Boden 50, 86 and 110 – were further removed due to a combination of their positions in the $U - B, B - V$ colour-colour diagram and associated τ^2 values (see Fig. 2.6). There was no obvious spread in the
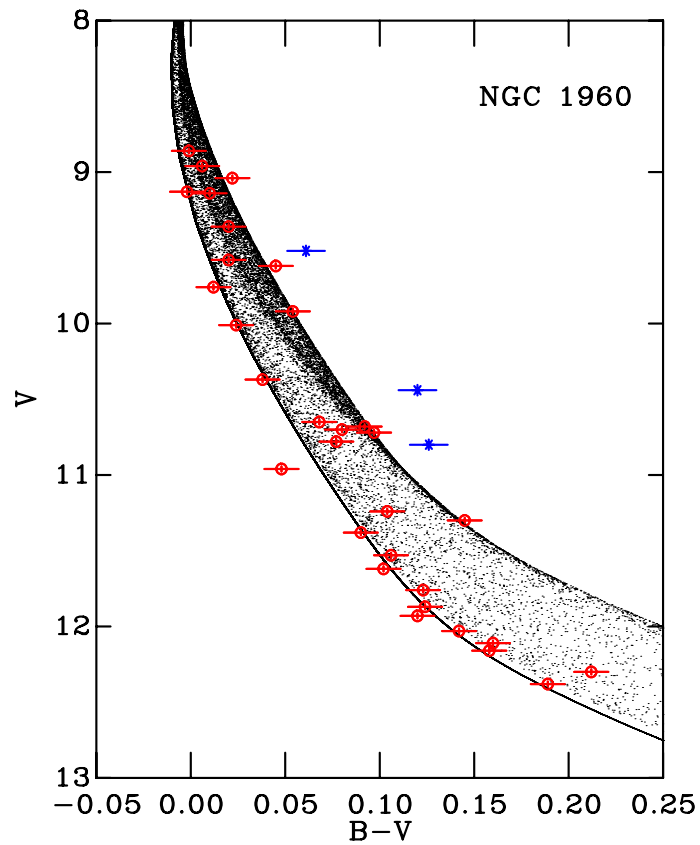
Figure 2.7: The best-fitting $V, B - V$ CMD for NGC 1960 with an age of 26.3 Myr and distance modulus $dm = 10.33$. The probability density ρ is shown as the greyscale isochrone. Circles represent the photometric data of Johnson & Morgan (1953) with the associated uncertainties shown as the bars. Asterisks represent stars that were clipped before deriving the best-fit (see text).
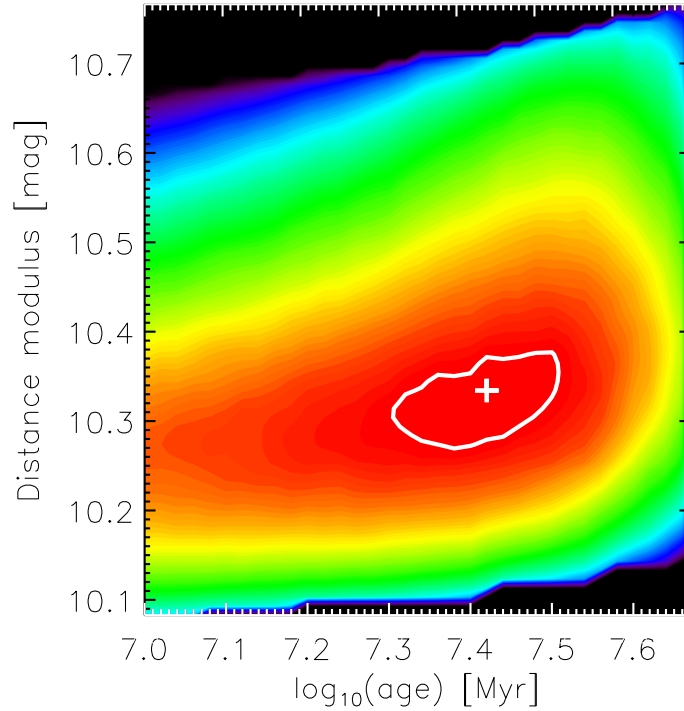
Figure 2.8: The colour scale τ^2 age-distance grid for NGC 1960. The large cross denotes the lowest τ^2 within the grid and hence the derived best-fitting values of age and distance. The contour is at the 68 % confidence level and defines the uncertainties on the derived age and distance.

$U - B, B - V$ colour-colour diagram, implying uniform extinction across the SFR. Fig. 2.6 shows the best fitting colour-colour diagram for NGC 1960 with a derived $E(B-V) = 0.20$ and associated $\Pr(\tau^2) = 0.25$. Three additional stars – Boden 13, 47 and 48 – were removed based on a combination of their position in the $V, B-V$ CMD and their associated τ^2 values (see Fig. 2.7). The remaining stars were fitted for distance and age simultaneously in the $V, B-V$ CMD, with a derived age of $26.3^{+3.2}_{-5.2}$ Myr and a distance modulus $dm = 10.33^{+0.02}_{-0.05}$ with $\Pr(\tau^2) = 0.67$. The best-fitting $V, B-V$ CMD and the τ^2 age-distance grid are shown in Figs. 2.7 and 2.8.

2.8.3 Example 2: λ Ori – Variable Reddening

The photometry of stars within half a degree of λ Ori from Murdin & Penston (1977) was used. Only stars blueward of $B - V = 0.2$ were retained. There is evidence of a spread in the $U - B, B - V$ colour-colour diagram and so individual reddenings were calculated on a star-by-star basis using the revised Q-method. A median $E(B - V) = 0.11$ was calculated with a range in the derived values of $\Delta E(B - V) = 0.24$ from stars that lie on the age-insensitive region of the $U - B, B - V$ isochrones ($B - V \lesssim 0.0$; see Fig. 2.9). Murdin & Penston (1977) do not publish uncertainties with their photometry and so a magnitude independent uncertainty of 0.01 mag in V and 0.008 mag in $B - V$ was used to obtain a reasonable probability that the model represents a good fit to the data. An age of $10.0^{+1.0}_{-1.1}$ Myr and distance modulus $dm = 8.02^{+0.04}_{-0.03}$ were derived with an

Figure 2.9: The application of the revised Q-method for λ Ori. The asterisks show the apparent $U - B, B - V$ colours of individual stars (Murdin & Penston 1977) and the circles show the de-reddened positions after applying the Q-method. Individual reddening trajectories are plotted as the dashed lines. The solid line is a 1 Myr Geneva-Bessell isochrone.

associated $Pr(\tau^2) = 0.49$, having removed two additional stars – HD 36881 and HD 36913 – which appeared to be non-members based on their position in the $V_\circ, (B - V)_\circ$ CMD (see Fig. 2.10). The best-fitting $V_\circ, (B - V)_\circ$ CMD and associated τ^2 age-distance grid are shown in Figs. 2.10 and 2.11.

2.8.4 Results

Having shown two examples of how to determine MS ages, distances and reddenings from SFRs where the extinction is either uniform or highly variable, the results for the remaining SFRs are now discussed.

2.8.4.1 Cep OB3b

The photometry and associated uncertainties from Blaauw et al. (1959), who performed a photometric survey of the OB stars in the region, was used. The memberships are based on those of Pozzo (2001), however BHJ 11 was discarded as the measurement provided by Blaauw et al. (1959) is a combined light measurement for a rather wide $\Delta m = 2.4$ mag binary. There is significant spread in the $U - B, B - V$ colour-colour diagram and so
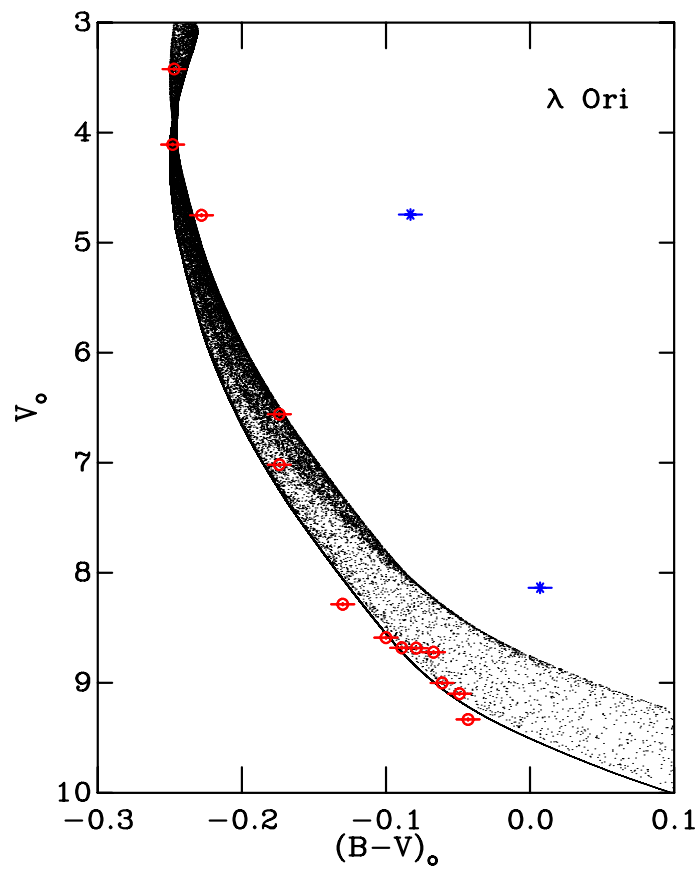
Figure 2.10: The best-fitting $V_\circ, (B - V)_\circ$ CMD for λ Ori with an age of 10.0 Myr and distance modulus $dm = 8.02$. The probability density ρ is shown as the greyscale isochrone. Circles represent the photometric data of Murdin & Penston (1977). The plotted uncertainties are the magnitude independent values discussed in Section 2.8.3. Asterisks represent stars that were clipped before deriving the best-fit (see text).
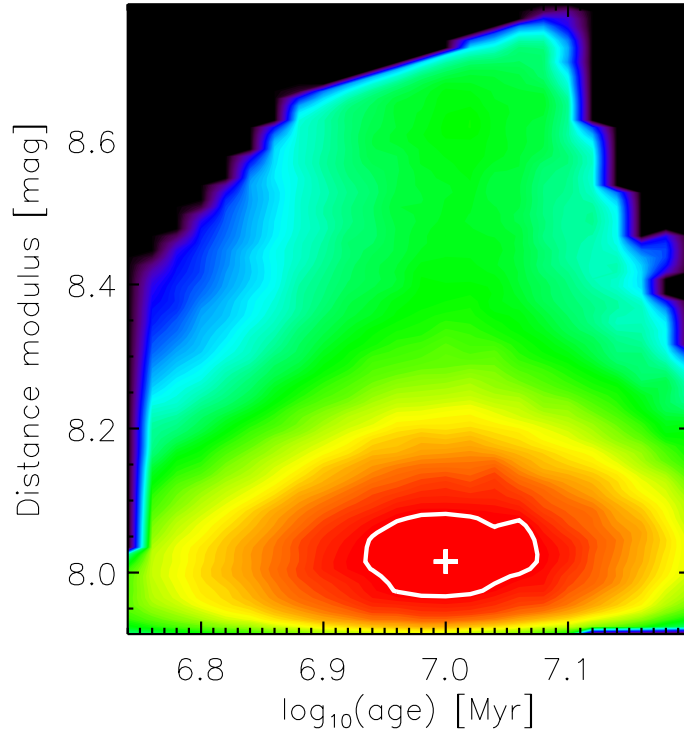
Figure 2.11: The colour scale τ^2 age-distance grid for λ Ori. The large cross denotes the lowest τ^2 within the grid and hence the derived best-fitting values of age and distance. The contour is at the 68 % confidence level and defines the uncertainties on the derived age and distance.

individual reddenings were calculated on a star-by-star basis using the revised Q-method, deriving a median value of $E(B-V) = 0.89$ (see Fig. 2.12) with a range of $\Delta E(B-V) = 0.41$. Fitting these stars in the $V_\circ, (B-V)_\circ$ CMD, an age of $6.0^{+0.6}_{-2.2}$ Myr and distance modulus $dm = 8.78^{+0.06}_{-0.08}$ were derived with $\mathrm{Pr}(\tau^2) = 0.26$. The best-fitting $V_\circ, (B-V)_\circ$ CMD is shown in Fig. 2.13.

2.8.4.2 χ Per

Photometric data for χ Per comes from Johnson & Morgan (1955). There is evidence of non-uniform extinction and so each star was individually de-reddened. Stars that have evolved past the TAMS in the $V, B-V$ CMD were removed and a median reddening of $E(B-V) = 0.52$ (see Fig. 2.14) was derived with a range of $\Delta E(B-V) = 0.28$. Additional stars – Oosterhoff 2008, 2155, 2170, 2185, 2188, and 2203 – that do not appear to be members based on their positions in the $V_\circ, (B-V)_\circ$ CMD and associated high τ^2 values were also removed. The remaining stars were then fitted for age and distance simultaneously, with an age of $14.5^{+2.2}_{-1.7}$ Myr and a distance modulus $dm = 11.80^{+0.06}_{-0.03}$ derived with $\mathrm{Pr}(\tau^2) = 0.49$. The best-fitting $V_\circ, (B-V)_\circ$ CMD is shown in Fig. 2.15.

Figure 2.12: The application of the revised Q-method for Cep OB3b. The asterisks show the apparent $U - B, B - V$ colours of individual stars (Blaauw et al. 1959) and the circles show the de-reddened positions after applying the Q-method. Individual reddening trajectories are plotted as the dashed lines. The solid line is a 1 Myr Geneva-Bessell isochrone.

2.8.4.3 IC 348

The photometric data for IC 348 from Harris et al. (1954) was used. The reddening across the region is very patchy and therefore each star was individually de-reddened using the revised Q-method. The majority of stars lie in the portion of the colour-colour diagram below which the reddening solution can be multi-valued (see Fig. 2.4). Hence the revised Q-method was used, in conjunction with spectral types, to determine the best-fit solution for stars earlier than A2 (Gingrich 4, 5, 12, 16, LF 24, and BD +31°643). A median reddening of $E(B - V) = 0.69$ (see Fig. 2.16) was derived with a range of $\Delta E(B - V) = 0.52$. These stars were then fitted for both an age and distance in the $V_\circ, (B - V)_\circ$ CMD. The MS population of IC 348 is too sparse and lacks a sufficient number of evolved stars to derive a MS age, however these stars can be used to derive a photometric parallax MS distance modulus of $dm = 6.98^{+0.19}_{-0.09}$.

2.8.4.4 IC 5146

The photometric data and associated uncertainties of IC 5146 are from Walker (1959). The stars were de-reddened individually due to the considerable spread observed in the
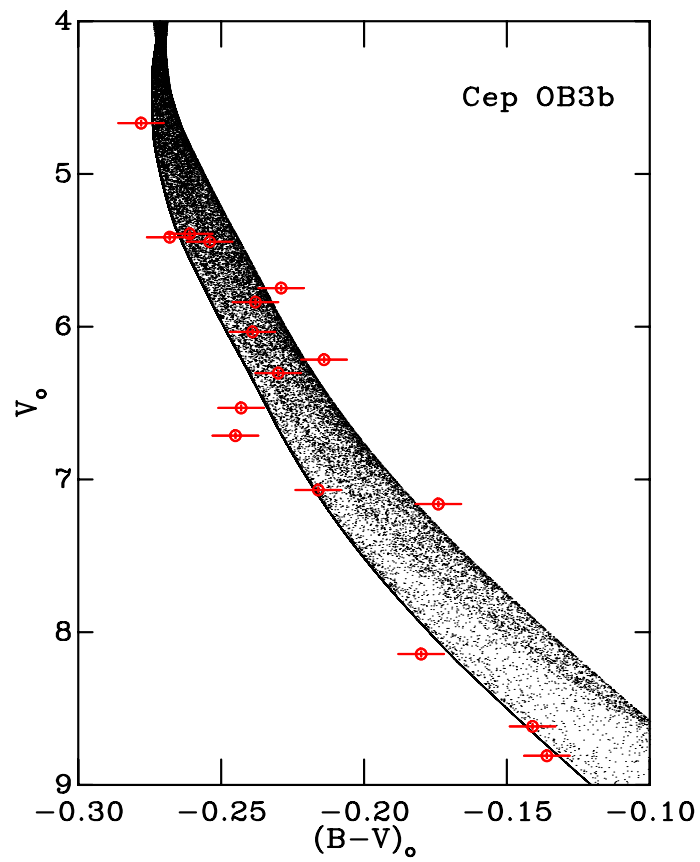
Figure 2.13: The best-fitting $V_\circ, (B - V)_\circ$ CMD for Cep OB3b with an age of $6.0\,\mathrm{Myr}$ and distance modulus $dm = 8.78$. The probability density ρ is shown as the greyscale isochrone. Circles represent the photometric data of Blaauw et al. (1959) with the associated uncertainties shown as the bars.

Figure 2.14: The application of the revised Q-method for χ Per. The asterisks show the apparent $U - B, B - V$ colours of individual stars (Johnson & Morgan 1955) and the circles show the de-reddened positions after applying the Q-method. Individual reddening trajectories are plotted as the dashed lines. The solid line is a 1 Myr Geneva-Bessell isochrone.

$U - B, B - V$ colour-colour diagram. As in the case of IC 348, a combination of the revised Q-method and spectral types were used to assign the most likely reddening solution to stars earlier than A1 (Walker 35, 42, 53, 62, 64, and 76). From these presumed MS stars, a median reddening of $E(B - V) = 0.75$ (see Fig. 2.17) was determined with a range of $\Delta E(B - V) = 0.61$. The age and distance were then calculated from the $V_\circ, (B - V)_\circ$ CMD. Similar to IC 348, the MS does not have a sufficient number of evolved stars to derive a MS age, however a photometric parallax distance modulus of $dm = 9.81^{+0.20}_{-0.19}$ was derived.

2.8.4.5 NGC 2169

The UBV photometry from Hoag et al. (1961) was used. Stars redward of $B - V = 0.25$ were neglected and Hoag 10, classified as a variable, was further removed due to its position in the $U - B, B - V$ colour-colour diagram. Hoag et al. (1961) do not publish uncertainties and so a magnitude independent uncertainty of 0.02 mag was used for both the $U - B$ and $B - V$ colours to obtain a reasonable $\Pr(\tau^2)$. A mean reddening of $E(B - V) = 0.16$ (see Fig. 2.18) was calculated with $\Pr(\tau^2) = 0.49$. Fitting the $V, B - V$ CMD, an age of $12.6^{+5.0}_{-2.1}$ Myr and a distance modulus $dm = 9.99^{+0.07}_{-0.09}$ were derived with an associated

Figure 2.15: The best-fitting $V_\circ, (B - V)_\circ$ CMD for χ Per with an age of $14.5\,\mathrm{Myr}$ and distance modulus $dm = 11.80$. The probability density ρ is shown as the greyscale isochrone. Circles represent the photometric data of Johnson & Morgan (1955) with the associated uncertainties shown as the bars.

Figure 2.16: The application of the revised Q-method for IC 348. The asterisks show the apparent $U - B, B - V$ colours of individual stars (Harris et al. 1954) and the circles show the de-reddened positions after applying the Q-method. Individual reddening trajectories are plotted as the dashed lines. The solid line is a 1 Myr Geneva-Bessell isochrone.

$Pr(\tau^2) = 0.20$ after having removed Hoag 2 on the grounds that its membership is disputed and using a magnitude independent uncertainty of 0.02 mag for the V magnitude. The best-fitting $V, B - V$ CMD is shown in Fig. 2.19.

2.8.4.6 NGC 2244

The photometric data and memberships published by Johnson (1962) was used. Stars blueward of $B - V = 0.4$ were retained and de-reddened on an individual star-by-star basis. A median value of $E(B - V) = 0.43$ (see Fig. 2.20) was derived with a range of $\Delta E(B - V) = 0.18$. Johnson (1962) do not publish uncertainties and so a magnitude independent uncertainty of 0.015 mag was used for the V magnitude and an uncertainty of 0.01 mag for the $B - V$ colour. Several stars – Johnson 108, 115, 133, 239, 241, and 253 – were further removed due to a combination of their position in $V, B - V$ CMD space and high τ^2 values. The remaining stars were fitted in the $V_\circ, (B - V)_\circ$ CMD and an age of $6.6^{+0.8}_{-0.8}$ Myr and distance modulus $dm = 10.70^{+0.05}_{-0.03}$ derived with $Pr(\tau^2) = 0.70$. The best-fitting $V_\circ, (B - V)_\circ$ CMD is shown in Fig. 2.21.
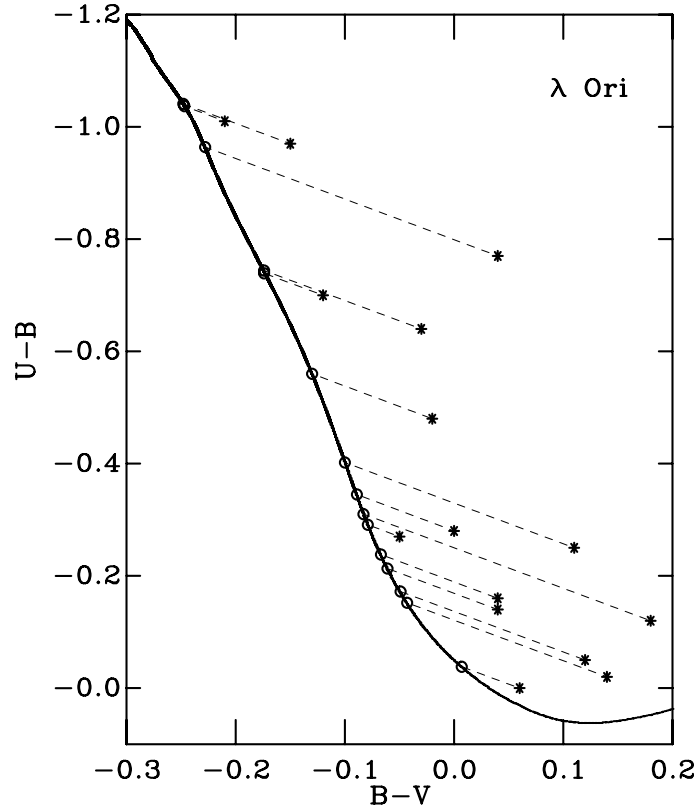
Figure 2.17: The application of the revised Q-method for IC 5146. The asterisks show the apparent $U - B, B - V$ colours of individual stars (Walker 1959) and the circles show the de-reddened positions after applying the Q-method. Individual reddening trajectories are plotted as the dashed lines. The solid line is a 1 Myr Geneva-Bessell isochrone.

2.8.4.7 NGC 2362

The photometric data, associated uncertainties and memberships from Johnson & Morgan (1953) were used. Stars blueward of $B - V = 0.04$ and those marked as members were retained. The $U - B, B - V$ colour-colour diagram was fitted for a mean extinction, however the following stars were removed; i) stars for which there was no U-band photometry, ii) τ CMa as it has evolved past the TAMS, and iii) Johnson 36 due to its position in the $U - B, B - V$ colour-colour diagram that suggests it is a non-member. A mean reddening of $E(B - V) = 0.07$ (see Fig. 2.22) was determined with an associated $\Pr(\tau^2) = 0.27$. Johnson 50 was further removed due to its position in the $V, B - V$ CMD and high τ^2 value. The remaining stars were then fitted for distance and age in the $V, B - V$ CMD, and an age of $12.6^{+2.7}_{-4.7}$ Myr and distance modulus $dm = 10.60^{+0.06}_{-0.03}$ derived with $\Pr(\tau^2) = 0.31$. The best-fitting $V, B - V$ CMD is shown in Fig. 2.23.

2.8.4.8 NGC 6530

The photometry and associated uncertainties of Walker (1957) was used. The irregular brightness of the nebulosity of NGC 6530 means that photoelectric observations stars with $V > 14 - 15$ have large uncertainties, therefore only stars brighter than $V = 13$ and
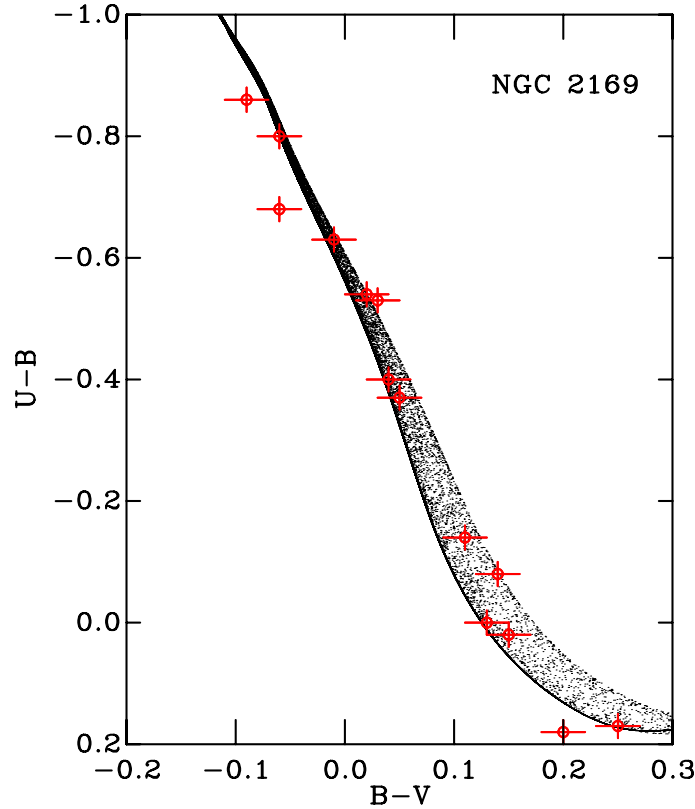
Figure 2.18: The best-fitting $U - B, B - V$ colour-colour diagram for NGC 2169 with a reddening $E(B-V) = 0.16$. The probability density ρ is shown as the greyscale isochrone. Circles represent the photometric data of Hoag et al. (1961). The plotted uncertainties are the magnitude independent values discussed in Section 2.8.4.5.

blueward of $B - V = 0.28$ were retained. Due to the variable reddening, each star was de-reddened on an individual basis using the revised Q-method. A median $E(B - V) = 0.32$ (see Fig. 2.24) was derived with a range of $\Delta E(B - V) = 0.23$. These stars were then fitted in the $V_\circ, (B - V)_\circ$ CMD, for which an age of $6.3^{+0.7}_{-0.6}$ Myr and distance modulus $dm = 10.64^{+0.04}_{-0.05}$ were determined with an associated $\Pr(\tau^2) = 0.98$. The best-fitting $V_\circ, (B - V)_\circ$ CMD is shown in Fig. 2.25.

2.8.4.9 NGC 6611

The UBV photometric data and associated uncertainties of Walker (1961) was used. A significant spread is visible in the $U - B, B - V$ colour-colour diagram and so the stars were de-reddened individually using the revised Q-method. As stated in Section 2.7.1.1, the extinction properties of NGC 6611 do not follow the standard ISM reddening law. The $A_V/E(B - V)$ and $E(U - B)/E(B - V)$ reddening vectors were re-derived using a value of $R_V = 3.75$ which it typical of the region (Hillenbrand et al. 1993). A median reddening of $E(B - V) = 0.71$ (see Fig. 2.26) was derived with a range of $\Delta E(B - V) = 0.58$. Note that there are several stars that lie above the single-star $(U - B)_\circ, (B - V)_\circ$ isochrone in the colour-colour diagram and due to the nature of the Q-method, it was not possible to de-redden these sources. These stars were therefore neglected from the derived $E(B - V)$
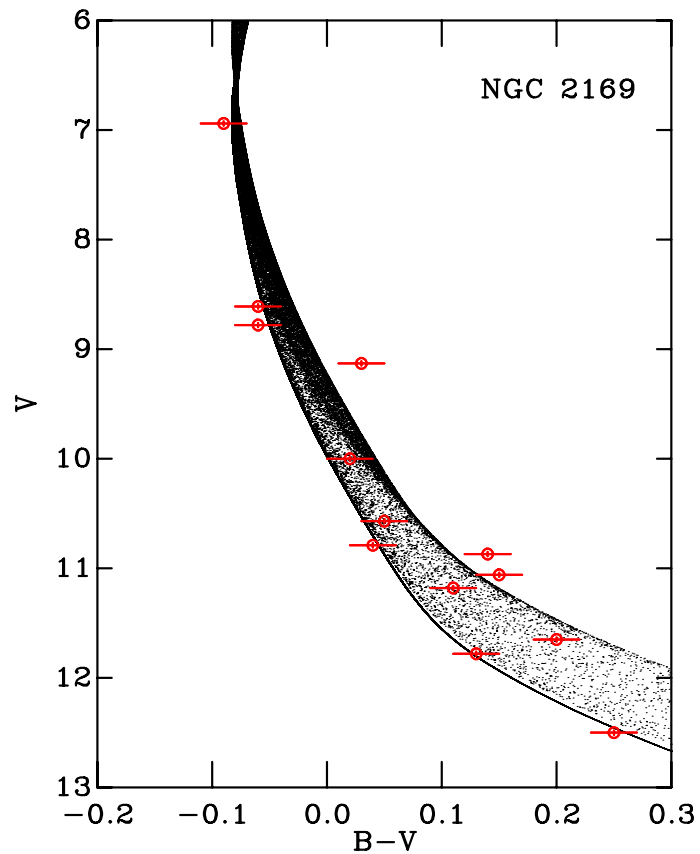
Figure 2.19: The best-fitting $V, B - V$ CMD for NGC 2169 using the updated Geneva-Bessell isochrones with an age of 12.6 Myr and distance modulus $dm = 9.99$. The probability density ρ is shown as the greyscale isochrone. Circles represent the photometric data of Hoag et al. (1961). The plotted uncertainties are the magnitude independent values discussed in Section 2.8.4.5.
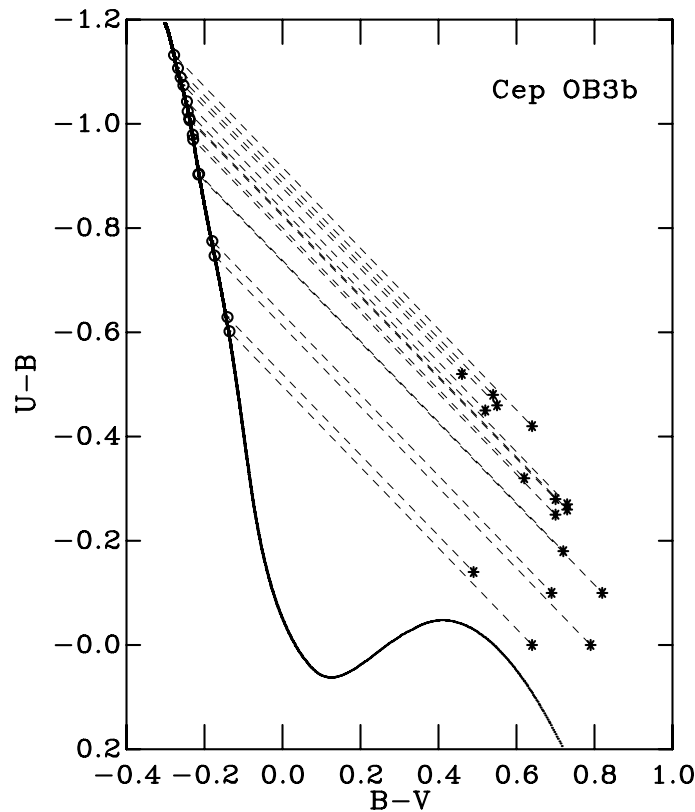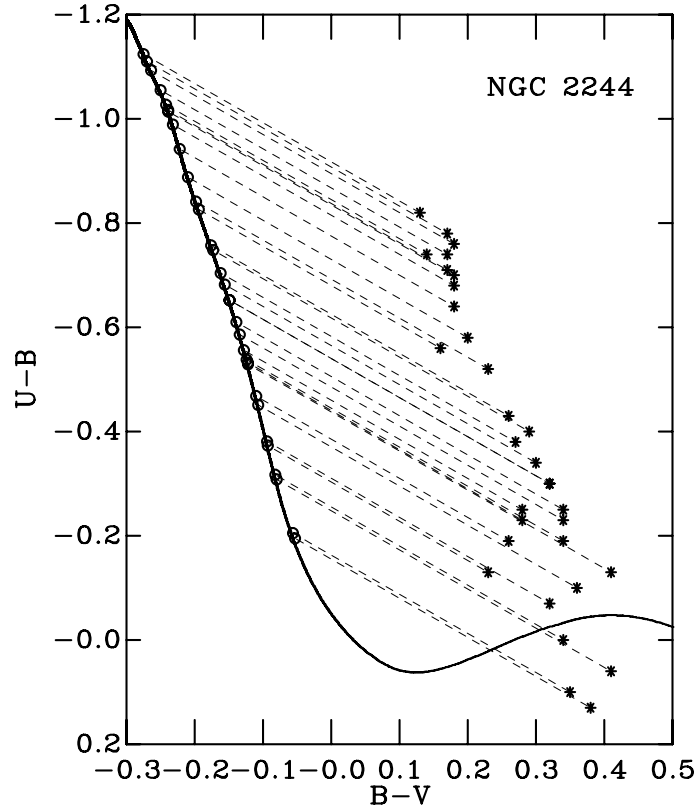
Figure 2.20: The application of the revised Q-method for NGC 2244. The asterisks show the apparent $U-B, B-V$ colours of individual stars (Johnson 1962) and the circles show the de-reddened positions after applying the Q-method. Individual reddening trajectories are plotted as the dashed lines. The solid line is a 1 Myr Geneva-Bessell isochrone.

and subsequent $V_\circ, (B-V)_\circ$ CMD. The remaining stars were then fitted in the $V_\circ, (B-V)_\circ$ CMD, for which an age of $4.8^{+1.2}_{-0.9}$ Myr and distance modulus $dm = 11.38^{+0.06}_{-0.30}$ was derived with $\Pr(\tau^2) = 0.17$. The best-fitting $V_\circ, (B-V)_\circ$ CMD is shown in Fig. 2.27.

2.8.4.10 NGC 7160

The photometric data of Hoag et al. (1961) was used. The revised Q-method was applied and each star de-reddened individually, with a resulting median value of $E(B-V) = 0.37$ (see Fig. 2.28) and a range of $\Delta E(B-V) = 0.37$. Only stars blueward of $(B-V)_\circ = 0.0$ were used and, furthermore, Hoag 8 was removed due to a large value of τ^2. With no uncertainties on the published photometry, a magnitude independent uncertainty of 0.02 mag for V and 0.015 mag for $B-V$ was used. An age of $12.6^{+1.3}_{-2.1}$ Myr and a distance modulus $dm = 9.67^{+0.09}_{-0.05}$ was calculated with an associated $\Pr(\tau^2) = 0.29$. The best-fitting $V_\circ, (B-V)_\circ$ CMD is shown in Fig. 2.29.

2.8.4.11 Orion Nebula Cluster

The UBV photometry and associated uncertainties of stars in the vicinity of the ONC by Walker (1969) was used. The following stars were removed; i) stars redward of $B-V =$
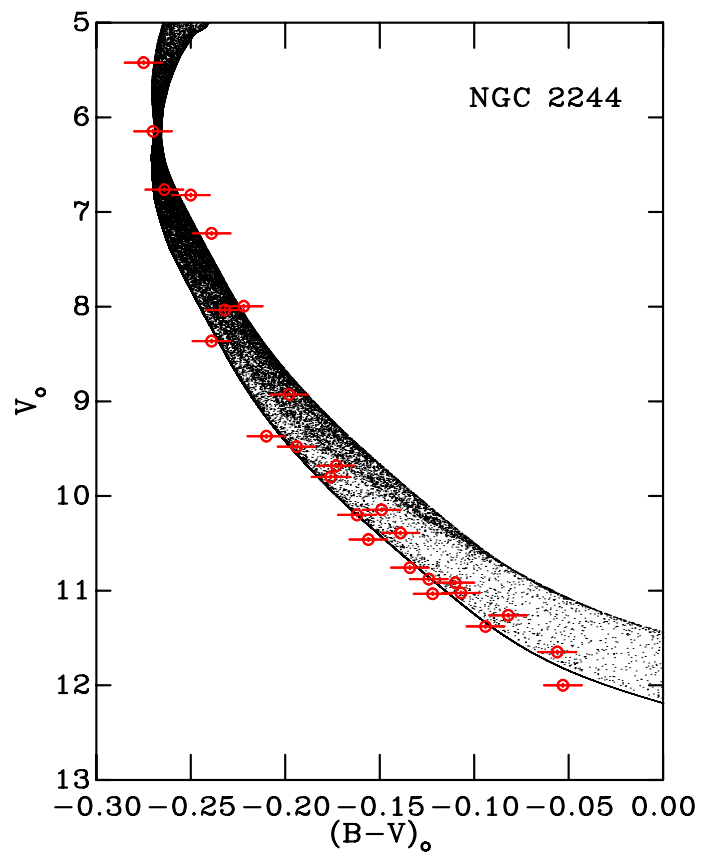
Figure 2.21: The best-fitting $V_\circ, (B-V)_\circ$ CMD for NGC 2244 with an age of 6.6 Myr and distance modulus $dm = 10.70$. The probability density ρ is shown as the greyscale isochrone. Circles represent the photometric data of Johnson (1962). The plotted uncertainties are the magnitude independent values discussed in Section 2.8.4.6.
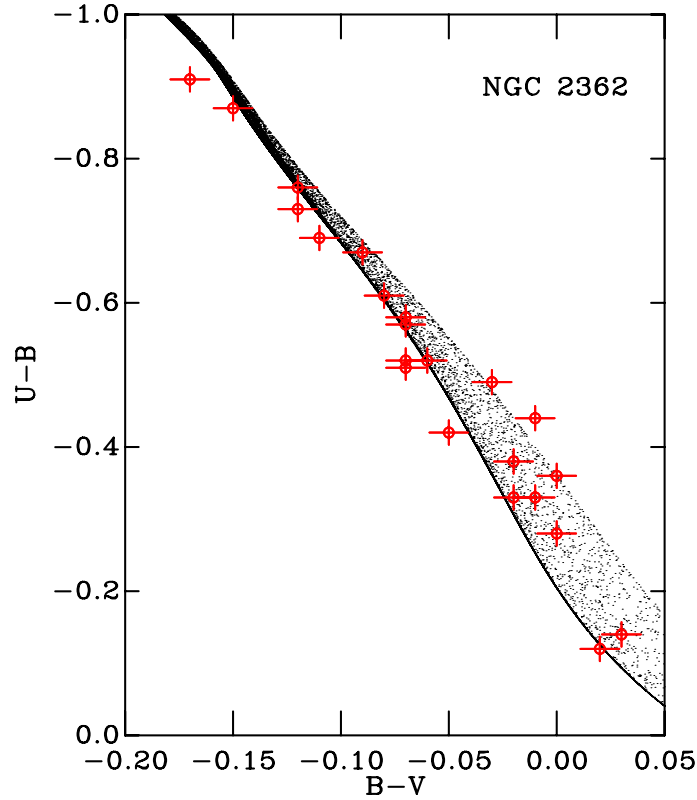
Figure 2.22: The best-fitting $U - B, B - V$ colour-colour diagram for NGC 2362 with a reddening $E(B - V) = 0.07$. The probability density ρ is shown as the greyscale isochrone. Circles represent the photometric data of Johnson & Morgan (1953) with the associated uncertainties shown as the bars.

0.02, ii) those marked as variable or visual doubles, and iii) three stars (Brun 598, 682 and 714) which were far removed from the sequence in the $U - B, B - V$ colour-colour diagram. The $U - B, B - V$ colour-colour diagram was fitted for a mean extinction and, after further removing an outlier in τ^2 – Brun 1012 – a value of $E(B - V) = 0.02$ (see Fig. 2.30) was derived with $\Pr(\tau^2) = 0.45$. The fact that the model is an adequate representation of the data thus suggests that the extinction is uniform across the SFR. This may seem unlikely given the vast amount of literature pertaining to the high variability of reddening across the SFR, however this high variability appears only to apply to stars in the very centre of the cluster. The remaining stars were fitted in the $V, B - V$ CMD and an age of $6.0^{+0.9}_{-1.1}$ Myr and distance modulus $dm = 7.94^{+0.05}_{-0.05}$ derived with $\Pr(\tau^2) = 0.47$. The best-fitting $V, B - V$ CMD is shown in Fig. 2.31.

2.8.4.12 σ Ori

The photometry of B-type stars in the region of Orion's Belt by Hardie et al. (1964) and the memberships of Sherry et al. (2008) were used. The complete list of members is not covered by the photometric observations and so additional photoelectric measurements of member stars were taken from Greenstein & Wallerstein (1958) for σ Ori C and Guetter (1979) for HD 294272 A and HD 294272 B. Hardie et al. (1964) provides only a combined
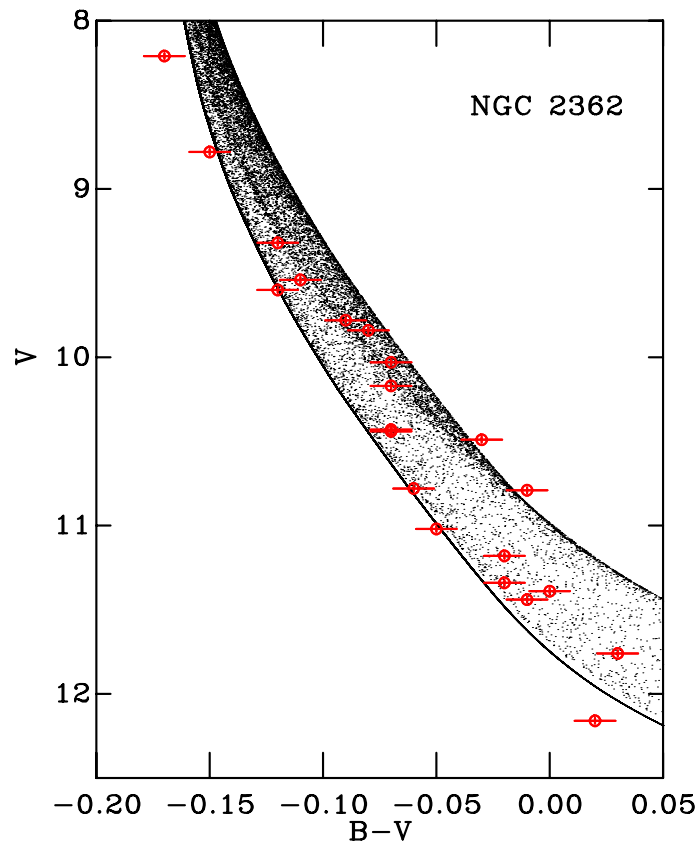
Figure 2.23: The best-fitting $V, B - V$ CMD for NGC 2362 with an age of 12.6 Myr and distance modulus $dm = 10.60$. The probability density ρ is shown as the greyscale isochrone. Circles represent the photometric data of Johnson & Morgan (1953) with the associated uncertainties shown as the bars.
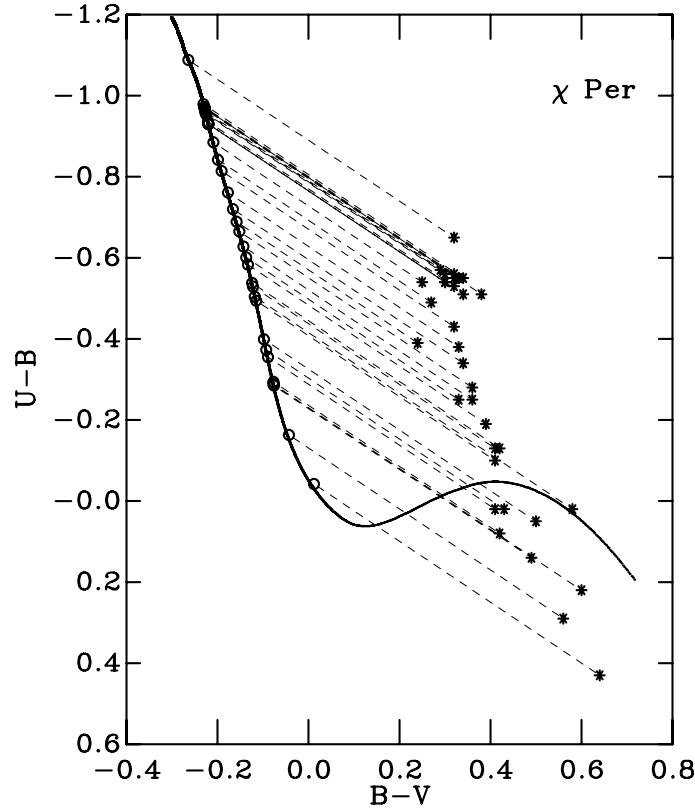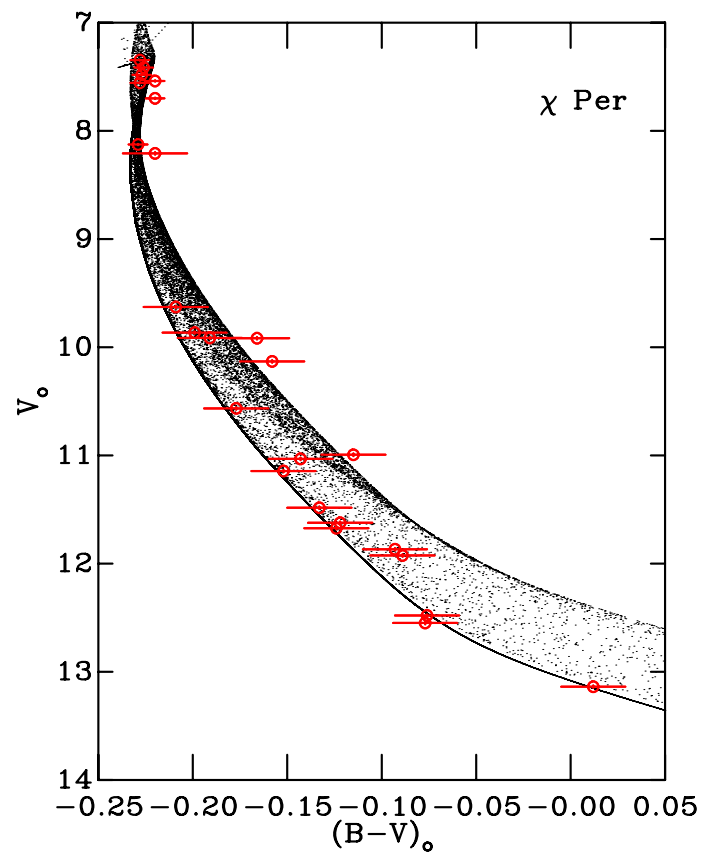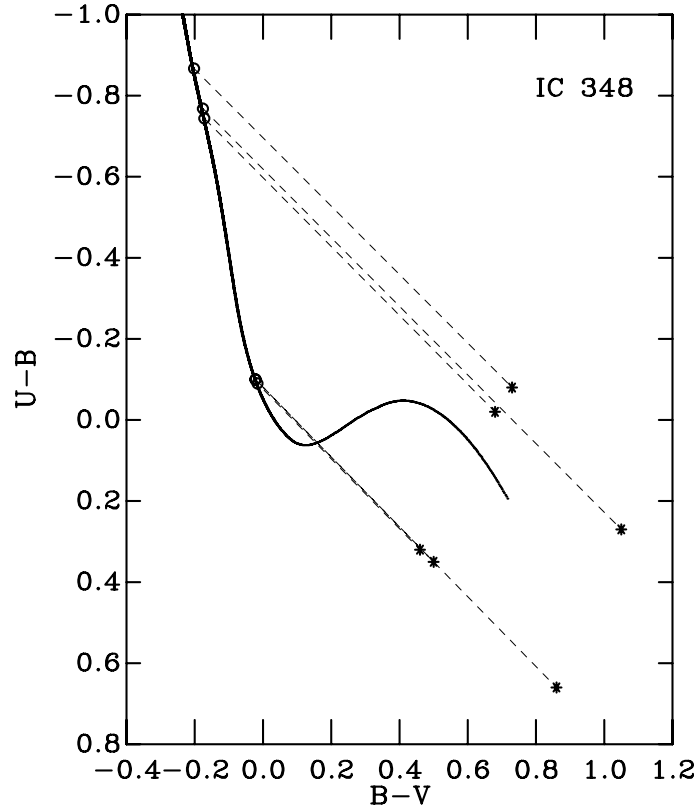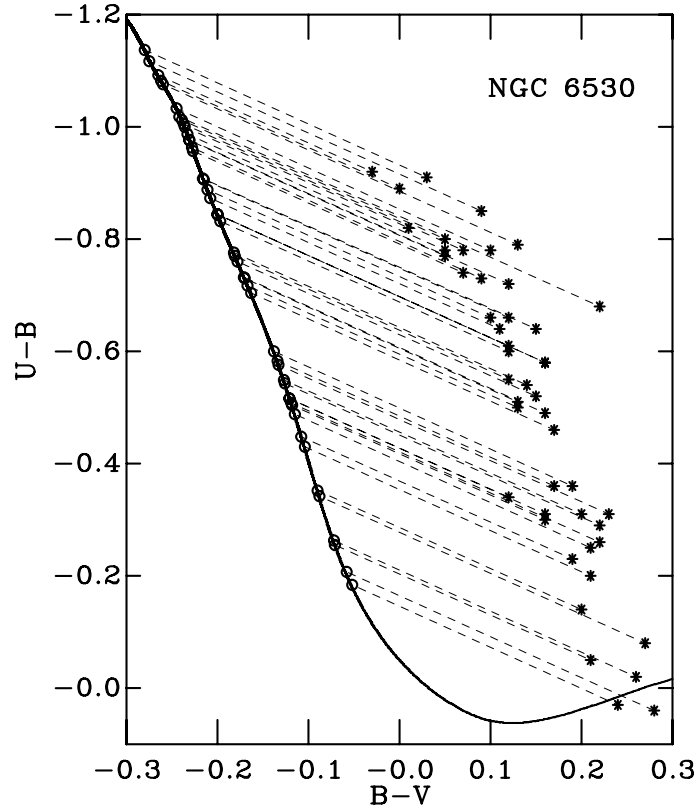
Figure 2.24: The application of the revised Q-method for NGC 6530. The asterisks show the apparent $U - B, B - V$ colours of individual stars (Walker 1957) and the circles show the de-reddened positions after applying the Q-method. Individual reddening trajectories are plotted as the dashed lines. The solid line is a 1 Myr Geneva-Bessell isochrone.

measurement for σ Ori ABC and so the UBV photometry of Greenstein & Wallerstein (1958) was used to disentangle the effect of σ Ori C. σ Ori A is itself a double-lined spectroscopic binary and hence the combined measurements of σ Ori AB after removing the effect of σ Ori C still consists of light from three distinct sources. To further deconstruct this measurement into individual components requires additional photometric information that is not available (this is further complicated by the non-uniform reddening associated with the SFR). Whilst the τ^2 fitting statistic can cope with higher order multiple systems, the interior models cannot, and so the combined measurement for σ Ori AB was neglected. Each star was de-reddened individually using the revised Q-method and a median $E(B - V) = 0.05$ (see Fig. 2.32) determined with a range of $\Delta E(B - V) = 0.12$. None of the photometry sources provide uncertainties and so a magnitude independent uncertainty of 0.01 mag for V and 0.008 mag for $(B - V)$ was used. The remaining stars were fitted in the $V_\circ, (B - V)_\circ$ CMD. An age of $8.7^{+4.7}_{-4.0}$ Myr and distance modulus $dm = 8.05^{+0.06}_{-0.06}$ were derived with an associated $\Pr(\tau^2) = 0.16$. The best-fitting $V_\circ, (B - V)_\circ$ CMD is shown in Fig. 2.33.
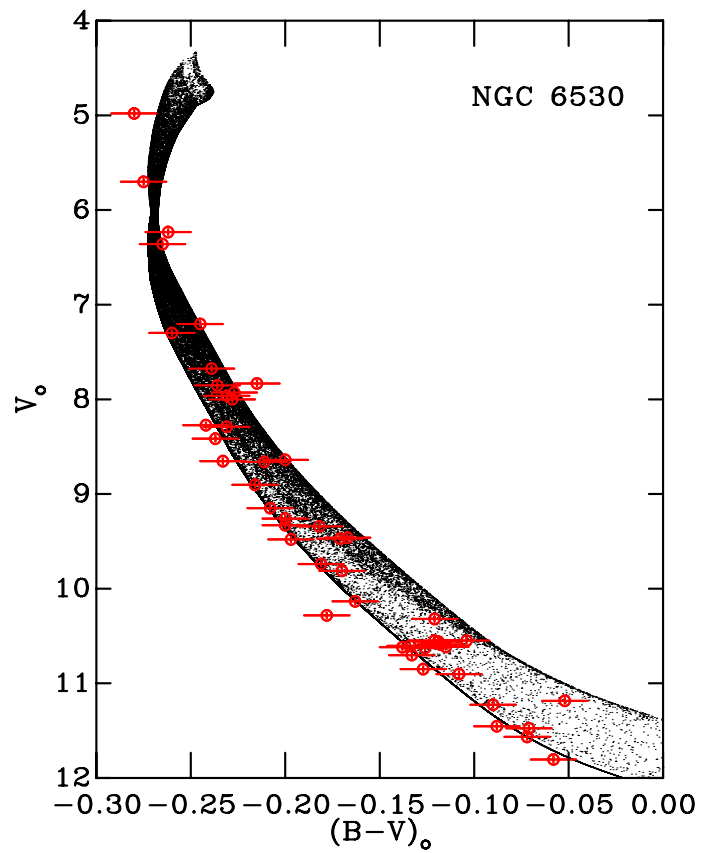
Figure 2.25: The best-fitting $V_\circ, (B-V)_\circ$ CMD for NGC 6530 with an age of $6.3\,\mathrm{Myr}$ and distance modulus $dm = 10.64$. The probability density ρ is shown as the greyscale isochrone. Circles represent the photometric data of Walker (1957) with the associated uncertainties shown as the bars.
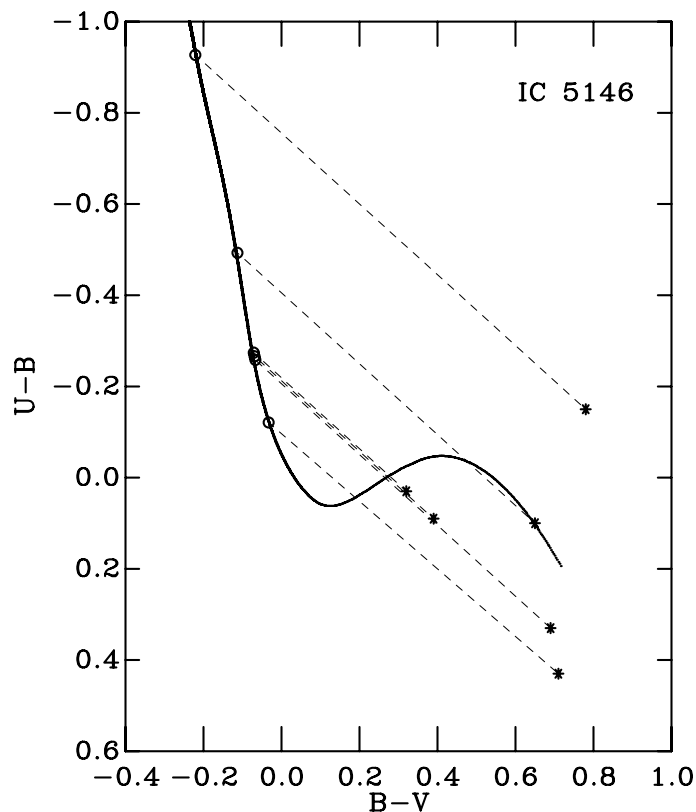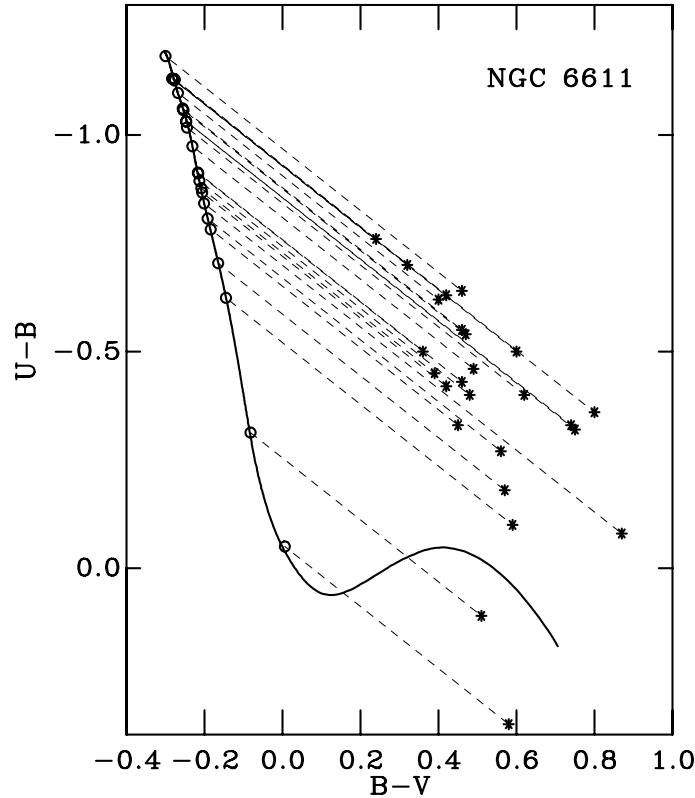
Figure 2.26: The application of the revised Q-method for NGC 6611. The asterisks show the apparent $U - B, B - V$ colours of individual stars (Walker 1961) and the circles show the de-reddened positions after applying the Q-method. Individual reddening trajectories are plotted as the dashed lines. The solid line is a 1 Myr Geneva-Bessell isochrone.

2.8.4.13 Pleiades

Whilst the pre-MS population of the Pleiades is not used to derive a pre-MS age, as for the SFRs presented in this section, the MS population is still fitted to ensure that two independent methods of determining both the age and distance are consistent (see Section 4.3.2 for an explanation). The photometry of Johnson & Morgan (1953) was used and stars blueward of $B - V = 0.0$ de-reddened on a star-by-star basis using the revised Q-method as there was a significant spread in the observed $U - B, B - V$ colour-colour diagram. Two stars – Hertzsprung 468 and 1432 – were removed as their colours suggest that they have evolved past the TAMS. The median value from these stars was $E(B - V) = 0.02$ (see Fig. 2.34) with a range of $\Delta E(B - V) = 0.06$. Stars redward of $B - V = 0.0$ were de-reddened using the updated reddening vectors derived in Section 2.7.1 assuming a median reddening of $E(B - V) = 0.02$ and the entire dataset was fitted for an age and distance. Note that the level of differential reddening across the cluster is small – in addition to the low level of intrinsic reddening – and also that the reddening vector is parallel to the isochrone at colours redward of $B - V = 0.0$. Hence the uncertainty introduced by applying a median reddening value to stars redward of $B - V = 0.0$ is less than 0.01 mag and does not affect the derived parameters. An age of $131.8^{+10.4}_{-14.9}$ Myr and distance modulus $dm = 5.63^{+0.02}_{-0.02}$ were derived with associated $\Pr(\tau^2) = 0.28$. The
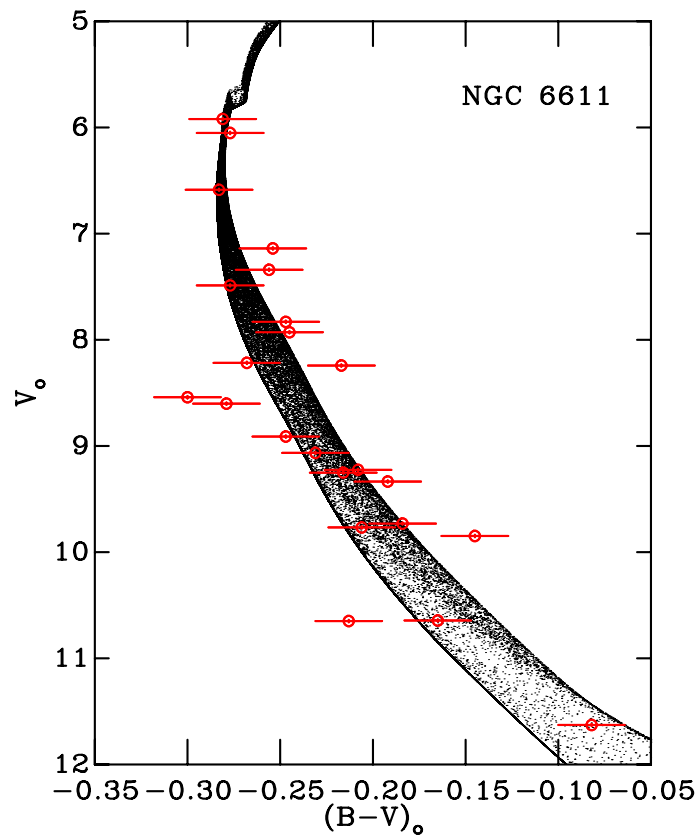
Figure 2.27: The best-fitting $V, B - V$ CMD for NGC 6611 with an age of 4.8 Myr and distance modulus $dm = 11.38$. The probability density ρ is shown as the greyscale isochrone. Circles represent the photometric data of Walker (1961) with the associated uncertainties shown as the bars.
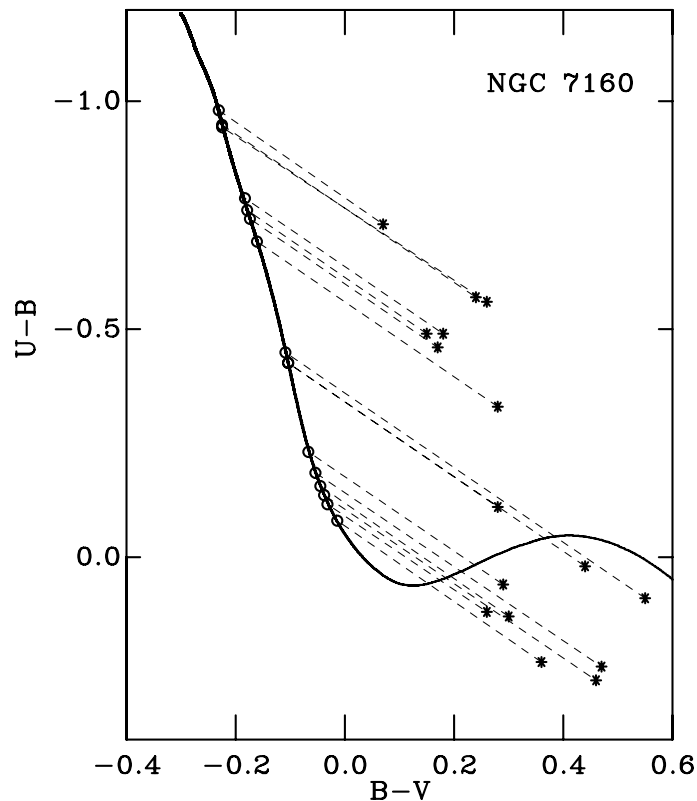
Figure 2.28: The application of the revised Q-method for NGC 7160. The asterisks show the apparent $U-B, B-V$ colours of individual stars (Hoag et al. 1961) and the circles show the de-reddened positions after applying the Q-method. Individual reddening trajectories are plotted as the dashed lines. The solid line is a 1 Myr Geneva-Bessell isochrone.

resulting fit is shown in Fig. 2.35.

2.9 Discussion

In this section a self-consistent set of MS ages, distances and reddenings have been derived for a sample of young (< 30 Myr) SFRs to, in most cases, a higher level of precision than that existing in the literature, and with statistically meaningful uncertainties on the derived ages and distances. It is instructive to place these new derivations in context by comparing them with previous determinations for these regions. Seven of the SFRs studied here have also been investigated by Naylor (2009). Comparing the results, the most obvious conclusions that can be drawn are; i) the best-fit MS ages presented in this thesis are, in all but one case, older than those in Naylor (2009), ii) the distances derived here are consistent with those of Naylor (2009), and iii) the associated $\Pr(\tau^2)$ values in this work are, in general, higher than those of Naylor (2009).

2.9.1 Derived Ages

Addressing the issue of the older MS ages, it is interesting to note that the interior models adopted in both studies are identical (set 'c' of Schaller et al. 1992), and therefore the
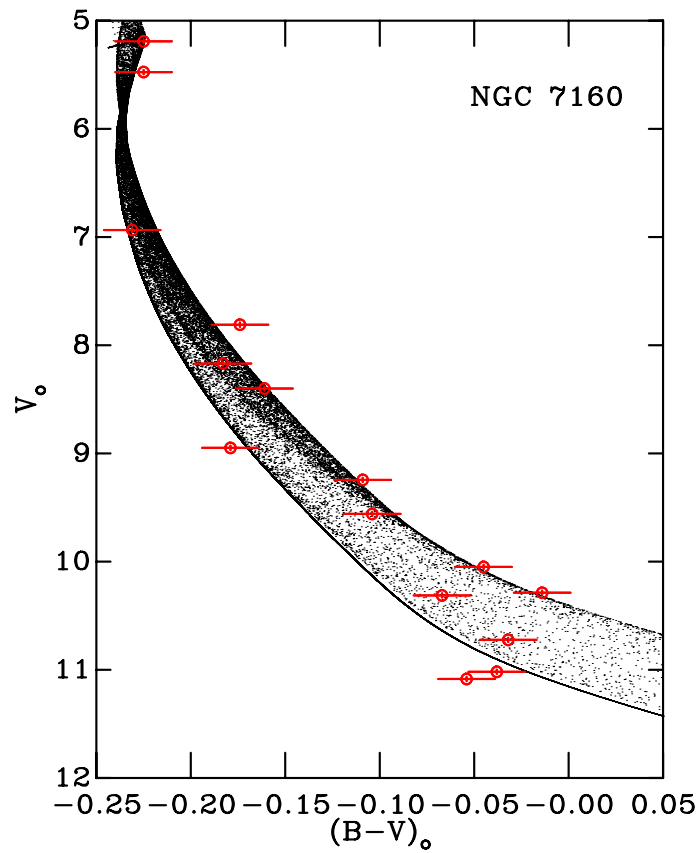
Figure 2.29: The best-fitting $V_\circ, (B - V)_\circ$ CMD for NGC 7160 with an age of 12.6 Myr and distance modulus $dm = 9.67$. The probability density ρ is shown as the greyscale isochrone. Circles represent the photometric data of Hoag et al. (1961). The plotted uncertainties are the magnitude independent values discussed in Section 2.8.4.10.
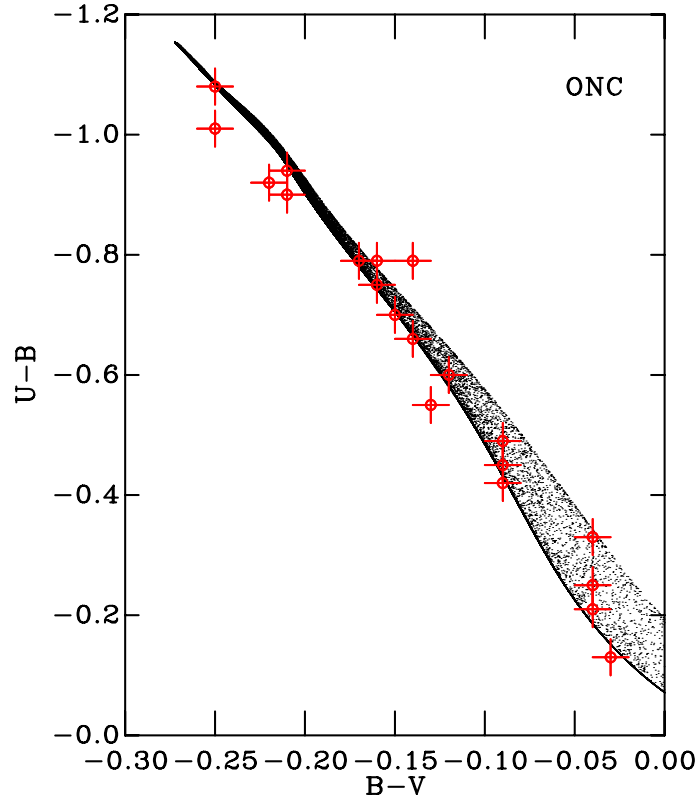
Figure 2.30: The best-fitting $U-B, B-V$ colour-colour diagram for stars in the vicinity of the ONC with a reddening $E(B-V) = 0.02$. The probability density ρ is shown as the greyscale isochrone. Circles represent the photometric data of Walker (1969) with the associated uncertainties shown as the bars.

older ages derived here are likely a consequence of adopting the updated ATLAS9/ODFnew atmospheric models as well as the revised colour- and extinction-dependent reddening vector. Fig. 2.36 shows the $1\,\mathrm{Myr}$ Schaller et al. (1992) interior model transformed into two observable planes – the intrinsic $(U-B)_\circ, (B-V)_\circ$ colour-colour diagram and the absolute magnitude-intrinsic colour $M_V, (B-V)_\circ$ CMD – using different BC-T_{eff} relations. The blue isochrones denote the interior model transformed using the BC-T_{eff} relation of Bessell et al. (1998) that uses the ATLAS9 'no-overshoot' atmospheric models (adopted in Naylor 2009), whereas the red isochrones are transformed using the BC-T_{eff} relation based on the updated ATLAS9/ODFnew models as derived in Section 2.5.1. The left panel of Fig. 2.36 shows how the U-band is modified by the updated atmospheric models and hence the adjustment to the shape of the $(U-B)_\circ, (B-V)_\circ$ isochrone in comparison to the Bessell et al. (1998) relation. Thus, when de-reddening stars individually, and for a given reddening vector, the derived $E(B-V)$ will be smaller than that derived when using the interior models transformed with the Bessell et al. (1998) BC-T_{eff} relation. Furthermore, this difference will increase as one moves to higher masses and in turn modify the de-reddened $V_\circ, (B-V)_\circ$ locus defined by the stars. The right panel of Fig. 2.36 shows that there is no similar modification to the shape of the $M_V, (B-V)_\circ$ isochrone and thus upon fitting for an age, an older age is required to best fit the photometric data.
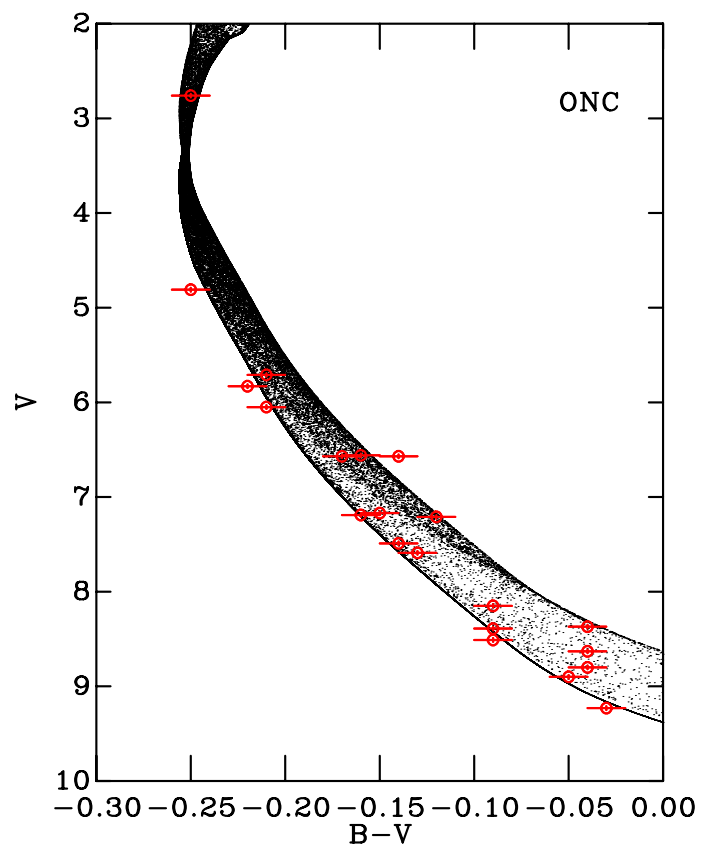
Figure 2.31: The best-fitting $V, B - V$ CMD for stars in the vicinity of the ONC with an age of $6.0\,\mathrm{Myr}$ and distance modulus $dm = 7.94$. The probability density ρ is shown as the greyscale isochrone. Circles represent the photometric data of Walker (1969) with the associated uncertainties shown as the bars.
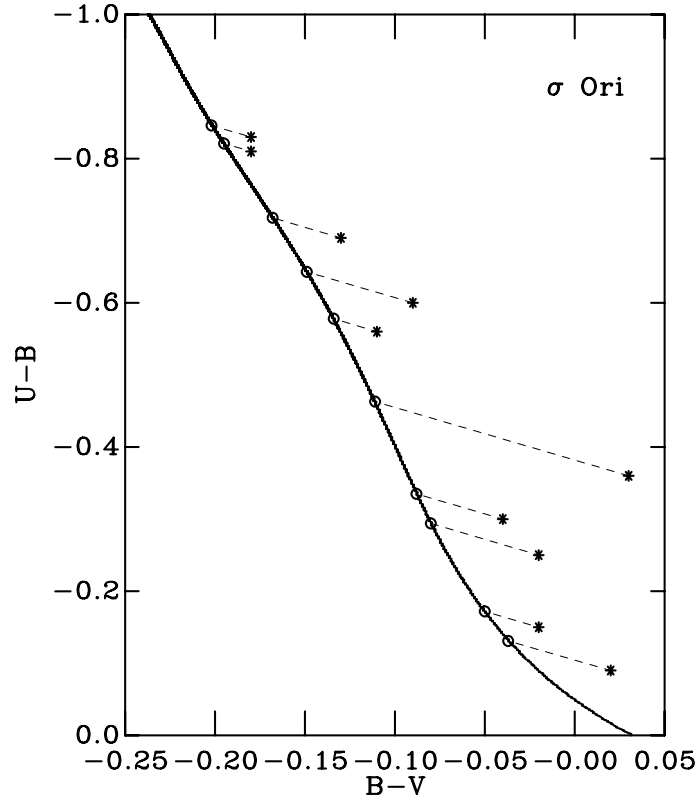
Figure 2.32: The application of the revised Q-method for σ Ori. The asterisks show the apparent $U - B, B - V$ colours of individual stars (Greenstein & Wallerstein 1958, Hardie et al. 1964, and Guetter 1979) and the circles show the de-reddened positions after applying the Q-method. Individual reddening trajectories are plotted as the dashed lines. The solid line is a 1 Myr Geneva-Bessell isochrone.

Given that the interior models used in both this thesis and Naylor (2009) are the same, the fact that the associated $\Pr(\tau^2)$ values for the MS distance-age fits are higher than those of Naylor (2009) suggests that the conversion from theoretical H-R to observable CMD space using the revised BC-T_{eff} relation, and the colour- and extinction-dependent reddening vectors, created using the more recent ATLAS9/ODFnew model atmospheres represent an improved description of the Johnson UBV photometric system compared to those of Bessell et al. (1998). Furthermore, it suggests that the MS parameters derived in Section 2.8 are more robust than those of Naylor (2009).

2.9.2 Derived Distances

The fact that the distances derived in this thesis are consistent with those of Mayne & Naylor (2008) and Naylor (2009) suggests that both the revised model isochrones and the fitting technique are robust. As the right panel of Fig. 2.36 demonstrates, there is negligible difference between the $V, B - V$ isochrones used in this thesis and the studies of Mayne & Naylor (2008) and Naylor (2009) – based on the BC-T_{eff} relations of Bessell et al. (1998) – to fit the MS population for a distance, and therefore the subtle differences between the distances likely stems from the use of a revised colour- and extinction-dependent reddening
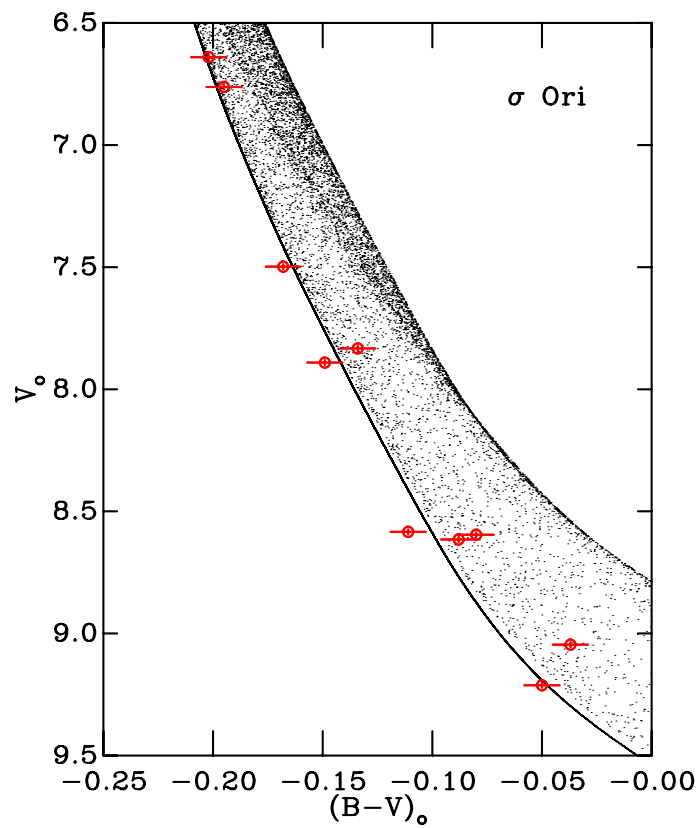
Figure 2.33: The best-fitting $V_\circ, (B-V)_\circ$ CMD for σ Ori with an age of $8.7\,\text{Myr}$ and distance modulus $dm = 8.05$. The probability density ρ is shown as the greyscale isochrone. Circles represent the photometric data of Greenstein & Wallerstein (1958), Hardie et al. (1964), and Guetter (1979). The plotted uncertainties are the magnitude independent values discussed in Section 2.8.4.10.
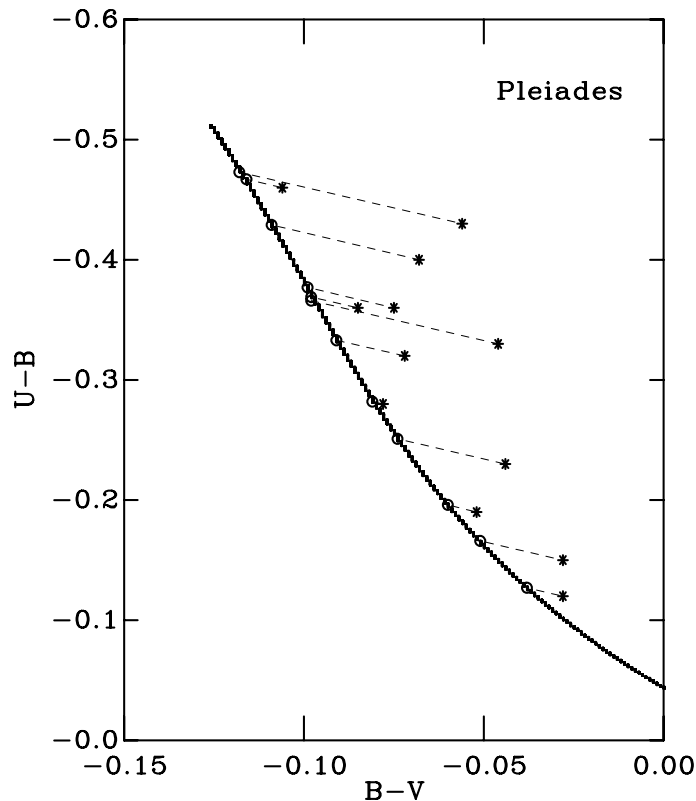
Figure 2.34: The application of the revised Q-method for the Pleiades. The asterisks show the apparent $U - B, B - V$ colours of individual stars (Johnson & Morgan 1953) and the circles show the de-reddened positions after applying the Q-method. Individual reddening trajectories are plotted as the dashed lines. The solid line is a 100 Myr Geneva-Bessell isochrone.

vector, and the slight variation it introduces into the trajectory of the reddening vector in both the $U - B, B - V$ and $V, B - V$ planes. As the distances derived in this chapter will be used in conjunction with pre-MS evolutionary models to derive ages from the pre-MS populations of the SFRs later in this thesis, it is instructive to compare the distances derived here with those generally assumed for these regions.

2.9.2.1 Cep OB3b

The distance derived for Cep OB3b of 570^{+16}_{-20} pc is significantly closer than previous estimates. Pozzo et al. (2003) calculated individual extinctions and distance moduli of O-, B- and A-type stars by comparing them with MS calibrations and calculated a distance of 851^{+82}_{-75} pc (see also the study of Jordi et al. 1996 which follows a similar process and derives a mean distance of 731 pc). It should be noted however that the reddening vectors adopted in these studies do not include the colour and intrinsic extinction dependence, and as the reddening towards Cep OB3b is very high – median $E(B - V) = 0.89$ – this could lead to appreciable differences in the positions of the de-reddened stars. Note also that the derived distance is closer than that based on maser parallax measurements for the Cep A molecular cloud (Moscadelli et al. 2009). Although Cep A is in the same molecular
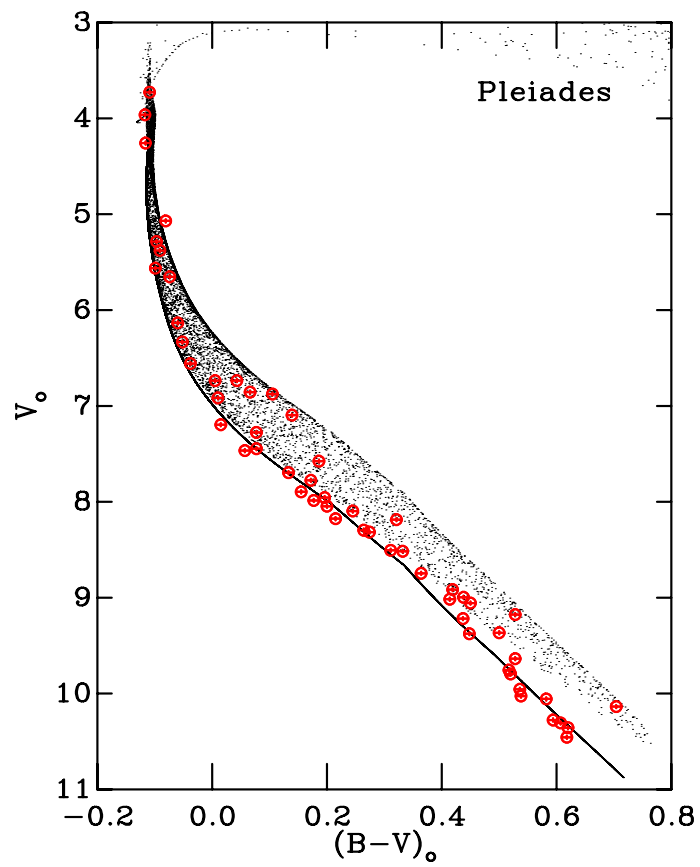
Figure 2.35: The best-fitting $V_\circ, (B-V)_\circ$ CMD for the Pleiades with an age of 131.8 Myr and distance modulus $dm = 5.63$. The probability density ρ is shown as the greyscale isochrone. Circles represent the photometric data of Johnson & Morgan (1953) with the associated uncertainties shown as the bars.
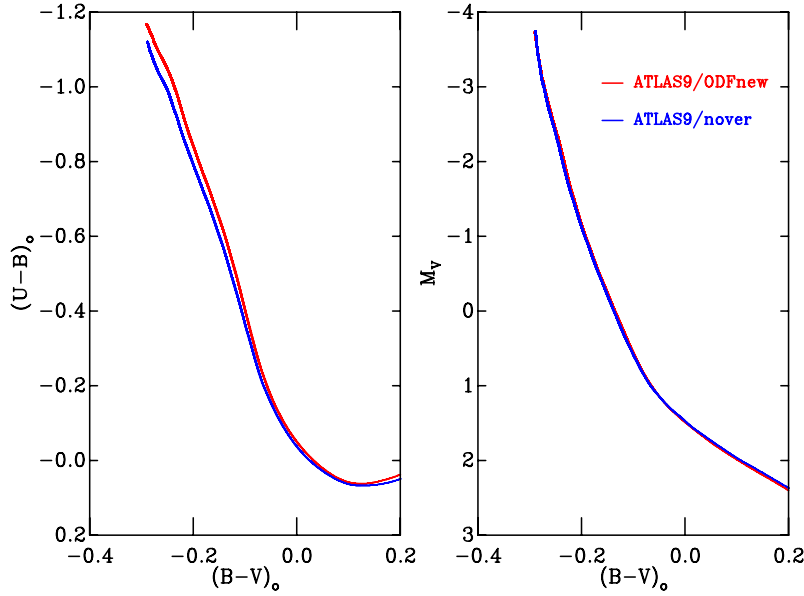
Figure 2.36: 1 Myr Geneva-Bessell isochrones. **Left:** Intrinsic $(U-B)_\circ, (B-V)_\circ$ colour-colour diagram. **Right:** Absolute magnitude-intrinsic colour $M_V, (B-V)_\circ$ CMD. The Schaller et al. (1992) interior models have been transformed into the observable plane using BC-$T_{\rm eff}$ relations based on the ATLAS9 'no-overshoot' models (Bessell et al. 1998; blue) and the updated ATLAS9/ODFnew model atmospheres as derived in this thesis (red). The ATLAS9/ODFnew model atmospheres result in a modified shape to the $(U-B)_\circ, (B-V)_\circ$ isochrone for colours $(B-V)_\circ \lesssim 0$. Note however that no similar effect is observed in the $M_V, (B-V)_\circ$ CMD.

complex as Cep OB3b, there is no evidence that the radial distance to both objects is similar and therefore the distance based on bona fide Cep OB3b members is preferred.

2.9.2.2 χ Per

The distance for χ Per based on the individually de-reddened members is $2.29^{+0.07}_{-0.03}$ kpc and is in excellent agreement with other estimates based on MS fitting of $\simeq 2.34$ kpc (e.g. Slesnick et al. 2002; Currie et al. 2010).

2.9.2.3 IC 348

Recent distance measurements to IC 348 range from $220 - 350$ pc with that derived in Section 2.8.4.3 (249^{+23}_{-10} pc) lying towards the lower end of this spectrum. A discussion in Herbig (1998) suggests that any difference in the distances to Per OB2 and IC 348, due to the associated uncertainties, are unproven and therefore adopts a distance of 316 pc based on *Hipparcos* parallax and reddening measurements of its members (de Zeeuw et al. 1999). There is evidence, however, that suggests Per OB2 may actually lie behind a complex of dark clouds – which IC 348 is associated with – and that the most recent extinction studies and parallax measurements of IC 348 members indicate a closer distance of $\simeq 250$ pc (Belikov et al. 2002; Černis & Straižys 2003).

2.9.2.4 IC 5146

The photometric parallax distance of 916^{+89}_{-76} pc is more precise yet closer than the most widely adopted distance of 1.20 ± 0.18 kpc by Herbig & Dahm (2002). This distance is based on the spectroscopic distances to the late B-type stars and uses two distinct MS calibrations. A distance of 1.1 kpc is calculated based on the Jaschek & Gomez (1998) absolute magnitude for B-type dwarf standards with a range of ages. Given that these stars have likely evolved away from the ZAMS, this calibration is probably inappropriate and likely overestimates the absolute magnitudes that are assigned to the late B-type stars in IC 5146. The more distant value of 1.4 kpc is based on the Schmidt-Kaler (1982) ZAMS (see Section 2.9.2.8 where it is shown that distances derived using this ZAMS calculation are typically too large). Distance fitting to the B-type population of IC 5146 generally converge at distances of $\simeq 1$ kpc (e.g. Walker 1959; Crampton & Fisher 1974; Elias 1978). A more recent estimate by Harvey et al. (2008), using the ONC as a calibrator, puts IC 5146 at a distance of 950 ± 80 pc and is in very good agreement with that derived here.

2.9.2.5 λ Ori

The derived MS distance 402^{+7}_{-6} pc for λ Ori using individual extinctions from the revised Q-method is consistent with previous estimates (Murdin & Penston 1977; Mayne & Naylor 2008). *Hipparcos* parallax measurements of five stars in the immediate vicinity of λ Ori give a mean distance of 380 ± 30 pc. Interestingly, the distance of 450 ± 50 pc derived by Dolan & Mathieu (2001) based on narrowband Strömgren photometry of OB-type stars and fitting the MS in the theoretical H-R diagram is still commonly adopted.

2.9.2.6 NGC 1960

The MS distance to NGC 1960 of $1.16^{+0.01}_{-0.02}$ kpc is significantly closer than the most recent determinations of 1.32 ± 0.12 kpc and 1.33 kpc by Sanner et al. (2000) and Sharma et al. (2006) respectively. In the case of the Sanner et al. (2000) study, the evolutionary models of Bono et al. (1997) were adopted, however it is unclear how these models were transformed into observable CMD space and thus whether the choice of empirical colours or a combination of atmospheric models and system responses may result in a systematic offset with the distance derived here. Furthermore, due to a lack of U-band photometry, the distance, extinction and age were simultaneously derived from fitting the $V, B - V$ CMD. A reddening of $E(B - V) = 0.25$ was derived by Sanner et al. (2000), which when compared to the photoelectric UBV photometry of Johnson & Morgan (1953), appears to be overestimated by $\simeq 0.05$ mag (see also the reddening and distance estimates of Mayne & Naylor 2008). An overestimation of the reddening would act to increase the distance required to fit the MS, thereby explaining the discrepancy between the two distances. A somewhat older study of Barkhatova et al. (1985) also uses the Johnson & Morgan (1953) UBV photometry and derives a distance of $\simeq 1.2$ kpc from MS fitting in both the $V, B - V$ and $V, U - B$ CMDs.

2.9.2.7 NGC 2169

The recent study of NGC 2169 by Jeffries et al. (2007) used the UBV photoelectric photometry of Sagar (1976) to derive a MS distance of 1062^{+29}_{-43} pc using the τ^2 fitting statistic and the MS model isochrones of Lejeune & Schaerer (2001). This distance is farther than that derived in Section 2.8.4.5 (995^{+33}_{-40} pc) and this discrepancy could stem from differences in the photometric datasets or model isochrones. To test which of these is the cause, the data of Sagar (1976) was fitted using the Geneva-Bessell MS isochrones and the resulting distance agrees to within 0.01 mag with that based on the photometry of Hoag et al. (1961). Hence, it is likely that the distance discrepancy is related to the model isochrones. Jeffries et al. (2007) uses the same interior models as those adopted here (set 'c' of Schaller et al. 1992) however the transformation from theoretical H-R to observable CMD space was based on the BC-T_{eff} relation of Lejeune & Schaerer (2001) which was created using different atmospheric models and UBV responses. Furthermore, the adopted reddening vector ($A_V/E(B-V) = 3.1$) does not include the subtle colour and intrinsic extinction dependence as described in Section 2.7.1.

2.9.2.8 NGC 2244

The distance derived from the individually de-reddened MS members is $1.38^{+0.03}_{-0.02}$ kpc. This compares well with both the distance estimated from disentangling the spectrum of the double-lined eclipsing binary V578 Mon (1.39 ± 0.1 kpc; Hensberge et al. 2000) and the ZAMS fitting to $V, B-V$ CMD (1.42 kpc; Ogura & Ishida 1981). Previous photometric studies have derived larger distances of $1.67^{+0.13}_{-0.12}$ and 1.66 kpc (Pérez et al. 1987 and Park & Sung 2002 respectively). The distance of Pérez et al. (1987) was derived by fitting the Schmidt-Kaler (1982) ZAMS to the $V, B-V$ CMD of high-mass stars. As discussed in Littlefair et al. (2010), the Schmidt-Kaler (1982) ZAMS calibration is significantly brighter than the more modern ZAMS calculations. This is due to the fact that the Schmidt-Kaler (1982) calculation is not based on ZAMS star observations, but is instead an empirical mean MS based on stars with ages of several Gyr. Hence the reason it is brighter is because the stars have had time to evolve off the ZAMS and thus it is no surprise that a larger distance is required to fit a given MS population in CMD space. The study of Park & Sung (2002) used stars with known spectral types to calculate a mean reddening towards the SFR and applied this to a calculated ZAMS (Sung & Bessell 1999), finding distances of between ~ 1.3 and ~ 2.0 kpc. They adopt a distance towards the more distant end of this spectrum on the assumption that the closer distance estimates are likely underestimated due to a combination of binary systems and the effects of evolution on high-mass stars. By using stars with known spectral types, only the very blue end of the MS in CMD space is fitted. This section of the CMD is almost vertical in the CMD and therefore the derived distance modulus is not well-constrained. In contrast, the revised Q-method is not dependent upon stars with known spectral types and thus fainter stars that lie on the redder section of the ZAMS can be used to better constrain the distance.

2.9.2.9 NGC 2362

The derived MS distance of 1318^{+37}_{-18} pc is closer than that typically assumed, either 1493^{+21}_{-20} pc or 1480 pc (see Balona & Laney 1996 and Moitinho et al. 2001 respectively), for isochrone fitting. Both distances are essentially based on MS fitting of photometry in CMD space. The distance of Moitinho et al. (2001) was derived by fitting the Schmidt-Kaler (1982) ZAMS to the $V, U - B$ CMD of bright cluster members. As explained in Section 2.9.2.8, the Schmidt-Kaler (1982) ZAMS will overestimate the distance to a given SFR when used to fit photometric data in CMDs. Note also that no uncertainties are given on the Moitinho et al. (2001) distance. Balona & Laney (1996) used narrowband Strömgren photometry to derive the distance, but only after having removed the five most discordant stars at the base of the MS. The ZAMS used in Balona & Laney (1996) is that of Balona & Shobbrook (1984), which for colours $(B - V)_\circ \gtrsim -0.20$ is almost identical to the Schmidt-Kaler (1982) calculation, and thus predicts a similarly large distance modulus.

2.9.2.10 NGC 6530

The distance of $1.34^{+0.03}_{-0.03}$ kpc – based on individually de-reddened stars using the revised Q-method – is consistent with recent estimates of ~ 1.25 kpc by Prisinzano et al. (2005) through ZAMS fitting of the high-mass members in both the $V, B-V$ and $V, V-I_c$ CMDs, and $1.25^{+0.16}_{-0.15}$ kpc by Arias et al. (2006) which is based on half a dozen early-type stars in M 8, whose distance moduli and extinction were calculated by fitting atmospheric models to the observed SEDs. The study of Sung et al. (2000) used stars with known spectral types to calculate a mean reddening towards the SFR and applied this to a calculated ZAMS (Sung & Bessell 1999), finding distances of ~ 1.4 and ~ 1.8 kpc. As in the case of NGC 2244, they adopt the larger distance on the assumption that the low distance estimate is likely due to fitting the upper envelope of the binary sequence. Interestingly, Mayne & Naylor (2008) used the photometric data of Sung et al. (2000), analysed in much the same way as in this thesis, and derive a nearer distance of $1.26^{+0.06}_{-0.01}$ kpc.

2.9.2.11 NGC 6611

The distance towards NGC 6611 is difficult to determine due to the highly variable reddening and the fact that the reddening law towards the SFR differs from that characteristic of the normal ISM (see Section 2.7.1.1). Over the past decades the distance has been significantly revised downwards from the early photometric works of Walker (1961) and Sagar & Joshi (1979) who found a distance of 3.2 ± 0.3 kpc based on the standard reddening law of $R_V \sim 3.1$. The distance of $1.89^{+0.05}_{-0.25}$ kpc, based on individually de-reddened stars using the revised Q-method, is in very good agreement with more recent estimates (see for example that of Belikov et al. 1999 who used all the available photometry at the time to derive a distance of 2.14 ± 0.1 kpc). Spectroscopic parallaxes for 24 high-mass cluster members suggest an even nearer distance of 1.8 ± 0.1 kpc (Dufton et al. 2006) which in

turn agrees very well with recent determinations based on the MS turn-off (e.g. Bonatto et al. 2006; Guarcello et al. 2007).

2.9.2.12 NGC 7160

The MS distance – and age – derived here represent the first derivations based on robust statistical fitting. The most recent distance modulus ($dm = 9.50$) from fitting the $V, B-V$ CMD (Kharchenko et al. 2005) does not account for the highly variable reddening across the SFR (see Section 2.8.4.10), and thus by not de-reddening each star on an individual basis, the distance fit suffers from the lack of a distinct MS and therefore has a large associated uncertainty. The derived distance for NGC 7160 using individually de-reddened stars from the revised Q-method (859^{+36}_{-20} pc) is slightly closer than that adopted by Sicilia-Aguilar et al. (2004, 2006a), who use a value of 900 pc based on observations of the upper MS of the young cluster Tr 37 which shares a common origin with NGC 7160 in the Cep OB2 association (Contreras et al. 2002). CO emission from the region defines a giant expanding shell, approximately 120 pc in diameter (Patel et al. 1998) with NGC 7160 at the centre and Tr 37 located on the shell rim. Hence, whether one can assign the same distance to both SFRs depends, of course, on the relative viewing angle of the two SFRs and is therefore uncertain.

2.9.2.13 Orion Nebula Cluster

The distance derived to the ONC based on MS fitting (387 ± 9 pc) is similar to previous estimates using an analogous MS fitting technique (e.g. Mayne & Naylor 2008; 391 ± 11 pc and Hernández et al. 2005; 393 ± 18 pc). This distance also agrees well with contemporaneous measurements based on different methods. Jeffries (2007) finds a distance of 392 ± 32 pc based on the rotational properties of pre-MS stars with spectral types between G6 and M2 (after removing objects with accretion discs on the basis of near-IR excess). Several trigonometric parallax measurements have recently implied distances ranging from $389 - 437$ (Sandstrom et al. 2007; Menten et al. 2007; Hirota et al. 2007). Furthermore, a dynamical parallax estimate from Kraus et al. (2007), who modelled the orbit of the binary θ^1Ori C, derived two possible distances of 387 ± 11 and 434 ± 11 pc due to weak constraints on the total mass of the system. They adopt the farther distance on the basis of comparison with the distance of Jeffries (2007) for all sources including those with evidence of active accretion.

2.9.2.14 σ Ori

The distance based on the individually de-reddened members of σ Ori is 407^{+12}_{-11} pc and is significantly larger than the generally adopted value of 352^{+166}_{-85} pc from the *Hipparcos* parallax measurement (e.g. Lodieu et al. 2009). More recent distance estimates have increased the precision on the distance, yet disagree as to the actual distance to the SFR. Caballero (2008) derived a dynamical distance for σ Ori AB of 334^{+25}_{-22} pc, assuming that

both stars are single and the age is $3\,\mathrm{Myr}$, however this distance increases to $\sim 385\,\mathrm{pc}$ if σ Ori AB is a triple system (as evidenced by Bolton 1974). A recent ZAMS fitting of the high-mass members by Sherry et al. (2008) suggests a distance of $440 \pm 30\,\mathrm{pc}$ based on stars brighter than $V = 11$ and within $30'$ of σ Ori AB using the empirical solar-metallicity ZAMS of Turner (1976, 1979). There is evidence that the metallicity of the σ Ori association is sub-solar (Cunha et al. 1998), the effect of which is to shift the ZAMS and therefore decrease the distance to $\sim 420\,\mathrm{pc}$.

2.9.2.15   Pleiades

The most discrepant distance, when compared to those of Naylor (2009), is that for the Pleiades ($\Delta dm \simeq 0.3$). In Naylor (2009) only stars blueward of $B - V = 0.0$ were used to derive the distance, with this paucity of stars leading to an erroneous distance estimate (see also the introductory section of Soderblom et al. 2005). A much stronger constraint on the distance is provided by using the full photometric catalogue of Johnson & Morgan (1953) which shows a well-defined MS. Furthermore, the precision on the derived distance to the Pleiades has been improved by a factor of two. Pinsonneault et al. (1998) derived a distance of $132 \pm 2\,\mathrm{pc}$ through fitting the $V_\mathrm{o}, (B - V)_\mathrm{o}$ and $V_\mathrm{o}, (V - I_\mathrm{c})_\mathrm{o}$ CMDs. Despite differences in both the stellar interior models and the BC-T_eff relations used to transform the model isochrones into CMD space between Pinsonneault et al. (1998) and this thesis, there is remarkable agreement between the two distance measurements. The MS distance derived is $134 \pm 1\,\mathrm{pc}$ thus providing the most precise distance to date for the Pleiades.

2.10   Model Dependency of Main-Sequence Ages

In this section the possible effects that the underlying assumptions in the MS interior and the atmospheric models have on the derived MS ages and distances are discussed. It has been shown that comparing ages and distances derived from different sets of MS models that incorporate the same, or very similar, prescriptions in the microphysics – for example the Geneva (Schaller et al. 1992) and the Padova (Girardi et al. 2002) models – and transformed into CMD space using the same atmospheric models results in differences of the order of $5 - 10\,\%$ (Mayne & Naylor 2008; Naylor 2009).

2.10.1   Effects of Updated Physical Inputs and Stellar Rotation

Many physical inputs used for MS models have changed since the Schaller et al. (1992) models and these may have an impact on the derived MS lifetime through isochrone fitting in CMDs. Updated MS models by the Geneva group have been published (Ekström et al. 2012) in which the following inputs have changed significantly. The initial chemical abundances have been revised, the opacities and reaction rates have been updated, the mass-loss prescription has been altered, and the degree of convective core overshoot has been modified. Fig. 6 of Ekström et al. (2012) shows that the non-rotating models of Ekström et al., when compared to those of Schaller et al., predict shorter MS lifetimes

by approximately 15 % for the lower masses, 5 % for the intermediate masses, whereas for stars with masses $> 30\,\mathrm{M}_\odot$ the MS lifetime is actually increased by $\simeq 4\,\%$ (which they ascribe to the difference in the mass-loss rates). In contrast, comparing the rotating and non-rotating models of Ekström et al. indicates that the inclusion of stellar rotation alone acts to increase the MS lifetime by between 15 and 20 % across almost the entire mass range.

S. Ekström has kindly computed a grid of these new MS models with a much finer age resolution than those available online (at the time of writing this thesis only models with ages $< 20\,\mathrm{Myr}$ are available). For this younger sub-set of SFRs, the ages and distances have been re-derived using the same methods as outlined above. Note that the calculated reddening vectors (see Section 2.7.1) are independent of the adopted interior models and are constructed using only atmospheric models, photometric system responses and a description of the interstellar reddening as a function of wavelength. Hence when de-reddening stars individually or fitting for a global mean reddening the $E(U-B)/E(B-V)$ and $A_V/E(B-V)$ vectors remain the same. The ages derived using the updated models of Ekström et al., including the effects of rotation, are older by approximately $15-25\,\%$, whereas the distance moduli tend to be smaller by, on average, $0.08\,\mathrm{mag}$ with a range of $\Delta dm = 0.15$, and furthermore, the associated $\mathrm{Pr}(\tau^2)$ is generally worse by approximately $0.05 - 0.1$.

2.10.2   Effects of Different Main-Sequence Interior Models

To ascertain the systematic effects introduced by adopting one set of MS interior models over another, it is imperative that a comparison with a distinct set of MS models be made. In contrast to the the studies of Mayne & Naylor (2008) and Naylor (2009), who used the Girardi et al. (2002) models for this comparison, here the newer interior models of Brott et al. (2011), which span a mass range of $5-60\,\mathrm{M}_\odot$, were adopted. A comprehensive discussion on the input physics of these models is beyond the scope of this thesis, however a full description of the physical processes is given in Brott et al. (2011) and an explanation of the evolutionary code in Heger et al. (2000).

It is not possible to perform a statistical fit to the photometric data using the τ^2 fitting technique with the Brott et al. (2011) interior models due to the lower mass limit of $5\,\mathrm{M}_\odot$ in the models. For the SFRs in the sample generally 50 % or more of the MS population fall below this lower mass limit and sit redward of the transformed isochrone. As the effects of rotation have been discussed above only the non-rotating Brott et al. models have been used here for comparison with the Schaller et al. (1992) models. For the comparison, a $10\,\mathrm{Myr}$ Brott et al. interior model was used as this age falls approximately in the middle of the range of MS ages derived in Section 2.8.

The $10\,\mathrm{Myr}$ Brott et al. model, plotted in the theoretical $\log L_\mathrm{bol} - \log T_\mathrm{eff}$ plane, lies approximately $0.05\,\mathrm{dex}$ fainter than that of the $10\,\mathrm{Myr}$ Schaller et al. model. Thus, if the interior model was transformed into CMD space using the BC-T_eff relation derived in Section 2.5.1 based on the ATLAS9/ODFnew model atmospheres, this 5 % difference

in L_{bol} would translate to derived distances that are $2-3\%$ closer than those derived in Section 2.8. This difference lies well within the uncertainty on most of the derived distances. The 10 Myr Brott et al. model also begins to turn away from the ZAMS at a slightly higher T_{eff} than that of Schaller et al., therefore implying that a younger age is necessary to fit a given dataset. Comparing with the next youngest Schaller et al. model in the resampled grid (log[age] = 6.98), the Brott et al. model lies between the Schaller et al. models of log(age) = 6.98 and 7.00 in the theoretical H-R diagram, suggesting that the difference in age is approximately $2-3\%$.

2.10.3   Effects of Assuming Local Thermodynamic Equilibrium

The ATLAS9/ODFnew atmospheric models used to create the BC-T_{eff} relation, and therefore transform a given interior model into CMD space, are computed based on the assumption of LTE. Whilst LTE may be a valid approximation for cooler stars, non-LTE effects become increasingly important at higher temperatures – such as those in OB-type stars – and lower gravities (see for example Mihalas 1978; Hubeny et al. 2003). To investigate what effects departures from LTE may have on the derived SFR parameters, models calculated using the TLUSTY atmospheric code have also been investigated. The TLUSTY atmospheric models adopted here are those of Lanz & Hubeny (2003, 2007)[6], designed specifically for O- and B-type stars respectively, covering $15\,000 \leq T_{\mathrm{eff}} \leq 55\,000\,\mathrm{K}$. TLUSTY models are calculated based on a plane-parallel, horizontally homogeneous model atmosphere in radiative and hydrostatic equilibrium, and incorporate departures from LTE and metal line-blanketing, using the hybrid complete linearisation and accelerated lambda iteration method (Hubeny & Lanz 1995). Convection is again based on the standard mixing length theory and the O-type atmospheres are calculated with a microturbulent velocity of $\xi = 10\,\mathrm{km\,s^{-1}}$, whereas a velocity of $\xi = 2\,\mathrm{km\,s^{-1}}$ is adopted for the B-type stars. The range of surface gravities provided by the grid ensures that, upon transforming a given interior model in CMD space, there is no need to extrapolate the models to the colour equal to that of the nearest $\log g$, as was the case when using the ATLAS9/ODFnew models (see Section 2.5.1).

For the comparison between the two sets of atmospheric models, the Schaller et al. (1992) models have been used. Two BC-T_{eff} relations were created based on the TLUSTY and the ATLAS9/ODFnew atmospheric models and these were in turn used to transform the 10 Myr Schaller et al. interior model into CMD space. Comparing the two isochrones in the $V, B - V$ CMD it is apparent that the transformation based on the TLUSTY atmospheric models results in an isochrone that is systematically bluer than that based on the ATLAS9/ODFnew models, with the difference increasing as a function of increasing mass (up to a maximum of $\Delta(B - V) = 0.007\,\mathrm{mag}$). This difference corresponds to derived distances, with respect to those derived in Section 2.8, that are of the order of $5-10\%$ closer. To estimate the effect that non-LTE atmospheric models have on the derived age, a series of Schaller et al. models – ranging from log(age) = $6.90-7.00$ in steps of $\Delta\log(\mathrm{age}) = 0.02$

---

[6]`http://nova.astro.umd.edu/Tlusty2002/tlusty-frames-models.html`

– were transformed into CMD space using the ATLAS9/ODFnew atmospheric models, and compared to the 10 Myr Schaller et al. model transformed using the TLUSTY atmospheric models. Allowing for the difference in the derived distance as a result of the two sets of atmospheres used to transform the model isochrone, the derived ages are affected at the $\lesssim 10\,\%$ level.

2.10.4 Summary

It is clear that despite differences in the physical inputs between various sets of MS evolutionary and atmospheric models, the derived parameters for a given SFR may vary by $\simeq 10\,\%$. This level of model dependency is similar to that calculated for other formalisms of MS evolutionary models (see Mayne & Naylor 2008; Naylor 2009), however, it is much smaller than the level of model dependency that is associated with the pre-MS evolutionary models which can result in age differences of up to factors of 3 (see Section 4.1). Thus the initial choice of the Schaller et al. (1992) evolutionary models and the use of the ATLAS9/ODFnew atmospheric models – that do not account for departures from LTE at extreme temperatures – have not introduced a large bias on the derived parameters and if one was instead to choose a different combination of interior and atmospheric models, the SFR parameters derived in Section 2.8 would not change by more than $10\,\%$.

Obviously, the effect of incorporating stellar rotation into evolutionary models can make a significant difference to the derived age or distance (see Section 2.10.1), and it will be interesting to see how, when the older Ekström et al. (2012) models become available, the MS ages for older clusters ($< 300\,$Myr) compare with less model-dependent age diagnostics such as the lithium depletion age. This method relies on locating the boundary, in terms of stellar mass, at which lithium reappears in the spectra of fully convective low-mass stars and brown-dwarfs (e.g. Rebolo et al. 1992; Basri et al. 1996; Bildsten et al. 1997; see also Section 1.4.3). To date, there is relatively good agreement between ages derived from the MS population of a given cluster and the lithium depletion age based on the lower mass population. For instance the Pleiades and IC 2602 have lithium depletion ages of 130 Myr (Barrado y Navascués et al. 2004b) and 46 Myr (Dobbie et al. 2010) respectively, which coincide with the derived MS ages of 132 Myr (see Section 2.8.4.13) and 44 Myr (Naylor 2009). Whilst this agreement is encouraging, it must be noted that the lithium depletion models are based on pre-MS evolutionary models that are at least a decade old (see Section 4.2). Over this timescale the heavy-element abundances of the Sun – which are used for calibration purposes in evolutionary models – have been revised downwards from the traditional $Z \simeq 0.02$ (Anders & Grevesse 1989) to $Z \simeq 0.014$ (Asplund et al. 2009). Thus a robust test of the next generation of pre-MS lithium depletion models would be to see if the calculated ages agree with the MS ages derived using the Ekström et al. models, thereby demonstrating a similar consistency as currently observed.

2.11 Effects of Assuming a Fixed Metallicity for Different Star-Forming Regions

A complete census of the chemical composition for the sample of SFRs is not presently available and therefore in this section an approximately solar composition ($Z \simeq 0.02$) has been assumed for both the MS interior and atmospheric models. Studies examining the chemical composition of SFRs within the Galactic disc have found that although the majority have approximately solar abundances, there is an extended tail of SFRs with sub-solar abundances and a less pronounced tail of super-solar abundance SFRs (Chen et al. 2003; James et al. 2006; Santos et al. 2008). It is important to understand how valid the assumption of a fixed metallicity is and what effect SFR-to-SFR variations in the metallicity may have on the derived ages and distances.

As an example, the dependence on the derived parameters will be investigated by adopting a sub-solar metallicity for χ Per. This SFR is chosen as there is a strong disagreement concerning the derived metallicity with some studies claiming a solar composition (Dufton et al. 1990; Smartt & Rolleston 1997), whereas Southworth et al. (2004) suggest an approximately half-solar composition ($Z \simeq 0.01$). Although the more recent study of Currie et al. (2010) does provide strong evidence for a solar composition, testing the effects of a metallicity variation is still illuminating. The reddening vectors $E(U-B)/E(B-V)$ and $A_V/E(B-V)$ were recalculated using the $Z = 0.01$ ATLAS9/ODFnew atmospheric models. The necessary sub-solar BC-T_{eff} relation was created using these atmospheric models to transform the $Z = 0.008$ – the nearest to half-solar composition available – interior models of Schaller et al. (1992) into colour-colour diagram and CMD space. The stars were individually de-reddened as before, and prior to fitting the $V_{\circ}, (B-V)_{\circ}$ CMD, the same stars as noted in Section 2.8.4.2 were removed. The revised distance modulus was $dm = 11.33^{+0.07}_{-0.03}$, whereas both the age and reddening were insensitive to changes in the metallicity. Hence, if the chemical composition of χ Per were indeed half-solar, the distance modulus would be ~ 0.5 mag smaller, thereby making the pre-MS population appear older (assuming that the lower metallicity does not affect the position of the pre-MS stars).

A cautionary note, however, is that whilst there is a reliable calibrator with a well-determined age and composition for solar metallicity models, the same is not true for the sub- and super-solar cases. Thus whether one can simply adjust the metallicity in the evolutionary code and leave all other inputs as for the solar case remains untested. So although different metallicities will most likely affect the derived distance, the magnitude of this difference is hard to define in absolute terms.

2.12 Summary

In this section it has been demonstrated how to derive the age, distance and reddening of SFRs from fitting MS stars using model isochrones in CMDs. The MS interior models and

atmospheric models, required to create the BC-$T_{\rm eff}$ relation so as to transform the model isochrones into CMD space, have both been described. The statistical fitting technique necessary to model the subtle evolution of stars between the ZAMS and TAMS has also been introduced and subsequently used to derive a self-consistent set of ages, distances and reddening for a sample of young SFRs. In cases where the MS population was too sparse – IC 348 and IC 5146 – the derivation of a MS age was not possible.

The effects that different evolutionary models and possible SFR variations in metallicity have on the derived parameters have also been discussed. Updated model isochrones that include stellar rotation, as well as revised existing inputs, result in MS ages that are older than those derived using models that neglect rotation, and yield distance moduli that are slightly lower. It was found that whilst the age and reddening are essentially unaffected by variations in the composition, the derived distances are heavily dependent upon the assumed metallicity. Thus it is vital to understand the chemical composition of a SFR before attempting to fit for a distance, and further use this to imply an age and to investigate evolutionary diagnostics, such as, for example the lifetime of circumstellar discs. A comprehensive study of the chemical composition of SFRs would remove this degeneracy and place any conclusions on a much firmer footing.

Having derived ages and distances, these can now be applied in the pre-MS regime and investigate whether agreement can be found between ages in these two distinct mass regimes. The derived MS ages, distances and reddenings are shown in Table 2.2.

Table 2.2: The ages, distances and reddenings derived from the MS populations of the sample of SFRs using the Geneva-Bessell model isochrones. The uncertainties in the age and distance were calculated using the τ^2 fitting statistic and represent the 68 % confidence level. Notes are as follows. (1) Age and distance derived after the application of the revised Q-method to de-redden stars individually. The median $E(B-V)$ value is quoted in the last column, with the range of the derived values in parentheses. (2) Parameters derived assuming the total-to-selective extinction ratio $R_V = 3.75$ (see Section 2.7.1.1). (3) Unable to calculate MS age due to insufficient number of evolved stars.

SFR	Age (Myr)		Distance modulus dm		$\Pr(\tau^2)$	$E(B-V)$
	Best-fit	68 % confidence	Best-fit	68 % confidence		
NGC 6611[1,2]	4.8	3.9–6.0	11.38	11.08–11.44	0.17	0.71 (0.58)
Cep OB3b[1]	6.0	3.8–6.6	8.78	8.70–8.84	0.26	0.89 (0.41)
ONC	6.0	4.9–6.9	7.94	7.89–7.99	0.47	0.02
NGC 6530[1]	6.3	5.7–7.0	10.64	10.59–10.68	0.98	0.32 (0.23)
NGC 2244	6.6	5.8–7.4	10.70	10.67–10.75	0.70	0.43 (0.18)
σ Ori[1]	8.7	4.7–13.4	8.05	7.99–8.11	0.16	0.05 (0.12)
λ Ori[1]	10.0	8.9–11.0	8.02	7.99–8.06	0.49	0.11 (0.24)
NGC 2169	12.6	10.5–17.6	9.99	9.90–10.06	0.20	0.16
NGC 2362	12.6	7.9–15.3	10.60	10.57–10.66	0.31	0.07
NGC 7160[1]	12.6	10.5–13.9	9.67	9.62–9.76	0.29	0.37 (0.37)
χ Per[1]	14.5	12.8–16.7	11.80	11.77–11.86	0.49	0.52 (0.28)
NGC 1960	26.3	21.1–29.5	10.33	10.28–10.35	0.67	0.20
IC 348[1,3]	–	–	6.98	6.89–7.17	–	0.69 (0.52)
IC 5146[1,3]	–	–	9.81	9.62–10.01	–	0.75 (0.61)
Pleiades[1]	131.8	116.9–142.2	5.63	5.61–5.65	0.28	0.02 (0.06)

Chapter 3

Characterisation and Calibration of the *Isaac Newton* Telescope Wide-Field Camera Photometric System

3.1 Motivation

In Chapter 2 the processes involved in deriving stellar parameters for MS stars were discussed and these were used to derive a homogeneous set of self-consistent reddenings, distances and ages for the sample of young SFRs. These parameters can now be used to fit the pre-MS members of the SFRs for an age. To test whether agreement between MS and pre-MS age derivations can be found for young ($< 30\,\mathrm{Myr}$) pre-MS SFRs, the main sources of uncertainty when attempting to fit pre-MS stellar populations with model isochrones in CMD space must be addressed. The primary issues affecting pre-MS isochrone fitting are; i) the photometric calibration of the data for what are very red stars, ii) the transformation of the model isochrones from the theoretical H-R to CMD plane, and iii) incorporating the colour and gravity dependence of the interstellar extinction.

Traditional photometric calibration relies on the comparison of instrumental magnitudes and colours to standard star observations to calculate zero-points, colour terms and extinction coefficients. The technique generally assumes that a single linear transformation is appropriate for all stars of a given colour. Furthermore, standard stars are predominantly MS field stars. Hence it is vital to test whether the difference between the instrumental and standard photometric system, and also how differences between the spectra of MS and pre-MS stars of the same colour, may introduce systematic uncertainties into the final calibrated photometry.

The transformation from H-R to CMD space requires a BC-T_{eff} relation to calculate colours and magnitudes. Empirical relations are based on observations of MS stars and are therefore of limited applicability for young or very low-mass stars due to differences

in the surface gravity ($\log g$) and hence the colour of the star at a given T_{eff}. Theoretical relations are based on the convolution of atmospheric models through the appropriate system responses. The line lists used in the computation of the atmospheric models are notoriously complicated and likely suffer from an incomplete detailed list of transitions. These missing sources of opacity result in an overestimation of the stellar luminosity for the coolest objects, thus predicting colours that are too blue for a given mass (see also Stauffer et al. 2007).

Reddening estimates for a given SFR can be derived from fitting the higher mass stars with a model isochrone in the $U - B, B - V$ colour-colour diagram assuming a given reddening vector (this often neglects the colour and intrinsic extinction dependency, see Section 2.7.1). This calculated value is then applied to stars of all spectral types, assuming a similar non-dependence on colour and extinction. This can inaccurately modify the shape of the pre-MS locus, especially if the target stars are highly reddened.

In the following chapters the above issues will all be addressed, however, in this chapter the calibration of photometric observations of pre-MS stars is discussed. Section 3.2 describes the observations taken as part of the large survey of young SFRs and Section 3.3 details the data reduction process. Section 3.4 examines the photometric calibration process for observations of pre-MS stars. In this section, the problems associated with transforming photometric observations of young pre-MS stars into a standard photometric system are discussed, and as a result the natural system in which in the observations were taken is characterised and calibrated. Section 3.5 summarises the findings presented in this chapter.

3.2 Observations

The observations were obtained using the 2.5-m *Isaac Newton* Telescope (INT) on La Palma. Despite the survey being split over two runs, the same instrumentation and filter set were used on both occasions, namely the four EEV 2048 × 4096 pixel CCD Wide-Field Camera (WFC) with a $34' \times 34'$ field-of-view and a pixel scale of $0.33''$, and the $(UgriZ)_{\text{WFC}}$ filter set. The four CCDs are arranged in an L-shaped configuration. There are small gaps between the CCDs and this results in approximately 2 % of the total field-of-view remaining unobserved in a single pointing. The observations presented here have not been tiled to account for the gaps in the CCD configuration. A combination of long and short exposures were used to ensure that any bright stars saturated in the longer exposures could be measured in the shorter exposures. The reader is directed to Appendix A for the exposure times for each field taken as part of the photometric survey.

Whilst the *gri* filters are based on the Sloan Digital Sky Survey (SDSS) design there are no similar u and z filters for the WFC and so the Royal Greenwich Observatory (RGO) U_{WFC} and Z_{WFC} filters were used. The first set of observations were taken during the 21$^{\text{st}}$ – 26$^{\text{th}}$ Oct. 2007 with the second run during the 13$^{\text{th}}$ – 19$^{\text{th}}$ Sept. 2008. Four fields in Stripe 82 of the SDSS were used as standard fields and routinely observed throughout

both runs (see Table A.3). This catalogue can be used as a standard reference on the basis that it is a homogeneously acquired dataset with multiple SDSS photometric observations in all *ugriz* filters (at least 4 in each filter, with a median of 10). The catalogue consists of over 1 million non-variable – rms scatter of all *g*-band measurements below 0.05 mag – and unresolved sources, spanning an *r*-band magnitude range of $14 - 22$. Calculated uncertainties are below 0.01 mag for stars brighter than 19.5, 20.5, 20.5, 20.0 and 18.5 mag in *ugriz* respectively with internal consistency in the spatial variation of photometric zero-point of $\simeq 0.01$ mag (rms).

3.2.1 Zero-Point Stability

Due to weather restrictions standard star observations were taken on five separate evenings. On only one of the five nights were conditions photometric throughout, the other four were affected to some degree by the presence of cloud. To ascertain over what temporal range the zero-point was stable the g_{WFC}-band zero-point was calculated for all standard field observations by taking the median of all the zero-point values in a single field via the comparison of the instrumental magnitudes to the real magnitudes in the standards catalogue. This was then corrected for extinction using a mean g_{WFC}-band extinction coefficient ($k_{g_{\mathrm{WFC}}} = 0.19$) for La Palma and the airmass at which the observation was taken. A time-series plot of the g_{WFC}-band zero-point for each evening allowed the identification of regions where the zero-point became unstable (see Fig. 3.1). This process defined half-nights of bona fide photometric conditions, which can be used for the photometric calibration procedure (the maximum deviation over the course of a single half-night was 0.06 mag). If observations of a given SFR were taken on two separate photometric nights then the mean of the two measurements in each colour was used for the final optical catalogue. For SFRs treated in this way, the standard deviation between the mean value and both individual measurements is 2 % across all colours. Due to a paucity of blue stars in the standards catalogue, the colour range which is most populated ($0.6 \leq (g - i)_{\mathrm{WFC}} \leq 1.0$) was used and the zero-point defined at a median colour of $(g - i)_{\mathrm{WFC}} = 0.8$. This colour range cut in $(g - i)_{\mathrm{WFC}}$ defines the necessary cuts in the other INT-WFC colours ($1.05 \leq (U - g)_{\mathrm{WFC}} \leq 1.96$, $0.14 \leq (r - i)_{\mathrm{WFC}} \leq 0.31$ and $0.02 \leq (i - Z)_{\mathrm{WFC}} \leq 0.18$ with median values of $(U - g)_{\mathrm{WFC}} = 1.505$, $(r - i)_{\mathrm{WFC}} = 0.225$ and $(i - Z)_{\mathrm{WFC}} = 0.1$). The seeing generally varied between 1 and $2''$ in the temporal regions defined in Fig. 3.1.

3.3 Data Reduction

The first task was to de-bias each image using a median stacked bias frame. Optical CCD detectors are often non-linear in their response and can result in non-linearities at levels of $\sim$ a few % (see also González-Solares et al. 2008). The corner of CCD 3 is affected by vignetting and, as such non-linearities occur at high counts, a vignetted region will never reach the non-linear regime and can thus be used to measure the actual level of
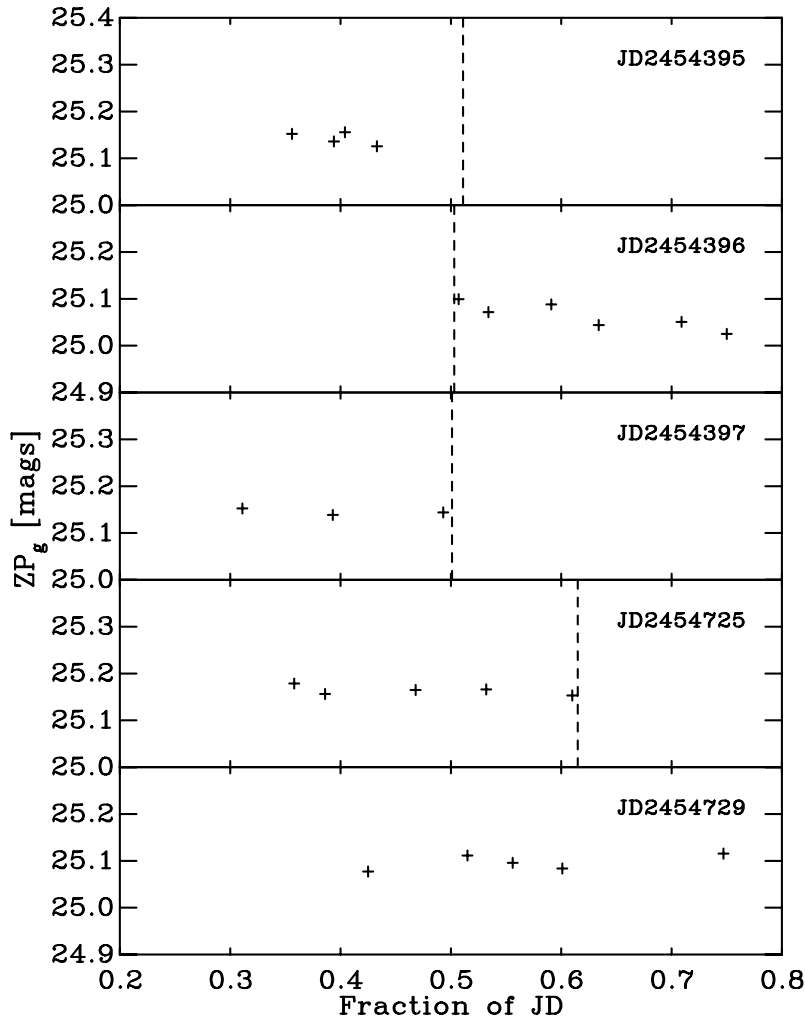
Figure 3.1: The stability of the g_{WFC}-band zero-point as a function of time on evenings which standard star observations were taken. The crosses represent the derived zero-point from the comparison of instrumental to standard star magnitudes (corrected using a mean g_{WFC}-band extinction coefficient and the airmass of the observation). The maximum spread over the course of a single half-night is 0.06 mag. The dashed lines represent the temporal limits that define photometric regions for each evening. Observations taken in non-photometric regions were not used unless overlapping photometric fields were available.

light the CCD has been exposed to. Linearity tests were performed on the four EEV 2048 $\times$ 4096 pixel CCDs by comparing the counts in this vignetted region relative to other regions across the CCDs. A series of CCD-specific linearity corrections from the *Isaac Newton* Group (ING) webpages were adopted and applied to the data prior to any further processing. Fig. 3.2 shows the linearity curves for the four individual EEV CCDs of the WFC after the linearity corrections have been applied and show that there are residual non-linearities on the $\pm 1.5\,\%$ level. Note, however, that this occurs for only some pixels of the brightest stars i.e. with counts greater than 50 000. In the data reduction process pixels with counts $\geq 50\,000$ are flagged as non-linear, and so typically the residual non-linearities are of the order of $< 1\,\%$. Images were then flat-fielded using a median stacked flat-field
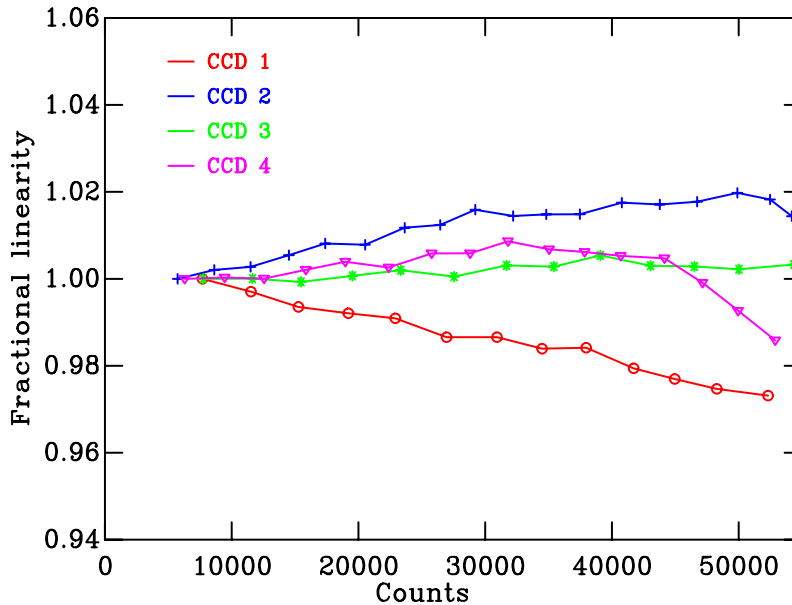
Figure 3.2: Linearity curves for the four individual EEV CCDs of the WFC as performed in September 2008 using the 'fast' readout mode on the INT.

frame consisting of several flat-fields in a single bandpass obtained in bright conditions during twilight. Flat-fielding identifies bad pixels/columns as well as encoding variations in the pixel sensitivities and the effects of vignetting across the detector. Images taken with the i_{WFC}- and Z_{WFC}-bands were de-fringed using library fringe frames. Fringing is the interference pattern caused by the reflections on the inside of thin, back-illuminated CCD detectors and are important at longer wavelengths. U_{WFC}, g_{WFC} and r_{WFC}-band images are unaffected by fringing, whereas the i_{WFC}-band shows fringing at $\simeq 2\,\%$ of the sky level and the Z_{WFC}-band is more seriously affected at $\simeq 6\,\%$ of the sky. After optimally removing the zeroth order of fringes, the typical residual fringe pattern is approximately 0.2 and 0.4 % of the sky in i_{WFC}- and Z_{WFC}-band respectively.

The data were analysed using the CLUSTER package. The extraction of photometry from the images followed the optimal extraction algorithm described in Naylor (1998) with its implementation in the construction of CMDs explained in Naylor et al. (2002), Burningham et al. (2003) and Jeffries et al. (2004). Photometry is carried out on an individual image basis to extract magnitudes and later combined using a weighted mean. This bypasses the issue of combining a series of images that may contain frames with poor seeing or high sky background which will affect the signal-to-noise ratio available from the better quality images. The full reduction process is explained below.

The i_{WFC}-band images for a particular field were combined – after calculating spatial transformations between separate frames – with the resultant deep image used for object identification and detection. The i_{WFC}-band was used on the basis that the observations were targeted towards pre-MS stars which are more luminous at redder wavelengths. The sky background was determined using sky boxes, which are sufficiently large so that when the sky is subtracted from a star the noise due to the sky measurement is negligible, and

then an interpolated sky is subtracted from each pixel. The sky pixel value histogram is fitted with a skewed Gaussian which allows a determination of the standard deviation (σ) of the sky. Stars are identified as pixels with counts $n\sigma$ above the sky background level and, based on an iterative process, the factor n is reduced until counts just under the sky background are identified. In each pass this produces a list of stars, with additional stars only added to this list on the condition that it does not contain the central pixel of a previously identified star. Duplicates are distinguished and subsequently removed by examining whether another star lies within a distance equal to the seeing of another previously identified star, hence an estimate of the seeing is of paramount importance.

In this summed image, stars which appear to have suspect profiles are flagged as these stars are unsuitable for point spread function (PSF) profiling. The majority of flags are described in Burningham et al. (2003), however for a comprehensive discussion the reader is directed to the Cluster Collaboration homepage. At this stage of object identification, several quality flags are introduced to identify stars that contain a pixel that is saturated ('S'), stars that lie within the non-linear regime of the CCD detector (taken as $\geq 50\,000$, 'L'), and stars that are non-stellar ('N'). The non-stellar flag is assigned on the basis of deviations of stellar profiles beyond a certain threshold and is applied to stars whose profile correction is not point-like. The flux of a star convolved through a mask size equal to FWHM of the seeing is compared to the flux measured through a mask of size 0.5 $\times$ FWHM. If the ratio of these fluxes is greater than 3σ of the median – where σ is the sum in quadrature of the uncertainty in each measurement and the rms about the median – then the star is flagged. Images with shorter exposures are then used to identify stars that may be saturated in the deep summed image (neglecting stars that have previously been flagged as non-stellar). This object detection results in the creation of two lists; a list of stars upon which optimal photometry will be performed and another list of bright suitable candidates with which to define the PSF.

Optimal photometry is performed on each individual image, however a suitable mask must first be chosen before implementing the optimal extraction. The 49 brightest, unsaturated sources from the list of PSF candidate stars are fitted with two-dimensional elliptical Gaussians and the mask parameters set according to the parameters of the star whose geometric mean FWHM is the median of the stars in the list. The PSF is then estimated by fitting a two-dimensional Gaussian to the PSF star. This is combined with estimates of the variance in the pixels to construct the optimal weight mask. For each star local sky background levels are determined and subtracted during this process. Optimal photometry is then carried out on all candidate stars within the list, with the addition of further quality flags (see Burningham et al. 2003 for a discussion). In optimal photometry each pixel is taken as an independent estimator of the flux in the profile. Hence, assuming the profile is well constrained, by measuring the flux in a given pixel and comparing it to the fraction of the total flux expected in that pixel, one can estimate the total flux in the profile. The measurement of the total flux is thus optimised by weighting the flux estimates from each pixel by the inverse of the square of their uncertainties before combining them.

At this stage an additional correction must be applied before a true representation of the stellar flux can be ascertained. This arises due to a difference between the extraction mask used for the optimal photometry and the true stellar profile – this correction is termed the profile correction. If the extraction mask was a perfect match to the observed profile then the profile correction would be zero, however this is unlikely to be the case given that the true PSF is unlikely to be represented by an elliptical Gaussian, due to atmospheric turbulence, and thus some degree of correction is generally required. The CCD image is divided into boxes and the brightest star in each box is used to determine the profile correction by comparing the instrumental magnitude calculated using the optimal mask and the instrumental magnitude measured using aperture photometry adopting a sufficiently large aperture. Inevitably the profile correction varied as a function of position, and thus the profile corrections for bright stars in each box were then fitted with a two-dimensional low-order polynomial as a function of CCD position. The two-dimensional profile corrections were then applied to all stars in the image.

Each image is corrected to the mean airmass of the group of images using extinction corrections derived using the standard stars. Prior to combining the photometry from each image, the relative transparency correction for each frame was determined. For each colour an image was assigned as the master image and the transparency corrections calculated by taking the weighted mean of the differences between the magnitudes of good quality stars in a given image and the master image. Each image was then corrected by its relative transparency correction multiplied by a factor $N/(N+1)$, where N is the number of frames. The master image was then corrected by the mean transparency correction. The individual profile corrected magnitudes of each star in each image were then combined by weighting each measurement in accordance with its signal-to-noise ratio. An additional statistical uncertainty was added at this stage to each measurement to ensure that the distribution of χ^2 resulting from combining the measurements versus signal-to-noise was independent of signal-to-noise and had a mean value around unity. The additional statistical uncertainty adopted ranged from $0.01 - 0.03$ mag and reflects uncertainties in the profile correction. Stars with a reduced $\chi^2 > 10$ are generally flagged as variable ('V'; see Burningham et al. 2003). The magnitudes at the mean airmass are then combined to give colours and magnitudes. These are then corrected for airmass – using the standard star coefficients – to give the final colours and magnitudes.

For some SFRs, photometric observations at two different epochs have been combined, and due to pre-MS variability over such timescales there are a number of sources that have thus been flagged 'V'. A cluster was not necessarily observed in all five $(UgriZ)_{\mathrm{WFC}}$ bands on all visits and so where possible, photometry for sources that displayed night-to-night variations has been replaced with colours and magnitudes from a single night. The night with the most colours available and the smallest uncertainty on the data in the i_{WFC}-band was chosen.

The final task was to obtain an astrometric solution for the photometric catalogues. This was performed by matching stars in the optical catalogues to those in a reference

catalogue of the same field-of-view. The Two-Micron All-Sky Survey (2MASS, Cutri et al. 2003) was used for the reference catalogues. A six-coefficient model was then used to perform the transformations from pixel coordinates to J2000.0 equatorial coordinates. The rms residual of the six coefficient fit were approximately $0.2''$.

For SFRs that required multiple fields-of-view for complete coverage, a normalisation procedure as described in Jeffries et al. (2004) was used to combine the fields. A running catalogue was created that contained all the calculated magnitudes and colours for each object identified in all fields. The mean magnitude and colour difference of stars in common between two overlapping fields were calculated, and the zero-points adjusted for each field to minimise these differences (in effect allowing for small variations in the zero-point between fields observed on different nights). This process ensures greater consistency between fields in the final catalogue. The resulting zero-point shift is an indicator of the internal consistency of the photometry, as well as the accuracy with which the profile corrections were performed, and suggests an accuracy of $\simeq 1 - 2\,\%$.

3.4 Photometric Calibration

3.4.1 Creating INT-WFC System Responses

To derive robust, precise stellar parameters a well constrained and characterised photometric system is required. The $(gri)_{\mathrm{WFC}}$ filter responses were designed to match the SDSS responses, and the RGO $(UZ)_{\mathrm{WFC}}$ were deemed sufficiently similar, to allow absolute photometric calibration into the standard SDSS system via the use of colour equations. Whilst the SDSS survey system and filter responses are well constrained and available on the SDSS webpages[7] (Doi et al. 2010), the responses on the ING webpages are only a combination of the filter throughput and the CCD detector quantum efficiency.

To model the system responses of the INT-WFC the cumulative effects of the transmission of the Earth's atmosphere, the reflectivity of the telescope mirror, the transmission of the prime focus corrector optics, the quantum efficiency of the detector, and the filter transmission were all included. The atmospheric transmission was calculated using the model for the La Palma atmosphere, derived by King (1985) that covers the wavelength region $3000 - 11\,000$ Å, for an airmass typical for the observations of 1.4. The wavelength dependence of the atmospheric extinction at the Observatorio del Roque de los Muchachos on La Palma is shown in Fig. 3.3. The three main components of extinction in the Earth's atmosphere that affect ground-based photometric observations are Rayleigh scattering by air molecules, molecular absorption and aerosol scattering. The model of King (1985) has a smooth variation with wavelength and does not include the molecular absorption features. These atmospheric absorption bands – primarily due to water vapour, carbon dioxide and ozone – were estimated using the spectrum of an F8 star observed using the Faint Object Spectrograph on the *William Herschel* Telescope. At low resolution the continuum of an F8 star is relatively smooth and thus the bands can be identified by fitting a low order

---

[7]`http://www.sdss.org/dr7/instruments/imager/index.html#filters`
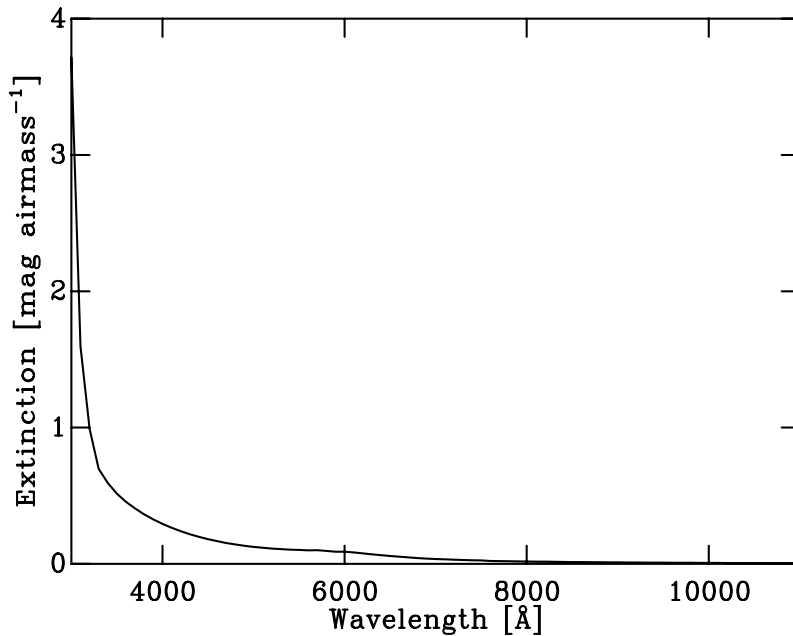
Figure 3.3: The calculated atmospheric extinction at the Observatorio del Roque de los Muchachos on La Palma in the wavelength region $3000 - 11\,000$ Å as calculated by King (1985). The smooth variation as a function of wavelength shows that molecular absorption effects have not been included.
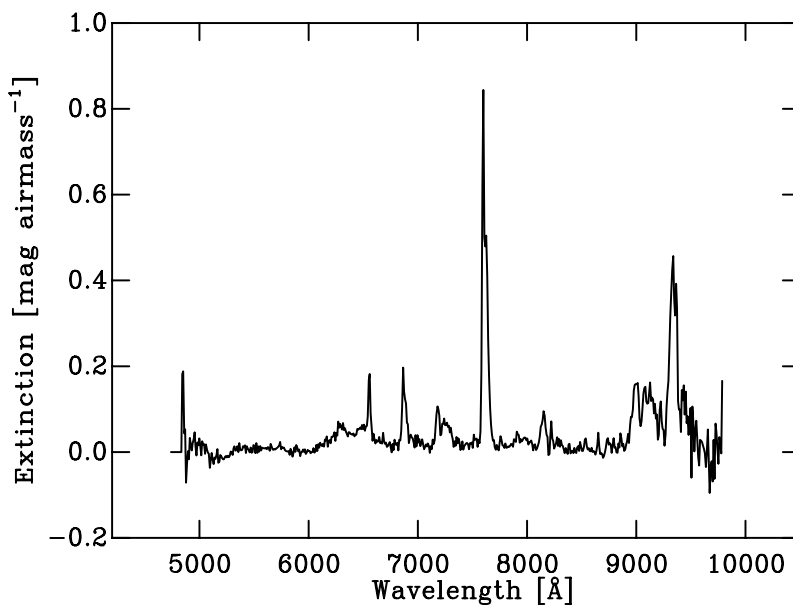
Figure 3.4: The atmospheric absorption bands modelled using an F8 star in the wavelength region $4700 - 9800$ Å by Shahbaz et al. (1996). The continuum has been fitted with a low order polynomial and subtracted from the entire spectrum.
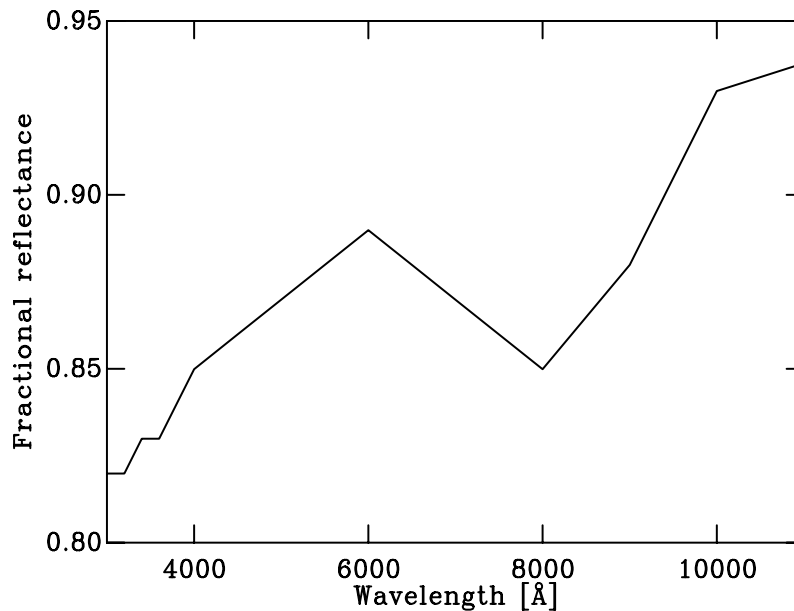
Figure 3.5: The combined reflectance spectrum that includes the single reflection from the aluminium coated primary mirror (Allen 1963) and the additional $2 - 3\,\%$ reflectivity arising from the three-element prime focus corrector in the wavelength region $3000 - 11\,000\,\text{Å}$.

polynomial to the continuum and subtracting this from the entire spectrum (Shahbaz et al. 1996). The continuum is modelled between $4700 - 9800\,\text{Å}$ and the absorption bands are shown in Fig. 3.4. At prime focus the INT optical path involves a single reflection from the aluminium coated primary mirror and this was modelled using the aluminium reflectivity spectrum of Allen (1963). A three-element prime focus corrector is used which is coated to minimise reflection and thus improve efficiency and reduce multiple (ghost) images. The first two elements are non-interchangeable and have a broadband single-layer MgF_2 coating. The third element, although interchangeable, typically comprises an additional single-layer of MgF_2 coating. These single-layer coatings produce total reflectivities smaller than $2\,\%$ in the wavelength region $3500 - 7400\,\text{Å}$. At longer wavelengths, the reflectivity from the prime focus corrector increases to $\simeq 3\,\%$ at $8000\,\text{Å}$. The combined reflectivity spectrum of the aluminium coated primary mirror and three-element prime focus corrector is shown in Fig. 3.5. The filter and detector responses were taken from the ING webpages[8]. The detector is comprised of four EEV 42-80 CCDs. The detector response on the ING webpages only extends to $3400\,\text{Å}$ in the blue, however the blue edge of the RGO U_{WFC} filter is at approximately $3000\,\text{Å}$ and so the detector response was extended blueward using data for an almost identical EEV 44-82 CCD to a wavelength of $3200\,\text{Å}$ (Cavadore & Dorn 2000) and further extrapolated to $3000\,\text{Å}$. The RGO Z_{WFC} filter response data becomes very noisy at wavelengths greater than $9000\,\text{Å}$ and so this response was extended redward using calculated 4-mm Schott RG850 data to $\simeq 10\,300\,\text{Å}$ where the detector response approaches zero. Any negative values for the filter responses

---

[8]`http://www.ing.iac.es/Astronomy/instruments/wfc/`
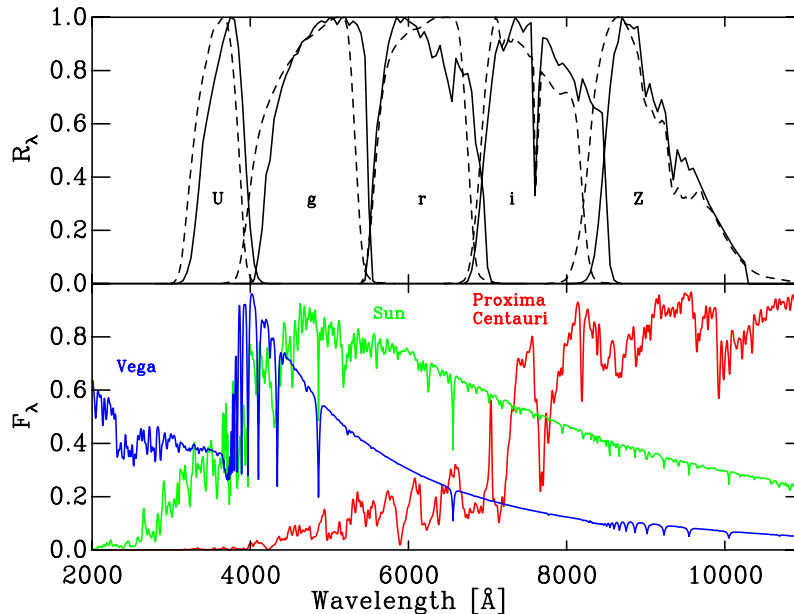
Figure 3.6: Upper panel: The normalised SDSS *ugriz* (dashed) and INT-WFC $(UgriZ)_{\mathrm{WFC}}$ (bold) system responses. The INT-WFC system responses are those calculated in Section 3.4.1 and include the effects of the telescope optics and atmospheric absorption. **Bottom panel:** Normalised model spectra of Vega (A0V), the Sun (G2V) and Proxima Centauri (M6V).

from the ING webpages were removed. Note also that the U_{WFC} filter used here does not include the recently discovered red leak near $7050\,\text{Å}$ (Verbeek et al. 2012). The calculated individual bandpass INT-WFC system responses are given in Table 3.1

3.4.2 Comparing the SDSS and the INT-WFC System Responses

Fig. 3.6 shows the normalised system responses for both the SDSS *ugriz* and the INT-WFC $(UgriZ)_{\mathrm{WFC}}$ filter sets. As stated in Section 3.2 there are no equivalents to the SDSS *u* and *z* filters as the RGO U_{WFC} and Z_{WFC} filters were deemed sufficiently similar to not warrant additional expenditure. Fig. 3.6 shows striking differences between the INT-WFC and SDSS system responses across all filters. The fact that the U_{WFC} and Z_{WFC} filters are not a particularly close match is unsurprising. What is revealing, however, is the mismatch of the g_{WFC}, r_{WFC} and i_{WFC} filters which have been specifically designed to match the SDSS survey filters. Unfortunately, the *ugriz* filters used on the SDSS survey telescope were housed in a vacuum during operation and as a result the layers in the interference coatings shrank slightly, altering the refractive index of the films and shifting the red edge of the *g*, *r* and *i* filters blueward by $\simeq 120\,\text{Å}$, $160\,\text{Å}$ and $175\,\text{Å}$ respectively (Doi et al. 2010). The INT-WFC system responses are, in general, redder than their SDSS counterparts.

Table 3.1: Normalised calculated INT-WFC system responses as shown in Fig. 3.6.

λ	U_{WFC}	λ	g_{WFC}	λ	r_{WFC}	λ	i_{WFC}	λ	Z_{WFC}
3050	0.000	4000	0.000	5400	0.000	6700	0.000	8050	0.000
3100	0.002	4050	0.015	5450	0.013	6750	0.010	8100	0.001
3150	0.011	4100	0.099	5500	0.142	6800	0.050	8150	0.002
3200	0.042	4150	0.203	5550	0.384	6850	0.142	8200	0.005
3250	0.097	4200	0.409	5600	0.586	6900	0.285	8250	0.015
3300	0.216	4250	0.463	5650	0.684	6950	0.462	8300	0.041
3350	0.356	4300	0.618	5700	0.812	7000	0.605	8350	0.104
3400	0.528	4350	0.676	5750	0.904	7050	0.745	8400	0.223
3450	0.614	4400	0.736	5800	0.957	7100	0.863	8450	0.391
3500	0.694	4450	0.781	5850	1.000	7150	0.915	8500	0.570
3550	0.767	4500	0.813	5900	0.980	7200	0.873	8550	0.736
3600	0.832	4550	0.855	5950	0.998	7250	0.906	8600	0.861
3650	0.902	4600	0.864	6000	0.986	7300	0.956	8650	0.906
3700	0.954	4650	0.905	6050	0.976	7350	1.000	8700	1.000
3750	1.000	4700	0.918	6100	0.966	7400	0.978	8750	0.974
3800	0.992	4750	0.930	6150	0.923	7450	0.945	8800	0.971
3850	0.885	4800	0.959	6200	0.946	7500	0.968	8850	0.956
3900	0.684	4850	0.976	6250	0.909	7550	0.980	8900	0.966
3950	0.425	4900	0.986	6300	0.848	7600	0.331	8950	0.829
4000	0.206	4950	0.979	6350	0.856	7650	0.736	9000	0.702
4050	0.074	5000	0.996	6400	0.894	7700	0.923	9050	0.751
4100	0.021	5050	0.998	6450	0.817	7750	0.919	9100	0.687
4150	0.005	5100	0.972	6500	0.758	7800	0.889	9150	0.645
4200	0.001	5150	0.997	6550	0.684	7850	0.848	9200	0.691
4250	0.000	5200	1.000	6600	0.845	7900	0.819	9250	0.640
		5250	0.970	6650	0.809	7950	0.828	9300	0.493
		5300	0.985	6700	0.784	8000	0.809	9350	0.390
		5350	0.972	6750	0.789	8050	0.789	9400	0.502
		5400	0.939	6800	0.721	8100	0.759	9450	0.458
		5450	0.851	6850	0.526	8150	0.686	9500	0.473
		5500	0.285	6900	0.455	8200	0.769	9550	0.426
		5550	0.011	6950	0.329	8250	0.731	9600	0.433
		5600	0.000	7000	0.061	8300	0.686	9650	0.400
				7050	0.008	8350	0.660	9700	0.366
				7100	0.003	8400	0.652	9750	0.333
				7150	0.001	8450	0.641	9800	0.299
				7200	0.000	8500	0.341	9850	0.272
						8550	0.068	9900	0.245
						8600	0.013	9950	0.219
						8650	0.003	10 000	0.192
						8700	0.000	10 050	0.167
								10 100	0.141
								10 150	0.119
								10 200	0.097
								10 250	0.080
								10 300	0.000

3.4.3 Transforming the Data into the Standard SDSS System

To investigate what effect variations in the system responses would have on the absolute photometric calibration of the data, the magnitude and colour difference between the two photometric systems was calculated as a function of colour using system responses and atmospheric models. The fact that atmospheric models were used does not matter as it is the relative differences that are important.

3.4.3.1 Calculating the Theoretical Transformations

The SDSS photometric system – as well as the corresponding natural INT-WFC photometric system – have been defined using CCD detectors and hence the flux is calculated in a slightly different fashion than the method in the Johnson UBV photoelectric photometric system. Switching from essentially an energy integrating system to one which is based on photon counting requires an additional factor of λ to be included in the definition of the apparent magnitude, hence

$$m_{R_\lambda} = -2.5 \log \left(\frac{\int_\lambda \lambda f_\lambda R_\lambda d\lambda}{\int_\lambda \lambda f^{\mathrm{o}}_\lambda R_\lambda d\lambda} \right) + m^{\mathrm{o}}_{R_\lambda}, \tag{3.1}$$

where the symbols retain the same meanings as in Section 2.5.1. This therefore transforms Eqn. 2.14 into

$$BC_{R_\lambda} = M_{\mathrm{bol},\odot} - 2.5 \log \left(\frac{4\pi(10\,\mathrm{pc}^2)F_{\mathrm{bol}}}{L_\odot} \right) + 2.5 \log \left(\frac{\int_\lambda \lambda F_\lambda 10^{-0.4A_\lambda} R_\lambda \, d\lambda}{\int_\lambda \lambda f^{\mathrm{o}}_\lambda R_\lambda \, d\lambda} \right) - m^{\mathrm{o}}_{R_\lambda}. \tag{3.2}$$

The SDSS photometric system differs from that of the Johnson UBV system in that it is a monochromatic AB (absolute) magnitude system, not a Vega system. In such photometric systems, the fluxes are on an absolute flux scale with the colours directly related to flux ratios, hence magnitudes can be easily converted to physical fluxes. In addition, unlike the Johnson UBV photometric system – which adopts α Lyr as the primary standard star – where the zero-point is defined by the spectral energy distribution of Vega, in the AB photometric system equal flux densities imply equal magnitudes. The AB system is based upon the absolute flux of the continuum of α Lyr. The monochromatic magnitude system was defined by Oke (1965) and Oke & Gunn (1983), with a full description pertaining to its use for the SDSS given by Fukugita et al. (1996), where

$$m_{AB,\nu} = -2.5 \log f_\nu - 48.60. \tag{3.3}$$

This definition thereby specifies that a reference spectrum of constant flux density per unit frequency of

$$f^{\mathrm{o}}_{AB,\nu} = 3.631 \times 10^{-20}\,\mathrm{erg\,s^{-1}\,cm^{-2}\,Hz^{-1}} \tag{3.4}$$
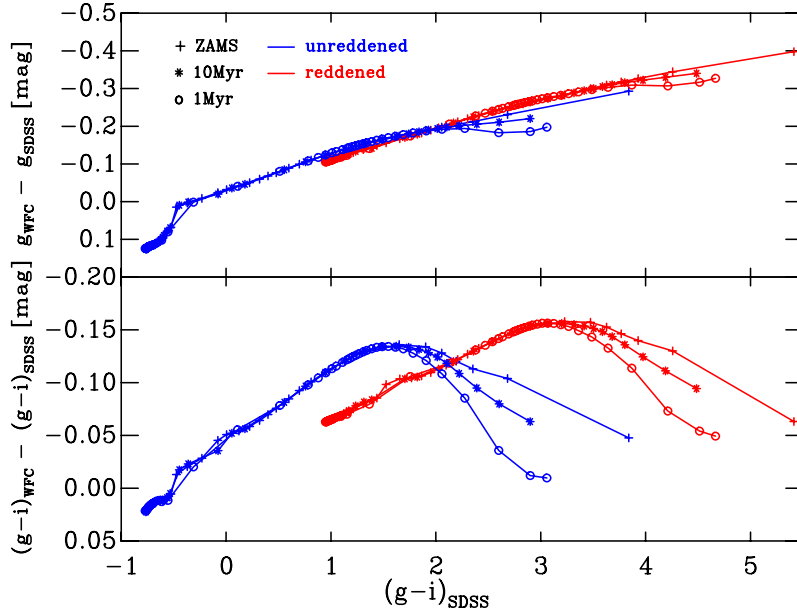
Figure 3.7: The calculated theoretical transformations between the SDSS and INT-WFC photometric systems. The transformations have been calculated for reddened (nominal $E(B-V) = 1\,\text{mag}$; red) and unreddened (blue) ZAMS (crosses), $10\,\text{Myr}$ (stars) and $1\,\text{Myr}$ pre-MS stars (circles). **Upper panel:** Δg versus $(g-i)_{\text{SDSS}}$. **Lower panel:** $\Delta(g-i)$ versus $(g-i)_{\text{SDSS}}$. No single – even non-linear – transformation will calibrate INT-WFC observations of both red $((g-i)_{\text{SDSS}} \gtrsim 1.8)$ MS and pre-MS stars into the SDSS standard system, and if either are reddened the situation becomes worse ($\simeq 0.15\,\text{mag}$) at a colour $(g-i)_{\text{SDSS}} \simeq 3$.

will yield reference AB magnitudes $m^{\text{o}}_{AB,\nu} = 0$ at all frequencies ν and hence define the zero-points of the photometric system. Converting this reference spectrum from per unit frequency to per unit wavelength, according to $f_\lambda = c/\lambda^2 f_\nu$, defines the reference f^{o}_λ and $m^{\text{o}}_{R_\lambda}$ for the photometric system. Hence, the magnitude differences between the standard SDSS and natural INT-WFC photometric systems are then simply calculated as the differences in the bolometric corrections.

The calculation of bolometric corrections that span a significant mass range in both the MS and pre-MS regimes were required. To model the changing T_{eff} and $\log g$ values along the MS – from $\log g \simeq 4$ for early B-type stars to $\simeq 5.5$ for late M-type – the calculated ZAMS of Siess et al. (2000) for stellar masses in the range $0.1 - 7\,\text{M}_\odot$ was used. For the pre-MS values, 1 and $10\,\text{Myr}$ Siess et al. (2000) interior models were adopted, with the corresponding T_{eff} and $\log g$ calculated over the same mass range. The reason for choosing the Siess et al. (2000) interior models over other pre-MS stellar interior models was simply because they span a greater range of stellar masses and so more thoroughly map the ZAMS. Bolometric corrections were calculated according to Eqn. 3.2 for each atmospheric model in the spectral library for both the SDSS and INT-WFC photometric systems, with the bolometric correction for a given T_{eff}, $\log g$ combination derived by linearly interpolating within the grid. Due to the degree of model dependency in the pre-MS evolutionary models, this process was repeated using the ZAMS T_{eff}, $\log g$ values of the

D'Antona & Mazzitelli (1997), Dotter et al. (2008) and Baraffe et al. (1998) evolutionary models (see Section 4.2 for a discussion on the various pre-MS evolutionary models). It was found that all four sets of evolutionary models agree to within 0.02 mag over the range of stellar masses in common. A tabulated version of the theoretical transformations between the SDSS and INT-WFC photometric systems for unreddened MS stars is shown in Table 3.2.

Fig. 3.7 shows the calculated theoretical transformations between the standard SDSS and natural INT-WFC photometric systems for both reddened and unreddened objects in the g-band magnitude and $g - i$ colour (for illustrative purposes a nominal reddening of $E(B - V) = 1$ is adopted; see Section 2.7.1). The simple formalism adopted in the derivation of the bolometric corrections allows the inclusion of the effects of interstellar reddening by applying a given extinction curve A_λ and calculating the bolometric correction as before. As in Section 2.7.1, the Cardelli et al. (1989) extinction curve (with $R_V = 3.2$) was used and thus the extinction derived in a given filter at a specific $E(B-V)$.

3.4.4 Traditional Photometric Calibration

Traditional photometric calibration relies on the comparison of instrumental magnitudes and colours to standard star observations to calculate zero-points, colour terms and extinction coefficients. These are then used to transform instrumental colours and magnitudes into a standard system. Typically, colours and magnitudes are transformed using linear functions of the form

$$g_{\text{stand}} = \psi_g(g - i)_{\text{inst}} - k_g\chi + z_g, \tag{3.5}$$

$$(g - i)_{\text{stand}} = \psi_{gi}(g - i)_{\text{inst}} - k_{gi}\chi + z_{gi}, \tag{3.6}$$

where χ is the airmass, k the extinction coefficients, z the zero-points and ψ the colour terms. Fig. 3.7 shows that there is no linear colour-dependent transformation that can be applied to INT-WFC observations of MS stars to calibrate them into the standard SDSS system. Even if non-linear MS transformations were created, it is clear that they could not be used to transform observations of red $((g - i)_{\text{SDSS}} \gtrsim 1.8)$ pre-MS stars into the standard system. This is due to differences in the spectra between MS and pre-MS stars of the same colour. These differences can result in both g-band magnitude and $g - i$ colour errors of order $0.1 - 0.15$ mag at a colour of $(g-i)_{\text{SDSS}} \simeq 3$, culminating in stars that ultimately occupy the wrong position in CMD space. Even larger errors can be caused by the difference between the spectrum of a reddened and an unreddened star of the same apparent colour (see Fig. 3.7). From the calculated ZAMS of Siess et al. (2000) the differential behaviour between MS and pre-MS transformations occurs at an approximate spectral type of between K6 and M0. Mayne et al. (2012) document a similar, though more extreme, situation which can result from using MS transformations for brown-dwarfs.

Table 3.2: The calculated theoretical transformations between the SDSS and INT-WFC photometric systems for unreddened MS stars where Δ represents (INT-WFC – SDSS).

$T_{\rm eff}$	$\log g$	Δg	$\Delta(g-i)$	$(g-i)_{\rm SDSS}$	$\Delta(u-g)$	$(u-g)_{\rm SDSS}$	$\Delta(r-i)$	$(r-i)_{\rm SDSS}$	$\Delta(i-z)$	$(i-z)_{\rm SDSS}$
2775	5.25	-0.29300	-0.04765	3.83961	0.01264	4.12961	0.24688	2.20001	-0.17476	1.22123
3290	5.11	-0.23094	-0.10391	2.68386	-0.02563	3.06419	0.12898	1.20809	-0.08704	0.66867
3528	4.98	-0.21237	-0.11299	2.35355	-0.03358	2.87477	0.09765	0.94887	-0.06707	0.53108
3683	4.92	-0.20428	-0.12031	2.19344	-0.03595	2.83717	0.07940	0.81597	-0.05550	0.45615
3829	4.87	-0.19761	-0.12806	2.05653	-0.03751	2.81937	0.06188	0.70141	-0.04429	0.38859
4008	4.78	-0.18928	-0.13399	1.90296	-0.03767	2.81750	0.04505	0.59085	-0.03316	0.32104
4287	4.68	-0.17430	-0.13597	1.65094	-0.02862	2.82826	0.02791	0.44596	-0.02053	0.23563
4698	4.59	-0.14746	-0.12680	1.24473	-0.00604	2.45699	0.01238	0.28043	-0.00887	0.14126
5047	4.52	-0.12587	-0.11204	0.97804	-0.00908	2.05090	0.00717	0.20880	-0.00634	0.09240
5334	4.44	-0.11048	-0.10074	0.81007	-0.01710	1.75568	0.00425	0.16560	-0.00529	0.05959
5556	4.35	-0.09946	-0.09249	0.69894	-0.02521	1.55150	0.00223	0.13722	-0.00460	0.03705
5788	4.27	-0.08902	-0.08465	0.59843	-0.03472	1.38466	0.00025	0.11092	-0.00386	0.01616
6070	4.21	-0.07656	-0.07570	0.47826	-0.04808	1.23654	-0.00269	0.07739	-0.00240	-0.01014
6284	4.15	-0.06810	-0.06976	0.39951	-0.06107	1.16036	-0.00486	0.05526	-0.00096	-0.02758
6498	4.08	-0.05968	-0.06414	0.31938	-0.07818	1.11366	-0.00733	0.03177	0.00108	-0.04532
6770	4.05	-0.05028	-0.05847	0.22468	-0.10044	1.08671	-0.01072	0.00244	0.00439	-0.06707
7120	4.04	-0.04119	-0.05416	0.12242	-0.12429	1.08866	-0.01519	-0.03181	0.00924	-0.09401
7476	4.04	-0.03194	-0.05080	0.00499	-0.15324	1.10998	-0.02076	-0.07319	0.01692	-0.12048
7832	4.03	-0.02435	-0.04798	-0.08863	-0.17347	1.11265	-0.02513	-0.10607	0.02365	-0.14096
8176	4.03	-0.01574	-0.04374	-0.19055	-0.19397	1.11417	-0.02907	-0.13938	0.03044	-0.15738
8824	4.02	0.00243	-0.03017	-0.37163	-0.22788	1.09105	-0.03272	-0.18972	0.03784	-0.17247
9705	4.04	0.01426	-0.02207	-0.48111	-0.23184	0.97483	-0.03550	-0.22639	0.04170	-0.19329
10 241	4.03	0.07044	0.00649	-0.52839	-0.21889	0.86236	-0.01917	-0.24223	0.02921	-0.17928
11 048	4.05	0.08221	0.01134	-0.56676	-0.19041	0.72778	-0.01944	-0.25639	0.02926	-0.19479
12 094	4.05	0.09614	0.01242	-0.60066	-0.14514	0.56569	-0.02126	-0.26896	0.02926	-0.21427
13 208	4.02	0.10585	0.01252	-0.62888	-0.10819	0.42636	-0.02331	-0.27913	0.02835	-0.23180
15 334	4.04	0.11432	0.01408	-0.67680	-0.06756	0.23922	-0.02593	-0.29640	0.02503	-0.25785
17 291	4.03	0.11963	0.01734	-0.71721	-0.04919	0.11592	-0.02715	-0.31097	0.02282	-0.27587
19 281	4.01	0.12594	0.02192	-0.75454	-0.03813	0.01591	-0.02725	-0.32467	0.02152	-0.29124

In principle, a polynomial colour-dependent offset would allow the calibration of instrumental magnitudes and colours over the observed colour range, however this would only accurately calibrate MS star observations. A further disadvantage of using a polynomial fit is that there is no guarantee that it represents equally well the relation outside of the specified colour range and thus extrapolation may result in calculated offsets that deviate widely from those that should be applied. This is especially important in the study of highly extincted SFRs as the standard star observations are unlikely to cover the full colour range specified by the reddened pre-MS stars (see for instance Da Rio et al. 2009).

A deviation of up to 0.15 mag may help explain, to some extent, why pre-MS isochrones do not simultaneously fit both the higher and lower mass members within a given cluster (Hartmann 2003; Stauffer et al. 2007; Jeffries et al. 2009; see also Section 4.1), although other factors such as photometric variability, variable extinction, unresolved binaries, accretion luminosity, and poorly constrained opacity line lists in the atmospheric models may also contribute (Hartmann 2001; Burningham et al. 2005b). Furthermore, this could also have severe implications for SFR age and mass function determinations. Allowing the pre-MS stars in a CMD to 'float' by 0.15 mag in both colour and magnitude can result in an age difference of a factor of two through isochrone fitting. The conversion from observable magnitudes and colours into mass estimates are highly age- and model-dependent. Hence an incorrect age would result in an erroneous mass function estimate, thus making meaningful comparison between SFR mass functions difficult at best.

3.4.5 Calibrating the Natural INT-WFC System

For the reasons explained in Section 3.4.4, the following work was carried out in the natural INT-WFC photometric system. This not only allowed the calibration of the photometry over the entire colour range, which is vital for redder colours, but also allowed rigorous testing of the INT-WFC system responses. Two surveys, namely the INT-WFC Photometric Hα Survey (IPHAS; Drew et al. 2005) and the UV-Excess Survey (UVEX; Groot et al. 2009) use a combination of the $(Ugri)_{\mathrm{WFC}}$ filters to survey the entire northern Galactic plane in the latitude range $-5^{\mathrm{o}} < b < +5^{\mathrm{o}}$, equating to a sky area of approximately 1800 square degrees. Calibration of the photometry is through observations of Landolt/SDSS standard fields (Drew et al. 2005). It was shown in Section 3.4.4 that INT-WFC observations can be transformed into the standard SDSS photometric, however this is only reliable for MS stars and on the condition that a non-linear polynomial colour-dependent offset is adopted. Errors in the absolute calibration of pre-MS stars in the IPHAS and UVEX surveys can be as large as 0.1 mag based on the comparison with SDSS standard fields. The addition of supplementary Landolt (1992) standards transformed into the SDSS photometric system, may further introduce unwanted errors into the calibration process. Several attempts to calculate transformation equations between the Johnson-Cousins $UBV(RI)_{\mathrm{c}}$ and SDSS $ugriz$ have shown that these transformations may only be accurate to within $\simeq 0.05$ mag, especially in the cool, low-mass regime (see for instance West et al. 2005; Jordi et al. 2006; Rodgers et al. 2006). Hence, whilst the

calibration of MS stars in both surveys may be robust, the uncertainties associated with the pre-MS photometric calibration may, in the worst case scenario, be $\simeq 0.15$ mag.

The complimentary surveys of the southern Galactic plane (VPHAS+) will use the 2.6-m VLT Survey Telescope (VST) on Paranal in conjunction with the OmegaCAM/*ugri* filters. VPHAS+ will also use a combination of Landolt/SDSS standard fields to perform photometric calibration. Given that the SDSS filters have become, in effect, the standard filter set for many of the upcoming large photometric surveys – including the SDSS analogous survey in the southern hemisphere SkyMapper – an unprecedented archive of photometric data will be available. These data can form the basis of a comprehensive Galactic map of star formation, however before theoretical models are used to constrain ages and distances, it is paramount that any differences between the 'local' SDSS and the standard SDSS photometric system be investigated and quantified.

3.4.6 Testing the Calculated INT-WFC System Responses

If the observations cannot be accurately transformed into a standard photometric system, then the photometry must remain in the natural photometric system of the observations and the theoretical models transformed into this system. To achieve this a reliable model for the throughput of each bandpass as a function of wavelength is required. It is stressed that this is not simply a matter of using the filter responses, or even multiplying the CCD quantum efficiency by the filter response, but involves allowing for every element from the Earth's atmosphere through to the CCD detector to create a *system* response. The best estimate for the INT-WFC system responses are presented in Section 3.4.1.

Having defined the system responses it is crucial to estimate how precise these are. In principle this can be achieved by folding the observed fluxes of spectrophotometric standards through the estimated system responses and seeing how closely the observed and predicted magnitude match. In practice such standards have not been measured in sufficient numbers with the range of colours and magnitudes to prove useful for such purposes. Instead, a sample of MS stars were taken and their observed SDSS colours used to establish their $T_{\rm eff}$. Model atmospheres of the appropriate $T_{\rm eff}$ were then folded through the estimated system responses to find their magnitudes in the INT-WFC system.

To calibrate the INT-WFC photometric data a catalogue of standard stars in the INT-WFC photometric system is needed. It is not feasible to transform the entire Stripe 82 subset, as defined by the four standard fields, due to the different stellar populations included, and so through a series of colour-colour diagrams the MS stars were isolated by trimming stars that obviously do not follow the observed sequence (see Figs. 3.8 – 3.10). The SDSS colours and magnitudes were then transformed into the INT-WFC photometric system using the transformations derived in Section 3.4.3.1. This transformed standard star INT-WFC catalogue is hereafter referred to as WFC$_{\rm calc}$.

With the INT-WFC standards established, it is possible to evaluate how well constrained the INT-WFC system responses are. A set of observed standard star magnitudes in the INT-WFC system were created by calculating zero-points in the colour ranges spec-
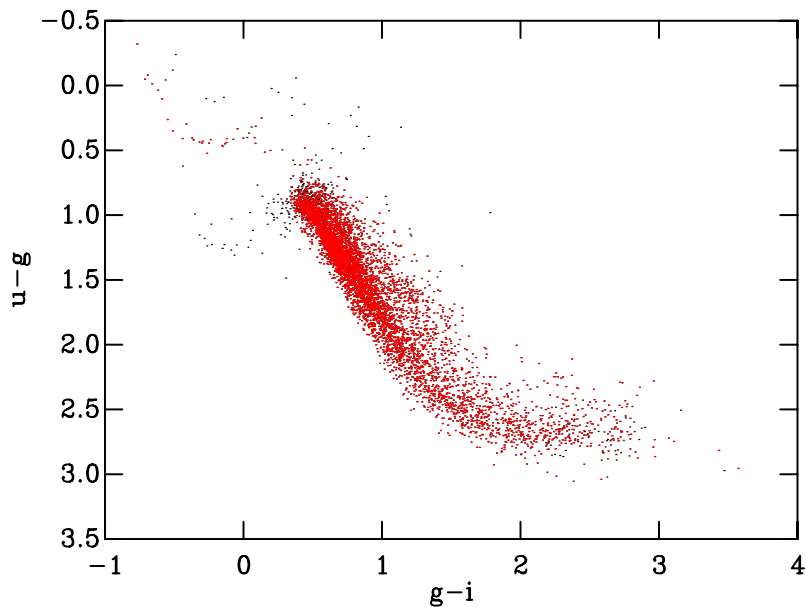
Figure 3.8: SDSS Stripe 82 $u - g, g - i$ colour-colour diagram containing stars within the four standard fields discussed in Section 3.2. The black dots show the full catalogue, whereas the red dots indicate the MS stars used to define the INT-WFC standard star catalogue.
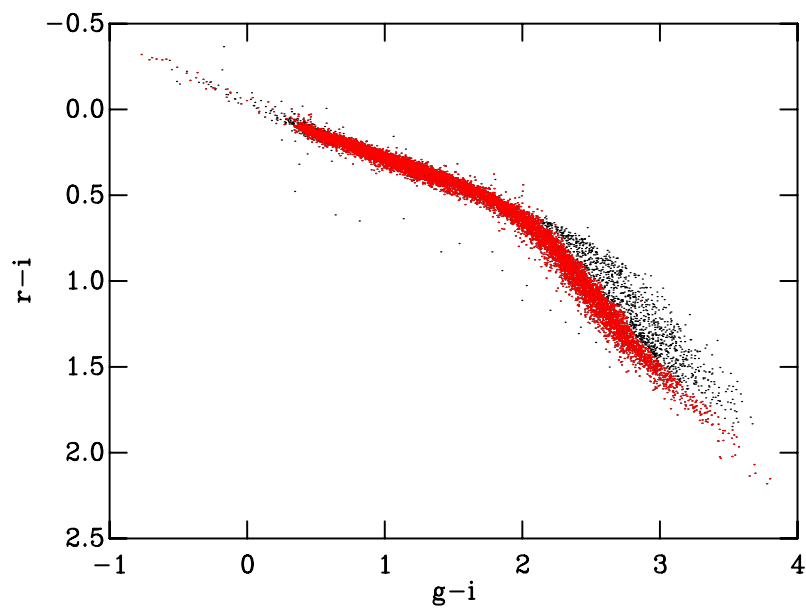
Figure 3.9: Same as Fig. 3.8 but showing the $r - i, g - i$ colour-colour diagram.
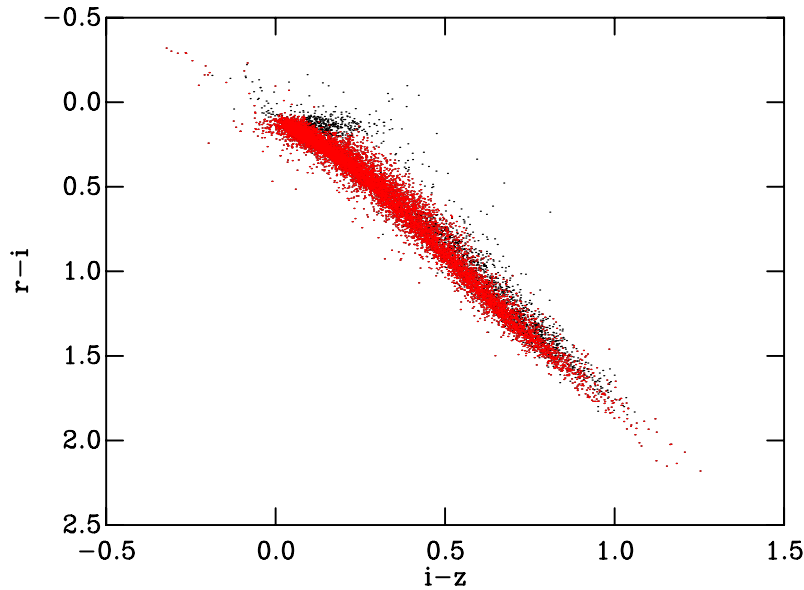
Figure 3.10: Same as Fig. 3.8 but showing the $r - i, i - z$ colour-colour diagram.

ified in Section 3.2.1 and applying these zero-points and extinction coefficients only – no colour terms – to all standard field observations. To create a single catalogue for each of the four standard fields the normalisation process described in Section 3.3 was performed. A catalogue of observed magnitudes of Stripe 82 standards in the INT-WFC photometric system was created by further merging all four fields into a single larger catalogue, hereafter referred to as $\mathrm{WFC_{obs}}$. After the normalisation procedure, each star was examined to calculate the magnitude shift between each observation and the mean observed magnitude. This is an indicator of the internal precision of the photometry and it was found that $g_{\mathrm{rms}} = 0.011\,\mathrm{mag}$, $(g - i)_{\mathrm{rms}} = 0.014\,\mathrm{mag}$, $(U - g)_{\mathrm{rms}} = 0.020\,\mathrm{mag}$, $(r - i)_{\mathrm{rms}} = 0.011\,\mathrm{mag}$ and $(i - Z)_{\mathrm{rms}} = 0.010\,\mathrm{mag}$. The slightly poorer precision in the U_{WFC}-band photometry is attributed to a lack of colour-dependent atmospheric extinction terms. The atmosphere is more transparent at redder wavelengths and thus the extinction coefficients depend on the colour and hence flux distribution of a given star. Not accounting for this dependence can affect the resultant magnitudes and colours at the few $0.01\,\mathrm{mag}$ level (Straižys 1977; Cousins & Caldwell 2001).

The differences $\mathrm{WFC_{calc}} - \mathrm{WFC_{obs}}$ are shown in Figs. 3.11 – 3.15. Using bin sizes of $0.25\,\mathrm{mag}$ in colour, and only data with uncertainties of less than $0.03\,\mathrm{mag}$, the median value in each colour bin was calculated as an indicator of the level of agreement between the $\mathrm{WFC_{calc}}$ and $\mathrm{WFC_{obs}}$ catalogues in a given colour range. Due to a paucity of data at extreme colours the restrictions on the uncertainty in the data were relaxed to less than $0.1\,\mathrm{mag}$, and where the number of stars was insufficient to calculate the median value in a given colour bin (taken as five) the individual data points were plotted. These plots show that the zero-points are reproduced to within $0.01\,\mathrm{mag}$ at the colours which were defined to calculate the zero-points in Section 3.2.1. The remaining residuals lie within the $\pm 0.02\,\mathrm{mag}$ level across the entire colour range except for a small region in the U_{WFC}-band
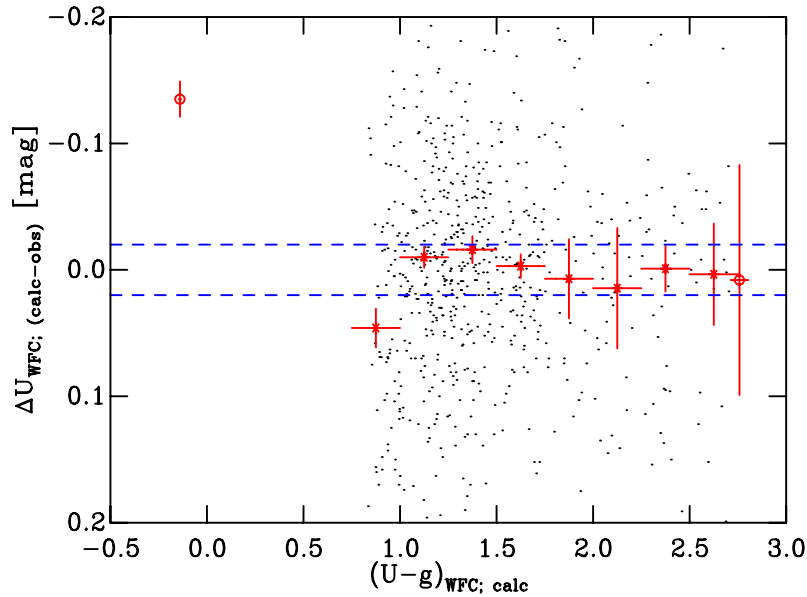
Figure 3.11: The magnitude difference in the U_{WFC}-band between the WFC$_{\mathrm{calc}}$ and WFC$_{\mathrm{obs}}$ photometric catalogues as a function of $(U - g)_{\mathrm{WFC;calc}}$. Asterisks represent the median value of all points in a given bin of size $0.25\,\mathrm{mag}$ in colour. The error bars on these symbols are the standard error about the median value. Open circles represent individual data points and are plotted where the number of points is insufficient to calculate the median value in a given bin (defined as five). The error bars on these symbols are the individual uncertainties associated with that point. The dashed lines represent the $\pm 0.02\,\mathrm{mag}$ level with respect to zero.
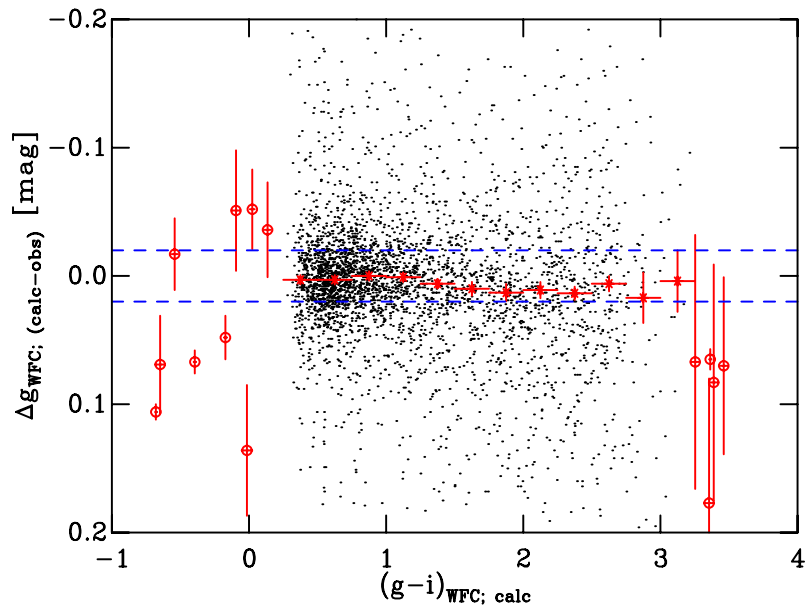
Figure 3.12: Same as Fig. 3.11 but for the difference in the g_{WFC}-band as a function of $(g - i)_{\mathrm{WFC;calc}}$.
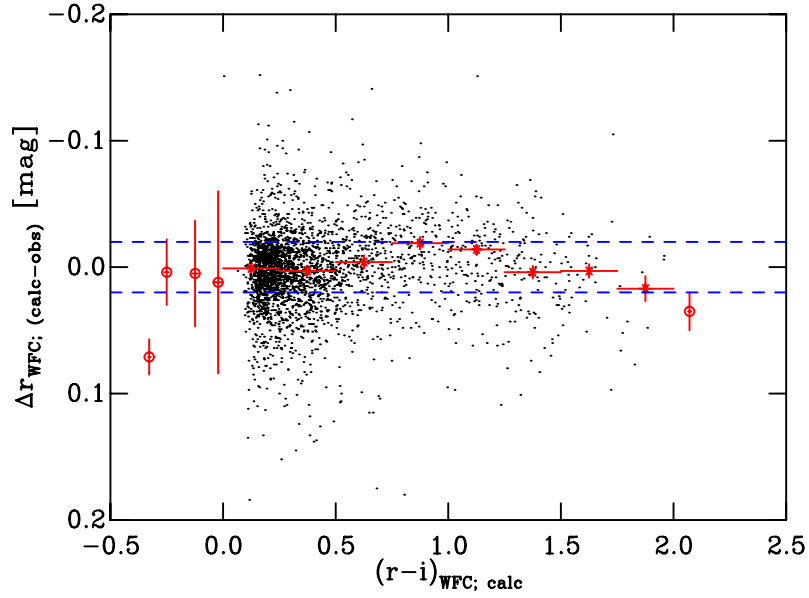
Figure 3.13: Same as Fig. 3.11 but for the difference in the r_{WFC}-band as a function of $(r-i)_{\mathrm{WFC;calc}}$.
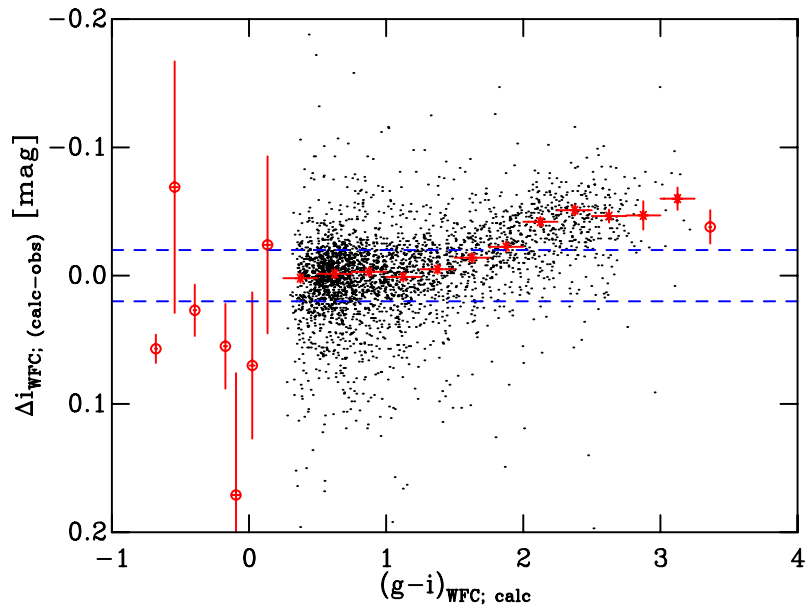
Figure 3.14: Same as Fig. 3.11 but for the difference in the i_{WFC}-band as a function of $(g-i)_{\mathrm{WFC;calc}}$.
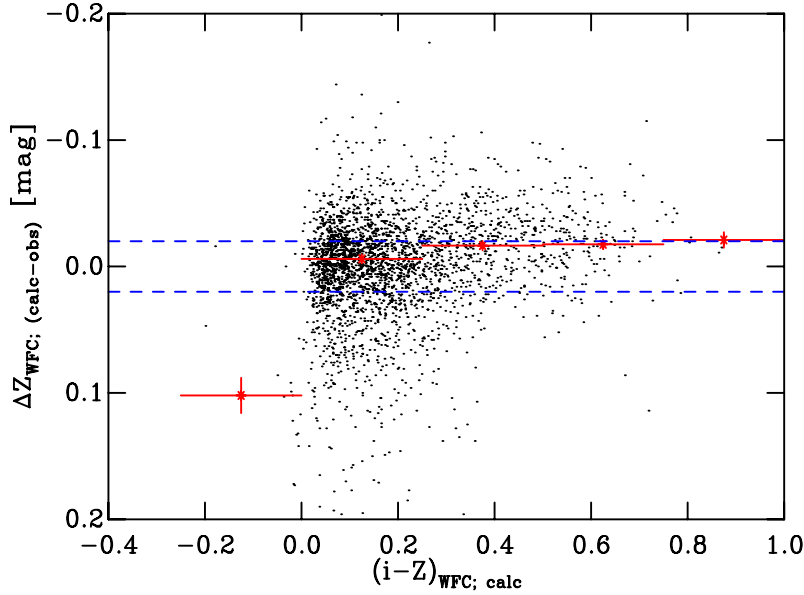
Figure 3.15: Same as Fig. 3.11 but for the difference in the Z_{WFC}-band as a function of $(i - Z)_{\mathrm{WFC;calc}}$.

and colours redder than $(g - i)_{\mathrm{WFC}} \simeq 2$ in the i_{WFC}-band.

The most obvious causes of any disagreement between $\mathrm{WFC_{calc}}$ and $\mathrm{WFC_{obs}}$ are that; i) the estimated system responses are incorrect and/or ii) the atmospheric models are incorrect. In an attempt to obtain some idea of the likely magnitude of the latter effect the transformations were recalculated using different atmospheric models – the PHOENIX/GAIA models of Brott & Hauschildt (2005) – and the observed spectral library of Pickles (1998). These changed the transformations by up to 0.02 mag, nicely explaining the majority of the residuals. It remains unclear whether the remaining residuals are due to errors in the atmospheric fluxes, or poorly modelled U_{WFC}- and i_{WFC}-band system responses. As a result, the system responses in their current calculated form are retained for the remainder of this thesis, and it is noted that uncertainties exist at the levels shown in Figs. 3.11 – 3.15.

3.4.7 Photometric Calibration Using the Transformations

To produce observations in the natural INT-WFC photometric system, the most straightforward procedure would be to observe the same standard star fields as those observed in this thesis. In doing so, one can then simply make use of the published INT-WFC magnitudes and colours for these stars. A traditional photometric calibration can be performed, with the colour terms set to zero, solving for the extinction coefficients and zero-points. If, however, these fields are unobservable, then it is advised that other SDSS fields are observed, although it is strongly recommended that Stripe 82 fields be used due to the robustness of the photometric calibration (Ivezić et al. 2007). MS stars can be selected and isolated in a series of colour-colour diagrams. The transformations derived in Section 3.4.3.1 can then be used to transform these MS stars from the SDSS to the INT-WFC

photometric system to be used as a standard star catalogue.

3.5 Summary

In this section the main problems faced when attempting to fit pre-MS populations with evolutionary models in CMDs to derive ages have been introduced, with particular emphasis placed on the process of photometric calibration for very red pre-MS objects. A model of the INT-WFC system responses in the optical $(UgriZ)_{\mathrm{WFC}}$ bandpasses that spans the $0.3 - 1.0\,\mu$m regime has been created, which includes every element of the total throughput from the Earth's atmosphere through to the CCD detector. These system responses have been tested using standard star observations and have been shown to be a good representation of the photometric system. Furthermore, it has been demonstrated that the traditional photometric calibration technique of adopting a simple linear colour-dependent offset – based on observations of standard stars – to transform instrumental INT-WFC colours and magnitudes into the standard SDSS photometric system does not work, even for ZAMS stars. This is due to a combination of subtle variations in the relative system responses and differences in the stellar spectra – $\log g$ and T_{eff} – between a MS and pre-MS star of the same colour. Such differences can result in stars occupying the wrong position in CMDs, and therefore it is crucial to transform the model isochrones into the natural photometric system of the observations to carry out precise photometric studies of pre-MS objects.

Chapter 4

A Benchmark Test for Pre-Main-Sequence Isochrones

4.1 Motivation

Robust and precise ages for young stars are a requirement for the advancement of our understanding of star and planet formation and evolution. These ages provide timescales with which to constrain the physical processes driving, for example, disc dissipation and planet formation (e.g. core accretion versus gravitational collapse; see for instance Pollack 1984 and Boss 1997). Pre-MS ages are based on the gravitational contraction of young stellar objects, which become increasingly faint as they contract towards the ZAMS, however these ages are heavily degenerate with distance (see Mayne et al. 2007; Mayne & Naylor 2008). Our understanding of time-dependent physical processes in young pre-MS and MS populations is fundamentally limited by poorly constrained timescales, the derivation of which requires the determination of ages for pre-MS stellar populations. These ages are generally derived via the comparison of photometric observations of pre-MS stars in young open clusters with theoretical models – or isochrones – using CMDs.

The use of pre-MS isochrones for deriving such fundamental stellar parameters has been ongoing for a couple of decades and has highlighted disparities between the theoretical isochrones and the observational data. It has been noted in numerous studies that the pre-MS isochrone generally does not fit the entire photometric dataset in CMDs e.g. whilst tracing the sequence defined by the higher mass members they will not simultaneously follow the sequence in the lower mass regime (see for instance Hartmann 2003; Stauffer et al. 2007). The initial choice of pre-MS interior model and BC-$T_{\rm eff}$ relation used to transform the isochrone into CMD space can result in differences in the inferred mass of up to a factor of 2 (Hillenbrand & White 2004) as well as age discrepancies of the order of several Myr (Hillenbrand 1997; Stauffer et al. 1997; White et al. 1999; Park et al. 2000; Dahm 2005). For example, Dahm (2005) studied the young SFR NGC 2362 and derived an age of $\simeq 1.8\,{\rm Myr}$ using the isochrones of D'Antona & Mazzitelli (1997) and between 3.5 and 5.0 Myr using the Baraffe et al. (1998) isochrones. Furthermore, the

same dataset compared to isochrones in different colours can also lead to different age determinations (e.g. Naylor et al. 2002). The situation has become even more uncertain with the realisation that ages derived from the MS are systematically older by a factor 1.5 to 2 than ages derived from the pre-MS (e.g. Naylor 2009). It is clear that such discrepancies will have severe implications, for instance, how can we trust or interpret features in mass functions when significantly varying masses are predicted from the various pre-MS formalisms? What effect do these discrepant ages have on the empirical study of circumstellar disc lifetimes? Also, is it possible to establish a robust T_{eff} scale for pre-MS stars and derive accurate luminosities, so as to interpret and understand the spreads observed in CMDs of young SFRs?

It is thus clear that the pre-MS models are in need of rigorous testing. The natural solution would be to utilise eclipsing binaries, allowing direct conversions between mass and colour or luminosity, however the drawback with this approach is that eclipsing binaries – especially in the pre-MS regime – are extremely rare and thus span only a limited range of ages and luminosities, hence they are unable to provide a comprehensive test of the BC-T_{eff} relation (Hillenbrand & White 2004). An alternative method of calibrating the BC-T_{eff} relation over a significant range of ages and masses is to investigate whether an isochrone can model a coeval stellar population in CMD space. The BC-T_{eff} relation is generally calculated using atmospheric models, however these models have come under scrutiny concerning the underlying physics, especially in the low T_{eff} regime ($< 3500\,\text{K}$) where the opacity is dominated by molecular species. Thus, eclipsing binaries and isochrone fitting are complementary, providing mass and T_{eff} calibration respectively and whilst there is currently a large effort underway into the detection and observation of such binary systems (Covino et al. 2000; Stassun et al. 2004b, 2007; Irwin et al. 2007; Cargile et al. 2008; Stempels et al. 2008; Hebb et al. 2010; Morales-Calderón et al. 2012), no similar investigation is being pursued into using isochrone fitting of low-mass pre-MS stellar populations that span a significant range in both mass and age to calibrate the BC-T_{eff} relation.

The photometric dataset presented in Chapter 3 offers a unique opportunity to test pre-MS isochrones over a significant mass and colour range. Section 4.2 introduces the pre-MS interior models that will be tested against the photometric dataset. Furthermore, the physical inputs of these models and differences in the treatment of various inputs are discussed. Section 4.3 describes the benchmark test of the pre-MS isochrones by comparing them to photometric data of the Pleiades over a contiguous wavelength regime of $0.4 - 2.5\,\mu\text{m}$ in CMD space. The masses predicted by the interior models are also compared with dynamical masses from a sample of binaries in Section 4.4. In Section 4.5 the likely reasons for the mismatch between the models and the data in CMD space are discussed, as are the implications for derived pre-MS ages using current pre-MS models after quantifying the observed mismatch. Section 4.6 summarises the benchmark test and its implications for ages derived for younger SFRs from CMDs.

4.2 Pre-Main-Sequence Models

The sets of pre-MS interior models that were tested were chosen on the basis that they; i) were publicly available, ii) covered a wide range in stellar mass, and iii) were designed specifically for the investigation of pre-MS evolution. These stipulations have therefore led to the exclusion of a number of pre-MS models. Neither the Victoria group (Swenson et al. 1994) nor the Palla & Stahler (1999) models have been made publicly available and are therefore neglected from this investigation. The Geneva group (Charbonnel et al. 1999) and Y^2 (Demarque et al. 2004) models are also not used here as the mass range is rather restrictive, extending only as low as $0.4\,M_\odot$ in both cases. The more recent formulations by the Pisa group (Tognelli et al. 2011) have also been excluded on the grounds that these models have a higher age limit of $100\,$Myr and a lower mass limit of $0.2\,M_\odot$, and, as shall be seen in Section 4.3.2, isochrones that extend to at least $130\,$Myr are required. As a result of these specifications the pre-MS interior models tested are those of the Lyon (Baraffe et al. 1998), Grenoble (Siess et al. 2000) and Dartmouth (Dotter et al. 2008) groups, as well the D'Antona & Mazzitelli (1997) models, hereafter termed BCAH98, SDF00, DCJ08 and DAM97 respectively[9].

4.2.1 Input Physics of the Interior Models

This section briefly highlights the underlying physical assumptions concerning the physics and structure of the stellar interior.

4.2.1.1 The BCAH98 Models

A series of models have been published (Baraffe et al. 1995; Chabrier & Baraffe 1997; Baraffe et al. 1998) spanning the low- to very-low-mass stellar range of $0.04-1.4\,M_\odot$, which have further been extended into the substellar and giant planet phase by Chabrier et al. (2000) and Baraffe et al. (2002, 2003) down to masses of $0.001\,M_\odot$. The equation-of-state is taken from Saumon et al. (1995) and is supplemented by the Alexander & Ferguson (1994) and Iglesias & Rogers (1996) opacities and the reaction rates from Chabrier & Baraffe (1997). An MLT convection treatment is adopted with alternative values for α of 1.0 (general mixing length parameter) and 1.9 (solar calibrated value) with initial abundances of $Y = 0.275, Z = 0.02$ and $Y = 0.0282, Z = 0.02$ respectively. Atmospheric treatment is based on the PHOENIX/NextGen non-grey atmospheres (Allard & Hauschildt 1995) which include the highly important TiO and H_2O molecular bands as well as accounting for the formation of dust grains. The models adopted are those presented in Baraffe et al. (1998) with mixing length parameters $\alpha = 1.0$ and 1.9. Note that for masses below $0.6\,M_\odot$ these two computations are identical, this is due to the insensitivity on the mixing length parameter in this mass regime (Baraffe et al. 2002).

---

[9]Whilst the DCJ08 models are not specifically designed for studying pre-MS evolution, these mass tracks cover the entire pre-MS phase over a significant mass range.

4.2.1.2 The SDF00 Models

Evolutionary models from the Grenoble group have been published in Forestini (1994), Siess et al. (1997) and most recently in Siess et al. (2000) covering the mass range $0.1 - 7.0 \, \mathrm{M_\odot}$. A modified equation-of-state from Pols et al. (1995) in conjunction with opacities from Alexander & Ferguson (1994) and Iglesias & Rogers (1996), and the reaction rates from Caughlan & Fowler (1988) are adopted in these calculations. Convection is based on the MLT with $\alpha = 1.5$, and initial abundance of $Y = 0.28$ and $Z = 0.02$. Unlike the grey atmospheric approach, Siess et al. (2000) instead base their models on a more realistic atmospheric outer boundary condition by matching the atmospheric temperature profile – as well as radiative pressure and gradient – to those derived from atmospheric models in regions where the optical depth $\tau < 10$. These atmospheric models are provided by Kurucz (1991) and Plez (1992). In this study the Siess et al. (2000) models with $\alpha = 1.5$ and computed assuming that there is no core overshooting are used. Note that the publicly available SDF00 models have a slightly modified chemical composition and mixing length parameter from the model which enables them to match the observed solar properties ($Z = 0.02$ and $\alpha = 1.5$ as opposed to $Z = 0.0249$ and $\alpha = 1.605$ in Siess et al. 2000).

4.2.1.3 The DCJ08 Models

The origins of the Dartmouth evolutionary models lie in the Dartmouth stellar evolution program (Chaboyer et al. 1999, 2001), which is a descendant of the Yale Rotating Stellar Evolution Code (Guenther et al. 1992). The models used in this study are those published in Dotter et al. (2008) which span a mass range of $0.1 - 5.0 \, \mathrm{M_\odot}$, with the majority of the underlying physics described in Chaboyer et al. (2001) and Bjork & Chaboyer (2006). Solar abundances were adopted from Grevesse & Sauval (1998) and the global solar parameters – luminosity, radius, surface abundances and age – taken from Bahcall et al. (2005). The equation-of-state is that of Rogers (1994) with the Debye-Hückel correction for masses greater than $0.8 \, \mathrm{M_\odot}$. For masses $0.1 - 0.8 \, \mathrm{M_\odot}$ the detailed equation-of-state code FreeEOS[10] developed by A. Irwin is adopted on the basis that it considers many non-ideal effects and is generally superior for use in high density, low temperature environments. Opacity tables for high temperatures ($\log_{10} T_{\mathrm{eff}} > 4.5$) are taken from Iglesias & Rogers (1996), whereas those of Ferguson et al. (2005) were adopted in the low temperature regime ($\log_{10} T_{\mathrm{eff}} < 4.3$). For $4.3 \leq \log_{10} T_{\mathrm{eff}} \leq 4.5$, the opacities were interpolated between the two sources. Surface boundary conditions are similar to those of the BCAH98 models, in that the PHOENIX/NextGen non-grey atmospheres (Hauschildt et al. 1999a) are adopted for $T_{\mathrm{eff}} \leq 10\,000 \, \mathrm{K}$ and the Castelli & Kurucz (2004) atmospheres used for $T_{\mathrm{eff}} > 10\,000 \, \mathrm{K}$. Convection is based on the MLT treatment, with the solar calibrated model yielding a value of $\alpha = 1.938$ with a metallicity of $Z = 0.01885$.

---

[10]`http://freeeos.sourceforge.net/`

4.2.1.4   The DAM97 Models

The original D'Antona and Mazzitelli models were published in D'Antona & Mazzitelli (1994) and covered the mass range $0.1 - 2.5\,M_\odot$. These models were computed using the equation-of-state of Magni & Mazzitelli (1979) and Mihalas et al. (1988), the opacities of Alexander et al. (1989), Kurucz (1991) and Rogers & Iglesias (1992), and the nuclear reaction rates computed by Fowler et al. (1975) and Caughlan & Fowler (1988). The treatment of convection was based either on the standard MLT with a mixing length to pressure scale height $\alpha = 1.2$ or the Canuto & Mazzitelli (1991, 1992) full spectrum of turbulence (FST) and initial abundances of $Y = 0.28$ and $Z = 0.019$ with a grey atmosphere approximation. D'Antona & Mazzitelli (1997) introduced an updated version of the original models which not only increased the mass range to $0.017 - 3.0\,M_\odot$ but also made the following modifications to the input physics. The equation-of-state of Mihalas et al. (1988) was used for $\log_{10} T_{\text{eff}} < 3.7$ and supplemented at higher T_{eff} by the Rogers et al. (1996) tables. The updated opacities of Iglesias et al. (1992) and Rogers & Iglesias (1993) were included alongside those of Rogers & Iglesias (1992). In addition, convection was computed using a pure FST approach. More recently, Montalbán et al. (2004) created a new version of the these models using both the MLT and FST treatments for convection as well as employing non-grey atmospheres such as the Allard et al. (1997) NextGen or the revised Heiter et al. (2002) ATLAS9 models, and stressed the importance of adopting a similar treatment of convection between the interior and atmospheric models, as previously discussed by Chabrier & Baraffe (1997). As the revised models of Montalbán et al. (2004) are not publicly available those presented in D'Antona & Mazzitelli (1997) are used instead.

4.2.2   Comparison of Pre-Main-Sequence Models

The preceding section describing the pre-MS models adopted in this work have highlighted the differences in the treatment of various physical aspects, as well as the values of adopted parameters. The most obvious differences are in the treatment of convection, the sources of opacity and the handling of the stellar interior/atmospheric boundary conditions (and to a lesser extent the initial chemical composition). To visualise these differences in the treatment of the physics and the subsequent effects these have on the low-mass stellar regime, Fig. 4.1 shows the predicted pre-MS tracks for several masses and Fig. 4.2 shows the resulting isochrones at $4.6\,\text{Gyr}$, the current age of the Sun.

The treatment of convection is one of the primary uncertainties in current sets of pre-MS evolutionary models. The general prescription is to adopt the standard MLT (Böhm-Vitense 1958), which simplifies the mathematically complex problem and is parameterised using the mixing length to pressure scale height parameter α. More recent treatments include the FST as introduced by Canuto & Mazzitelli (1991, 1992) which no longer assumes a one-eddy model as in the MLT approach, but instead accounts for the full spectrum of eddies expected in the turbulent interiors of low-mass stars. The choice of the α parameter can have a marked effect on the resultant temperature profile and thus it is
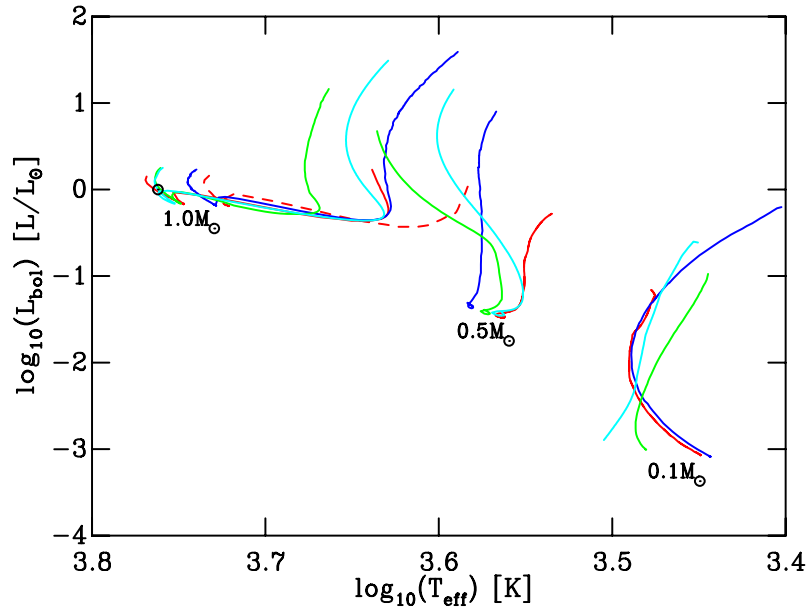
Figure 4.1: Variations in the pre-MS evolutionary tracks for masses of 0.1, 0.5 and $1.0\,M_\odot$ for the models adopted in this thesis – BCAH98 $\alpha = 1.9$ (red, continuous), BCAH98 $\alpha = 1.0$ (red, dashed), SDF00 (blue), DCJ08 (cyan) and DAM97 (green). The small solar symbol denotes the solar values of L_{bol} and T_{eff}. Note that for masses $< 0.6\,M_\odot$ both computations of the BCAH98 models are identical, this is due to the insensitivity to the adopted mixing length parameter α in this mass regime.
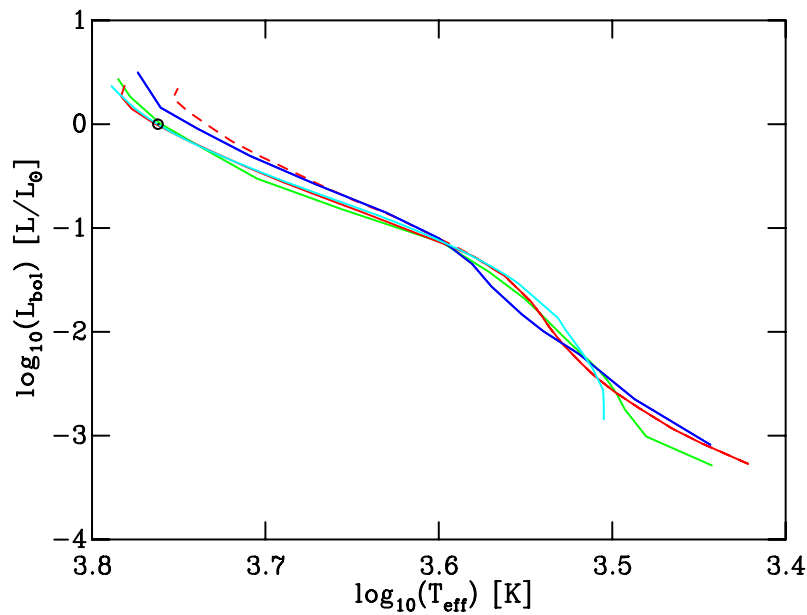
Figure 4.2: Variations in the pre-MS isochrones at an age of 4.6 Gyr for the models adopted in this thesis – BCAH98 $\alpha = 1.9$ (red, continuous), BCAH98 $\alpha = 1.0$ (red, dashed), SDF00 (blue), DCJ08 (cyan) and DAM97 (green). The small solar symbol denotes the solar values of L_{bol} and T_{eff}.

usually constrained by ensuring that a $1\,M_\odot$ model predicts the solar values of $L_{\rm bol}$ and $T_{\rm eff}$ at an age of $4.6\,$Gyr. This value is not only dependent upon the adopted outer boundary condition (see for example Tognelli et al. 2011), but also depends on the adopted age of the solar values. Since its arrival, the Sun has evolved away from the ZAMS becoming hotter and more luminous. Fig. 4.1 shows that the DCJ08, DAM97 and BCAH98 $\alpha = 1.9$ models have been calibrated to fit the present day values of the Sun, as evidenced by the mass tracks that extend beyond the ZAMS. The predicted stellar properties also depend on the opacity – and hence chemical composition – of the stellar interior, as this will dictate how the convective energy transfer propagates through the stellar interior.

4.3   Comparing the Models and the Data – I. The Pleiades

The primary reason for a precise test of the pre-MS models is to make further progress in understanding the limitations of current pre-MS isochrones and to determine whether the pre-MS ages could be in error by factors of the order of 1.5 to 2 (see Naylor 2009). Furthermore, such a test will identify whether any parts of the pre-MS or any colour combinations are reliable age indicators. The longer term aim is that by identifying and understanding such limitations of the pre-MS ages, a reliable pre-MS age scale may be created.

To set up a benchmark test for pre-MS isochrones a cluster is required that fulfils the following criteria; i) it must contain a significant number of pre-MS objects, as well as a populated MS to show that the models at least fit these more evolved stars, ii) it should have distance and age determinations which are independent of the CMD, iii) it should preferably have a low extinction (which might otherwise complicate transformations into CMD space), iv) it should have an approximately solar composition given that most pre-MS isochrones are only available for solar metallicity, and v) it should be nearby so that the lowest possible masses can be accessed. The Pleiades is the only cluster which fits all these criteria, and Stauffer et al. (2007) have already undertaken a comparison in the optical $VI_{\rm c}$, which shows that at least the V-band luminosity is not matched by two models available at the time.

Having characterised the natural INT-WFC photometric system and calculated the corresponding system responses, the Pleiades will be used to assess which of the most commonly used pre-MS models best match the data. By quantifying the remaining mismatch, a realistic assessment of its impact on pre-MS ages can be made. The mismatch will be traced as a function of wavelength using observations in a set of bandpasses which are contiguous in wavelength and cover 0.4 to $2.5\,\mu$m. The data reach cooler temperatures than the Stauffer et al. study, and are free of the uncertainties introduced by transforming heterogeneous datasets into a standard photometric system.
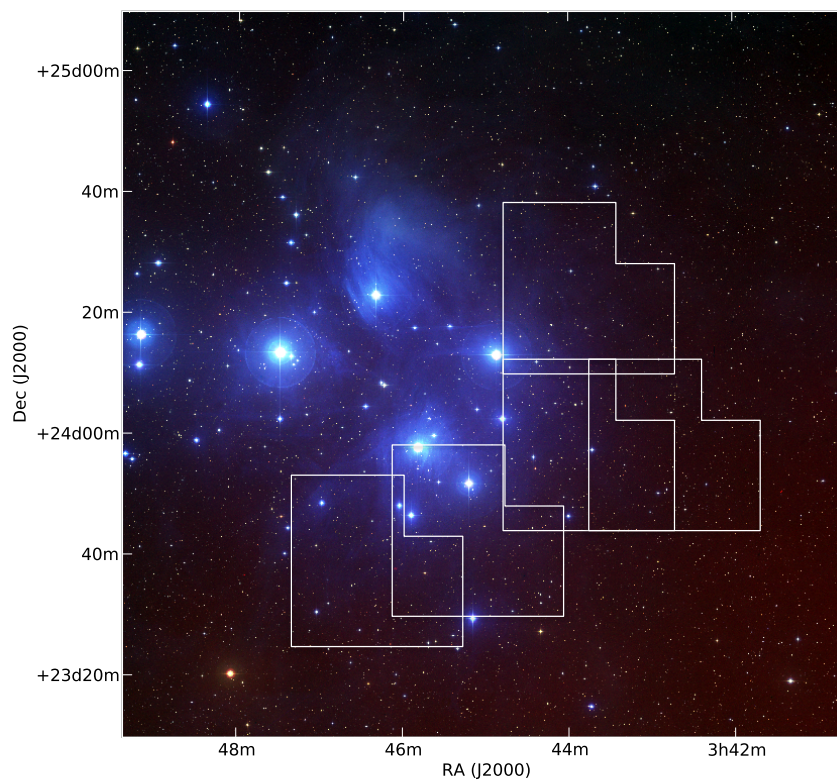
Figure 4.3: Two square degree three-colour mosaic image of the Pleiades from the ESO Digital Sky Survey with the five INT-WFC CCD positions overlaid. Note that the image is slightly displaced from the central coordinates of $\alpha_{\mathrm{J2000.0}} = 03^{\mathrm{h}}\,47^{\mathrm{m}}\,24.0^{\mathrm{s}}, \delta_{\mathrm{J2000.0}} = +24°\,07'\,00.0''$ to illustrate the region chosen to identify low-mass members

4.3.1 The Pleiades Catalogue

The Pleiades catalogue comprised a mosaic of five individual fields-of-view, as displayed in Fig. 4.3, which were observed over the course of the two runs (see Section 3.2 and Table A.2). These were reduced as described in Section 3.3 and a normalisation procedure (Jeffries et al. 2004) applied to create a single photometric catalogue of the surveyed region. A list of approximately 180 members was obtained by cross-correlating the full photometric catalogue with the combined memberships catalogues of Stauffer et al. (2007) and Lodieu et al. (2012).

The membership catalogue of Stauffer et al. (2007) represents a number of photometric, photoelectric and photographic surveys which have been combined with a host of proper motion surveys to assign membership probabilities. The reader is directed to Appendix A1 of Stauffer et al. (2007) for a full and comprehensive discussion of the catalogues used. The resultant memberships from these literature sources have been assigned on the basis of a series of colour-colour and CMDs where the photometry of each candidate member must yield a position consistent with cluster membership. For stars with radial velocity measurements, membership was assigned on the basis that it was considered a radial velocity member in the original source. Individual proper motion membership data was also used and if the candidate fractional probability was less than 0.1, it was excluded from the final membership list. Where a star appears in multiple proper motion membership studies it was included if the assigned probability was less than 0.1 in only one catalogue. As the photometric observations presented here extend to lower masses, it was necessary to supplement the Stauffer et al. (2007) membership catalogue with lower mass members from Lodieu et al. (2012). The Lodieu et al. membership catalogue is based on a combination of a deep wide-field near-IR survey of the Pleiades cluster taken as part of the UKIRT Infrared Deep-Sky Survey (UKIDSS) Galactic Clusters Survey (GCS) with proper motions derived from multiple epochs provided by the UKIDSS GCS. These data have also been used to provide revised memberships for all previously published Pleiades low-mass stars and brown-dwarfs.

4.3.2 Model Parameters

A distance modulus $dm = 5.63$ was used which is taken from the space-based trigonometric parallax measurement of Soderblom et al. (2005). The lithium depletion age was adopted, since although it is based on the predictions of stellar interior models, Jeffries & Oliveira (2005) show there is a very high level of agreement between the various models. Furthermore, the age adopted is that based on the boundary in the near-IR $K_{\rm s}$-band of 130 Myr (Barrado y Navascués et al. 2004b), since, as will be shown in Section 4.4.3, the $K_{\rm s}$-band is the best predictor of luminosity of the bandpasses studied. A reddening of $E(B-V) = 0.04$ is used based on the mean extinction of $A_V = 0.12$ (Stauffer et al. 1998) and $R_V = 3.2$. Hence, to transform the theoretical models into the observable plane, the atmospheric models were first reddened by a nominal $E(B-V)$ that equates to a measured

$E(B - V) = 0.04$ using the relation derived from Fig. 2.3 assuming the reddening law of Cardelli et al. (1989), and then the bolometric corrections were calculated using Eqn. 3.2.

Note that in Section 2.8.4.13 independent determinations of both the age and distance were derived by fitting the MS population of the Pleiades in the $V_\circ, (B - V)_\circ$ CMD. It is reassuring to find that these independent measurements for both the age and distance are in excellent agreement with the values adopted above, and this not only suggests that the MS fitting technique is robust, but also ensures that the conclusions are placed on a well-defined absolute age scale.

4.3.3 Discussion

Fig. 4.4 shows six CMDs of the Pleiades with the pre-MS isochrones of BCAH98, SDF00, DAM97 and DCJ08 overlaid. The break between the MS and pre-MS stars in the Pleiades occurs at $(g - i)_{\mathrm{WFC}} \simeq 2$, and is marked by a paucity of stars in all CMDs. It is apparent that the isochrones all follow the Pleiades MS reasonably well, though as will be shown in Section 4.5, this is in part due to compensating errors in each individual bandpass. None of the models, however, trace the observed pre-MS locus, with each predicting colours that are too blue for a given stellar mass. This issue has already been highlighted in Stauffer et al. (2007) (see their Fig. 13), though from their data one could only be certain there was a problem in the V-band, whereas the data here show that all optical bands are affected.

This is part of a broader picture where it is known that MS stars are similarly affected, at least in the V-band (see Section 4.4.3). It is well known that there are sources of opacity missing from the atmospheric models for cool stars ($T_{\mathrm{eff}} \lesssim 3700\,\mathrm{K}$) in the optical regime of the spectrum (Leggett et al. 1996; Alvarez & Plez 1998; Baraffe et al. 1998, 2002). Although the BT-Settl models are computed using more complete line lists than previous generations of PHOENIX models, there is still a need for additional data to provide fully comprehensive line lists, especially for the molecular opacities (H_2O, TiO, VO, CH_4, etc.; see for instance Partridge & Schwenke 1997; Schwenke 1998; Allard et al. 2011).

To be quantitative about the missing opacity, the missing flux must be measured individually in each bandpass, rather than as a function of colour. The most straightforward way of achieving this is to identify a photometric bandpass where the missing sources of opacity are minimal, and create colours with respect to that band. This is equivalent to using the luminosity in that band to define T_{eff}. To test the T_{eff} scale requires masses – from which the models predict T_{eff} – from binaries, data which are simply not available for the Pleiades. Instead, as the opacity problem affects MS stars as well as pre-MS stars (in the same T_{eff} range), MS binaries can be used to identify a bandpass.

4.4 Comparing the Models and the Data – II. Main-Sequence Binaries

Although there are many MS binaries with well-determined masses and distances that could be used to test the models, the outstanding problem is the small sub-sample of
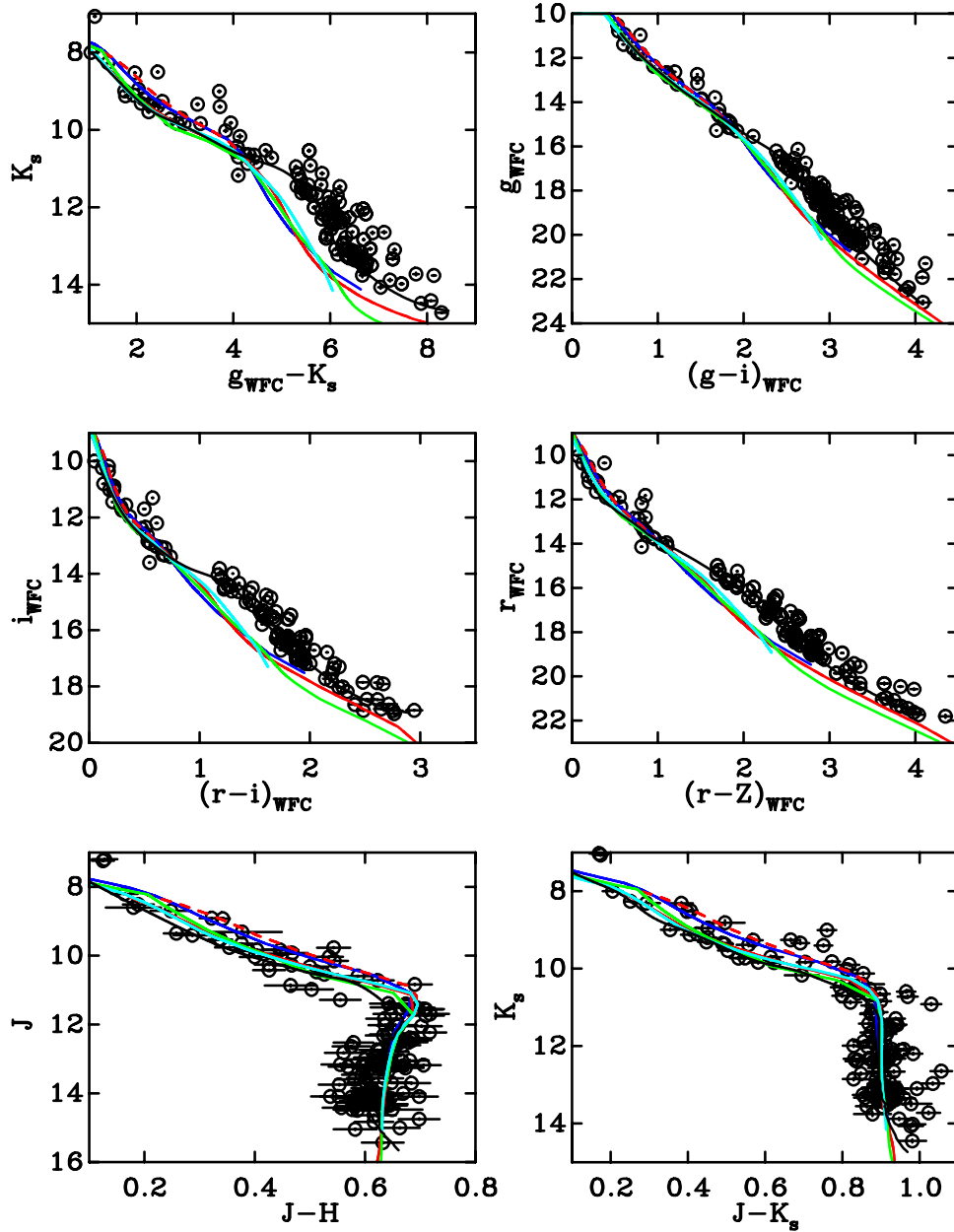
Figure 4.4: Optical/near-IR CMDs of the Pleiades members as defined by cross-correlation with the combined membership catalogue of Stauffer et al. (2007) and Lodieu et al. (2012). The 130 Myr pre-MS isochrones of BCAH98 $\alpha = 1.9$ (red, continuous), BCAH98 $\alpha = 1.0$ (red, dashed), SDF00 (blue), DAM97 (green) and DCJ08 (cyan) are overlaid, adopting a distance modulus $dm = 5.63$ and a reddening $E(B - V) = 0.04$. The isochrones have been transformed into the observable plane using bolometric corrections derived by folding the atmospheric flux distributions through the calculated INT-WFC system responses. The black line in each panel represents the spline fit (by-eye) to the Pleiades single-star sequence. The open circles represent the photometric data, with the associated uncertainties in colour and magnitude shown as the bars. **Top left:** $K_s, g_{WFC} - K_s$ CMD. **Top right:** $g_{WFC}, (g - i)_{WFC}$ CMD. **Middle left:** $i_{WFC}, (r - i)_{WFC}$ CMD. **Middle right:** $r_{WFC}, (r - Z)_{WFC}$ CMD. **Bottom left:** $J, J - H$ CMD. **Bottom right:** $K_s, J - K_s$ CMD.

these which have individual magnitudes in many colours. Astrometric binaries are often separated only in the IR, and so lack individual optical colours, and eclipsing binaries often have lightcurves in only a small number of colours. To overcome this problem the system magnitude can instead be modelled, which, as shall be discussed later, still gives significant insight as a function of stellar mass (or equivalently T_{eff}).

4.4.1 The Sample

To create the sample data for low-mass binaries from Delfosse et al. (2000) were supplemented with data for higher mass binaries from Andersen et al. (1987), Clausen et al. (2008), Clausen et al. (2009), Clement et al. (1997b), Clement et al. (1997a), Lacy et al. (1997), Lacy et al. (2005), López-Morales & Ribas (2005), Popper et al. (1986), Popper (1994), Popper (1997), Torres et al. (1997), and Torres et al. (2009). An upper limit was imposed to the mass uncertainty on both the primary and secondary components of $10\,\%$, and in addition, only non-contact binaries were used so that the results were not biased by the effects of tidal forces and mass transfer. An additional limit was enforced so that the sample of binaries only included those with associated uncertainties in the parallax of $\leq 11\,\%$, thus the conclusions are unaffected by the Lutz-Kelker bias (Lutz & Kelker 1973). The Lutz-Kelker bias results in stellar parallaxes that are systematically overestimated due to not properly accounting for the larger volume of space that is sampled at smaller parallax values. This in turn results in systematically smaller distances, and hence corresponding uncertainties on the derived luminosities.

The sample spans the mass range $0.1 \leq \text{M}_{\odot} \leq 1.4$ for the individual components, with the higher mass limit chosen as the BCAH98 models only extend to such masses. For the low-mass systems in Delfosse et al. (2000) the apparent magnitudes were taken from the homogeneous dataset of Leggett (1992). A number of higher mass systems only had a Strömgren $b - y$ colour and so these were transformed into $V - I_{\text{c}}$ colours using the relation of Bessell (1979) which is accurate to within $0.01\,\text{mag}$ for MS stars. Near-IR measurements were taken from the 2MASS point source catalogue (Cutri et al. 2003). Parallax measurements were taken from the *Hipparcos* catalogue (Perryman et al. 1997), the Yale General Catalogue of Trigonometric Stellar Parallaxes (van Altena et al. 1995), and Ségransan et al. (2000). The sample of MS binaries with associated optical VI_{c} and near-IR JHK_{s} system apparent magnitudes, dynamical masses, parallaxes, and spectral types is given in Table 4.1.

Table 4.1: The sample of MS binaries with optical VI_c and near-IR JHK_s system apparent magnitudes, dynamical masses, parallaxes, and spectral types.

System	Star	Mass (M$_\odot$)	Spectral type	π (mas)	V	I_c	J	H	K_s
BL Cet	A	0.102 ± 0.010	M5.5V	373.7 ± 2.7	12.00	8.31	6.28	5.69	5.34
GJ 65	B	0.100 ± 0.010	M6V						
FL Vir	A	0.143 ± 0.011	M4V	227.9 ± 4.6	12.46	8.92	7.00	6.40	6.04
GJ 473	B	0.131 ± 0.010	M7V						
V577 Mon	A	0.203 ± 0.011	M4.5V	243.7 ± 2.0	11.08	8.06	6.38	5.75	5.49
GJ 234	B	0.103 ± 0.004	M8V						
GJ 747	A	0.214 ± 0.001	M4.5V	120.2 ± 0.2	11.25	8.65	7.06	6.47	6.33
CSI+32 3326 5	B	0.200 ± 0.001	M5V						
CM Dra	A	0.231 ± 0.001	M4.5V	69.2 ± 2.5	12.91	9.99	8.50	8.04	7.80
GJ 630.1 A	B	0.214 ± 0.001	M4.5V						
DO Cep	A	0.271 ± 0.010	M2V	247.5 ± 1.5	9.59	6.91	5.58	5.04	4.78
GJ 860	B	0.176 ± 0.007	M4V						
HU Del	A	0.286 ± 0.006	M6V	112.9 ± 0.3	13.06	9.96	8.23	7.67	7.31
GJ 791.2	B	0.126 ± 0.003	M6V						
BB Cap	A	0.291 ± 0.013	M4.5V	117.5 ± 2.0	12.01	9.02	7.32	6.70	6.38
GJ 831	B	0.162 ± 0.007	M5V						
GJ 623	A	0.343 ± 0.030	M3.5V	124.34 ± 1.16	10.26	7.96	6.64	6.14	5.92
TYC 3495-601-1	B	0.114 ± 0.008	M5.5V						
GJ 661	A	0.379 ± 0.035	M3.5V	156.66 ± 1.37	9.40	6.89	5.55	5.07	4.83
BD+45° 2505	B	0.369 ± 0.035	M3V						

Table 4.1: *continued*

System	Star	Mass ($M_\odot$)	Spectral type	π (mas)	V	I_c	J	H	K_s
CU Cnc	A	0.434 ± 0.001	M3.5Ve	78.05 ± 5.69	11.89	9.09	7.51	6.89	6.60
GJ 2069 A	B	0.399 ± 0.001	M3.5Ve						
GJ 570	B	0.566 ± 0.003	M1.5V	169.8 ± 0.9	8.09	5.97	3.66	3.09	3.05
BD−20° 4123	C	0.377 ± 0.002	M3V						
YY Gem	A	0.603 ± 0.001	M1ve	74.7 ± 2.5	9.07	7.09	6.07	5.42	5.24
BD+32° 1582	B	0.607 ± 0.001	M1ve						
GU Boo	A	0.610 ± 0.006	M1v	7.52 ± 0.90	13.60	11.70	11.05	10.36	10.22
GSC 02566-00776	B	0.600 ± 0.006	M1v						
HS Aur	A	0.898 ± 0.019	G8v	8.24 ± 0.33	10.10	9.43	8.80	8.44	8.38
BD+47° 1350	B	0.877 ± 0.017	K0v						
RW Lac	A	0.926 ± 0.006	G5v	5.16 ± 0.23	10.44	9.76	9.30	8.96	8.87
TYC 3629-740-1	B	0.869 ± 0.004	G7v						
CG Cyg	A	0.941 ± 0.014	G9.5v	12.29 ± 0.93	9.36	8.38	8.35	7.90	7.75
BD+34° 4127	B	0.814 ± 0.013	K3v						
V636 Cen	A	1.052 ± 0.005	G1v	13.91 ± 0.56	8.69	7.99	7.47	7.13	7.06
HD 124784	B	0.855 ± 0.003	K2v						
ZZ Uma	A	1.139 ± 0.005	G0v	5.30 ± 0.18	9.77	9.12	8.71	8.41	8.33
BD+62° 1132	B	0.969 ± 0.005	K0v						
BH Vir	A	1.166 ± 0.008	F8v	6.45 ± 0.39	9.40	8.76	8.46	8.19	8.07
HD 121909	B	1.052 ± 0.006	G5v						

Table 4.1: *continued*

System	Star	Mass (M$_\odot$)	Spectral type	π (mas)	V	I_c	J	H	K_s
EW Ori	A	1.174 ± 0.012	G0V	5.87 ± 0.23	9.82	9.15	8.81	8.60	8.50
HD 287727	B	1.124 ± 0.009	G5V						
LV Her	A	1.193 ± 0.010	F8V	2.84 ± 0.18	10.93	10.24	9.91	9.67	9.63
TYC 2076-1042-1	B	1.170 ± 0.008	F8V						
FL Lyr	A	1.218 ± 0.016	F8V	7.52 ± 0.32	9.21	8.58	8.24	7.99	7.90
HD 179890	B	0.958 ± 0.012	G8V						
WZ Oph	A	1.227 ± 0.007	F7V	6.41 ± 0.26	8.97	8.39	8.57	8.37	8.27
HD 154676	B	1.220 ± 0.006	F8V						
HS Hya	A	1.255 ± 0.008	F4V	9.72 ± 0.24	8.12	7.60	7.21	7.03	6.96
HD 90242	B	1.219 ± 0.007	F5V						
VZ Hya	A	1.271 ± 0.009	F3V	6.81 ± 0.37	8.87	8.34	8.08	7.85	7.78
HD 72257	B	1.146 ± 0.006	F6V						
IT Cas	A	1.332 ± 0.009	F5V	2.03 ± 0.02	10.90	10.30	10.21	9.96	9.92
TYC 3650-959-1	B	1.329 ± 0.008	F5V						
V1143 Cyg	A	1.388 ± 0.016	F5V	25.45 ± 0.88	5.89	5.37	4.98	4.84	4.77
HD 185912	B	1.344 ± 0.013	F5V						

4.4.2 The Models

As these binaries are located in the field, it is expected that they are old systems, and therefore 2 Gyr isochrones were adopted with which to compare the observations against the models. Note that at such ages, the mass scale is insensitive to changes in age. For each binary component, $L_{\rm bol}$, defined by the stellar interior models, was converted into an absolute magnitude using bolometric corrections calculated using Eqn. 3.2 by folding the atmospheric models through the standard $UBVRI$ responses of Bessell (1990) and the $JHK_{\rm s}$ responses of Cohen et al. (2003). As in Section 2.5.1 for the Johnson UBV bolometric corrections, the Vega reference spectrum adopted was the CALSPEC alpha_lyr_stis_005 with $V = 0.03$ and all colours equal to zero. For the 2MASS responses the bandpass specific reference spectra and zero-point offsets of Cohen et al. (2003) were used (see their Table 2 and Section 5 respectively). The absolute magnitude was then converted into a flux, and the fluxes for a given binary pair were then summed and converted back into a system absolute magnitude. Where possible, the effects of interstellar reddening have been included by adopting literature values. These values range from $E(B - V) = 0.0 - 0.11$. The atmospheric models were reddened accordingly and the bolometric corrections calculated as described in Section 4.3.2.

4.4.3 Discussion

Fig. 4.5 shows the residuals (calculated – observed) in the mass-luminosity relation for the $VI_{\rm c}JHK_{\rm s}$ bandpasses. As the binary mass ratio $q \rightarrow 1$ both components have the same mass, whereas when $q \rightarrow 0$ the primary component is likely to dominate the flux output of the system. Hence the difference in absolute magnitude can be plotted as a function of the measured primary mass. The range of q as defined by the sample is $q = m_2/m_1 = 0.33 - 1.0$, where for 65 % of these the ratio $q > 0.9$. Regardless of the choice of interior model, there are significant systematic deviations – especially in the optical regime – for masses below $\simeq 0.4 - 0.5 \, {\rm M}_\odot$. Fig. 4.5 shows that the differences between the observed and the calculated system absolute magnitude decreases as one moves to redder bandpasses, from approximately 2.5 mag in the V-band to less than 1 mag in the $K_{\rm s}$-band. In the near-IR, and in particular, the $K_{\rm s}$-band, there is far less spread for a given stellar mass (see also Martín et al. 2000 and Delfosse et al. 2000), with the interior models predicting similar luminosities. This further highlights the fact that there is a problem with the optical colours predicted by the atmospheric models for masses below $\simeq 0.4 - 0.5 \, {\rm M}_\odot$ ($T_{\rm eff} \lesssim 3700 \, {\rm K}$).

It has been noted in the literature that short-period, close-in binary system components have radii which are inflated of order 10 % with respect to evolutionary models of low-mass stars (e.g. Kraus et al. 2011). To test whether this effect is observed in the photometry of these systems, Fig. 4.5 has also been plotted as a function of physical separation. Fig. 4.6 shows no evidence for the models to either under- or overestimate the system absolute magnitude for short-period binaries with smaller physical separations.
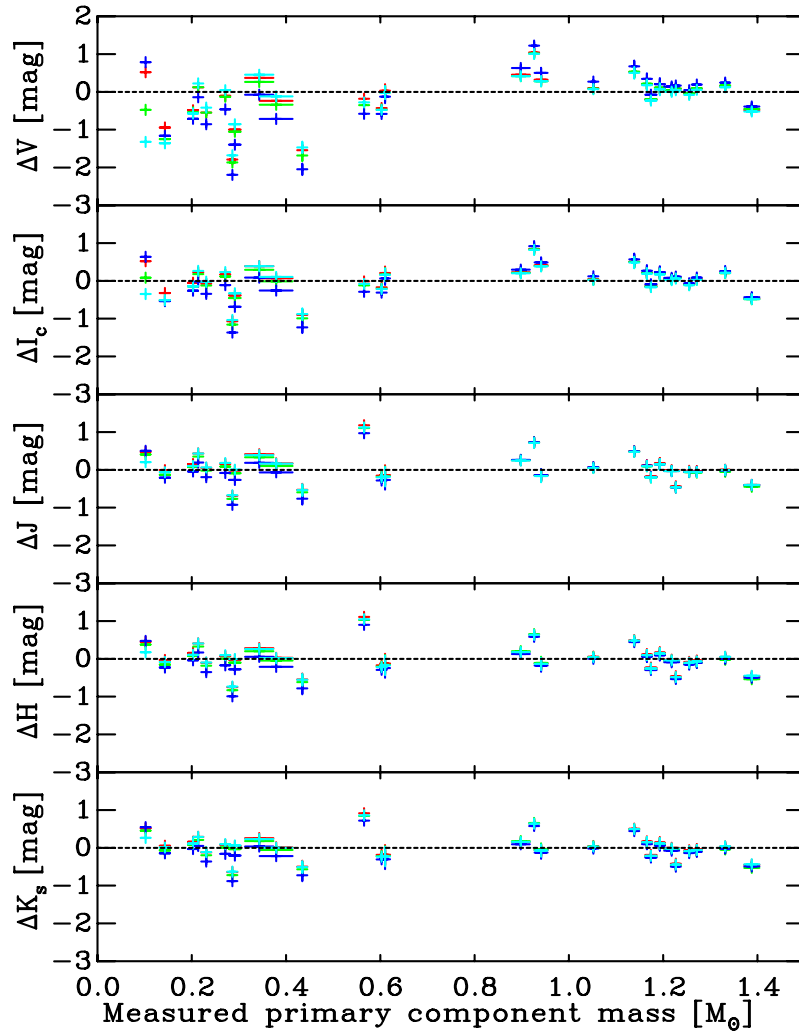
Figure 4.5: The difference between the observed and calculated system absolute magnitudes (where Δ implies calculated – observed) for the 28 binary systems as a function of the measured primary component stellar mass. Bolometric luminosities have been calculated using 2 Gyr interior models of BCAH98 $\alpha = 1.9$ (red), SDF00 (blue), DAM97 (green) and DCJ08 (cyan). The atmospheric model flux distributions were folded through the standard $UBVRI$ responses of Bessell (1990) and the $JHK_{\rm s}$ responses of Cohen et al. (2003) to create bolometric corrections which were used to derive the predicted absolute magnitudes. **Upper panel:** ΔV. **Upper middle panel:** $\Delta I_{\rm c}$. **Middle panel:** ΔJ. **Lower middle panel:** ΔH. **Lower panel:** $\Delta K_{\rm s}$.
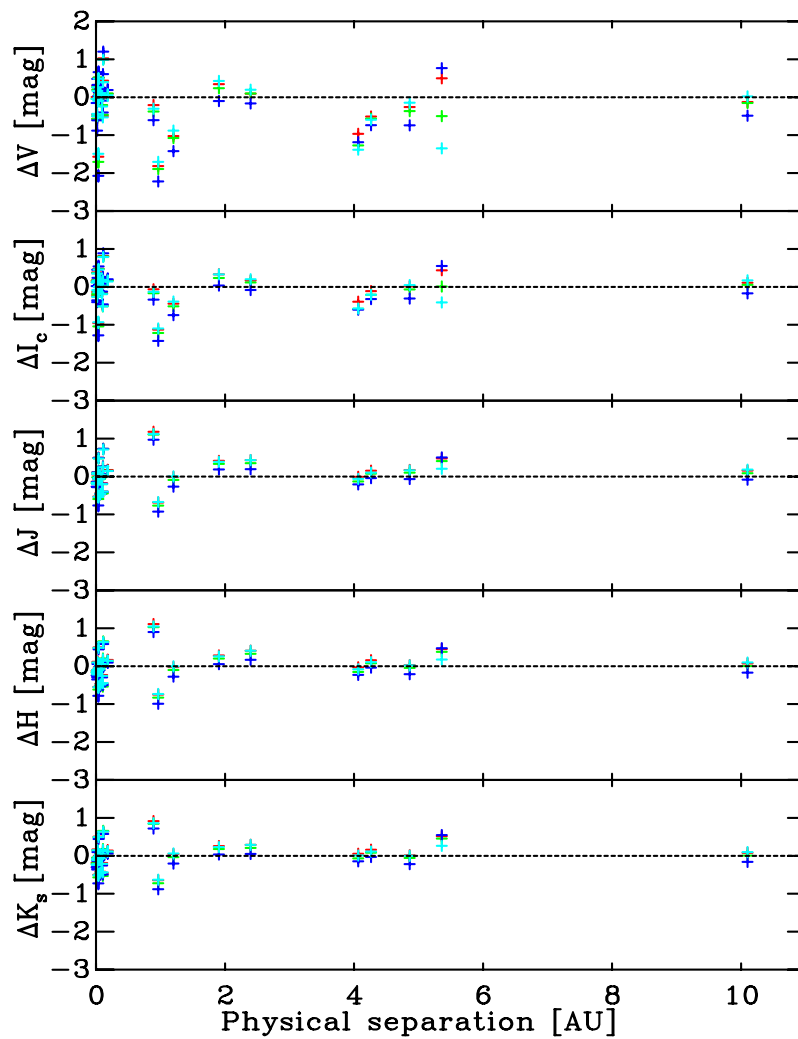
Figure 4.6: Same as Fig. 4.5, but plotted as a function of the physical separation between the binary components. **Upper panel:** ΔV. **Upper middle panel:** ΔI_c. **Middle panel:** ΔJ. **Lower middle panel:** ΔH. **Lower panel:** ΔK_s.

What is clear, however, is that of all the bands available, the K_s-band magnitude is the closest to that predicted by the models for a given T_eff, both in terms of mean magnitude and spread. This is perhaps, unsurprising, since the K_s-band is less affected than either the J- or H-band by the missing sources of opacity that arise from incomplete H_2O line lists (see the discussion on the completeness of the BT2 H_2O line lists as a function of wavelength by Barber et al. 2006). Furthermore, current uncertainties in the absolute values of C, N and O in derived solar abundances (cf. Grevesse & Sauval 1998 and Asplund et al. 2009) have a knock-on effect for computed atmospheric models that result in systematic uncertainties. The incompleteness of line lists was mentioned at the beginning of Chapter 3, however recent studies (Sharp & Burrows 2007; Freedman et al. 2008) have shown that atmospheric models suffer from incompleteness in warm opacity line lists for key molecular species. For example, current line lists for CH_4 are incomplete at wavelengths below $1.6\,\mu$m and the NH_3 line lists in this regime are non-existent. Thus in a given bandpass the atmospheric models will tend to overestimate the luminosity as a result of these missing sources of opacity, and similarly, result in colours which are too blue. In what follows, therefore, the K_s-band magnitude is used to determine the T_eff of Pleiades members.

4.5   Quantifying the Discrepancy

The approach for quantifying the effects of the missing opacity is to determine the T_eff of a given Pleiad by comparing its K_s-band magnitude with that predicted by a given model. The predicted luminosity in any other band can then be compared with that of the members in question to calculate the missing flux. In practice it is better to work with a sequence rather than individual members and so the single-star Pleiades sequence was defined in the INT-WFC and 2MASS colours by fitting a spline (by-eye) to the observed sequence in various CMDs. Only stars with uncertainties in both colour and magnitude of less than 0.1 mag were used. This spline lies slightly above the lower envelope of the sequence to account for photometric uncertainties and takes into consideration that the equal-mass binary sequence lies $\simeq 0.75$ mag above the single-star sequence (with very few systems of higher multiplicity). Appendix B lists the Pleiades single-star sequence in the INT-WFC $(griZ)_\mathrm{WFC}$ and 2MASS JHK_s bandpasses.

Starting, for instance, with the $K_\mathrm{s}, (g_\mathrm{WFC} - K_\mathrm{s})$ Pleiades CMD, the theoretical 130 Myr isochrone was compared to the observed spline and the difference between the colours at a given T_eff – provided by the model isochrone – calculated. Assuming that the problem, in this case, lies in the g_WFC-band and not K_s, this then defines the required corrections (ΔBC; defined as $\mathrm{BC_{obs}} - \mathrm{BC_{calc}}$) for the g_WFC-band at a specific T_eff. This process was then repeated over the T_eff range of the theoretical isochrone or the colour range defined by the observed spline, whichever was more restrictive, thus providing ΔBC as a function of T_eff for the g_WFC-band. Repeating this for all four pre-MS evolutionary models (including both the BCAH98 computations), the model dependent ΔBCs as a
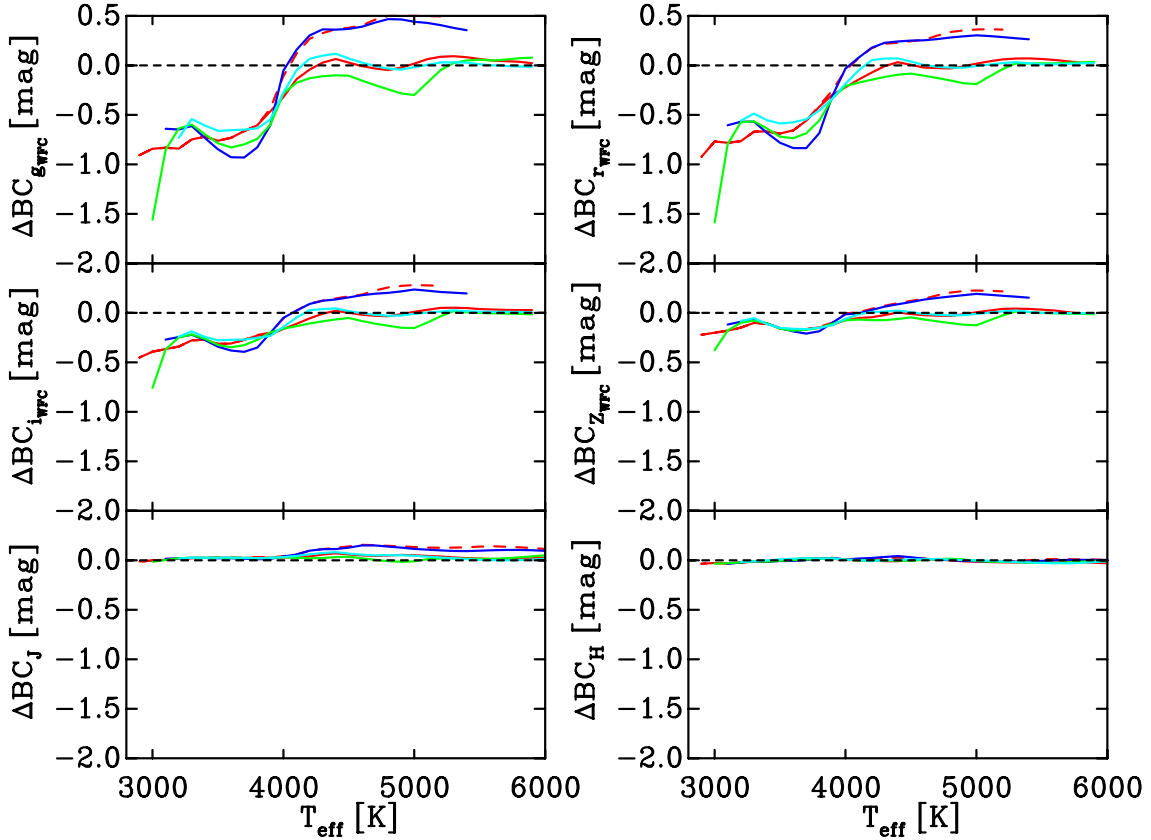
Figure 4.7: The model dependent corrections (ΔBC) calculated as a function of T_{eff} in the INT-WFC $(griZ)_{\text{WFC}}$ and 2MASS JH bandpasses. The corrections were calculated as the difference between the theoretically predicted colour and the observed colour of the Pleiades sequence at a given T_{eff}. Corrections have been calculated for the following models – BCAH98 $\alpha = 1.9$ (red, continuous), BCAH98 $\alpha = 1.0$ (red, dashed), SDF00 (blue), DAM97 (green), and DCJ08 (cyan). For $T_{\text{eff}} \lesssim 4000\,\text{K}$ all models fail to match the data in the optical regime, with the magnitude of the mismatch decreasing with increasing wavelength.

function of T_{eff} for the $(griZ)_{\text{WFC}}JH$ bandpasses were calculated.

The final results are shown in Fig. 4.7. In the Pleiades, stars cooler than $T_{\text{eff}} \simeq 4000\,\text{K}$ are on the pre-MS, and all models fail to match the data in the optical in this regime. The discrepancy is large, $0.75\,\text{mag}$ in g_{WFC}, but this decreases with increasing wavelength. This is a clear improvement, however, over the PHOENIX/GAIA models (Brott & Hauschildt 2005), for which a discrepancy of around $1\,\text{mag}$ is observed. This highlights the challenges of deriving absolutely calibrated pre-MS ages through isochrone fitting. The fact that a given isochrone is unable to reproduce the observed Pleiades locus for masses $\lesssim 0.4 - 0.5\,\text{M}_\odot$ therefore limits their applicability for younger SFRs.

Whilst the missing sources of opacity in the atmospheric models no doubt play a role (see Section 4.4.3) it is unlikely the exclusive reason for the observed discrepancy. A well documented source of uncertainty in the evolutionary models is the treatment of convection, parameterised using the mixing length parameter α. In the standard MLT, the computation of convection is a very simplistic one-dimensional approach that does

not account for the time-dependence and non-locality of the convective flows, where the parameter α can be tuned to match the Sun. In the evolutionary models tested the value of α is assumed to be constant for all evolutionary stages and identical for all stellar masses. Studies investigating whether this is a valid assumption (e.g. Ludwig et al. 1999, 2008) have found that α can vary as a function of spectral type, the effects of which would be more pronounced at younger evolutionary phases where the stars are fully convective and the superadiabatic region is more extended.

In addition to inadequacies in the theoretical models, there are also physical processes that affect the SEDs associated with pre-MS stars, and these can be almost impossible to incorporate into evolutionary codes. An obvious example is the enhanced levels of activity observed on pre-MS stars. High levels of activity, presumably driven by intense surface magnetic fields, can inhibit the convective flows at the stellar surface and result in starspots covering a large fraction of the photosphere. Thus the colours of young low-mass stars can be somewhat different than the colours of older stars of the same mass and T_{eff} (e.g. Stauffer et al. 2003). An additional consequence of the inhibited convective flows is that the radii and T_{eff} of stars with intense magnetic fields can differ from stars of a similar mass but with a much weaker magnetic field (e.g. Chabrier et al. 2007; Yee & Jensen 2010). These combined effects further complicate the transformation from H-R to CMD space i.e. for a star of given mass, metallicity, and $\log g$ there is not a single conversion from, for example, $(g-i)_{\mathrm{WFC}}$ to T_{eff} but instead a range.

The effect that this overestimation in the flux of the atmospheric models has on the derived ages for $T_{\mathrm{eff}} < 4000\,\mathrm{K}$ can be tested in the following way. If this discrepancy is independent of age (and therefore $\log g$), the roughly logarithmic age spacing between the isochrones in CMD space means that the resulting error in age is best represented as a fractional rather than an absolute difference. So to start, the ΔBCs derived above were added to the theoretical BC-T_{eff} relation at a given age and a corrected BCAH98 $\alpha = 1.9$ isochrone was produced. The closest matching uncorrected BCAH98 $\alpha = 1.9$ isochrone, in CMD space, was then found. A comparison shows that for ages between 3 and 10 Myr, the difference in age is approximately a factor 3 in $g_{\mathrm{WFC}}, (g-i)_{\mathrm{WFC}}$ and 2 in $r_{\mathrm{WFC}}, (r-Z)_{\mathrm{WFC}}$.

The message here is very clear, one should use the reddest bandpass possible to determine an age. Unfortunately by the time one reaches the near-IR JHK_{s} bandpasses, the pre-MS isochrones are almost vertical with a colour $J - K_{\mathrm{s}} \simeq 0.85$ for $2500 < T_{\mathrm{eff}} < 4000\,\mathrm{K}$. Although individual stars descend with age, the resulting sequences are almost degenerate with age, and for young SFRs ($< 10\,\mathrm{Myr}$), observations are further complicated by the presence of discs. Thus the JHK_{s} near-IR is unlikely to yield reliable young SFR ages. Masses do not suffer from such a degeneracy and therefore the H-band may be a reliable mass indicator when K_{s} is affected by circumstellar material.

Perhaps more surprising is the fact that in the MS regime, hotter than $T_{\mathrm{eff}} \simeq 4000\,\mathrm{K}$, only two models fit the data in the optical. The reason the BCAH98 $\alpha = 1.0$ and SDF00 models tend to overestimate the luminosity at a given T_{eff} is that neither is tuned to the Sun, as explained in Sections 4.2.1.1 and 4.2.1.4. Once the BCAH98 models have a tuned

mixing length parameter ($\alpha = 1.9$) based on matching observed solar values they are a good match to the MS data. Similarly for the DCJ08 models. A possible reason why the DAM97 models only fit the MS for $T_{\mathrm{eff}} \gtrsim 5100\,\mathrm{K}$ may be because of their treatment of convection.

4.6 Summary

In this section the various sets of pre-MS interior models that will be tested against the calibrated photometric dataset of young SFRs have been introduced. The physical inputs of these models and a brief discussion on the differences between these inputs have been given, including how these affect the evolution and placement in a CMD. A simple benchmark test has been performed by comparing the pre-MS models to the Pleiades dataset in a series of well-calibrated CMDs that span a contiguous wavelength regime of $0.4 - 2.5\,\mu\mathrm{m}$. These tests show that for $T_{\mathrm{eff}} \lesssim 4000\,\mathrm{K}$, none of the pre-MS models match the observed pre-MS locus of the Pleiades in the optical, however better agreement is noted in the near-IR regime. Furthermore, the predicted masses of the interior models have been tested by comparing them to dynamical masses from a sample of eclipsing and spectroscopic binaries. By modelling the system magnitude, it was shown that the K_{s}-band is the most reliable predictor of stellar mass of the available tested photometric bandpasses. The K_{s}-band magnitude of Pleiades members has therefore been used to quantify the discrepancy between the models and the data as a function of T_{eff} in individual photometric bandpasses. This shows that the models systematically overestimate the flux by a factor two at $0.5\,\mu\mathrm{m}$, though this decreases with wavelength becoming negligible at $2.2\,\mu\mathrm{m}$. Finally, the effects that this discrepancy would have on the derived pre-MS ages for stars cooler than $T_{\mathrm{eff}} \lesssim 4000\,\mathrm{K}$ have been calculated. It was found that these ages could be underestimated by factors of between 2 and 3 depending on the colours adopted. This benchmark test has demonstrated the fact that the pre-MS models are not able to reproduce the observed pre-MS at an age of $130\,\mathrm{Myr}$ in optical colours. Hence, some attempt to account for the missing opacity must be made before these models are used to derive ages for much younger SFRs. Note, however, that others factors such as the inadequate treatment of convection and physical processes that affect the observed photospheric properties of young, low-mass stars that are generally not included in the evolutionary models, are also likely to have an impact on the observed disparity.

Chapter 5

Fitting the Pre-Main-Sequence Population of Young Star-Forming Regions

5.1   Motivation

In previous chapters the primary factors that can result in errors when fitting pre-MS stellar populations with evolutionary models in CMDs have been discussed. Chapter 3 addressed the issue of calibrating pre-MS star photometry using observations of MS standard stars and found that this can result in the pre-MS occupying the wrong position in CMD space. Furthermore, in Chapter 4 it was demonstrated that commonly used pre-MS isochrones are unable to match the observed pre-MS as defined by the observations of the Pleiades, especially in the optical colours. This discrepancy was attributed, primarily, to missing sources of opacity in the line lists used to calculate the atmospheric models, but may also be due to additional factors including physical processes that are not incorporated into the theoretical models. Therefore, before ages can be derived from the pre-MS populations this discrepancy must be addressed.

In Section 5.2 the observations and photometric data reduction process are discussed. The various diagnostics used to distinguish between pre-MS stars and foreground/background objects are introduced in Section 5.3. Also in this section, there is a discussion on how to identify likely members when no such diagnostics are available. The recalibration of the pre-MS evolutionary models using the K_s-band luminosity and observed colours of Pleiades members is described in Section 5.4. Section 5.5 discusses the colour and intrinsic dependence of the reddening vector in the pre-MS regime and how this is incorporated into the pre-MS evolutionary models. Pre-MS ages for the SFRs are then derived in Section 5.6. Finally, Section 5.7 summarises the chapter.

5.2 Observations and Data Reduction

The observations for the young SFRs were taken over the course of the two observing runs discussed in Section 3.2, with the exposure times for each SFR shown in Table A.1. The data were reduced as described in Section 3.3, and where necessary (e.g. σ Ori and λ Ori), a normalisation procedure (Jeffries et al. 2004) was applied to create a single photometric catalogue of the surveyed region. For Cep OB3b, χ Per, IC 5146, λ Ori Field A, and NGC 6611 observations were taken on two separate nights for which there is a photometric solution. The two sets of observations were reduced separately and a normalisation procedure performed on the two optical photometric catalogues, so that the zero-point is the average from the two nights. As discussed in Section 3.3, the calculated zero-point shift is a good indicator of the internal consistency of the photometry, as well as the accuracy with which the profile corrections were performed. For regions where the normalisation procedure was used an accuracy of $2 - 3\,\%$ was found across all colours g_{WFC}, $(g - i)_{\mathrm{WFC}}$, $(U - g)_{\mathrm{WFC}}$, $(r - i)_{\mathrm{WFC}}$, and $(i - Z)_{\mathrm{WFC}}$.

For the field-of-view centred on IC 348, in all but the central CCD there were too few stars to create the profile correction necessary to correct the optimal photometry. Whilst a profile correction could be created in the central CCD (accurate to $\simeq 0.3\,\%$), there was no point in relaxing this condition in the other CCDs as there were too few stars about the immediate cluster. Hence for stars in these regions aperture photometry was performed with the radius of the aperture matching that used in the case of the profile correction (15 pixels). The resultant fluxes were then processed in an identical manner to that in the standard reduction. The only difference is that the non-stellar flag 'N' is now based on the ratio of the flux measured through an aperture of radius 15 pixels and the flux measured through an aperture of half this radius. To create the final optical photometric catalogue, all stars flagged as 'H' (poor profile correction) in the optimally extracted catalogue were replaced with measurements based on the aperture photometric reduction.

Contrastingly, in the central CCD of the ONC it was impossible to find enough uncrowded stars within a 15 pixel aperture and therefore a radius of 7 pixels was used instead. By decreasing the radius of the aperture, some light from the stars about which the aperture was placed will be lost and hence the profile correction was not as good as for the other SFRs. Therefore, the condition for an acceptable profile correction was relaxed to $2\,\%$ (nominally $0.3\,\%$). Moreover, as the standard 15 pixel aperture was used for extracting the colours and magnitudes of the standard stars, a systematic offset between the standard stars and the ONC object stars – on the order of $0.2\,\mathrm{mag}$ in all bandpasses – was calculated based on the comparison of derived magnitudes extracted with the two different sized apertures for the same stars. Apart from the reduced aperture size and the relaxed criterion for the profile correction, the measured fluxes were measured using exactly the same method as for the standard reduction.

5.3 Isolating the Pre-Main-Sequence

Many of the SFRs studied in the sample lie in or near the Galactic plane and as such a CMD for a given field-of-view will contain a high number of field star contaminants. Thus before an age can be estimated by fitting model isochrones to the data, the issue is first to identify bona fide pre-MS members.

Pre-MS stars exhibit several characteristics that highlight their youth (see Section 1.4) which can be used to separate them from the field stars. Note however that these indicators only differentiate between different types of stellar populations and not between distinct young populations (see for example Jeffries et al. 2006). In most cases, literature sources were used to identify members, however in the case of of χ Per where no robust literature memberships were available, an approach based on relative positions on the sky to identify possible members was used instead. This method has the obvious drawback of including a higher fraction of non-members into the selection.

5.3.1 Literature Memberships

In this section the literature memberships used for the identification of pre-MS stars in the sample of SFRs are described. Table 5.1 shows the various membership indicators for each SFR with associated references.

5.3.1.1 Cep OB3b

X-ray members are from Naylor & Fabian (1999) and Getman et al. (2006) using the ROSAT PSPC and *Chandra*/ACIS instruments respectively. A combination of both sources was used as the area covered by the ROSAT pointing is larger than the *Chandra* field-of-view. For stars common to both catalogues, the positions were taken from the *Chandra* dataset due to the improved spatial resolution and sensitivity.

Spectroscopic members are taken from Pozzo et al. (2003). They took spectra of objects within an initial photometric cut made in the $V, V - I_c$ CMD, with a $B - V, V - I_c$ colour-colour diagram using optical counterparts to the Naylor & Fabian (1999) ROSAT sources to identify regions with a high fraction of probable members. Spectroscopic follow-up measurements provided $W_\lambda(\text{Li\,I})$, $W_\lambda(\text{H}\alpha)$ and radial velocities. Memberships were assigned based on the comparison between individual radial velocities and the group mean, in addition to strong spectroscopic features. Additional Hα members are from Ogura et al. (2002) which comprise a subset of a Herbig-Haro object survey observed using a narrowband Hα filter ($\Delta\lambda = 100\,\text{Å}$).

Periodic variables are from an I-band variability study by Littlefair et al. (2010). A recent *Spitzer*/IRAC and MIPS study (Allen et al. 2012) has demonstrated that the young stars within the cluster are concentrated into two sub-clusters – an Eastern sub-cluster near the Cep B molecular cloud and a Western sub-cluster near the Cep F molecular cloud. The literature memberships listed above only cover the Eastern sub-cluster, whereas the variability study of Littlefair et al. (2010) covers both sub-clusters. To not bias the

Table 5.1: Literature sources used in the identification of pre-MS stars in the sample of SFRs.

SFR	Membership type	Source
Cep OB3b	X-ray (ROSAT)	Naylor & Fabian (1999)
	X-ray (*Chandra*)	Getman et al. (2006)
	Spectroscopic (Li I, Hα)	Pozzo et al. (2003)
	Hα	Ogura et al. (2002)
	Periodic variability	Littlefair et al. (2010)
IC 348	Spectroscopic (Hα)	Herbig (1998)
	Spectroscopic (Hα, Na I, K I)	Luhman et al. (2003, 2005a,b)
	X-ray (*Chandra*)	Preibisch & Zinnecker (2002)
	X-ray (ROSAT)	Second ROSAT PSPC catalogue
	Periodic variability	Cohen et al. (2004)
	Periodic variability	Littlefair et al. (2005)
IC 5146	Spectroscopic (Hα)	Herbig & Dahm (2002)
	IR excess	Harvey et al. (2008)
λ Ori	Spectroscopic (Li I)	Dolan & Mathieu (1999, 2001)
	Spectroscopic (Hα)	Barrado y Navascués et al. (2004a)
	Spectroscopic (Li I, Hα)	Sacco et al. (2008)
	IR excess	Barrado y Navascués et al. (2007)
	X-ray (XMM-*Newton*)	Barrado et al. (2011)
NGC 1960	Spectroscopic (Li I)	Jeffries et al. (in preparation)
NGC 2169	Spectroscopic (Li I)	Jeffries et al. (2007)
NGC 2244	X-ray (*Chandra*)	Wang et al. (2008)
	IR excess	Balog et al. (2007)
NGC 2362	Spectroscopic (Li I, Hα)	Dahm (2005)
	X-ray (*Chandra*)	Damiani et al. (2006b)
	IR excess	Dahm & Hillenbrand (2007)
NGC 6530	X-ray (*Chandra*)	Damiani et al. (2004)
	Spectroscopic (Li I, Hα)	Prisinzano et al. (2007)
	Periodic variability	Henderson & Stassun (2012)
NGC 6611	X-ray (*Chandra*)	Guarcello et al. (2007)
	IR excess	Guarcello et al. (2009)
NGC 7160	Spectroscopic (Li I, Hα) and extinction	Sicilia-Aguilar et al. (2004, 2005)
	IR excess	Sicilia-Aguilar et al. (2006a)
ONC	Periodic variability	Rebull (2001)
	Periodic variability	Herbst et al. (2002a)
	IR excess	Rebull et al. (2006a)
	X-ray (*Chandra*)	Getman et al. (2005)
σ Ori	Spectroscopic (Li I, Na I)	Kenyon et al. (2005)
	Spectroscopic (Li I, Na I)	Burningham et al. (2005b)
	Spectroscopic (Li I, Hα)	Sacco et al. (2008)
	X-ray (XMM-*Newton*)	Sanz-Forcada et al. (2004)
	Periodic and aperiodic variability	Cody & Hillenbrand (2010)
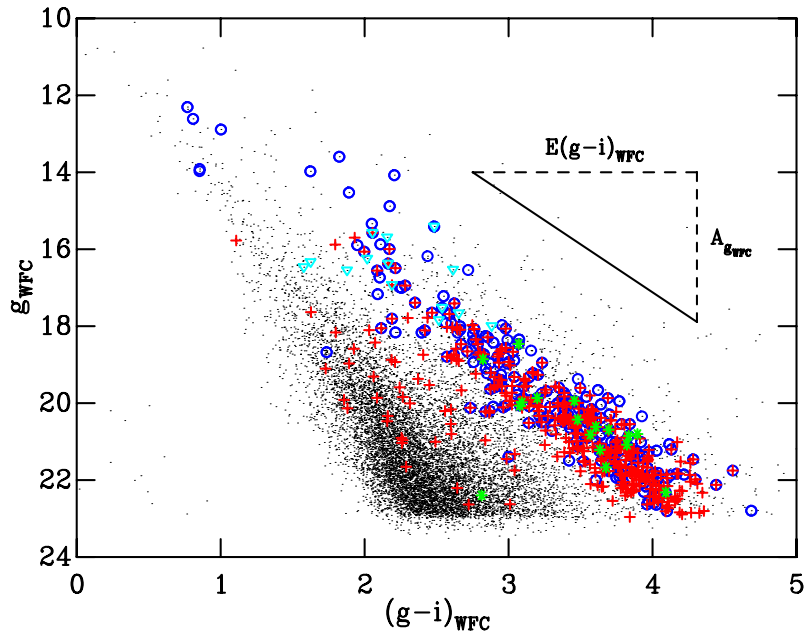
Figure 5.1: The $g_{\mathrm{WFC}}, (g-i)_{\mathrm{WFC}}$ CMD of Cep OB3b with literature members overlaid. Crosses are the periodic variable members from Littlefair et al. (2010), circles are X-ray sources from Naylor & Fabian (1999) and Getman et al. (2006), asterisks are spectroscopic members from Pozzo et al. (2003), and triangles are Hα sources from Ogura et al. (2002). The diagonal line represents the reddening vector for a star with $T_{\mathrm{eff}} \simeq 4500\,\mathrm{K}$ and $\log g \simeq 4$ based on the median value of $E(B-V) = 0.89$ derived in Section 2.8.4.1.

selection of pre-MS members, the positions on the sky of the other literature sources were used to define a region within which variability members were adopted. An example of the $g_{\mathrm{WFC}}, (g-i)_{\mathrm{WFC}}$ CMD for Cep OB3b with the literature members overlaid is shown in Fig. 5.1.

5.3.1.2 IC 348

Hα members are taken from Herbig (1998) who carried out a wide-field grism spectrograph survey of the region, discarding stars with $W_\lambda(\mathrm{H}\alpha) < 2\,\text{Å}$. Spectral types – through comparison to dwarf spectral standards – and extinctions were derived for 80 of these stars using follow-up spectroscopy. Additional spectroscopic members are taken from Luhman et al. (2003, 2005a,b). Memberships were assigned using a combination of spectral types, spectral features (Hα, Na I, and K I) and positions within extinction-corrected CMDs.

X-ray members are from Preibisch & Zinnecker (2002) taken with the *Chandra*/ACIS detector (supplemented with additional data from the Second ROSAT PSPC catalogue[11]).

Periodic variables are from Cohen et al. (2004) and Littlefair et al. (2005), both of which are based on wide-field *I*-band surveys.

---

[11]`http://ledas-www.star.le.ac.uk/rosat/rra/`

5.3.1.3   IC 5146

Hα members are taken from Herbig & Dahm (2002) who conducted a wide-field grism spectrograph survey to identify emission stars to a limit of $W_\lambda(\text{H}\alpha) \simeq 3\,\text{Å}$ and limiting magnitude of $R_{\text{c}} = 20.5$. Only stars with $W_\lambda(\text{H}\alpha) > 5\,\text{Å}$ and that lie above the Pleiades MS at a distance of $1.2\,\text{kpc}$, as described in Herbig & Dahm (2002), were used.

Additional IR excess members are based on the *Spitzer*/IRAC and MIPS photometry of Harvey et al. (2008). The identification of YSOs from *Spitzer* data is generally based on some combination of IR excess in addition to a brightness limit (set by the limiting magnitude fainter than which extragalactic contamination becomes too high to reliably distinguish between objects). A combination of colour-colour diagrams and CMDs were used to identify predominantly Class I and Class II objects.

5.3.1.4 λ Ori

Lithium (Li I) abundance members come from Dolan & Mathieu (2001), which extended the previous study of Dolan & Mathieu (1999). An initial photometric cut for stars with $12 \leq R_{\text{c}} \leq 16$ was made, with the probable cluster members chosen based on their position relative to a $30\,\text{Myr}$ isochrone in the $R_{\text{c}}, (R-I)_{\text{c}}$ CMD. Follow-up spectroscopic measurements were taken and $W_\lambda(\text{Li I})$ was used as a youth indicator, where stars with $W_\lambda(\text{Li I}) \geq 0.2\,\text{Å}$ were retained as members.

Additional spectroscopic members come from Barrado y Navascués et al. (2004a) where optical $(RI)_{\text{c}}$ photometry was combined with near-IR 2MASS JHK_{s} data to initially identify possible member candidates in CMD space. Follow-up spectroscopic measurements were taken to determine $W_\lambda(\text{H}\alpha)$. Memberships were assigned to those stars that satisfied both spectroscopic and photometric criteria. Later, Barrado y Navascués et al. (2007) used *Spitzer*/IRAC photometry to identify probable low-mass members based on IR excess using IRAC colour-colour diagrams in conjunction with optical and IR CMDs. Further members are from the spectroscopic study of Sacco et al. (2008) who measured both $W_\lambda(\text{Li I})$ and $W_\lambda(\text{H}\alpha)$ in addition to radial velocities. Final membership is based on a combination of individual candidate velocities that are consistent with the cluster dispersion, the presence of strong $W_\lambda(\text{Li I})$ and the presence of strong Hα emission.

X-ray members are taken from Barrado et al. (2011) observed using the XMM-*Newton*/EPIC detector.

5.3.1.5   NGC 1960

Spectroscopic members come from an upcoming paper by Jeffries et al. (in preparation). Optical VI_{c} photometry was used to identify possible cluster members from their position in CMD space, selecting objects with $14 < V < 18.5$. Spectroscopic measurements were used to identify the presence of Li I and derive radial velocities. Objects identified with strong Li I features were cross-correlated against the PPMXL catalogue (Roeser et al. 2010) adopting the central cluster proper motion – $\mu_\alpha \cos\delta = 2.9 \pm 2.7\,\text{mas}\,\text{yr}^{-1}$ and

$\mu_\delta = -8.0 \pm 2.5 \, \mathrm{mas \, yr^{-1}}$ – as derived by Sanner et al. (2000). Those that were consistent within the uncertainties were retained as likely members.

5.3.1.6   NGC 2169

Spectroscopic members are from Jeffries et al. (2007) in which optical $(RI)_\mathrm{c}$ photometry was used to highlight possible cluster members from their position in CMD space. Follow-up spectroscopic observations were made to identify the presence of Li I and Hα in addition to measuring radial velocities. A combination of all three diagnostics were used to assign final memberships.

5.3.1.7   NGC 2244

X-ray members are from Wang et al. (2008) taken with the *Chandra*/ACIS instrument. Cross-correlation against existing photometric studies showed that, when plotted in the $J-H, H-K_\mathrm{s}$ colour-colour diagram, the majority of X-ray sources occupy a region indicative of disc-less Class III objects. A significant fraction of sources were also identified as having a K_s-band excess and are thus believed to be pre-MS stars harbouring circumstellar discs.

Additional IR excess sources are taken from Balog et al. (2007) who use *Spitzer*/IRAC and MIPS photometry to identify the Class I and Class II populations using IR colour-colour diagnostics.

5.3.1.8   NGC 2362

Spectroscopic members are taken from Dahm (2005). He used a wide-field Hα survey to identify probable cluster members that lay above the ZAMS in the $V, V - I_\mathrm{c}$ CMD. Spectroscopic follow-up on these objects was used to ascertain the presence of Li I and Hα features. *Spitzer*/IRAC photometry (Dahm & Hillenbrand 2007) was used in conjunction with existing Hα emission data, optical $V(RI)_\mathrm{c}$ and near-IR JHK photometry, and moderate-resolution spectroscopy to identify the disc-bearing population.

X-ray members are from Damiani et al. (2006b) taken with the *Chandra*/ACIS detector. They find that 88 % of the X-ray sources have optical counterparts that are good candidate low-mass pre-MS stars based on their position in the $V, V - I_\mathrm{c}$ CMD.

5.3.1.9   NGC 6530

X-ray members are from the *Chandra*/ACIS observations of Damiani et al. (2004). Prisinzano et al. (2005) used this data, alongside optical BVI_c photometry, to assign pre-MS status to approximately 90 % of the identified X-ray sources, based on their position in the $V, V - I_\mathrm{c}$ CMD. Spectroscopic follow-up on a subset of candidate members was performed by Prisinzano et al. (2007) to identify $W_\lambda(\mathrm{Li \, I})$, $W_\lambda(\mathrm{H}\alpha)$ and measure radial velocities. These were combined with the X-ray catalogue to compile a list of cluster members. Extinction-free Q indices (analogous to the Johnson Q index; see Damiani et al. 2006a) were used, in conjunction with optical BVI_c and 2MASS JHK_s photometry, to identify

sources with IR excess (the Hα spectra were used to differentiate between CTTS and WTTS).

Periodic variables are from the wide-field, high-cadence I_c-band variability study of Henderson & Stassun (2012).

5.3.1.10 NGC 6611

Members are taken from the studies of Guarcello et al. (2007, 2009). Guarcello et al. (2007) compiled a multiband photometric catalogue including measurements in the optical BVI_c and near-IR 2MASS JHK_s bandpasses. These were supplemented by *Chandra*/ACIS X-ray observations (Linsky et al. 2007). Stars with circumstellar discs were identified using extinction-free Q indices (Damiani et al. 2006a) using a combination of optical and near-IR colour indices. A lower Q index limit corresponding to photospheric emission was computed using the MS colours of Kenyon & Hartmann (1995). Near-IR excess was identified on the basis that the Q index is smaller than the photospheric limit by $3\sigma_Q$, where σ_Q is the mean error in Q. Stars with circumstellar discs were then cross-correlated against the X-ray catalogue of Linsky et al. (2007). X-ray sources with neither an optical nor a 2MASS counterpart were not considered members. Furthermore, X-ray sources that appeared to lie in an area dominated by foreground objects in the $V, V - I_c$ CMD were also classified as non-members. Guarcello et al. (2009) extended this membership list using *Spitzer*/IRAC data. Stars with circumstellar discs were identified using a combination of IRAC colour-colour diagrams and the extinction-free Q indices.

5.3.1.11 NGC 7160

Members are taken from the studies of Sicilia-Aguilar et al. (2004, 2005, 2006a). An initial photometric cut was made in the $V, V - I_c$ CMD to rule out stars near or below the SDF00 ZAMS, assuming an average extinction for all stars. This selection was further refined using optical $(RI)_c$ variability. Spectroscopic measurements of $W_\lambda(\text{Li\,{\sc i}})$ and $W_\lambda(\text{H}\alpha)$ were used to assign memberships to probable candidates. The spectroscopic observations were used to calculate spectral types and extinctions for these sources. Final membership is based on the standard deviation (σ) from the average cluster extinction, which naturally relies on the adopted spectral typing and intrinsic colours. Retained members are those that lie within 1σ of the average extinction.

5.3.1.12 Orion Nebula Cluster

Periodic variables are from the *I*-band variability studies of Rebull (2001) and Herbst et al. (2002a) who observed the ONC flanking fields and the ONC inner core respectively. IR excess members are taken from the *Spitzer*/IRAC photometry of Rebull et al. (2006a), with IRAC colour-colour diagrams used to identify stars with and without circumstellar discs. X-ray members are from the COUP observations of Getman et al. (2005) using the ACIS instrument.

5.3.1.13 σ **Ori**

Spectroscopic members are taken from Kenyon et al. (2005) and Burningham et al. (2005b). In Kenyon et al. (2005) a photometric cut was made to select stars lying close to a 5 Myr BCAH98 isochrone in the range $14.8 \leq I_c \leq 18.2$ in the $I_c, (R-I)_c$ CMD. Spectroscopic follow-up was used to measure $W_\lambda(\text{Li\,I})$, $W_\lambda(\text{Na\,I})$ and radial velocities. Membership was assigned on the basis that the radial velocity and the gravity sensitive Na I doublet measurements were coincident with the cluster mean, in addition that $W_\lambda(\text{Li\,I}) \geq 0.2\,\text{Å}$. Similarly, Burningham et al. (2005b) initially used a photometric cut to select candidate members, however a broader selection – in terms of colour range for a given magnitude; see their Fig. 1 – was chosen to compliment those already observed by Kenyon et al. (2005). Membership status was again based on radial velocities, $W_\lambda(\text{Na\,I})$ and $W_\lambda(\text{Li\,I})$. The study of Burningham et al. (2005b) found additional low-mass pre-MS members of σ Ori, however, none of these occupied CMD space outside of the more restrictive photometric cut of Kenyon et al. (2005), suggesting that photometric selection techniques do not miss significant numbers of bona fide members. Members from Kenyon et al. (2005) were only used if they satisfied all selection criteria, however only those with a membership probability greater than $80\,\%$ were used from Burningham et al. (2005b). Additional spectroscopic members are from Sacco et al. (2008) who use the criteria as described in Section 5.3.1.4.

X-ray members are taken from Sanz-Forcada et al. (2004) using the XMM-*Newton*/EPIC detector. Positions of X-ray sources have been cross-correlated against the optical photometric catalogue.

Periodic and aperiodic variability members are from Cody & Hillenbrand (2010) based on high-precision, high-cadence I_c-band photometric monitoring.

As discussed in Jeffries et al. (2006), the pre-MS members of the σ Ori association are split into two kinematically distinct sub-groups, concluding that; i) the two groups have a different spatial distribution, ii) on average Group 1 (as defined by Jeffries et al.) is older than Group 2, but by an uncertain amount, and iii) the two groups occupy similar positions in the CMD. Furthermore, they conclude that Group 1 is associated with either Orion OB1a or Orion OB1b (or more likely a mixture of the two), whereas Group 2 is clustered around σ Ori. At declinations less than $\delta_{\text{J2000.0}} = -02° 18' 00.0''$ the region is dominated by members of Group 2. From the membership selections used above all but six stars lie in this region (these have subsequently been removed).

5.3.1.14 Inherent Biases

In Section 1.4 the various youth diagnostics were discussed along with the inherent biases associated with each method. To derive consistent pre-MS ages from the CMDs of such populations it is vital that these biases be understood, and if possible minimised. In brief, IR excesses predominantly identify objects with circumstellar discs, X-rays are more likely to select stars that are not actively accreting, Hα is biased towards stars that are actively

accreting, and periodic variability preferentially selects WTTS (although CTTS can be identified if the temporal density of observations is sufficiently high; e.g. Littlefair et al. 2010). Members that have been selected via non-spectroscopic methods are more likely to suffer from foreground and background Galactic contamination (e.g. distant active Galactic nuclei or young field stars).

Spectroscopic measurements are the only unbiased diagnostic, however herein lies a subtle bias which can be introduced through a pre-selection of candidate targets. Full spectroscopic coverage of all stars in a given field-of-view is unfeasible and so a subset of stars is chosen, generally based on their positions in CMD space. This therefore introduces an inherent bias into the observed subset of stars, however as demonstrated by the studies of Kenyon et al. (2005) and Burningham et al. (2005b), even adopting a relatively conservative photometric selection does not exclude a statistically significant number of members, and hence the observed pre-MS locus is largely unbiased by such pre-selection.

5.3.2 Isolating the Pre-Main-Sequence Without Literature Memberships

There is a lack of bona fide pre-MS member diagnostics for χ Per. The so-called 'spectroscopically confirmed' members of Currie et al. (2010) are not based on the presence of spectral features – such as Li I or Hα – but represent a sequence defined by a combined 14 Myr MS and pre-MS isochrone in the de-reddened V-band magnitude versus spectral type diagram. The width of this sequence was determined by; i) the physical extent of the cluster, ii) binarity, and iii) uncertainties in the derived spectral types. Cross-correlation of the Currie et al. (2010) members with the optical photometric catalogue presented here results in a poorly defined pre-MS locus with less than 10 stars occupying the single-star sequence at magnitudes $g_{\mathrm{WFC}} > 18$.

The photometric catalogue extends to $g_{\mathrm{WFC}} \simeq 22.5$ and therefore stellar positions on the sky were instead used to choose an area that minimises foreground/background contamination (see Mayne et al. 2007). Fig. 5.2 shows the $g_{\mathrm{WFC}}, (g - i)_{\mathrm{WFC}}$ CMD of χ Per with the sequence clearly visible throughout the entire CMD. Stars brighter than $g_{\mathrm{WFC}} \simeq 14$ lie blueward of the contamination and thus represent a subset of the χ Per stellar population where the field star contamination is minimal. Fig. 5.3 shows that the positions of the bright stars overlaid on the positions of the entire photometric catalogue. Circular positional selections from 5′ down to 1′ in increments of 1′ were made around the central cluster coordinates of $\alpha_{\mathrm{J2000.0}} = 02^{\mathrm{h}} 22^{\mathrm{m}} 05.02^{\mathrm{s}}, \delta_{\mathrm{J2000.0}} = +57° 07′ 43.44″$ (Mayne et al. 2007) and the resulting sequence visually examined (by-eye). The best results – fraction of candidate member-to-field stars – was found for a radius of 3′. To ensure that the selection of the cluster centre was not biased, the positions of proper motion members from Uribe et al. (2002) and likely members based on spectral types from Slesnick et al. (2002) were also overlaid. In both cases, the central coordinates from each source were almost identical.
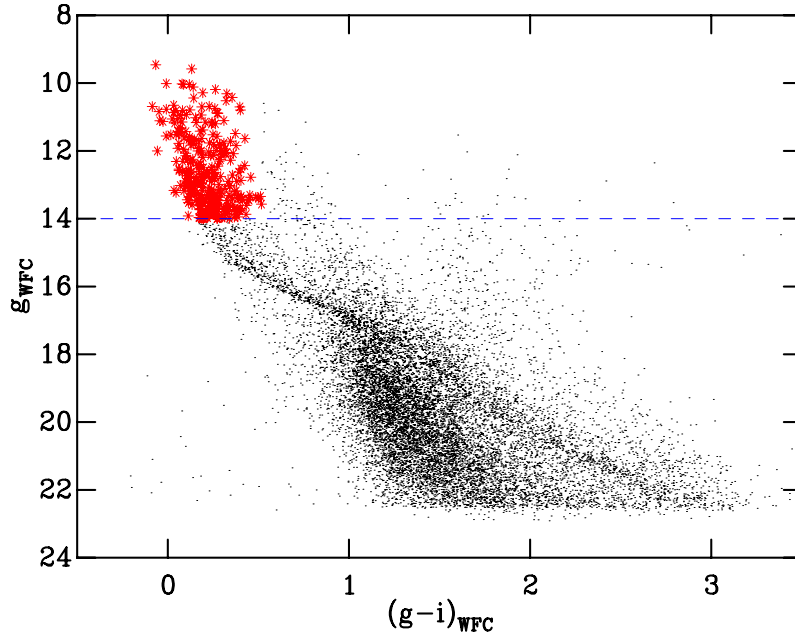
Figure 5.2: The $g_{\mathrm{WFC}}, (g-i)_{\mathrm{WFC}}$ CMD of χ Per. The dashed line denotes the bright stars ($g_{\mathrm{WFC}} < 14$) which lie blueward of the contamination. Asterisks represent stars used for the identification of the cluster based on sky positions.
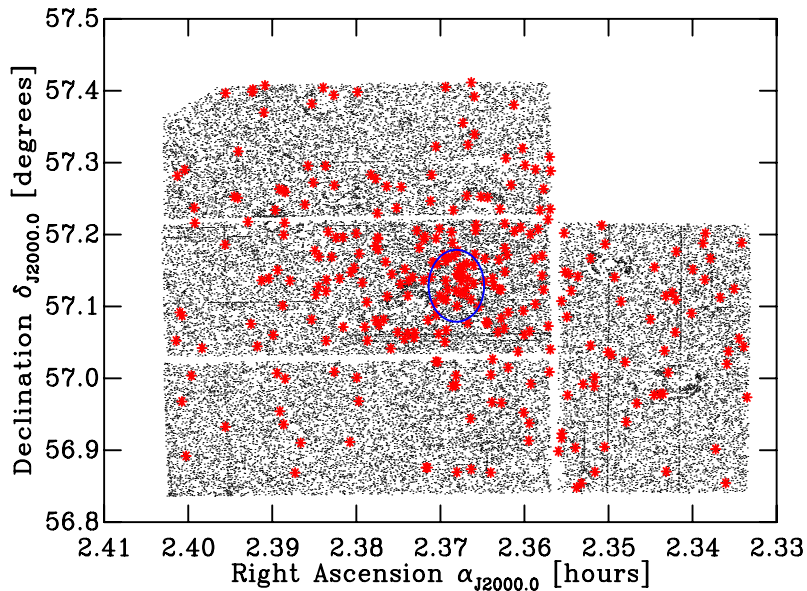
Figure 5.3: The sky positions of all stars in the photometric catalogue of χ Per. The asterisks are the bright stars ($g_{\mathrm{WFC}} < 14$) and the ellipse represents the region selected based on iterative radial cuts.

5.4 A Semi-Empirical Bolometric Correction-T_{eff} Relation

One approach to overcoming the difficulties in fitting pre-MS model isochrones to young stellar populations is to use an empirical sequence at a given age to 'tune' the model isochrones and then apply these recalibrated models to younger SFRs. In Section 4.5, the discrepancy between the models and the data was quantified as a function of T_{eff} in individual bandpasses, and in doing so, a set of model dependent empirical corrections have effectively been derived. These can then be applied to the original theoretical relation to create a BC-T_{eff} relation that can transform the evolutionary models so as to fit the observed Pleiades sequence at an age of 130 Myr. The concept of recalibrating a BC-T_{eff} relation based on the Pleiades – also known as 'Pleiades tuning' – is not a particularly new idea, having been proposed in Stauffer et al. (1998) and utilised by Jeffries et al. (2001) to determine cluster parameters including the luminosity and mass function of NGC 2516, which is of a similar age to the Pleiades. The original technique is fully described in Jeffries et al. (2001), however it shall be briefly discussed here again as in doing so two distinct differences between the original and the revised approach will be identified.

5.4.1 The Jeffries et al. Empirical Recalibration

A Pleiades catalogue consisting of BVI photometry was obtained from the Open Cluster Database (maintained and operated by J. Stauffer and C. Prosser). This was supplemented with additional photometry for cooler members, with the $V - I$ indices transformed from the observed Kron into the Cousins system using the relation of Bessell & Weis (1987). It was assumed that there is a single colour-T_{eff} relation that applies to all stars at the approximate age of the Pleiades, for which Jeffries et al. (2001) adopted an age of 120 Myr, a distance modulus $dm = 5.6$, and a reddening $E(B - V) = 0.04$ ($E(V - I_{\mathrm{c}}) = 0.05$) and an extinction of $A_V = 0.13$. A spline was fitted (by-eye) to both the $V, B - V$ and $V, V - I_{\mathrm{c}}$ Pleiades sequences. At points along this spline absolute magnitudes and intrinsic colours were defined. The magnitudes were then converted into L_{bol} using empirical MS bolometric correction-colour relationships. At the assumed age of the Pleiades (120 Myr), the outputs of theoretical evolutionary models were used to determine a T_{eff} value appropriate for a particular L_{bol}. This then defines a set of colour-T_{eff} points that can be used to transform the models into CMD space, thereby producing recalibrated isochrones over the colour range of the Pleiades dataset or mass range of the model isochrone.

Whilst this technique is based on empirical data, there are two obvious shortcomings. First, Jeffries et al. (2001) assume that the empirical BC$_V$ relation for MS stars is correct (at an age of 120 Myr). Thinking in terms of bolometric corrections, and concentrating on the $V, V - I_{\mathrm{c}}$ recalibration, by essentially fixing BC$_V$ as a function of colour (and hence T_{eff}), Jeffries et al. have therefore recalibrated the BC$_{I_{\mathrm{c}}}$-T_{eff} relation using the observed Pleiades sequence i.e. the recalibrated $V - I_{\mathrm{c}}$ colour-T_{eff} relies on a combination of MS and pre-MS bolometric corrections. The implicit assumption that the MS empirical BC$_V$ relation is correct may also affect masses derived from the recalibrated models. Typically,

the mass of a given star would be estimated by using the absolute magnitude of a star (at a given colour). The appropriate BC_V would be used to determine the bolometric magnitude ($M_{\rm bol}$) and the mass would then be read from the evolutionary models. Whilst this technique is unlikely to affect derived masses for stars of ages of the Pleiades and older, atmospheric models suggest that the $\log g$ dependence of the BC_V-$T_{\rm eff}$ relation could result in masses that are systematically underestimated, especially in the low $T_{\rm eff}$ regime ($T_{\rm eff} \lesssim 4000\,{\rm K}$).

Second, it is well known that the colour-$T_{\rm eff}$ relation does not remain constant as a function of age. The relation in the pre-MS regime is sensitive to age, changing as the star descends its Hayashi track towards the ZAMS. Spectral line strengths are determined by the electron pressure in the stellar atmosphere and are thus strongly dependent upon $\log g$. During contraction in the pre-MS phase, $\log g$ increases leading to variations in line strengths of spectral lines and ultimately changes in the colour of the star. Based on the interior and atmospheric models, for a given $T_{\rm eff}$, there is a difference in colour of $(g - i)_{\rm WFC} \simeq 0.15 - 0.2\,{\rm mag}$ between a star at an age of $1\,{\rm Myr}$ ($\log g \simeq 3.5$) and a star on the ZAMS ($\log g \simeq 5.0$). The colour-$T_{\rm eff}$ relation defined by the technique of Jeffries et al. (2001) corresponds to a specific set of $\log g$ colours for given $T_{\rm eff}$ values. Hence at younger ages, the $\log g$ for a star of given mass will be lower than at an age of $120\,{\rm Myr}$ and thus the colour of the star does not correspond to that defined by the recalibrated colour-$T_{\rm eff}$ relation.

5.4.2   A Revised Semi-Empirical Recalibration

By using the $K_{\rm s}$-band magnitude of Pleiades members to quantify the discrepancy, and thereby define the required adjustment to the BC-$T_{\rm eff}$ relation necessary to fit the observed sequence, the mass and $T_{\rm eff}$ scales have effectively been calibrated to that of the Pleiades. The $K_{\rm s}$-band is more sensitive to circumstellar material than either the J- or H-band, however at an age of $\simeq 130\,{\rm Myr}$ the contribution from such material will be minimal (Meyer & Beckwith 2000; Stauffer et al. 2005) and thus not affect the derived ΔBC corrections.

By defining a polynomial colour-$T_{\rm eff}$ relation at a fixed age of $120\,{\rm Myr}$ the Jeffries et al. (2001) technique should not be applied to stars younger than $120\,{\rm Myr}$, unless it is used under the erroneous assumption that the colour-$T_{\rm eff}$ relation is age insensitive. An attempt to incorporate the $\log g$ dependence at younger ages can be made by positing that the *absolute* adjustment to the BC-$T_{\rm eff}$ relation required for the Pleiades is valid for *all* ages i.e. the absolute shift applied is age insensitive. Due to a lack of additional information concerning how ΔBC varies as a function of $\log g$, the dependence on $\log g$ as defined by the calculated bolometric corrections is adopted. This is termed a semi-empirical recalibration to distinguish it from the original Jeffries et al. technique. It is worth stressing the point that creating isochrones for younger pre-MS populations does not require the use of the apparent $K_{\rm s}$-band magnitudes and hence any derivations of either age or mass are not affected by the likely contamination in the $K_{\rm s}$-band due to

circumstellar material.

5.5   Reddening and Extinction for Pre-Main-Sequence Stars

In Section 2.7.1, the causes of non-linear trajectories in the $U - B, B - V$ colour-colour diagram were discussed and hence updated reddening vectors were derived using the atmospheric models, photometric system responses and the reddening law of Cardelli et al. (1989) that explicitly incorporated the intrinsic colour and reddening of the source. Figs. 5.4 and 5.5 show how the calculated extinction and reddening, in the g_{WFC}-band and $(g - i)_{\mathrm{WFC}}$ colour respectively, vary as a function of T_{eff} for stars with $2000 \leq T_{\mathrm{eff}} \leq 20\,000\,\mathrm{K}$ for a nominal $E(B - V) = 0.5$. For hot stars ($T_{\mathrm{eff}} > 10\,000\,\mathrm{K}$) there is little variation at higher T_{eff} in the calculated extinction and reddening, thus one can reliably derive reddening vectors for stars in this regime that apply over a large T_{eff} (or equivalently spectral type) range. The same, however, is not true for cool stars where a difference in the extinction of $\simeq 0.1\,\mathrm{mag}$ and reddening of $\simeq 0.04\,\mathrm{mag}$ is calculated between stars of $T_{\mathrm{eff}} = 3000$ and $T_{\mathrm{eff}} = 10\,000\,\mathrm{K}$. This not only demonstrates that applying the extinction and reddening derived from high-mass stars in a given SFR to those in the low-mass regime is incorrect, but furthermore that the same reddening vectors should not be used for all spectral types.

    The colour and reddening dependence of the extinction in a given photometric bandpass means that accounting for reddening in the pre-MS regime is more complex. The pre-MS population is predominantly late spectral types and thus – as shown in Figs. 5.4 and 5.5 – the associated extinction and reddening are lower than for the high-mass stars. Without spectra for a large sample of objects in a given field-of-view, it is not possible to de-redden sources on an individual basis and then fit the isochrones in the extinction-corrected CMD. Instead, the model isochrone must be appropriately reddened and then applied to the photometric data. The only consistent and homogeneous way to redden the pre-MS isochrones, as a function of T_{eff}, is to create extinction grids based on atmospheric models, the photometric system responses and a description of the interstellar extinction law. The atmospheric models were reddened according to the parameterised extinction law of Cardelli et al. (1989) and folded through the calculated INT-WFC system responses. The models were reddened in steps of 0.5 from a nominal $E(B - V) = 0.0$ to 2.0, with the grids comprising extinction in all five INT-WFC bandpasses as a function of T_{eff} and $\log g$ (both of which come from the atmospheric models). Thus to redden a pre-MS isochrone, the reddening derived from the more massive MS members (see Table 2.2) is used to calculate a nominal $E(B - V)$ that represents the column density of interstellar material between the Earth and the star (see Fig. 2.3). This nominal $E(B - V)$ is then used to interpolate within the extinction grids for the extinction and reddening – difference in extinction between two photometric bandpasses – for a star of given T_{eff} and $\log g$ as defined by the pre-MS interior models. This process is then repeated for each point along the model isochrone.
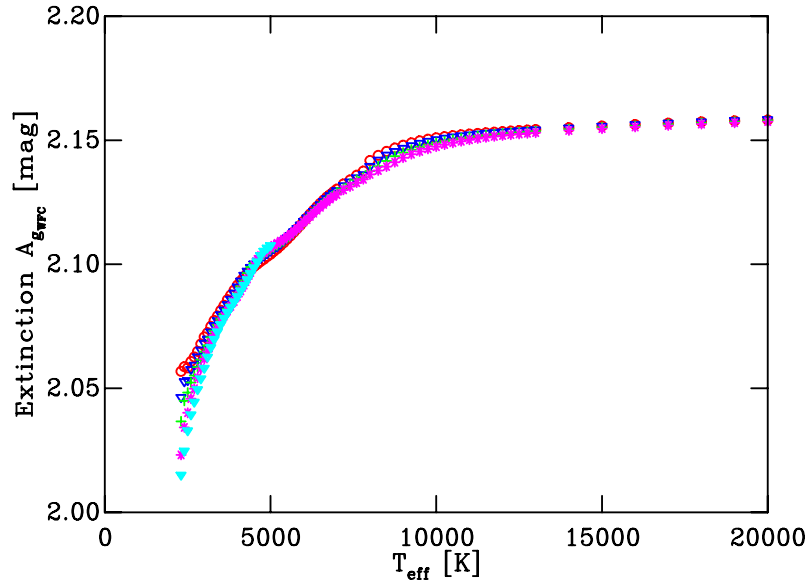
Figure 5.4: The variation in $A_{g_{\mathrm{WFC}}}$ as a function of T_{eff} between 2000 and 20 000 K for a nominal $E(B - V) = 0.5$ calculated using the atmospheric models and the interstellar extinction law of Cardelli et al. (1989). The different colour symbols represent different surface gravities – $\log g = 3.5$ (red), 4.0 (blue), 4.5 (green), 5.0 (magenta), and 5.5 (cyan).
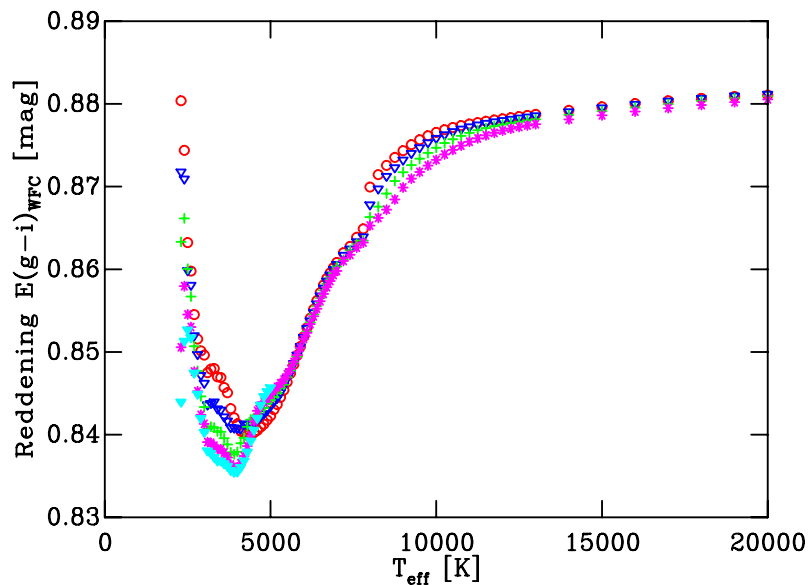
Figure 5.5: Same as Fig. 5.4 but showing the variation in $E(g - i)_{\mathrm{WFC}}$ as a function of T_{eff}. The different colour symbols are the same as in Fig. 5.4.
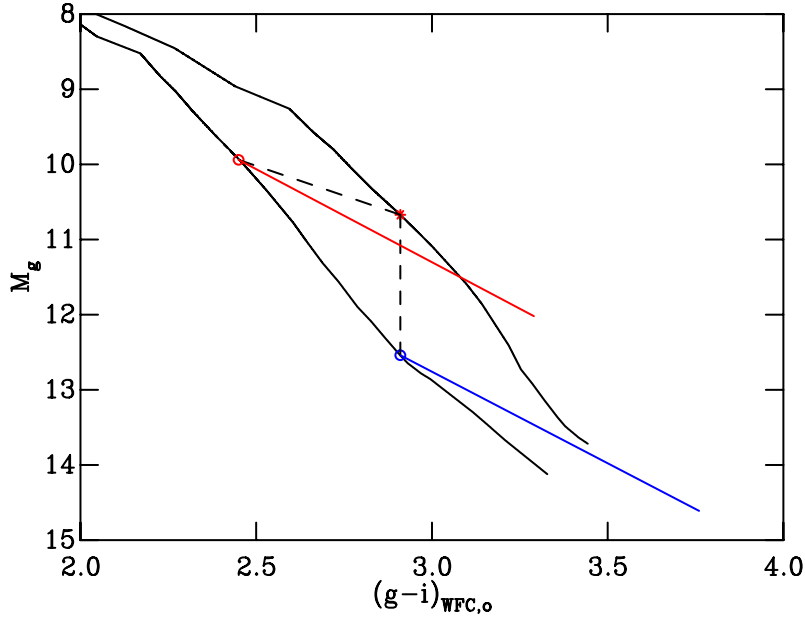
Figure 5.6: Two 5 Myr BCAH98 $\alpha = 1.9$ isochrones transformed into CMD space using the original BC-$T_{\rm eff}$ relation (lower isochrone) and the recalibrated BC-$T_{\rm eff}$ relation (upper isochrone). The red circle represents a star of mass $0.3\,M_\odot$ based on the original BC-$T_{\rm eff}$ relation, the red asterisk is a star of the same mass using the recalibrated BC-$T_{\rm eff}$ relation, and the blue circle is a star of the same colour as that on the recalibrated isochrone. The red and blue diagonal lines denote the reddening vectors for the red and blue circles respectively (calculated at a nominal $E(B-V) = 0.5$ using the interstellar extinction law of Cardelli et al. 1989).

For $T_{\rm eff} \lesssim 4000\,{\rm K}$ it has been demonstrated that the magnitude in a given bandpass is underestimated (see Section 4.5) and this was attributed to the atmospheric models, and in particular missing sources of opacity as a result of incomplete line lists. It is stressed that the extinction and reddening for a given object is based upon the $T_{\rm eff}$ predicted by the interior models and not the intrinsic colour as defined by the BC-$T_{\rm eff}$ relation derived using the atmospheric models. By applying the ΔBC corrections to the BC-$T_{\rm eff}$ relation and using this to transform model isochrones into CMD space, the shape of the SED for a star of given $T_{\rm eff}$ has effectively been modified across each bandpass. The extinction grids, however, have been derived using the atmospheric models, for which no modifications to the SEDs have been made. To investigate what effect using a reddening vector calculated for a star with an unmodified SED and applying it to a star, of the same $T_{\rm eff}$, with a slightly modified SED would have, the following test was performed.

A star of mass $0.3\,M_\odot$ at an age of 5 Myr has an associated $T_{\rm eff} \simeq 3400\,{\rm K}$ and $\log g \simeq 4$ according to the interior models of BCHA98 $\alpha = 1.9$. The original BC-$T_{\rm eff}$ relation (as derived in Section 4.3) predicts that this star should have an intrinsic colour of $(g-i)_{\rm WFC,o} \simeq 2.45$, whereas the recalibrated BC-$T_{\rm eff}$ relation, at the same $T_{\rm eff}$, suggests an intrinsic colour of $(g-i)_{\rm WFC,o} \simeq 2.91$. Fig. 5.6 shows two 5 Myr BCAH98 $\alpha = 1.9$ isochrones in intrinsic colour-absolute magnitude space – the upper isochrone has been transformed using the recalibrated BC-$T_{\rm eff}$ relation and the lower isochrone using the original BC-$T_{\rm eff}$

relation. The red circle represents the $0.3\,\mathrm{M_\odot}$ star based on the original BC-T_{eff} relation, the red asterisk is a star of the same T_{eff} based on the recalibrated BC-T_{eff} relation, and the blue circle is a star of the same colour as that on the recalibrated isochrone. The red circle represents the SED that has been used to calculate the reddening vector for the red asterisk and the blue circle represents an SED with the same observed colour as the red asterisk. The associated reddening vectors (for a nominal $E(B-V) = 0.5$ using the interstellar extinction law of Cardelli et al. 1989) are shown as the similarly coloured diagonal lines. A difference of only $0.01\,\mathrm{mag}$ was calculated in both the derived extinction Ag_{WFC} and reddening $E(g-i)_{\mathrm{WFC}}$ between these two reddening vectors. Hence, the extinction and reddening applied to stars with colours created using the recalibrated BC-T_{eff} relation do not suffer from inconsistencies arising from differences in the associated SEDs.

5.6 Fitting the Data

Conceptually, there is no difference between fitting the pre-MS and MS populations of a given SFR using the τ^2 fitting statistic. There are a couple of examples in the literature (e.g. Naylor & Jeffries 2006; Cargile & James 2010) where τ^2 has been used to derive pre-MS ages by fitting the positions of probable low-mass members using models isochrones. In these examples, the clusters represent relatively old pre-MS populations ($\gtrsim 30\,\mathrm{Myr}$) in which the pre-MS locus is well defined, and as such the age and distance were fitted simultaneously. These studies showed that the main contributor to the error budget on the age were uncertainties in the derived distance. This is unsurprising as the age derived via the comparison of data to pre-MS models in CMDs is heavily degenerate with the assumed distance.

As one moves to slightly younger populations ($\simeq 10\,\mathrm{Myr}$), the pre-MS locus, though still obvious in CMD space, starts to become slightly more bloated, perhaps as a result of astrophysical processes in the form of, for example, variability and unresolved multiple systems. This spread can, however, be exaggerated by the inclusion of non-members in the sample. In Section 5.3.1 it was noted that non-spectroscopic methods of member identification are more likely to include contamination from foreground and background objects than memberships based on purely spectroscopic methods. One way of ensuring that such non-members do not influence the derived age is to adopt a so-called soft-clipping approach, whereby datapoints with colours and magnitudes that lie several σ away from the observed sequence are assigned an arbitrary low probability as they are not well described by the model isochrone (e.g. Naylor & Jeffries 2006). In Section 5.6.1 a model dealing with such interlopers by modelling a background population of non-member stars in conjunction with the bona fide cluster members is introduced. The assumption of a uniform distribution of non-members is a poor description of the physical distribution, and will result in unphysical uncertainties on the derived parameters (e.g. age and distance). However, it is shown below that as the uncertainty in the derived age is primarily driven by the uncertainty in the distance, one can fit the low-mass members for an absolute age given

an assumed distance. The uncertainty in the absolute age is then simply the propagated uncertainty in the assumed distance. In Section 5.6.2 this model is then implemented and the τ^2 fitting statistic is used to derive pre-MS ages for SFRs with MS ages $\gtrsim 10\,\mathrm{Myr}$.

Moving to even younger ages ($< 10\,\mathrm{Myr}$) the spread in CMD space, at a given colour, becomes more pronounced (see Section 1.3.4 for a discussion on the possible sources). For these youngest SFRs it is found that the pre-MS models are unable to be used to assign absolute ages to these regions because; i) there is insufficient knowledge of what causes the observed luminosity spread and ancillary data, in many cases, to attempt to model this and ii) in some cases, the gradient of the model isochrone is not parallel with the pre-MS locus. This could result from the various astrophysical sources described in Section 1.3.4, but may also signify that the theoretical dependence on $\log g$ (for $T_{\mathrm{eff}} \lesssim 4000\,\mathrm{K}$) which was assumed from the atmospheric models is incorrect. Thus whilst it is not possible to derive absolute ages from these SFRs, it is possible to create groups of SFRs that share common positions in CMD space relative to a pre-MS isochrone at a given age. Therefore, in Section 5.6.3 the SFRs are assigned to such groups and nominal ages for each SFR discussed.

5.6.1   A Model for Dealing with Possible Non-Member Contamination

A CMD of a given SFR, even after isolating the pre-MS using youth indicators, may contain some contamination from foreground or background sources that have not been rejected by the selection process. This is in contrast to the MS regime, where only bona fide members of the SFRs were fitted. Therefore, a prescription is needed to deal with a possible non-member population which may influence the derived age when fitting for a pre-MS age using the τ^2 statistic. One way of dealing with this is to assume a certain fraction of the stars in a given pre-MS population – as defined by the youth indicators – are actually non-members.

Starting from the original definition of τ^2

$$\tau^2 = -2 \sum_{i=1,\,N} \ln \iint U_i(x - x_i, y - y_i)\, \rho(x, y))\, dx\, dy. \tag{5.1}$$

Now consider a model distribution that comprises two components – one representing the cluster member model distribution (ρ_{c}) and the other signifying the non-member model distribution (ρ_{n}), such that $\rho = \rho_{\mathrm{c}} + \rho_n$, then Eqn. 5.1 becomes

$$\tau^2 = -2 \sum_{i=1,\,N} \ln \iint U_i(x - x_i, y - y_i)\, \{\rho_{\mathrm{c}}(x, y) + \rho_{\mathrm{n}}(x, y)\}\, dx\, dy. \tag{5.2}$$

In regions away from the cluster sequence, it is assumed that $\rho_{\mathrm{c}} = 0$ and ρ_{n} is a constant i.e. the model is simply a uniform distribution comprised of non-member stars with no contribution from cluster members. Thus, far from the sequence, for the ith point

$$\tau_i^2 \;\; = \;\; -2\ln\rho_{\mathrm{n}}\iint U_i(x-x_i, y-y_i)\,dx\,dy \tag{5.3}$$

$$= \;\; -2\ln\rho_{\mathrm{n}},$$

due to the normalisation of the uncertainty function U (see Section 2.6.1). This therefore defines a maximum value of τ_i^2, which shall be called τ_{c}^2, and ρ_{n} can be expressed as

$$\rho_{\mathrm{n}} = e^{-0.5\tau_{\mathrm{c}}^2}. \tag{5.4}$$

Defining the fraction of members within a model CMD as $\mathfrak{F}$, and remembering from Section 2.6.1 that the integral of the model distribution over the entire CMD is also unity (i.e. $\iint \rho(x,y)\,dx\,dy = 1$), $\mathfrak{F}$ can be written as

$$\mathfrak{F} \;\; = \;\; \frac{\iint\{\rho_{\mathrm{c}}(x,y)+\rho_{\mathrm{n}}(x,y)\}\,dx\,dy - \iint\rho_{\mathrm{n}}(x,y)\,dx\,dy}{\iint\{\rho_{\mathrm{c}}(x,y)+\rho_{\mathrm{n}}(x,y)\}\,dx\,dy} \tag{5.5}$$

$$= \;\; 1 - Ae^{-0.5\tau_{\mathrm{c}}^2},$$

where A is the area of the CMD. This can be re-arranged for a specific τ_{c}^2, which represents the fraction of stars believed to be members within the CMD model, such that

$$\tau_{\mathrm{c}}^2 = -2\ln\left(\frac{1-\mathfrak{F}}{A}\right). \tag{5.6}$$

As way of an example, the model CMD for λ Ori extends approximately $10\,\mathrm{mag}$ in g_{WFC} and $3.5\,\mathrm{mag}$ in $(g-i)_{\mathrm{WFC}}$. Assuming that $80\,\%$ of stars in the sample of pre-MS objects are members, then $\tau_{\mathrm{c}}^2 \simeq 10$.

Practically, in the code, the integration from the brightest to the faintest star in the model CMD implies $\iint \rho_{\mathrm{c}}\,dx\,dy = 1$. This therefore modifies Eqn. 5.6, so that

$$\tau_{\mathrm{c}}^2 = -2\ln\left(\frac{1-\mathfrak{F}}{\mathfrak{F}A}\right), \tag{5.7}$$

however provided that $\mathfrak{F} \geq 0.5$, the value of τ_{c}^2 only changes by $\simeq 1.5$.

There are two distinct points which need to be addressed concerning the implementation of a uniform background contamination population; i) is the uniform contamination model distribution sufficient to model the non-uniform contaminating population and ii) does the fraction of the contamination model distribution, relative to the member stars, affect the derived age? To assess the effects of these points, λ Ori shall be used as an example. Concerning the first point, the fainter and bluer contamination of λ Ori was isolated in CMD space. A random selection of this contaminating population was added to the catalogue of members (varying from $0-40\,\%$ of the members) and the τ^2 fitting

statistic used to derive the pre-MS age for a given value of τ_c^2. The best-fit age was affected by less than 10% as a result of increasing the contaminating population. For the second point, a fixed level of contamination was adopted and the value of τ_c^2 varied from $10-1$ in steps of 1. For each value of τ_c^2, the pre-MS age was again derived and it was found that varying the level of the uniform background contamination also affects the best-fit age by less than 10%. Hence, whilst adopting a uniform background distribution of contaminating stars is unrealistic, the model implementing this description is sufficiently robust to derive reliable ages. Note, however, that whilst the derived age is effectively insensitive to the adopted value of τ_c^2, it is important that the effect of including possible contamination due to non-members is accounted for in the fitting procedure.

It is worth mentioning that the prescription presented here is mathematically equivalent to the soft-clipping scheme discussed in the original description of τ^2 by Naylor & Jeffries (2006), as well as being analogous to the $n\sigma$ clipping scheme in the χ^2 statistic. The subtle difference is that whereas in the χ^2 statistic, where data points that are clipped are assigned a zero probability, in the τ^2 regime, these points are simply assigned a very low probability (equal to the constant ρ_n).

5.6.2   Pre-Main-Sequence Ages Derived using τ^2

Pre-MS ages have been calculated for the SFRs with MS ages $\gtrsim 10\,\text{Myr}$ using the τ^2 fitting statistic in the $g_{\text{WFC}}, (g-i)_{\text{WFC}}$ CMD. The memberships listed in Table 5.1 have been used to select pre-MS member stars for each SFR. As there is a lack of bona fide pre-MS members for χ Per, although it has a MS age greater than $10\,\text{Myr}$, pre-MS ages are not derived using the τ^2 fitting statistic as the number of non-members retained from the rudimentary selection of likely members based on relative sky positions is too large. To create semi-empirical pre-MS model isochrones, the interior model computations of BCAH98 $\alpha = 1.9$, DCJ08, and DAM97 were used and transformed into observable CMD space using the appropriate BC-T_{eff} relation with the corresponding ΔBC corrections as a function of T_{eff} for the g_{WFC} and i_{WFC}-bands. Note that the interior models of BCAH98 $\alpha = 1.0$ and SDF00 were not used in this analysis as both failed to match the observed Pleiades MS (see Fig. 4.7). From Fig. 4.7 it is clear that for the various model isochrones different adjustments to the BC-T_{eff} relation are required to fit the observed Pleiades sequence. Whilst it is reasonable to account for missing sources of opacity due to incomplete line lists in the low T_{eff} regime, accounting for the mismatch observed in both the BCAH98 $\alpha = 1.0$ and SDF00 models – primarily due to not tuning the mixing length parameter – for masses up to and greater than the Sun by recalibrating the BC-T_{eff} relation is less so.

To fit stars selected as pre-MS members, grids of model isochrones were created for each interior model spanning a range of ages using the recalibrated BC-T_{eff} relation at the appropriate SFR reddening as derived in Section 2.8. In SFRs where there is evidence for variable reddening the median reddening as calculated from the individually de-reddened stars using the Q-method was adopted. Although there is a distribution of reddenings due
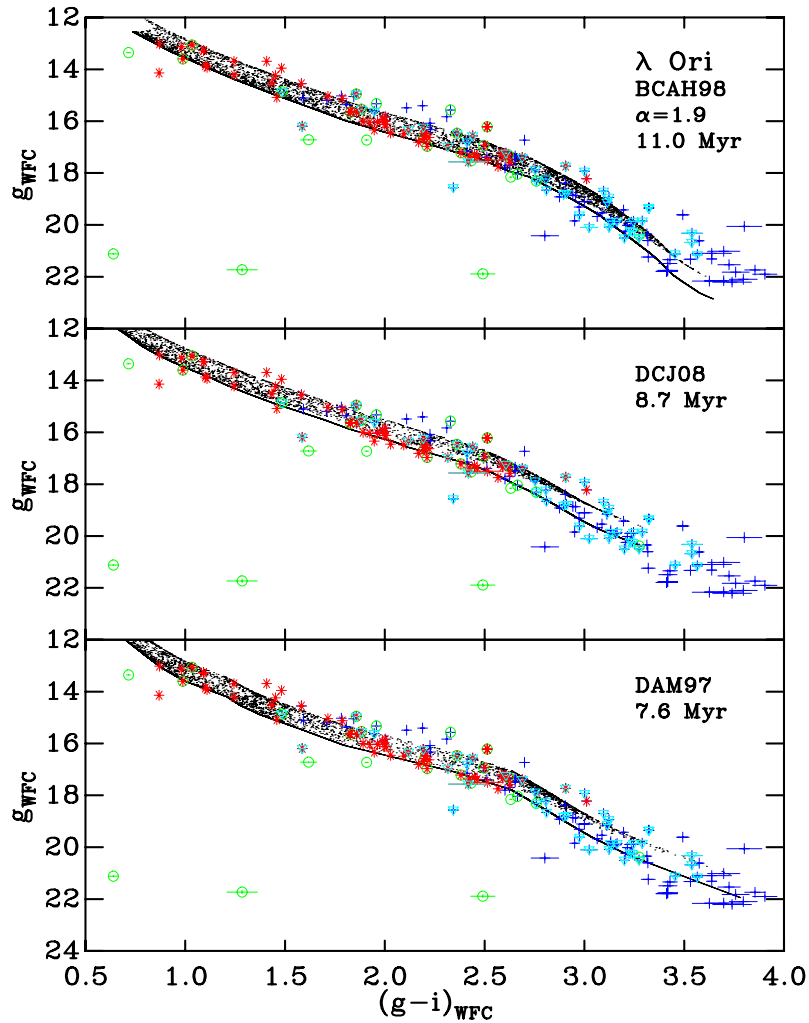
Figure 5.7: Pre-MS stars selected as members of the λ Ori association in the $g_{\mathrm{WFC}}, (g-i)_{\mathrm{WFC}}$ CMD. Asterisks are Li I spectroscopic members from Dolan & Mathieu (2001), crosses are the combined Hα spectroscopic and IR excess sources from Barrado y Navascués et al. (2007), triangles are Li I and Hα spectroscopic members from Sacco et al. (2008), and circles are the X-ray sources from Barrado et al. (2011). The best-fitting pre-MS model isochrones are overlaid at the best-fit MS distance and reddened assuming the median value derived in Section 2.8 according to the prescription described in Section 5.5. **Upper panel:** BCAH98 $\alpha = 1.9$. **Middle panel:** DCJ08. **Bottom panel:** DAM97.
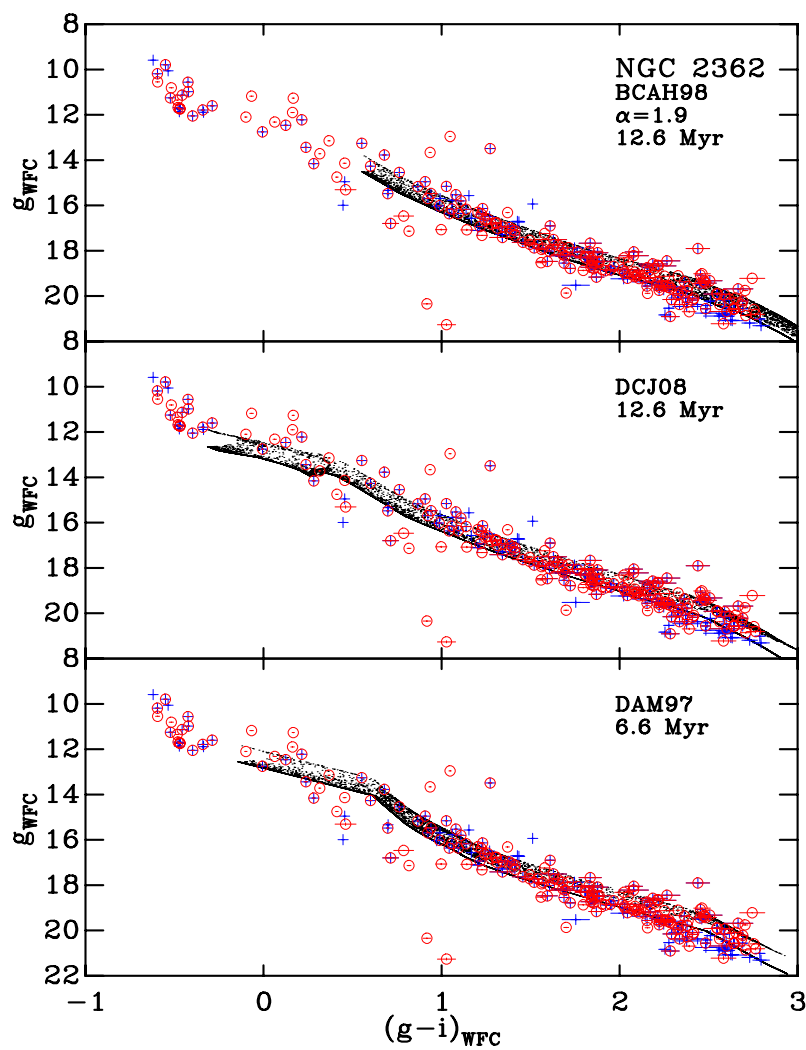
Figure 5.8: Same as Fig. 5.7 but for NGC 2362. Crosses are the combined Li I and Hα spectroscopic and IR excess sources from Dahm & Hillenbrand (2007) and circles are X-ray sources from Damiani et al. (2006a).
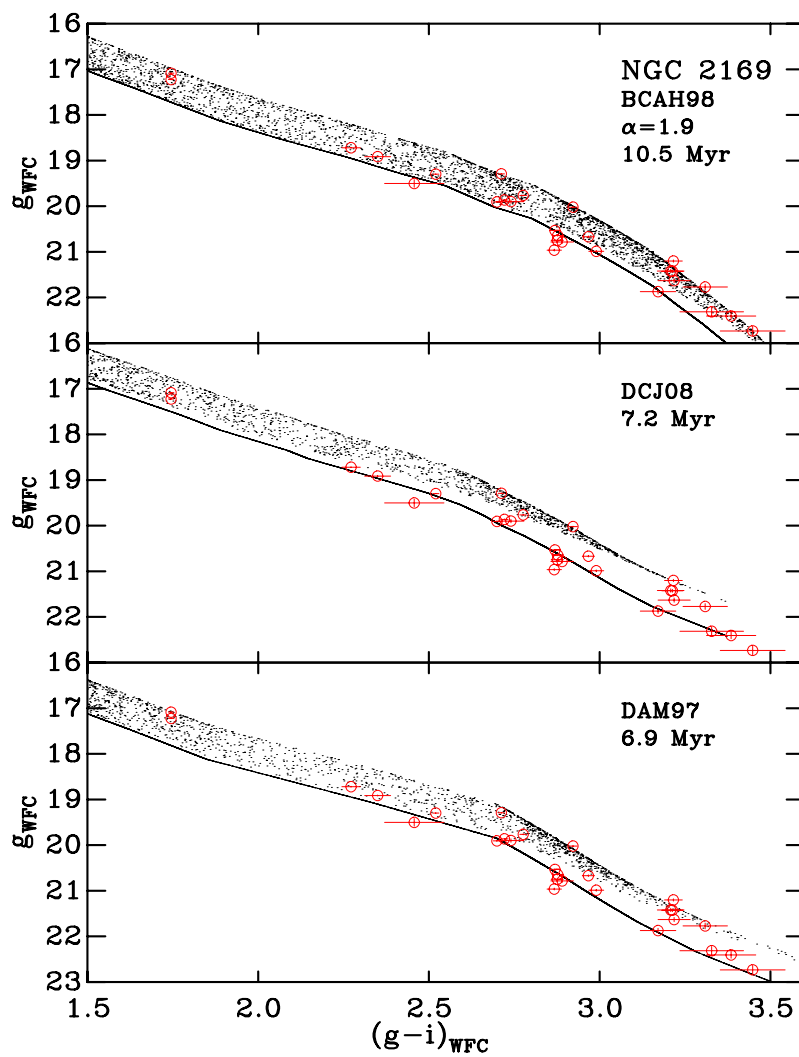
Figure 5.9: Same as Fig. 5.7 but for NGC 2169. Circles are Li I spectroscopic members from Jeffries et al. (2007).
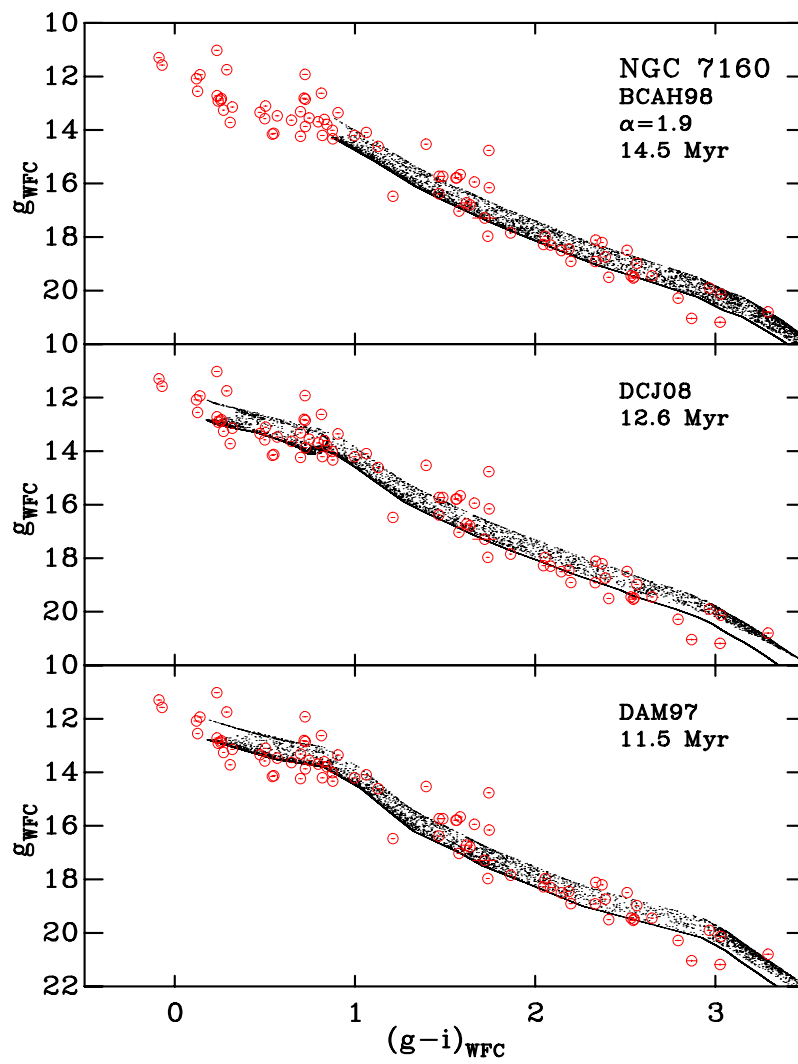
Figure 5.10: Same as Fig. 5.7 but for NGC 7160. Circles are Li I and Hα spectroscopic, IR excess and extinction-based members from Sicilia-Aguilar et al. (2006a).
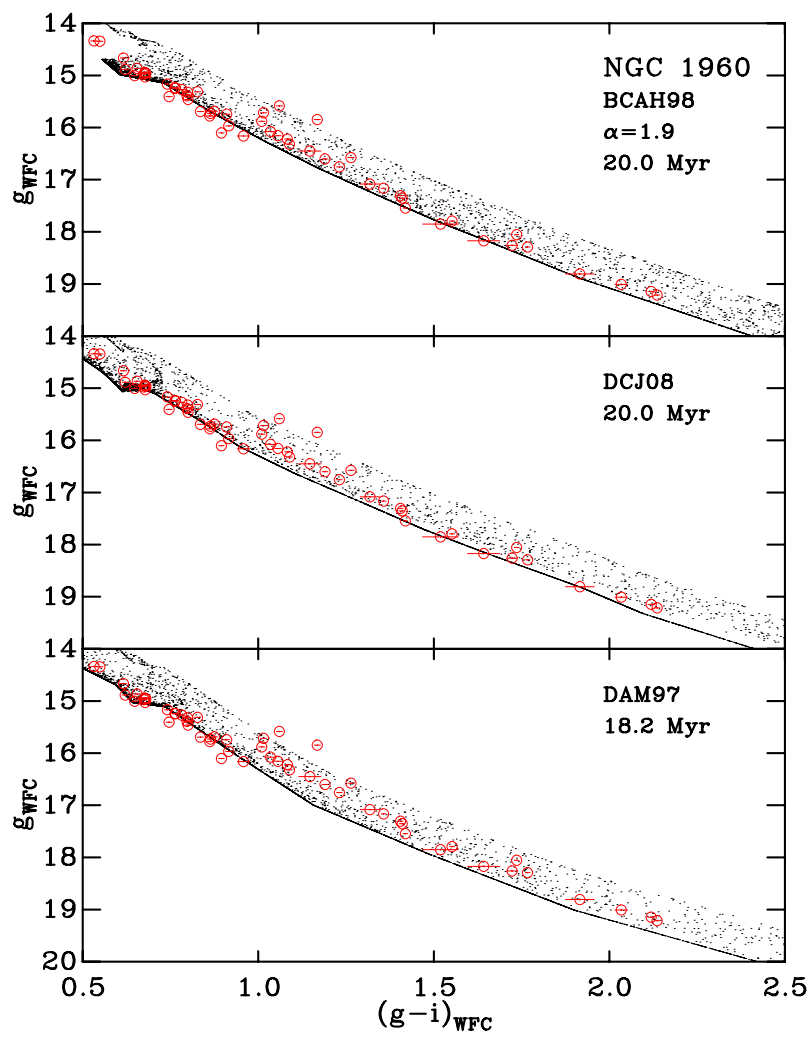
Figure 5.11: Same as Fig. 5.7 but for NGC 1960. Circles are Li I spectroscopic members from Jeffries et al. (in preparation).

Table 5.2: Absolute pre-MS ages for SFRs with MS ages $\gtrsim 10\,\mathrm{Myr}$ derived using semi-empirical pre-MS model isochrones and fitted using the τ^2 fitting statistic. The best-fit pre-MS age is derived assuming the best-fit MS distance and the uncertainty in the pre-MS age represents the uncertainty in the MS distance translated into an age uncertainty.

SFR	Absolute Pre-MS Age (Myr)					
	BCAH98 $\alpha = 1.9$		DCJ08		DAM97	
	Best-fit	68 %	Best-fit	68 %	Best-fit	68 %
NGC 2169	10.5	9.5–11.5	7.2	6.3–8.1	6.9	6.0–7.6
λ Ori	11.0	10.5–11.5	8.7	7.9–9.1	7.6	6.9–7.9
NGC 2362	12.6	11.0–13.2	12.6	11.0–13.2	6.6	5.8–7.6
NGC 7160	14.5	12.6–16.6	12.6	11.0–14.5	11.5	10.5–12.5
NGC 1960	20.0	19.5–20.5	20.0	19.5–20.5	18.2	17.6–19.1

to variable extinction across a given region, the reddening vector in the $g_{\mathrm{WFC}}, (g-i)_{\mathrm{WFC}}$ CMD lies almost parallel to the observed pre-MS locus (see Fig. 5.1) and therefore applying a fixed reddening to the pre-MS model isochrone does not significantly affect the derived age.

Figs. 5.7 – 5.11 show the $g_{\mathrm{WFC}}, (g-i)_{\mathrm{WFC}}$ CMDs of stars selected as pre-MS members of λ Ori, NGC 2362, NGC 2169, NGC 7160, and NGC 1960 with the best-fitting BCAH98 $\alpha = 1.9$, DAM97 and DCJ08 isochrones – assuming an intrinsic binary fraction of 50 % – overlaid at the best-fit MS distance. The largest source of uncertainty in the derived pre-MS age is attributable to the associated uncertainty in the assumed distance, therefore the uncertainty in the pre-MS age is calculated by deriving the corresponding pre-MS age at the upper and lower distance uncertainty limits as given by the 68 % confidence contour in the MS age-distance τ^2 grid (see for example Fig. 2.8).

Table 5.2 lists the derived pre-MS ages and associated uncertainties for the 5 SFRs that have been fitted with the τ^2 fitting statistic. It is clear that there is a trend between the pre-MS age derived and the initial choice of pre-MS model. The models of BCAH98 $\alpha = 1.9$ predict the oldest pre-MS ages, whereas the DAM97 models yield the youngest ages. The ages derived using the models of DCJ08 lie in between these two extremes. Table 5.2 further demonstrates that, even with the use of recalibrated pre-MS models, there is a distribution of ages for a given SFR depending on which model is used in the derivation, with the difference being as large as a factor of 2 in the case of NGC 2362. Clearly then, there is a need to distinguish which of these possible pre-MS age scales is the most reliable.

Looking at λ Ori as an example (see Fig. 5.7), the rudimentary model of fitting a pre-MS population with possible non-member contamination appears to be rather robust, with the model isochrones following the general shape of the pre-MS locus. One feature of the τ^2 fitting routine is that the model distribution fit tends to lie towards the lower envelope of the observed pre-MS locus. This has the obvious effect of making the derived age older, however it is worth noting that the general (by-eye) method of pre-MS isochrone fitting typically does not account for the binary nature of the model distribution. In such

cases, a single-star sequence is adopted and then adjusted for an assumed distance with the median of the pre-MS locus fitted (e.g. Dolan & Mathieu 2001). Fig. 5.7 shows that the majority of the spread at a given colour is accounted for by the intrinsic binary fraction of the model distribution, and therefore by fitting the lower envelope of the pre-MS locus the ages have not been biased. There is a small population of objects that lie above the equal-mass binary envelope, however these lie in the region of the CMD where stellar systems of higher multiplicity are expected.

5.6.3 Nominal Pre-Main-Sequence Ages

5.6.3.1 Star-Forming Regions with Main-Sequence Ages < 10 Myr

In Section 5.6 it was discussed how the observed spread in CMDs of pre-MS clusters increases as one moves to younger ages (see Section 1.3.4 for the possible physical processes responsible). In theory, one could attempt to include astrophysical processes that may give rise to such spreads and then fit the pre-MS population as demonstrated in Section 5.6.1. An early example of this was performed by Burningham et al. (2005a), who attempted to quantify the spread attributable to individual sources of dispersion and model the sequence. Photometric observations of two epochs were used to empirically assess the effects of photometric variability for two young SFRs – Cep OB3b and σ Ori – which show large luminosity spreads in their CMDs. Accounting for correlated variability in colours and magnitudes, and the non-Gaussian distribution of variability-induced dispersion, a coeval population of pre-MS stars was simulated that also included the effects of binarity and observational uncertainties on the model distribution. This model was found to underestimate the observed spread in both CMDs. More sophisticated statistical methods (e.g. Da Rio et al. 2010a) have used a maximum-likelihood technique – akin to the τ^2 fitting statistic – to fit a two-dimensional synthetic surface density to the CMD of the young SFR LH 95 in the Large Magellanic Cloud. The two-dimensional model distribution includes the combined effects of rotational variability due to cool starspots, accretion variability, unresolved binarity, differential extinction, as well as crowding in the field. Da Rio et al. (2010a) concluded that the spread observed in the CMD is too large to be accounted for by the various astrophysical sources of scatter in their model distribution and interpret the residual scatter as a real age spread with FWHM $2.8 - 4.4$ Myr.

In practice, it is evident that for some SFRs with MS ages < 10 Myr the semi-empirical pre-MS isochrones do not match the shape of the observed pre-MS locus as well as in the case of the older more evolved SFRs, with the models tending to cut through the pre-MS locus (see Fig. 5.12 where this is shown in the case of NGC 2244). Furthermore, the level of mismatch between the isochrones and the sequence depends on the initial choice of interior models. This mismatch between the models and the data therefore suggests that the assumptions concerning the age insensitivity of the absolute correction to the BC-T_{eff} relation and the $\log g$ dependence of the bolometric corrections as defined by the atmospheric models are likely less robust in this age regime than for ages $\gtrsim 10$ Myr.
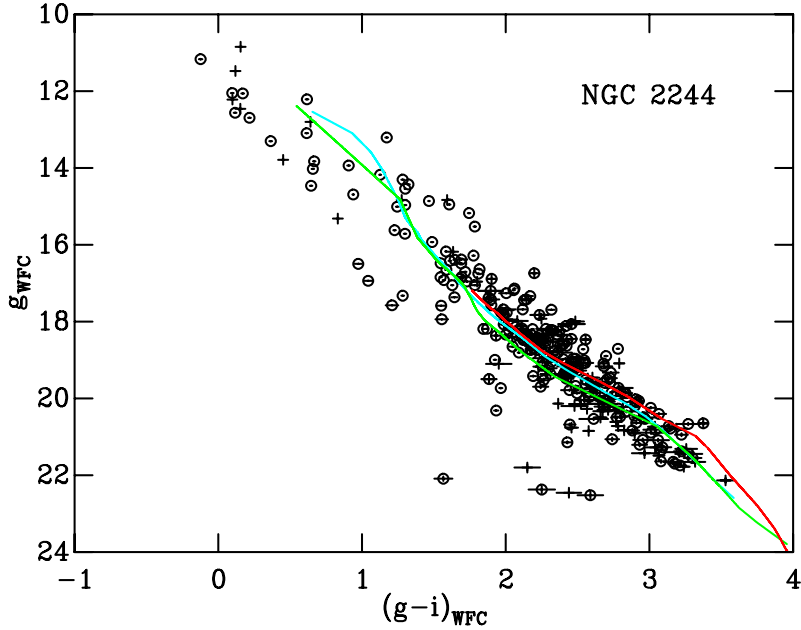
Figure 5.12: Pre-MS stars selected as members of NGC 2244 in the $g_{\text{WFC}}, (g-i)_{\text{WFC}}$ CMD. Circles are the X-ray sources from Wang et al. (2008) and crosses are IR excess objects from Balog et al. (2007). Semi-empirical BCAH98 $\alpha = 1.9$ (red), DCJ08 (cyan) and DAM97 (green) single-star isochrones at ages of 2 Myr are overlaid at the best-fit MS distance and reddened assuming the median value derived in Section 2.8 according to the prescription described in Section 5.5. Note how all three isochrones do not follow the shape of the observed pre-MS locus.

This, however, is only an issue for $T_{\text{eff}} \lesssim 4000\,\text{K}$ and therefore at higher temperatures this suggests that other factors are likely the cause (e.g. activity, starspots, etc.). Hence as opposed to deriving absolute ages for these regions, SFRs that share common positions in CMD space, when compared to a semi-empirical single-star pre-MS isochrone of a given age, can be grouped together. The pre-MS loci could simply be de-reddened by applying a given reddening vector and shifted vertically using the derived MS distance, thereby comparing the populations in the absolute magnitude-intrinsic colour plane (e.g. Mayne et al. 2007). However, as was shown in Section 5.5, the reddening and extinction for a given object depends upon its T_{eff} and therefore the reddening vector in the $g_{\text{WFC}}, (g-i)_{\text{WFC}}$ plane is not a fixed trajectory. As there is no spectroscopic information concerning the T_{eff} of the low-mass pre-MS objects, the sequence is therefore left in the apparent magnitude-apparent colour plane and the model isochrone is instead reddened using the appropriate reddening and distance modulus for the SFR. By comparing the data to the models in this way SFRs can be grouped, in order of increasing age, according to whether – i) the isochrone sits systematically below the sequence, ii) the isochrone sits approximately in the middle of the sequence, or iii) the isochrone sits systematically above the sequence.

As the distance moduli to the SFRs cover a range of $\Delta dm \simeq 4.5$ the mass regimes probed across the sample of SFRs varies. In addition, there are inherent lower/upper mass limits on the pre-MS interior models, which may further be restricted due to the lowest

Table 5.3: Nominal pre-MS ages for SFRs with MS ages < 10 Myr estimated using semi-empirical pre-MS isochrones. The ages were derived at a mass of 0.75 M$_\odot$ and assuming the best-fit MS distance. Notes are as follows. (1) Age derived assuming the total-to-selective extinction ratio $R_V = 3.75$ (see Section 2.7.1.1).

SFR	Nominal Pre-MS Age ($\simeq$ Myr)		
	BCAH98 $\alpha = 1.9$	DCJ08	DAM97
NGC 6611[1]	2	1	0.5
IC 5146	2	1	0.5
NGC 6530	3	2	1
NGC 2244	3	2	1
σ Ori	6	5	3
ONC	6	6	3
IC 348	7	6	4
Cep OB3b	7	7	3

$T_{\rm eff}$ limit defined by the ΔBC corrections (see Fig. 4.7 and Section 4.5). Of the model isochrones tested, it is clear that the BCAH98 $\alpha = 1.9$ and DCJ08 models represent the best fit to the observed Pleiades MS (for $T_{\rm eff} \gtrsim 4000\,{\rm K}$). Due to an upper mass limit of 1.4 M$_\odot$ on the BCAH98 $\alpha = 1.9$ models, the observed pre-MS loci are compared to a semi-empirical DCJ08 single-star model isochrone at a given age of 6 Myr, which, when looking at the MS ages derived in Section 2.8, seems appropriate.

Figs. 5.13 – 5.20 show the $g_{\rm WFC}, (g - i)_{\rm WFC}$ CMDs of stars selected as pre-MS members of Cep OB3b, NGC 2244, NGC 6530, NGC 6611, ONC, and σ Ori with a 6 Myr semi-empirical DCJ08 single-star pre-MS model isochrone overlaid. It is clear that for SFRs with MS ages < 10 Myr these can be separated into two distinct groups based on the comparison of the pre-MS populations with the model isochrone (with the appropriate reddening and distance modulus applied). In ascending age order these two groups comprise;

- NGC 6611, IC 5146, NGC 6530, and NGC 2244 – for which the isochrone sits below the observed pre-MS locus;

- Cep OB3b, the ONC, σ Ori, and IC 348 – for which the isochrone sits approximately in the middle of the observed pre-MS locus.

For the younger group it is clear that the semi-empirical single-star pre-MS model isochrone lies below the observed pre-MS locus in all cases implying that a pre-MS age of 6 Myr is too old for these SFRs. In contrast, the CMDs of the older group suggest that a pre-MS age of $\simeq 6$ Myr seems reasonable, with the semi-empirical DCJ08 model isochrone tracing the approximate middle of the observed pre-MS locus in each SFR (allowing for some intrinsic spread either side of the isochrone).

Due to the fact that the semi-empirical pre-MS model isochrones do not follow the shape of the observed pre-MS locus, and that the mass ranges sampled are different due to differences in the distance between the SFRs, a pre-MS age derived by simply laying a
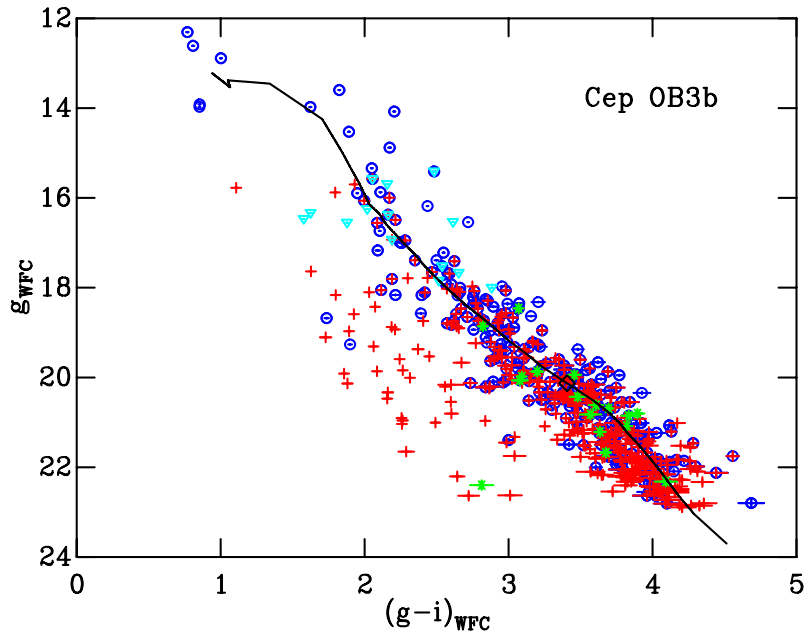
Figure 5.13: Pre-MS stars selected as members of the Cep OB3b association in the $g_{\rm WFC}, (g-i)_{\rm WFC}$ CMD. Crosses are the periodic variables from Littlefair et al. (2010), circles are X-ray sources from Naylor & Fabian (1999) and Getman et al. (2006), asterisks are spectroscopic members from Pozzo et al. (2003), and triangles are Hα sources from Ogura et al. (2002). The 6 Myr semi-empirical DCJ08 single-star pre-MS model isochrone is overlaid at the best-fit MS distance and reddened assuming the median value derived in Section 2.8 according to the prescription described in Section 5.5. The diamond marks the position of a 0.75 M$_\odot$ star according to the DCJ08 isochrone.
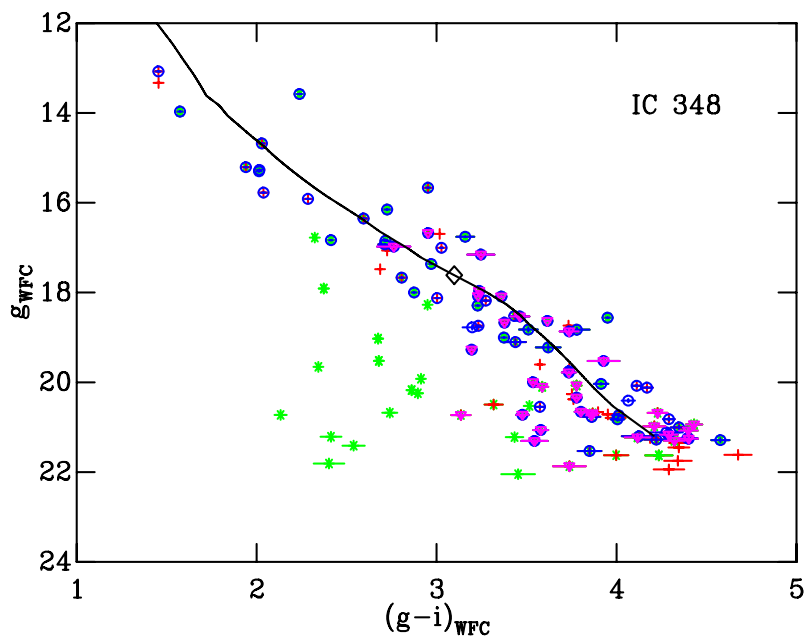
Figure 5.14: Same as Fig. 5.13 but for IC 348. Circles are the X-ray sources from Preibisch & Zinnecker (2002), the crosses are the Hα, Na I, and K I spectroscopic members from Luhman et al. (2003, 2005a,b), the triangles are the Hα spectroscopic members from Herbig (1998), and the asterisks are the combined periodic variable sources from Cohen et al. (2004) and Littlefair et al. (2005).
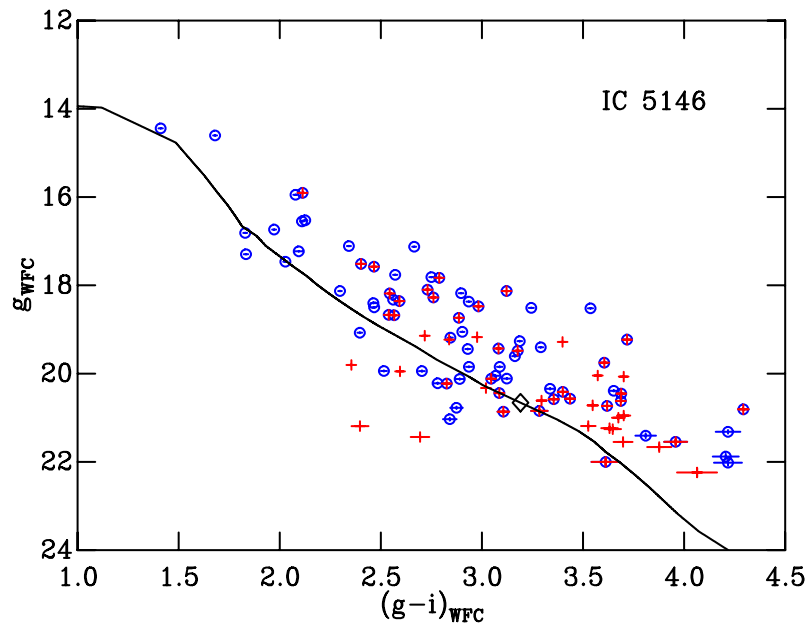
Figure 5.15: Same as Fig. 5.13 but for IC 5146. Circles are the IR excess sources of Harvey et al. (2008) and the crosses are spectroscopic members from Herbig & Dahm (2002).
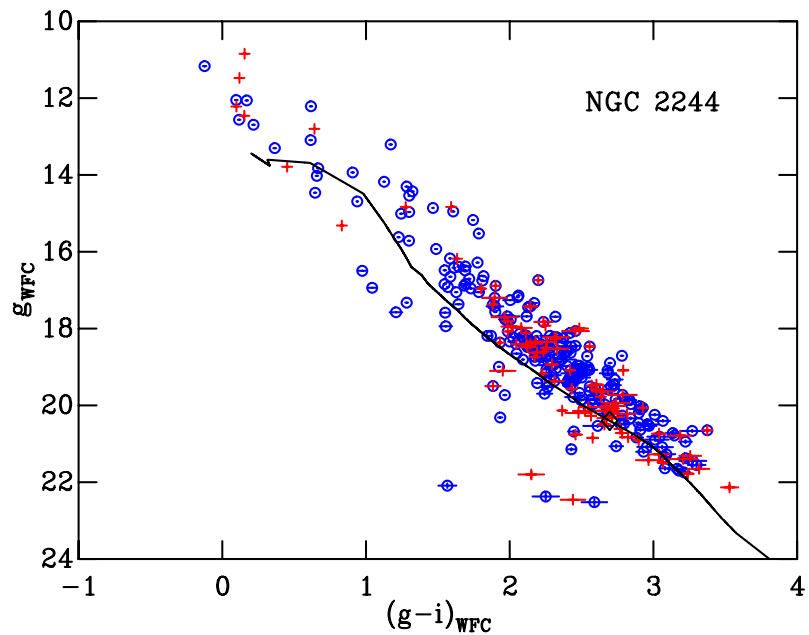
Figure 5.16: Same as Fig. 5.13 but for NGC 2244. Circles are the X-ray sources from Wang et al. (2008) and the crosses are IR excess objects from Balog et al. (2007).
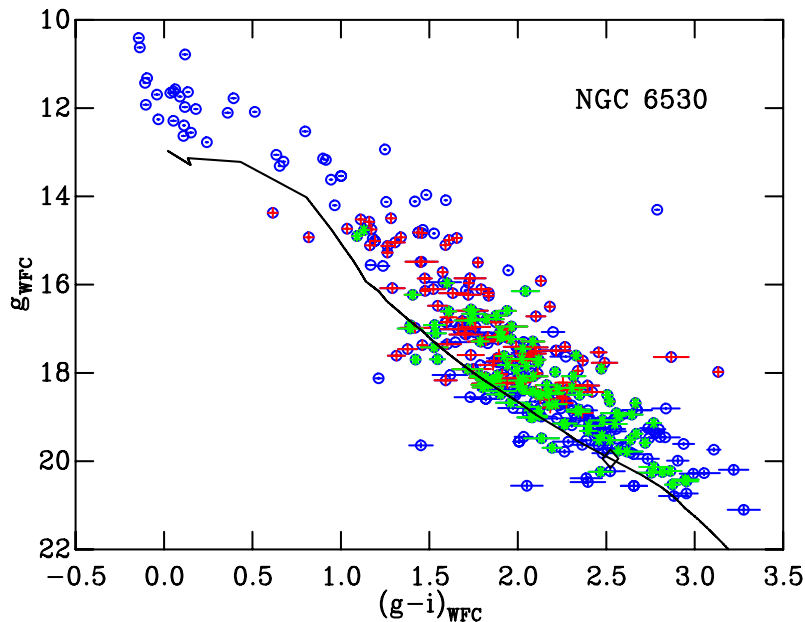
Figure 5.17: Same as Fig. 5.13 but for NGC 6530. Circles are the X-ray sources from Damiani et al. (2004), the crosses are spectroscopic members from Prisinzano et al. (2007), and the asterisks are periodic variables from Henderson & Stassun (2012).
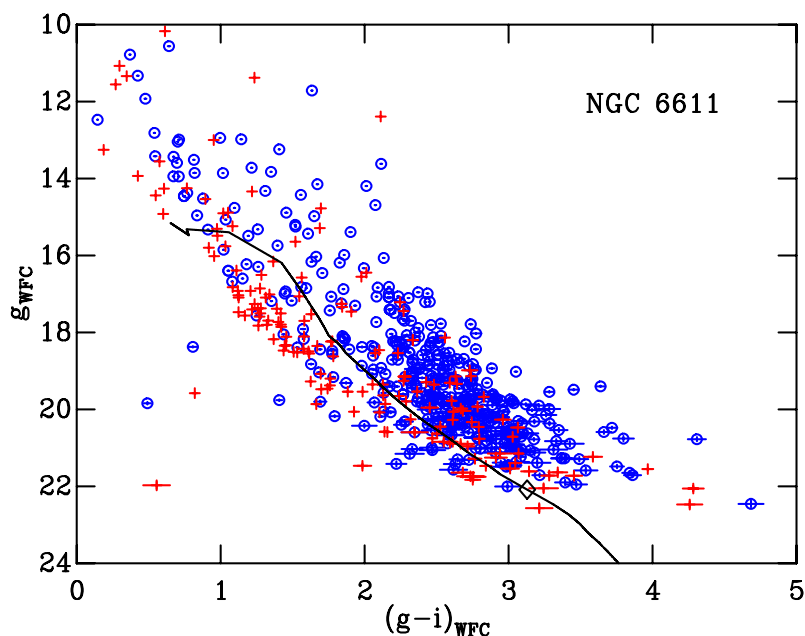
Figure 5.18: Same as Fig. 5.13 but for NGC 6611. Circles are the X-ray sources from Guarcello et al. (2007) and the crosses are IR excess sources from Guarcello et al. (2009). Note that both the isochrone and the reddening vector have been calculated adopting a total-to-selective extinction ratio $R_V = 3.75$.
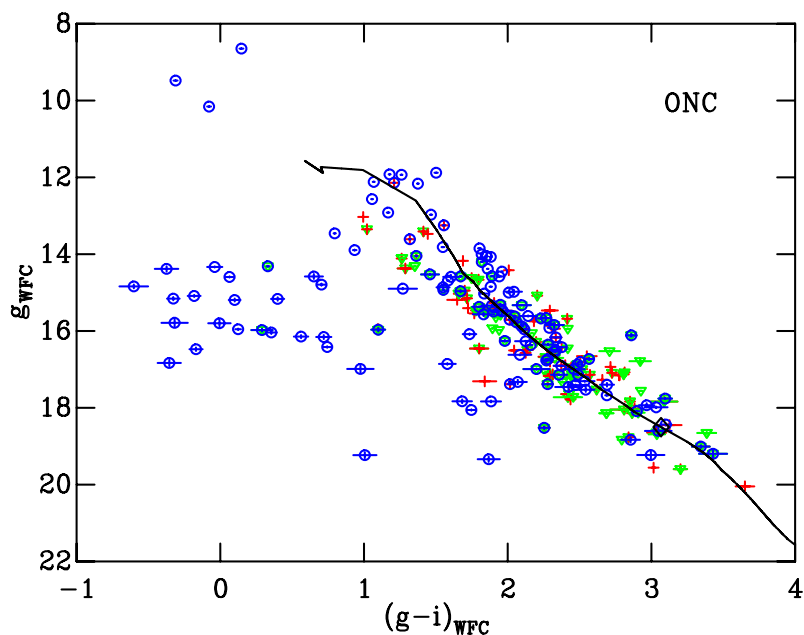
Figure 5.19: Same as Fig. 5.13 but for the ONC. Circles are the X-ray sources from Getman et al. (2005), the crosses are IR excess sources from Rebull et al. (2006a), and the triangles are the combined periodic variables from Rebull (2001) and Herbst et al. (2002a).
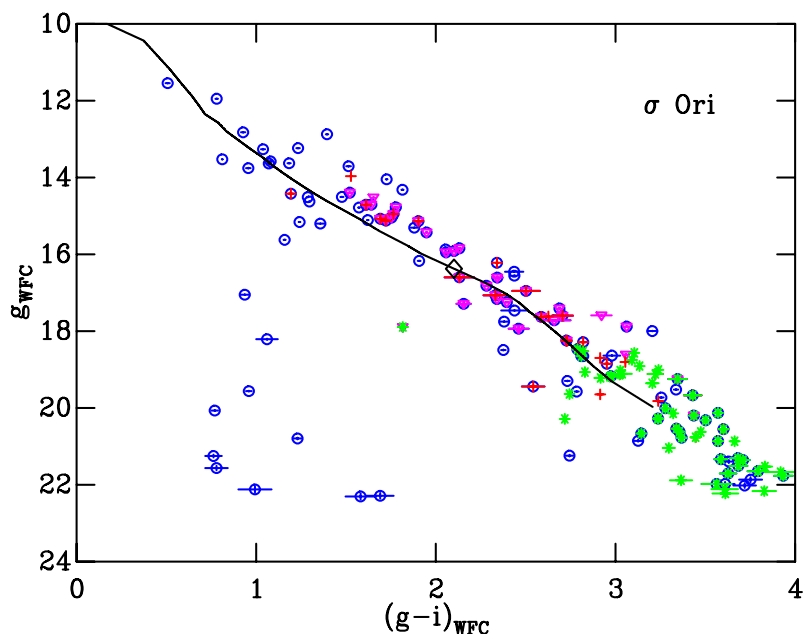
Figure 5.20: Same as Fig. 5.13 but for the σ Ori association. Circles are the X-ray sources from Sanz-Forcada et al. (2004), the crosses are periodic and aperiodic variables from Cody & Hillenbrand (2010), the asterisks are the combined Li I and Na I spectroscopic members from Kenyon et al. (2005) and Burningham et al. (2005b), and the triangles are the Li I and Hα spectroscopic members from Sacco et al. (2008).

model isochrone over the photometric data will be biased depending on which section of the sequence is fitted. Therefore, a more consistent approach is to estimate the pre-MS age of a given SFR by comparing the position of a model star of given mass – having applied the reddening and distance modulus as for the comparison with the 6 Myr DCJ08 model isochrone – with the approximate middle of the observed pre-MS locus. Such ages are termed nominal ages and estimated adopting a mass of $0.75 \, \mathrm{M}_\odot$. Table 5.3 shows the nominal pre-MS ages for the SFRs with MS ages $< 10 \, \mathrm{Myr}$.

5.6.3.2 χ Per

χ Per could not be fitted using the simple τ^2 model that accounts for a non-member population as the fraction of non-members – introduced by the selection based purely on positions on the sky relative to the cluster centre – was simply too high. Given the derived best-fit MS age of 14.5 Myr, one learns nothing by comparing the pre-MS locus, which is well-defined in the optical CMD and shows no evidence of an obvious luminosity spread, with a 6 Myr pre-MS model isochrone. Therefore in Fig. 5.21 the semi-empirical single-star pre-MS isochrones of BCAH98 $\alpha = 1.9$, DCJ08 and DAM97 at the MS age of 14.5 Myr are overlaid adopting the best-fit MS distance modulus $dm = 11.80$ and reddened by the median value $E(B - V) = 0.52$ according to the prescription described in Section 5.5.

From Fig. 5.21 it is apparent that both the BCAH98 $\alpha = 1.9$ and DCJ08 models match the shape of the observed pre-MS well over the whole colour range, with the DCJ08 model also following the sequence across the pre-MS-MS transition. Hence for these models the consistency between the MS and pre-MS ages, as demonstrated for other SFRs with ages $> 10 \, \mathrm{Myr}$, is still evident. In contrast, whilst the age appears to be approximately correct for the DAM97 model, with the isochrone tracing the shape of the lower MS, it appears slightly too old in the pre-MS regime, sitting just below the observed pre-MS locus. This effect is also observed in NGC 1960 (see Fig. 5.11), however it is less obvious in the case of χ Per due to the fact that the pre-MS locus is not as well-defined due to the method of selecting members based on sky positions alone. Given that the DAM97 models have been recalibrated so as to fit the observed Pleiades sequence at 130 Myr, the fact that they are unable to simultaneously model the pre-MS and MS populations of a given SFR in CMD space at ages of $\sim 15 - 20 \, \mathrm{Myr}$ suggests a problem with the underlying physics in the DAM97 models. The nominal ages for χ Per based on the three semi-empirical pre-MS models are $\simeq 14 \, \mathrm{Myr}$ for both the BCAH98 $\alpha = 1.9$ and DCJ08 isochrones, and $\simeq 12 \, \mathrm{Myr}$ for the DAM97 isochrones.

5.7 Summary

In this section the process of recalibrating the pre-MS model isochrones by incorporating an empirical BC-T_{eff} relation based on the observed K_{s}-band luminosity of Pleiades members, with theoretical corrections for the dependence on $\log g$, has been described. These semi-empirical pre-MS models have then been used to derive pre-MS ages from the low-mass
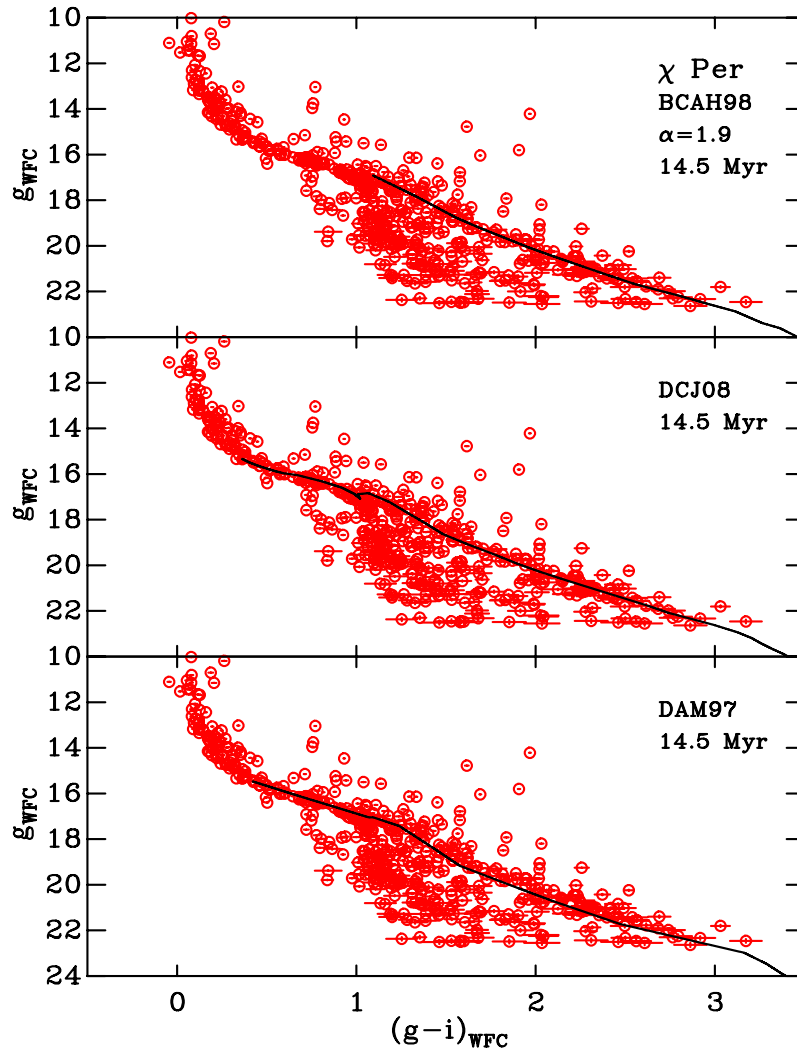
Figure 5.21: Stars selected as possible members of χ Per based on their positions on the sky relative to the cluster centre (see Section 5.3.2) in the $g_{\mathrm{WFC}}, (g-i)_{\mathrm{WFC}}$ CMD. Overlaid are 14.5 Myr semi-empirical single-star pre-MS model isochrones at the best-fit MS distance and reddened assuming the median value derived in Section 2.8 according to the prescription described in Section 5.5. **Upper panel:** BCAH98 $\alpha = 1.9$. **Middle panel:** DCJ08. **Bottom panel:** DAM97.

pre-MS populations of the sample of SFRs which have been isolated through the use of various stellar youth diagnostics.

For older SFRs (with MS ages $\gtrsim 10\,\mathrm{Myr}$) absolute ages using the semi-empirical pre-MS models of BCAH98 $\alpha = 1.9$, DCJ08 and DAM97 have been derived using the τ^2 fitting statistic in the $g_{\mathrm{WFC}}, (g-i)_{\mathrm{WFC}}$ CMD. At such ages the pre-MS loci of the SFRs are well-defined with the observed spread at a given colour accounted for by the inclusion of an intrinsic binary fraction in the model isochrones. Furthermore, a model that accounts for possible contamination of the pre-MS due to non-members that have not been rejected by the stellar youth diagnostics has been introduced. The semi-empirical pre-MS isochrones appear to follow the shape of the observed pre-MS loci, suggesting that the recalibration process is rather robust. At younger ages (MS ages $< 10\,\mathrm{Myr}$), however, the semi-empirical pre-MS model isochrones do not follow the observed shape of the pre-MS loci. This then implies that the use of the observed colours at the age of the Pleiades or the theoretical dependence on $\log g$ as defined by the atmospheric models – or a combination of both – is unfounded. Moreover, this disparity may be related to the fact that the evolutionary models do not include physical processes that are known to affect the SEDs of young, low-mass pre-MS stars (e.g. activity, starspots, rotation, etc.). Thus, in this age regime the τ^2 fitting statistic cannot be used to derive absolute ages, and therefore so-called nominal ages have been estimated based on the comparison of a model star of mass $0.75\,\mathrm{M_\odot}$ – with the appropriate reddening and distance modulus applied – with the observed pre-MS locus. For both the absolute and nominal ages, it was found that the BCAH98 $\alpha = 1.9$ and DCJ08 models predict similar pre-MS ages, however those derived using the DAM97 models are typically a factor of $1.5 - 2$ times younger.

Chapter 6

The Revised Pre-Main-Sequence Age Scale

6.1 Motivation

In Chapters 2 and 5 it was shown how to derive two independent age estimates from the MS and pre-MS populations of a given SFR. Whilst the model dependency, assuming the inclusion of similar physics, in the MS regime is not significant, affecting the derived ages on the $\simeq 5\,\%$ level (see Naylor 2009), the same is not true in the pre-MS regime, where distinct pre-MS age scales are derived depending on the choice of pre-MS interior models (see also Jeffries et al. 2009).

From Section 4.1 onwards, the discussion in this thesis has been the critical assessment of pre-MS ages derived using current formalisms of evolutionary models with the aim of beginning the process of attempting to calibrate these models so that they can be used to derive absolute ages. As discussed in Hillenbrand & White (2004), fundamental calibration of pre-MS evolutionary tracks is yet to be established. Tests have been proposed to compare the masses predicted by the models with dynamical masses measured directly from eclipsing binaries (e.g. Steffen et al. 2001) or those inferred indirectly using methods such as the velocity profiles of rotating circumstellar discs (e.g. Simon et al. 2000). Alternatively, the ages predicted by the models can be compared – under the assumption of coevality – to the position of pre-MS binaries (e.g. Prato et al. 2003), stellar systems of higher multiplicity (e.g. White et al. 1999) and young SFRs (e.g. Luhman et al. 2003). The problem however is that these tests are fundamentally limited by the accuracy with which either the data are transformed into the H-R diagram (see Section 1.3.3) or the models transformed into CMD space.

Having attempted to rectify the transformation of the models into CMD space and used these recalibrated models to derive pre-MS ages for the SFRs in the sample, in Section 6.2 the MS and pre-MS ages for each SFR are compared to test which of the various pre-MS age scales is the most reliable. The age for each SFR is then assigned in Section 6.3 and these revised estimates compared with previous literature values. Section 6.4 discusses

some of the main findings presented in this thesis on the use of pre-MS evolutionary models to derive ages. The implications of the revised ages are then discussed in terms of circumstellar disc survival times and the lifetimes of different phases of YSO evolution in Section 6.5. Finally, Section 6.6 discusses the findings presented in this chapter.

6.2 Comparing the Main-Sequence and Pre-Main-Sequence Ages

Having derived ages from the MS and pre-MS members for the sample of SFRs, it is now possible to draw these two age diagnostics together. In Section 5.6 it was shown that the pre-MS ages for young SFRs are heavily model dependent, even after recalibrating the transformation between theoretical H-R and observable CMD space based on the observed colours of Pleiades members. Thus a valuable exercise is then to compare SFR ages derived from different mass regimes that rely on different aspects of stellar physics. Agreement between the two age diagnostics would instill confidence in the accuracy of SFR ages, thereby allowing an absolute age scale for young SFRs to be constructed. Disagreement, however, would highlight possible weaknesses in our current understanding of stellar evolution and force us to re-evaluate the underlying treatment of various physical aspects and assumptions in current evolutionary models.

Fig. 6.1 plots the MS ages against the pre-MS ages for the SFRs in the sample. All MS ages have been derived using the Geneva-Bessell isochrones and fitted to the MS photometric data using the τ^2 fitting statistic. The pre-MS ages shown in Fig. 6.1 are either; i) absolute age derivations using semi-empirical pre-MS isochrones and fitted to the pre-MS photometric data using the τ^2 fitting statistic (blue circles) or ii) nominal ages at a model mass of $0.75\,\mathrm{M_\odot}$ estimated by overlaying semi-empirical single-star pre-MS isochrones on top of the photometric data (red asterisks). Pre-MS ages have been derived using the interior models of BCAH98 $\alpha = 1.9$, DCJ08 and DAM97.

The most obvious statement that can be drawn from Fig. 6.1 and the comparison of MS with pre-MS ages is that the DAM97 pre-MS age scale is inconsistent with the MS age scale across almost the entire sample. That the DAM97 models tend to predict younger pre-MS ages than other pre-MS models is not a new finding (see also Dahm 2005), however comparing these to a well-constrained age scale allows one to place the DAM97 pre-MS ages in context. The level of agreement between the MS age scale and the pre-MS age scales of BCAH98 $\alpha = 1.9$ and DCJ08 are much higher than for the DAM97 models. For SFRs with pre-MS ages of $\gtrsim 6\,\mathrm{Myr}$ – on the BCAH98 $\alpha = 1.9$ and DCJ08 scales – both models predict pre-MS ages that are generally consistent with the MS ages derived in Section 2.8, however at younger pre-MS ages ($< 6\,\mathrm{Myr}$) there is a discrepancy between the two age diagnostics where the MS ages are approximately a factor of 2 older than the pre-MS ages (see also Naylor 2009).

Hence, as demonstrated by Fig. 6.1, it is then clear that the discordance between the MS age scale and the pre-MS age scale suggests that pre-MS ages derived using the
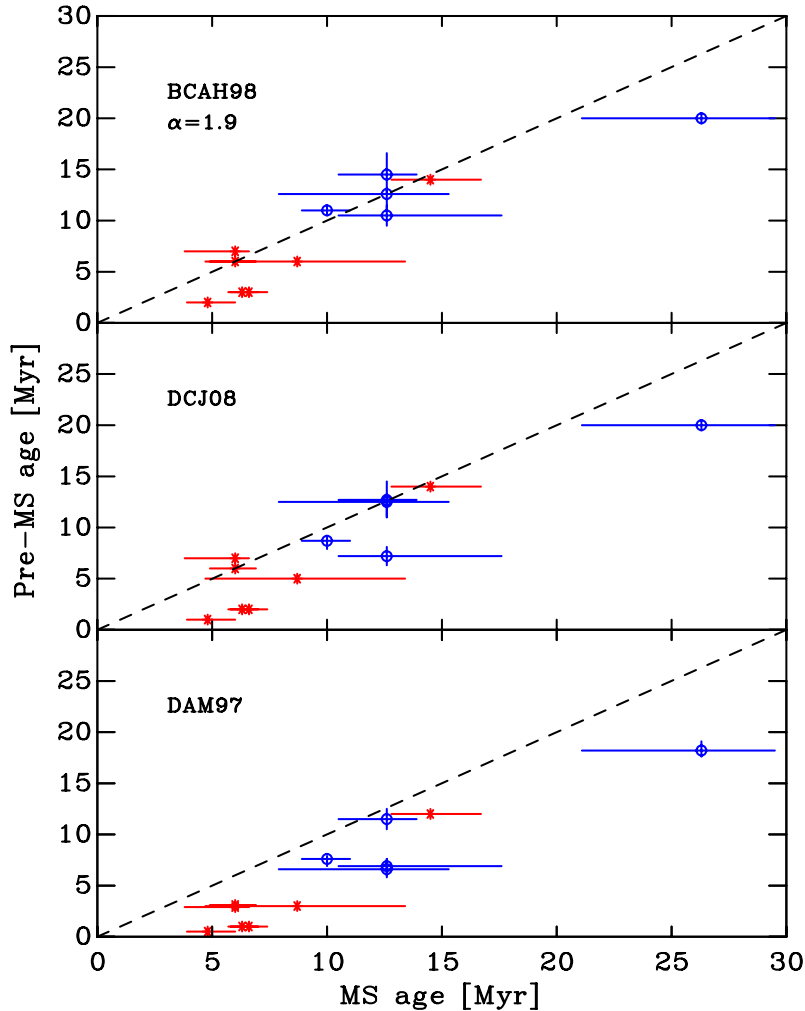
Figure 6.1: The MS versus pre-MS ages for the SFRs in the sample. The circles represent the SFRs where both the MS and pre-MS age were derived using the τ^2 fitting statistic. Asterisks denote SFRs where the MS age was derived using the τ^2 fitting statistic, however the pre-MS age was estimated by overlaying a semi-empirical single-star pre-MS model isochrone on the pre-MS population and is a nominal age at a mass of $0.75 \, \mathrm{M_\odot}$ (see Section 5.6.3). The uncertainties in the MS age were calculated from the standard age-distance fit (see Section 2.8) and represent the 68 % confidence levels. Uncertainties in the pre-MS age were only calculated for those SFRs where the age was derived using the τ^2 fitting statistic and represent the uncertainty in the derived MS distance translated into an age (see Section 5.6). There is generally good agreement between pre-MS ages derived using the BCAH98 $\alpha = 1.9$ and DCJ08 models and the MS ages, whereas the DAM97 models tend to predict pre-MS ages that are much younger than the MS determinations. For all models, however, at MS ages less than $\sim 6 \, \mathrm{Myr}$ there is an obvious discrepancy between the derived MS and estimated pre-MS ages. **Upper panel:** BCAH98 $\alpha = 1.9$. **Middle panel:** DCJ08. **Bottom panel:** DAM97.

DAM97 models are unlikely to represent the true pre-MS age scale. Therefore, the DAM97 models should not be used to age young pre-MS SFRs, especially when such timescales are combined with ancillary data in an effort to perform empirical studies of physical process occurring during the pre-MS phase. Instead, based on the inability to distinguish which of the two remaining pre-MS age scales is more probable, either the BCAH98 $\alpha = 1.9$ or DCJ08 models should be used to age young, low-mass pre-MS populations. A cautionary note, however, is to stress the importance of comparing theoretical evolutionary models to photometric data in the natural system of the observations (see Sections 3.4) and the need to recalibrate the evolutionary models using an empirical sequence (see Section 5.4).

6.3 Final Assigned Pre-Main-Sequence Ages

Having demonstrated that the DAM97 pre-MS age scale is inconsistent with the MS age scale and that both the BCAH98 $\alpha = 1.9$ or DCJ08 pre-MS age scales are generally consistent with the MS ages, it is now possible to assign the finalised pre-MS age to each of the 14 SFRs in the sample. There is a subtle level of model dependency resulting in slight differences between the pre-MS ages derived using the BCAH98 $\alpha = 1.9$ and DCJ08 models, however these are typically of the order of $\simeq 1 - 2\,\mathrm{Myr}$. Hence a mean of the two pre-MS ages will be adopted for a given SFR. There is still the question of what pre-MS age to assign for the very youngest SFRs (pre-MS ages of $< 6\,\mathrm{Myr}$). The MS ages, although well-constrained with a range of $\simeq 2\,\mathrm{Myr}$ on the $68\,\%$ confidence level, are derived using MS populations that number in the tens, whereas the pre-MS populations are an order of magnitude more numerous. Furthermore, there is no reason that for these SFRs the $(UgriZ)_{\mathrm{WFC}}$ photometry should be less reliable than for other regions, and it is apparent from Section 5.6.3 that they represent stellar populations at an earlier stage of evolution, when compared to say σ Ori or Cep OB3b. Although different nominal ages have been assigned to various SFRs (see Table 5.3), these have been calculated assuming the best-fit MS distance. Hence allowing for the uncertainties in the derived distance it is not clear whether the ages for these SFRs can be differentiated in CMD space, thus the final pre-MS ages are categorised into two distinct groups. The resulting ages that should be adopted for the SFRs in further studies are;

- $\sim 2\,\mathrm{Myr}$ for NGC 6611, IC 5146, NGC 6530, and NGC 2244;

- $\sim 6\,\mathrm{Myr}$ for the ONC, σ Ori, Cep OB3b, and IC 348;

- $\simeq 9\,\mathrm{Myr}$ for NGC 2169;

- $\simeq 10\,\mathrm{Myr}$ for λ Ori;

- $\simeq 12\,\mathrm{Myr}$ for NGC 2362;

- $\simeq 13\,\mathrm{Myr}$ for NGC 7160;

- $\simeq 14\,\mathrm{Myr}$ for χ Per;

- $\simeq 20\,\mathrm{Myr}$ for NGC 1960.

On the balance of the evidence presented in the previous chapters, the above distinction between the youngest ($\simeq 2\,\mathrm{Myr}$) and young ($\simeq 6\,\mathrm{Myr}$) groups seems justifiable. Although it is statistically impossible to differentiate between these two groups based on their MS ages – all clustered around $6\,\mathrm{Myr}$ – there is an obvious difference in the pre-MS ages (see Section 5.6.3.1) between those SFRs where a 6 Myr semi-empirical single-star pre-MS model isochrone lies systematically below the observed pre-MS locus and those SFRs where the isochrone traces the approximate middle of the locus. Furthermore, there are visible differences between the magnitude of the observed luminosity spread between the youngest and young groups. For a given colour, the spread in the youngest group covers approximately 3 mag, whereas in the young group the observed spread is approximately a magnitude smaller. Note also that in the older SFRs this spread almost entirely vanishes and is explainable by the presence of intrinsic binarity in these stellar populations.

For the young group, an age of $\simeq 6\,\mathrm{Myr}$ is assigned as the MS ages for all the SFRs in this group suggest this. Further evidence in favour of such an age is that a pre-MS isochrone of 6 Myr appears to trace the middle of the pre-MS locus in CMD space. Moreover, the observed luminosity spread appears to be approximately a magnitude larger than that observed in older SFRs (e.g. NGC 2169 and λ Ori). It is also worth pointing out that for these older SFRs, where the τ^2 fitting statistic was used to derive the pre-MS age, an intrinsic binary fraction has been accounted for in the fit, whereas the presence of binaries has been neglected in the young group pre-MS age estimates (based solely on a single-star isochrone). Thus, there is a suggestion that the ages for the young group may require a correction to account for binarity. The difference between the lower single-star and upper equal-mass binary envelopes in a coeval isochrone is $\simeq 0.75\,\mathrm{mag}$, and therefore in the most extreme case – assuming $50\,\%$ of stars are single and $50\,\%$ are in equal-mass binaries – this would necessitate that the single-star isochronal age be increased by a factor that translates to a shift of $\simeq 0.38\,\mathrm{mag}$ fainter. For more realistic mass ratio distributions, however, this shift would be smaller. Adopting the most extreme case, such a shift would increase the pre-MS ages for the young group by an additional factor of $1.5 - 2$, thereby placing them at a similar age to NGC 2169 and λ Ori, and erasing the agreement between the MS and pre-MS ages for these SFRs. Furthermore, at ages of $\simeq 10\,\mathrm{Myr}$, one would expect to see evidence of evolved high-mass stars in SFRs like the ONC, which are not observed in the optical CMD (see Fig. 2.31). Therefore, a nominal age for the young group of $\simeq 6\,\mathrm{Myr}$ seems reasonable, however there is a remaining caveat that these nominal ages may need rectifying in future studies to account for; i) the lack of understanding on the underlying causes of the observed luminosity spread and the resulting implications for the evolution of single- and binary-star systems and ii) the effects of young, accreting objects observed with a range of accretion rates and viewing angles (see Mayne & Harries 2010).

For the youngest group, a very similar argument holds, however here there is the added uncertainty due to the obvious discrepancy between the MS and pre-MS ages. Based on a combination of the isochronal age of the more numerous pre-MS populations

and the increased magnitude of the observed luminosity spread, a nominal age of $\simeq 2\,\mathrm{Myr}$ appears reasonable. Naturally, there is the argument, again, of whether the effects of binarity should be taken into consideration. Due to the logarithmic age scale in CMD space, a given absolute shift in magnitude results in a similar shift in age, hence an additional increase of approximately a factor of 2 would be inferred (in the most extreme case). This would then place the youngest group an at age of $\simeq 4 - 5\,\mathrm{Myr}$ and, as these regions represent the earliest visible stages of the star formation process, suggests that only after approximately $4\,\mathrm{Myr}$ do embedded protostars become optically visible. This would consequently decrease the disparity between the pre-MS and MS ages, however when combined with the fact that the young group would then be of a similar age to SFRs where no obvious luminosity spread is observed, this conclusion appears unlikely. Once again, a nominal age of $\simeq 2\,\mathrm{Myr}$ for the youngest group is adopted, however the caveats mentioned above for the young group remain relevant.

6.3.1 Comparison with Literature Ages

Having identified the main uncertainties in the derivation of pre-MS ages by comparing theoretical evolutionary models with photometric data using CMDs (see Section 3.1), it is therefore instructive to now compare the revised pre-MS ages derived in this thesis with those generally adopted in the literature to gauge what the global effects are in addressing these uncertainties.

6.3.1.1 Youngest Group $\sim$ 2 Myr

These SFRs are all very young and represent the earliest optically visible stages of the star formation process. Due to the uncertainties on the derived MS distances and the large observed luminosity spreads, in addition to the uncertainties in the pre-MS evolutionary models at such ages (see Baraffe et al. 2002), it is not obvious whether these regions can be differentiated in age based on their pre-MS ages alone.

NGC 6611

Most previous age derivations for the region suggest an age of $< 1\,\mathrm{Myr}$ (e.g. Hillenbrand et al. 1993), however more recent studies infer a slightly older age with a median of $\simeq 1 - 2\,\mathrm{Myr}$ (e.g. Guarcello et al. 2007). The distance derived in Section 2.8.4.9 is consistent with those typically assumed in recent works, and at such a distance only stars more massive than $\simeq 0.6 - 0.7\,\mathrm{M_\odot}$ are visible in the optical CMDs, hence the use of recalibrated semi-empirical pre-MS isochrones for this SFR is inconsequential. Therefore, it is likely that the slightly older age is a result of the small differences in both magnitude and colour resulting from leaving the photometric data in the natural plane of the observations.

IC 5146

The study of IC 5146 by Herbig & Dahm (2002) concluded that the median age of the region is $\leq 1\,\mathrm{Myr}$ with extended populations at both younger and older ages. The distance

derived in Section 2.8.4.4 is $\simeq 0.4$ mag smaller than that adopted in Herbig & Dahm (2002) and therefore easily accounts for the difference in the derived pre-MS age for the region.

NGC 6530

Pre-MS ages for NGC 6530 have been derived by Prisinzano et al. (2005) who used the SDF00 isochrones to derive an age of 2.3 Myr and by Sung et al. (2000) who fitted the pre-MS isochrones of Swenson et al. (1994) to Hα selected members after converting them into theoretical H-R space, yielding 1.5 Myr. The distance adopted in these studies are $\simeq 0.1$ mag smaller and $\simeq 0.45$ mag larger than that derived in Section 2.8.4.8 respectively. As the Swenson et al. (1994) models were not tested in this thesis, it is difficult to ascertain the level of model dependency on the derived age with respect to other models. The effects of leaving the photometry in the natural system and the difference between the adopted distances – between the study of Prisinzano et al. (2005) and this thesis – effectively cancel out, and thus the nominal age is consistent with current age estimates for the region.

NGC 2244

There are not many age determinations for NGC 2244, the first being the Hα study of Park & Sung (2002) who derived a mean age in the range of $0.5-0.9$ Myr after transforming the photometric observations into an H-R diagram (based on MS bolometric corrections and a MS T_{eff} scale). The difference in distance between the study of Park & Sung (2002) and that derived in Section 2.8.4.6 is $\simeq 0.4$ mag, and therefore large enough to account for the difference in the derived ages. Note that a spectroscopic analysis of the eclipsing binary V578 Mon (Hensberge et al. 2000) derived a distance and an age that are consistent with those derived in this thesis.

6.3.1.2 Young Group $\sim$ 6 Myr

σ Ori

Age estimates for the low-mass pre-MS population of σ Ori based on comparison with evolutionary models in CMDs cluster around 3 Myr. Zapatero Osorio et al. (2002) used the DAM97 models to derive a median age of 3 Myr, which is the same as the nominal age derived in Section 5.6.3.1 using the same models. Note, however, that the distance adopted in the Zapatero Osorio et al. (2002) study was the *Hipparcos* measurement of 352 pc. This distance is $\simeq 0.3$ mag smaller than the distance derived in Section 2.8.4.12 and will act to make the SFR appear approximately a factor of two older. The more recent study of Sherry et al. (2004) derived a similar age using the BCAH98 models transformed into CMD space using MS bolometric corrections and a MS T_{eff} scale. Using MS bolometric corrections can result in isochrones that are $\simeq 0.1-0.15$ mag redder and fainter than those based on atmospheric models at the appropriate $\log g$. This, combined with a distance that is $\simeq 0.2$ mag larger than that used here, will make the derived age of Sherry et al. (2004) too young by $\simeq 2-3$ Myr, thereby bringing it into agreement with the nominal age derived in Section 5.6.3.1.

It is interesting to note that the apparent coeval nature of both σ Ori and λ Ori, as found in Mayne & Naylor (2008), is no longer observed in this thesis (see also the discussion of Sacco et al. 2008). The VI_c datasets for the two SFRs come from different sources – the σ Ori data was taken by Mayne et al. (2007) whereas the λ Ori data was taken from the study of Dolan & Mathieu (2001). Cross-correlating the VI_c photometry of bona fide members against the $(gi)_\mathrm{WFC}$ photometry there is a subtle difference of approximately $0.1 - 0.15\,\mathrm{mag}$ in the V-band magnitude and $V - I_\mathrm{c}$ colour between the two datasets, implying that σ Ori is indeed slightly younger than λ Ori. A further subtle technicality is that the study of Mayne & Naylor (2008) created empirical isochrones by fitting the middle of a given sequence assuming a given distance and reddening. The distance adopted in Mayne & Naylor (2008) and derived in Section 2.8.3 for λ Ori agrees to within $0.01\,\mathrm{mag}$, whereas the distance for σ Ori assumed in Mayne & Naylor (2008) is $\simeq 0.1\,\mathrm{mag}$ smaller than that derived in Section 2.8.4.12, and as a result, the empirical isochrone for σ Ori would appear too old. Moreover, the fact that there is an increased luminosity spread in the σ Ori optical CMD is not accounted for in the study of Mayne & Naylor (2008).

Orion Nebula Cluster

The ONC is arguably the most intensively studied SFR, representing the archetype for local high-mass star formation. Recent sophisticated H-R diagram analyses (Da Rio et al. 2010b; Reggiani et al. 2011) suggest an age of $2 - 3\,\mathrm{Myr}$ based on the SDF00 model isochrones after accounting for astrophysical sources of scatter such as accretion, binarity, etc. The revised nominal age for the ONC derived in Section 5.6.3.1 is a factor of 2–3 older than these recent estimates. Photometric observations of the ONC are made problematic by the high background nebulosity associated with the region. To examine whether the photometric observations are systematically affected, with respect to other observations presented in this thesis, the optical photometry was compared to the unreddened photometry of Hillenbrand (1997). Cross-correlating the VI_c photometry of members stars with the $(gi)_\mathrm{WFC}$ photometry, this was then compared to the cross-correlated catalogues described above for σ Ori and λ Ori. Comparing these, there is no obvious systematic offsets between the g_WFC- and i_WFC-band photometry with respect to either σ Ori or λ Ori, suggesting that the $(gi)_\mathrm{WFC}$ photometry of the ONC is reliable.

The nominal age derived in Section 5.6.3.1 is based on the comparison at a model mass of $0.75\,\mathrm{M_\odot}$. Applying such a method to the H-R diagram of Da Rio et al. (2010b) suggests an age of $3 - 4\,\mathrm{Myr}$ based on the SDF00 models. Allowing for the model dependency in derived ages using pre-MS evolutionary models, this translates to an age of $4 - 5\,\mathrm{Myr}$ using the BCAH98 $\alpha = 1.9$ models. The distance derived in Section 2.8.4.11 is $\simeq 0.15\,\mathrm{mag}$ smaller than that used in Da Rio et al. (2010b), and thus when combined with the pre-MS model dependency, therefore accounts for the older age estimated in Section 5.6.3.1.

Cep OB3b

Pre-MS ages for Cep OB3b are not abundant in the literature, with the majority of age estimates based on the evolved MS population (e.g. 5.5 and 7 Myr; Jordi et al. 1996 and Blaauw 1991 respectively). Mayne et al. (2007) placed it on a relative pre-MS age scale, adopting a distance modulus $dm = 9.65$ and assigning a nominal age of 3 Myr. A revised distance ($dm = 8.8$) was derived in Littlefair et al. (2010) and this, tempered by the use of different reddening vectors, subsequently pushed the age slightly older to 4.5 Myr. The distance derived in Section 2.8.4.1 agrees to within 0.02 mag with that of Littlefair et al. (2010) and therefore the small increase in the age is likely due to a combination of leaving the photometry in the natural system of the observations and the more sophisticated method in dealing with the high reddening to this SFR that does not alter the shape of the pre-MS.

IC 348

The nominal age for IC 348 is approximately a factor of $2-3$ older than current estimates. Ages inferred from the pre-MS population are generally derived using de-reddened optical CMDs or H-R diagrams (e.g. Herbig 1998 and Luhman et al. 2003 respectively). Herbig (1998) derived a mean age of 1.3 Myr using the DAM97 models, based on a distance modulus $dm = 7.5$. This distance is $\simeq 0.5$ mag larger than that derived in Section 2.8.4.3. Interestingly, Herbig (1998) also calculates an age assuming a distance of $dm = 7.0$ – which is in excellent agreement to that derived in Section 2.8.4.3 – with the DAM97 models suggesting a mean age of $\simeq 3$ Myr, thereby agreeing with the nominal age derived in Section 5.6.3.1 using the same models. A similarly large distance is adopted in Luhman et al. (2003), who furthermore use the MS bolometric corrections of Kenyon & Hartmann (1995) to transform the photometric data into the H-R diagram, deriving an age of $\simeq$ 2 Myr. Thus the older age is predominantly a result of adopting a much closer distance to IC 348 (see also Enoch et al. 2006; Kirk et al. 2006).

6.3.1.3 Older Star-Forming Regions

NGC 2169

Interestingly, the age of $\simeq 9$ Myr is the same as that derived in Jeffries et al. (2007), who calculated a distance $\simeq 0.15$ mag larger than that derived in Section 2.8.4.5. Note, however, that the pre-MS ages derived in Section 5.6.2 are the most discrepant of all the SFRs, with the BCAH98 $\alpha = 1.9$ models implying that the SFR is 3 Myr older than suggested by the DCJ08 models. Thus when combined with the age diagnostics from the MS members, this could imply that the age is slightly underestimated. Jeffries et al. (2007) also used the τ^2 fitting statistic to fit the pre-MS members and recalibrated the model isochrones using the observed colours of Pleiades members (see Section 5.4.1). The assigned age is a mean age based on fits using the BCAH98 $\alpha = 1.0$ and SDF00 models. These models have been shown to overestimate the luminosity of stars with masses $\gtrsim 0.6\,M_\odot$, and hence effectively

cancel out the effect of a larger adopted distance, resulting in ages that are similar to those derived in Section 5.6.2.

λ Ori

The age derived for λ Ori of $\simeq 10\,\mathrm{Myr}$ is older than that generally quoted in the literature by approximately a factor of 2 (cf. $5\,\mathrm{Myr}$; see Dolan & Mathieu 2001; Barrado y Navascués et al. 2004a and references therein). The distance adopted in Dolan & Mathieu (2001) is $\simeq 0.25\,\mathrm{mag}$ larger than that derived in Section 2.8.3 and results in an age that is approximately a factor of 1.5 too young.

H-R diagrams and optical/near-IR CMDs of low-mass members of λ Ori (see Fig. 2 in Barrado y Navascués et al. 2007 and Fig. 11 in Bayo et al. 2011) clearly show that an age of $5\,\mathrm{Myr}$ is too young and does not accurately reflect the median age of the association. The accepted age of $5\,\mathrm{Myr}$ is generally based on fitting a single-star model isochrone to the approximate middle of the observed sequence in optical CMDs, and thus it is likely that a combination of the transformation of the evolutionary models into CMD space, possible errors introduced in the photometric calibration process (see Section 3.4) and not accounting for an intrinsic binary fraction are the main reasons for this age disparity.

The H-R diagram of Bayo et al. (2011) shows a considerable luminosity spread for stars with $T_{\mathrm{eff}} \lesssim 5000\,\mathrm{K}$ – equivalent to an age spread of $\simeq 30\,\mathrm{Myr}$ based on the interior models of BCAH98 – which is not observed in Fig. 5.7. To ensure that the memberships used to identify pre-MS objects are not the cause for the tighter observed sequence, the spectroscopically confirmed members of Bayo et al. (2011) were cross-correlated with the optical photometric catalogue of λ Ori. There is no evidence for an increased observed luminosity spread at a given colour using the Bayo et al. membership list. A possible reason for the large luminosity spread in the Bayo et al. H-R diagram is that L_{bol} values are calculated using bolometric corrections derived from a combination of PHOENIX and ATLAS9 atmospheric models. In Section 4.5 it was shown that the most recent sets of atmospheric models – with improved opacity line lists – systematically overestimate the flux in a given bandpass, and therefore the calculated bolometric corrections – especially for $T_{\mathrm{eff}} \lesssim 4000\,\mathrm{K}$ – are likely overestimated. Additional error in the calculation of L_{bol} is introduced by assuming that the extinction across the region is uniform (see Section 2.8.3 where this was shown not to be the case). Furthermore, the discretisation of the calculated spectral type-T_{eff} relation can act to artificially increase any intrinsic spread in L_{bol} at a given T_{eff}. Thus the apparent luminosity spread is likely an artefact of the transformation of the photometric data into the theoretical H-R diagram.

NGC 2362

The age derived for NGC 2362 is also a factor of 2 older than the generally adopted $5\,\mathrm{Myr}$ (e.g. Dahm 2005). The distance derived in Section 2.8.4.7 is $\simeq 0.3\,\mathrm{mag}$ smaller than that typically assumed (e.g. Moitinho et al. 2001; Dahm 2005), which translates into an age difference of $\simeq 3-4\,\mathrm{Myr}$. Thus whilst this is not large enough to explain the

age discrepancy, errors introduced into the position of the pre-MS by transforming the photometry into a standard system and the use of MS colours and bolometric corrections to transform the model isochrones into CMD space to fit the pre-MS members (e.g. Dahm 2005) could explain the difference.

NGC 7160

The marginal increase in the age of NGC 7160, when compared with the accepted age of 12 Myr (Sicilia-Aguilar et al. 2006a), is likely attributable to a combination of using the slightly closer distance derived in Section 2.8.4.10 which is $\simeq 0.1$ mag smaller and leaving the photometry in the natural plane of the observations.

χ Per

The age for χ Per is in excellent agreement with the recent study of Currie et al. (2010), who derive ages of 14 Myr based on isochrone fitting to the pre-MS, MS and M-type supergiant populations.

NGC 1960

The age derived for NGC 1960 is the first calculated based solely on low-mass pre-MS members, however a LDB age is also currently being investigated (Jeffries et al. in preparation).

6.4 Closing Words on Pre-Main-Sequence Isochrones

This section reiterates a number of the important findings that have been discovered over the course of this thesis on the use of pre-MS isochrones to derive ages from young stellar populations in CMDs.

- Traditional photometric calibration, using observations of MS standard stars to transform the data into a standard photometric system, should not be used for studies of pre-MS stars. Differences in $\log g$ and $T_{\rm eff}$ between a MS and pre-MS star of the same colour can, for instance, result in errors of $\simeq 0.1 - 0.15$ mag in both the $g_{\rm WFC}$-band and $(g - i)_{\rm WFC}$ colour for red stars. Hence it is crucial that precise photometric studies – especially of pre-MS objects – be carried out in the natural photometric system of the observations.

- An accurate model of the system responses for a given photometric system must include all the contributing components, from the Earth's atmosphere through to the CCD detector, not simply the filter responses.

- Having tested several sets of commonly used pre-MS evolutionary models, it has been shown that for all optical colours none of the models follow the observed Pleiades sequence for $T_{\rm eff} \lesssim 4000$ K. The models overestimate the flux by a factor of 2 at $0.5 \, \mu$m, with the difference decreasing with increasing wavelength. Note that the

models of SDF00 and BCAH98 $\alpha = 1.0$ systematically overestimate the luminosity of stars with masses $\gtrsim 0.6\,\mathrm{M_\odot}$ and do not match the observed Pleiades MS.

- This disparity for $T_\mathrm{eff} \lesssim 4000\,\mathrm{K}$ is primarily due to missing sources of opacity in the atmospheric models used to transform the evolutionary models into CMD space, but may also represent missing physics in the interior models themselves. Prior to deriving ages in this temperature regime, an empirical recalibration of the isochrones is necessary.

- The models that match the observed Pleiades MS at an age of $\simeq 130\,\mathrm{Myr}$ for $T_\mathrm{eff} > 4000\,\mathrm{K}$ (DAM97, BCAH98 $\alpha = 1.9$ and DCJ08) may not necessarily match the shape of the observed pre-MS in SFRs younger than $\simeq 10\,\mathrm{Myr}$. This may be due to inherent uncertainties in the models at such young ages (see Baraffe et al. 2002), but may also reflect the fact that physical processes affecting observed SEDs of young low-mass objects – such as chromospheric activity – are generally not included in the evolutionary models.

- The DAM97 evolutionary models systematically underestimate the ages of young stellar populations. These ages are not consistent with ages derived from the higher mass members, and therefore these models should not be used to age young SFRs.

6.5   Implications of the Revised Pre-Main-Sequence Age Scale

In Section 6.3 a set of revised pre-MS ages were assigned to a sample of young ($< 30\,\mathrm{Myr}$) SFRs. The evolution of YSOs and survival timescales for circumstellar discs were described in Chapter 1, both of which are heavily dependent upon the age assumed for a given region. Therefore, in this section the implications of the revised age scale on these current theories are briefly discussed.

6.5.1   Circumstellar Disc Lifetimes

Circumstellar discs appear to be a ubiquitous by-product of the star formation process and are a driving factor in the evolution of stars and planetary systems. Mid- to far-IR *Spitzer* observations of low-mass pre-MS stars indicate that by $\simeq 5\,\mathrm{Myr}$ approximately 80 % of primordial discs have dissipated (Carpenter et al. 2006; Dahm & Hillenbrand 2007), agreeing with estimates based on near-IR observations (Haisch et al. 2001b; Hillenbrand 2005). These timescales are almost exclusively based on ages determined from pre-MS isochrone fitting to young stellar populations and thus any revision of pre-MS SFR ages will naturally alter the expected lifetime of circumstellar discs.

Fig. 6.2 shows the disc frequency of late-type stars – typically mid K-type and later – with near-IR excess emission in different SFRs as a function of age. Disc fractions have generally been taken from studies based on *Spitzer* observations including NGC 6611 (Guarcello et al. 2007), IC 5146 (Harvey et al. 2008), NGC 2244 (Balog et al. 2007),
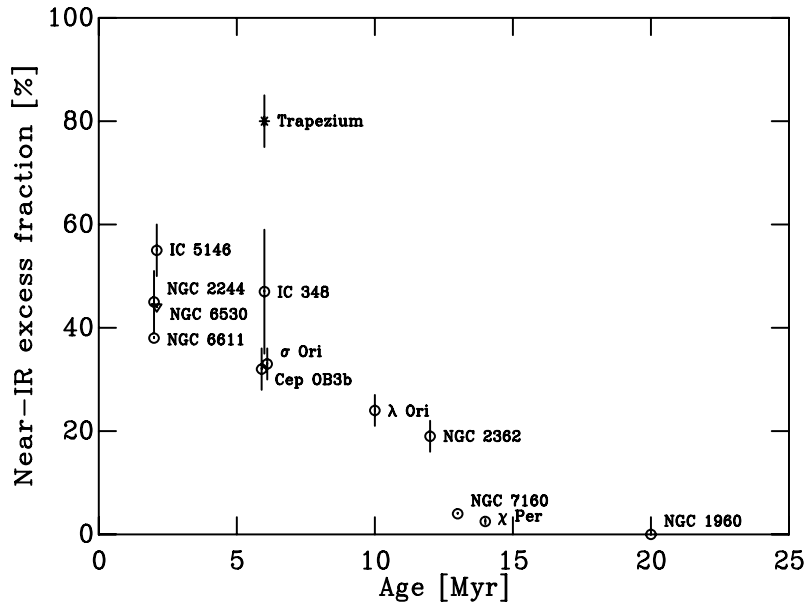
Figure 6.2: Fraction of stars – spectral types mid K-type and later – with near-IR excess disc emission as a function of revised age. Circles represent the disc fraction for TTS based on *Spitzer* observations (see text for references). The triangle represents the disc fraction based on JHK_s excess emission for NGC 6530 from Prisinzano et al. (2007). The asterisk denotes the disc fraction for the Trapezium cluster (the central 6×6 arcmin of the ONC) based on $JHKL$ observations from Haisch et al. (2001b). Note that the ages for IC 5146, NGC 6530, σ Ori and Cep OB3b have been shifted slightly to highlight the uncertainties on individually derived disc fractions.

Cep OB3b (Allen et al. 2012), σ Ori (Hernández et al. 2007), IC 348 (Lada et al. 2006), λ Ori (Barrado y Navascués et al. 2007), NGC 2362 (Dahm & Hillenbrand 2007), NGC 7160 (Sicilia-Aguilar et al. 2006a), χ Per (Currie et al. 2007), and NGC 1960 (Smith & Jeffries 2012). Note that in the case where both *Spitzer* and Haisch et al. (2001b) disc fractions were available, those of *Spitzer* have been adopted as they are less likely to be affected by sensitivity issues, particularly in the *L*-band (see Lyo et al. 2003). For SFRs where no newer *Spitzer* analysis have been performed, as in the case of the ONC, the disc fraction from Haisch et al. (2001b) has been adopted. The disc fraction quoted in Haisch et al. (2001b) corresponds to the Trapezium cluster only, which represents the core region of the ONC (central 6×6 arcmin) and is therefore not necessarily representative of the disc fraction of the entire ONC region. The disc fraction associated with NGC 6530 comes from the study of Prisinzano et al. (2007) who use JHK_s colour-colour diagrams and various Q-indices to determine stars with excess, which they attribute to circumstellar material. As demonstrated by Kenyon & Gómez (2001), *L*-band photometry is almost essential for constraining the disc bearing population of a given sample of stars. The JHK bandpasses do not extend to long enough wavelengths to unambiguously demonstrate the presence of circumstellar material, whereas observations at wavelengths $\gtrsim 3.5\,\mu$m provide a higher contrast relative to photospheric emission from the central star. Thus the value quoted by Prisinzano et al. (2007) should only be treated as an approximation. NGC 2169 does not

Table 6.1: Near-IR excess fraction as a function of revised pre-MS age. Fractions have been derived for late-type stars – typically mid K-type and later – based on *Spitzer* observations except where stated. Note are as follows. (1) Fraction derived based on 2MASS JHK_s observations. (2) Fraction derived using $JHKL$ observations and is for the Trapezium cluster only (the central 6×6 arcmin of the ONC).

SFR	Revised pre-MS age (Myr)	Near-IR excess fraction (%)	Reference
NGC 6611	2	$\simeq 38$	Guarcello et al. (2009)
IC5146	2	55 ± 5	Harvey et al. (2008)
NGC 6530[1]	2	$\simeq 44$	Prisinzano et al. (2007)
NGC 2244	2	45 ± 6	Balog et al. (2007)
Cep OB3b	6	32 ± 4	Allen et al. (2012)
σ Ori	6	33 ± 3	Hernández et al. (2007)
IC 348	6	47 ± 12	Lada et al. (2006)
ONC[2]	6	80 ± 5	Haisch et al. (2001b)
λ Ori	10	24 ± 3	Barrado y Navascués et al. (2007)
NGC 2362	12	19 ± 3	Dahm & Hillenbrand (2007)
NGC 7160	13	$\simeq 4$	Sicilia-Aguilar et al. (2006a)
χ Per	14	$2 - 3$	Currie et al. (2007)
NGC 1960	20	0	Smith & Jeffries (2012)

have a reported disc fraction. An upper limit of $8 - 10\%$ was estimated by Jeffries et al. (2007) based on a combination of K_s-band excess and Hα emission. Given that neither of these diagnostics are particularly robust, NGC 2169 is not shown in Fig. 6.2. The disc fractions taken from these various literature sources are also tabulated in Table 6.1.

It is hard to draw definitive conclusions from Fig. 6.2, but what is evident is that circumstellar discs appear to survive longer than previously believed, indicating a disc half-life of $\simeq 5 - 6$ Myr with approximately 80% of stars having lost their discs on timescales of $\simeq 10 - 12$ Myr. A young SFR region not studied in this thesis, but which deserves a mention is Upper Sco. Recent analysis of F-type stars in Upper Sco showed that they were a factor of 2.5 less luminous compared with predictions for a 5 Myr old population by four sets of pre-MS models (Pecaut et al. 2012). Isochronal ages were derived separately for B-, A- and F-type stars, as well as the M-type supergiant Antares, indicating an overall mean age of $\simeq 11$ Myr (i.e. a factor of 2 older than previously believed). This SFR, in addition to λ Ori, has been used as a benchmark for the study of circumstellar disc lifetimes and fractions. Hernández et al. (2010) showed that the disc fraction for stars of spectral type K and later in λ Ori ($18.5 \pm 4.0\%$) is comparable to that in Upper Sco ($19 \pm 4\%$; Carpenter et al. 2006). Furthermore, similar evolved disc fractions were estimated for earlier spectral types ($\sim 31\%$ in both cases; Carpenter et al. 2009; Hernández et al. 2009) and circumstellar disc fractions in the substellar regime (40 and $50 \pm 12\%$ respectively; Barrado y Navascués et al. 2007; Bouy et al. 2007). Using Hα as a proxy for stars that are actively accreting, Barrado y Navascués et al. (2007) re-analysed the data of Dolan & Mathieu (2001) and found that $\simeq 11\%$ of stars are actively accreting in λ Ori (see also Sacco et al. 2008), compared with $\simeq 10\%$ in Upper Sco (Lodieu et al. 2011).

As discussed in Ayliffe & Bate (2009), there is a long-standing concern that the timescales required by numerical models to form a gas giant Jupiter-like planet ($\simeq 10$ Myr; Perri & Cameron 1974; Pollack et al. 1996) may be larger than the observed circumstellar disc lifetime ($\simeq 5$ Myr; Haisch et al. 2001b). Fortier et al. (2007) demonstrated that whilst a $4.2\,\mathrm{M_{\oplus}}$ core can be formed in 1.1 Myr assuming a nebula density 10 times that of the Minimum Mass Solar Nebula, at an equivalent density they were unable to form a $10\,\mathrm{M_{\oplus}}$ core in 10 Myr. Note, however, that the core mass of gas giant planets are not well constrained, for example Saturn's is $9 - 22\,\mathrm{M_{\oplus}}$ based on the interior models of Saumon & Guillot (2004). Hence the findings presented here offer a simple solution to this apparent discrepancy. If the SFRs used to measure the dissipation timescale of circumstellar discs are on average a factor of 2 older, then the discs survive for approximately twice as long and thus provide the necessary reservoirs to form gas giant planets on $\simeq 10$ Myr timescales.

6.5.2 Evolutionary Lifetimes of Young Stellar Objects

Having discussed the effects of the revised age scale in terms of circumstellar disc lifetimes, this naturally leads onto the lifetimes of different evolutionary stages of YSOs. The generally adopted method to derive such timescales is to use the number of objects in each class to establish relative lifetimes (e.g. Wilking et al. 1989). A recent study by Evans et al. (2009) proposed that if star formation is a continuous process with a duration larger than the age of Class II objects (CTTS), then relative YSO evolutionary lifetimes can be estimated by taking the ratio of objects in each class and multiplying by the adopted lifetime for a Class II object. Based on various studies of young SFRs, a lifetime of $\simeq 2$ Myr was assigned to the Class II evolutionary phase, with the lifetimes of the other classes derived accordingly.

It is clear then that any revision to the pre-MS ages of young SFRs will have an impact on the adopted Class II lifetime used to calculate relative lifetimes for other YSO evolutionary phases. Whilst an in-depth discussion on how the relative ages are affected by the revised ages is beyond the scope of this thesis, Fig. 6.2 suggests that the adopted lifetime of Class II objects is likely underestimated. The ages derived in Section 5.6 are approximately a factor of two older than current ages for the same SFRs. Regions, such as λ Ori, with two independent age determinations at $\simeq 10$ Myr (see also Upper Sco; Pecaut et al. 2012) which show that $\simeq 20\,\%$ of stars retain their circumstellar discs (indicative of Class II status) and that $\simeq 10\,\%$ of stars are still accreting, imply a longer Class II lifetime somewhere in the region of $\simeq 4 - 5$ Myr. Propagating this age to the earlier Class I lifetime, based on the number of YSOs presented in Evans et al. (2009) and ignoring environmental effects, indicates an average lifetime of $\simeq 1$ Myr.

6.6 Summary

For SFRs with revised ages of $\gtrsim 9$ Myr, this study represents the first statistically robust comparison of ages derived from different mass regimes using isochrone fitting and fur-

thermore shows agreement for the first time between the MS and pre-MS ages for SFRs $< 50\,\mathrm{Myr}$ (see Piskunov et al. 2004; Lyra et al. 2006; Naylor 2009). Thus it suggests, at least for ages $\gtrsim 9\,\mathrm{Myr}$, the assumption that the absolute shift in the BC-T_{eff} relation is age insensitive and that the attempt to incorporate the $\log g$ dependence based on the predictions of the atmospheric models are reasonable. For younger SFRs, however, these approximations do not appear to be as valid. Furthermore, we stress the point that even for $T_{\mathrm{eff}} > 4000\,\mathrm{K}$, where the pre-MS evolutionary models have not been recalibrated, the shape of the model isochrones with respect to the observed sequence is discrepant. This suggests that some of the underlying assumptions may be in need of further investigation (e.g. the inadequate treatment of convection, missing opacities and exclusion of physical processes that affect the photospheric properties of young stars). A new generation of the BCAH98 models are currently being prepared and should hopefully be ready in the coming months. Whilst it is unclear what the exact modifications are to the underlying physics, the photometric dataset presented in this thesis would make an ideal testbed for these new models.

Chapter 7

Conclusions and Future Work

7.1 Conclusions

This thesis has presented a critical assessment of commonly used theoretical pre-MS stellar evolutionary models by comparing the predictions to the low-mass pre-MS populations of 14 young SFRs in CMDs.

Before comparing the pre-MS models with the photometric data, a self-consistent set of ages, distances and reddenings were derived from the MS population of the SFRs. For this, updated reddening vectors have been created using a combination of atmospheric models, the appropriate photometric bandpasses and a law describing the interstellar extinction as a function of wavelength. A set of MS interior models were introduced and the necessary techniques described to transform these models into CMD space. In some cases the extinction across the region is highly variable and therefore a revised version of the original Q-method, based on a combination of the MS interior models and the updated reddening vectors, was used to de-redden stars individually using photometric data alone. The MS models were then fitted to the photometric data in the $V, B - V$ CMD using the τ^2 fitting statistic that derives statistically significant uncertainties on both the age and the distance of the best-fit. Furthermore, it was demonstrated that uncertainties in both the assumed distance and composition remain the largest source of uncertainty for deriving pre-MS ages.

The main uncertainties associated with fitting evolutionary models to pre-MS populations in CMDs were discussed, these include; i) the photometric calibration of the data (especially for very red pre-MS objects), ii) the transformation of the model isochrones from theoretical H-R to observable CMD space and iii) incorporating the colour and gravity dependence of the interstellar reddening. Addressing the first point, it was shown that using observations of MS stars to calibrate pre-MS photometric data can introduce significant errors in the position of the pre-MS locus in CMD space. The traditional technique of adopting a linear colour-dependent offset – based on MS star observations – to transform instrumental INT-WFC colours and magnitudes into the standard SDSS photometric system does not work due to combination of subtle differences in the relative system responses and differences in the $\log g$ and T_{eff} between a MS and pre-MS star of the same colour.

Hence precise photometric studies of such objects should be carried out in the natural system of the observations. This therefore necessitates that a robust model of the system responses for the instrument used to take the observations be created. Thus, the system responses for the INT-WFC have been calculated that incorporate every contribution to the total throughput from the Earth's atmosphere through to the CCD detector quantum efficiency. These system responses have been tested using a colour-selected sample of MS stars over a large range of colours and have been shown to be a good representation of the photometric system.

A benchmark test of the pre-MS model isochrones was performed by comparing them against a set of well-calibrated CMDs of the Pleiades over a contiguous wavelength range of $0.4 - 2.5\,\mu$m. This test showed that all of the models (BCAH98, SDF00, DAM97, and DCJ08) systematically overestimate the flux in optical colours for $T_{\mathrm{eff}} \lesssim 4000\,\mathrm{K}$. This discrepancy was primarily attributed to incomplete line lists used in the calculation of the BT-Settl atmospheric models that were subsequently used to create the necessary bolometric corrections to transform the models into CMD space, however additional effects, such as physical processes unaccounted for in the evolutionary models, may also contribute. It was also demonstrated that both the BCAH98 $\alpha = 1.0$ and SDF00 models overestimate the luminosity of stars with masses $\gtrsim 0.6\,\mathrm{M_{\odot}}$. This is due to the fact that neither have a solar-calibrated mixing length parameter. The masses predicted by the evolutionary models were then tested against dynamical masses using a sample of MS eclipsing and spectroscopic binaries by calculating the system magnitude in a given photometric bandpass. The overestimation of the flux noted above was observed to decrease as a function of increasing wavelength, becoming negligible in the K_{s}-band. On the assumption that the K_{s}-band magnitude, as predicted by a combination of the interior and atmospheric models, is correct, the mismatch between the models and the data was quantified using the K_{s}-band magnitude to determine the T_{eff} of Pleiades members. Comparing the predicted magnitude in the other photometric bandpasses with that of the Pleiades members, it was found that the models overestimate the flux by approximately a factor of 2 at $0.5\,\mu$m, though this decreases, becoming negligible at $2.2\,\mu$m. Thus for stars with $T_{\mathrm{eff}} \lesssim 4000\,\mathrm{K}$, this could result in the derived ages for pre-MS stars being underestimated by between factors of 2 and 3 depending on the adopted colours.

The quantified mismatch was used to recalibrate the pre-MS evolutionary models before using them to derive ages from the low-mass populations of the SFRs. In the case of the older SFRs, with no apparent luminosity spread, these recalibrated semi-empirical pre-MS isochrones were used, in conjunction with the τ^2 fitting statistic, to derive absolute ages. For younger SFRs, however, it was noted that the semi-empirical pre-MS isochrones do not always follow the shape of the observed pre-MS locus – even for $T_{\mathrm{eff}} > 4000\,\mathrm{K}$ where no recalibration was necessary – and hence, when combined with the large observed luminosity spread, it was not possible to derive absolute ages. The reasons for this mismatch remain unclear, however it is possible that uncertainties in the evolutionary models at such ages – for example due to the inaccurate treatment of

convection or physical processes that affect the SEDs of young low-mass stars that are not included – may be responsible. In such cases, so-called nominal ages have been derived by effectively comparing the position of a model $0.75\,M_\odot$ star with the approximate middle of the observed spread. Having derived two independent age estimates from different mass regimes that rely on different stellar physics, the MS and pre-MS ages were then compared. The pre-MS age scale based on the DAM97 models was shown to be inconsistent with the MS ages, with the pre-MS ages being systematically younger than the MS ages, and therefore the DAM97 pre-MS age scale was rejected. Conversely, the age scale of both the BCAH98 $\alpha = 1.9$ and DCJ08 were in general agreement with the MS scale, and hence these were used to assign final ages to the 14 SFRs in the sample. These revised ages are approximately a factor of 2 older than previous derivations, a result with wide-ranging implications, including that protoplanetary disc and Class II YSO lifetimes are approximately twice as long ($\simeq 10$ and $\simeq 4 - 5\,\mathrm{Myr}$ respectively) as currently believed.

7.2 Future work

Complementary future projects arising from the work presented in this thesis can be categorised into two distinct areas. First, there is the derivation of consistent ages and investigating the effects of environment on the evolution of young stars. Second, there is the longer term plan to calibrate the pre-MS evolutionary models.

7.2.1 Consistent Ages and Investigating Environmental Effects

7.2.1.1 Extension to Other Star-Forming Regions

The most obvious extension of the work presented in this thesis is to apply the developed techniques to other SFRs that are of particular interest but not included in the current sample – such as NGC 2024, NGC 2264, etc. – to create a database of young SFRs with self-consistent ages, distances and reddenings. This database can then be combined with ancillary data such as X-ray and IR observations, and follow-up spectroscopy to allow a comprehensive unbiased study of the circumstellar disc fraction in young SFRs. The characterisation of properties such as accretion, activity and rotation could then be used to discuss stellar evolution in terms of SFR environment, and in particular, what effect high-mass stars have on the ensuing star formation in the immediate vicinity.

The sample of SFRs in this thesis only represent a subset of SFRs in the northern hemisphere alone and therefore another obvious extension is to study SFRs in the southern hemisphere. Whilst the VPHAS+ survey will hopefully soon begin collecting broadband *ugri* and narrowband Hα photometry across the entire southern Galactic plane, the intention to calibrate the photometric observations using a combination of Landolt and SDSS standard fields may affect the final photometry, especially for the youngest and reddest objects (see Section 3.4.5). Therefore a proposal is currently being worked on to use the wide-field OmegaCAM on the 2.6-m VST to significantly increase the sample of SFRs. Obviously an initial test of the pre-MS models, as was performed in Bell et al. (2012),

will be necessary to see how the models compare with an empirical sequence in a different natural photometric system and for these purposes Blanco 1 provides the equivalent benchmark cluster in the southern hemisphere.

7.2.1.2 Investigating the Effects of Environment on Young Stars

Studying how the properties of young stars – and discs – vary with the physical conditions in which they form and subsequently evolve can offer significant insight into the underlying physics of star and planet formation. For example, the presence of high-mass stars may act to photoevaporate circumstellar discs due to high levels of wind and radiation from the massive stars (see Section 1.2.5.1), and this is therefore easily tested by investigating the fraction of stars with discs in regions with and without such massive stars. Furthermore, there are suggestions in the literature that the IMF may vary between environments of low and high density (e.g. Luhman et al. 2009), however the problem with interpreting the IMF is that the conclusions are heavily dependent upon the assumed age for a given region, which as has been shown are extremely uncertain (see for example Section 4.1). Circumstellar disc fractions may vary with the proximity of massive stars, however they definitely vary as a function of age, and therefore robust ages for stellar populations are essential to disentangle the two effects.

A proposal to perform a large-scale photometric study of the archetypal low-mass, low-density SFR of Taurus has recently been approved. Given that there are no high-mass objects in Taurus, an age must be determined from the low-mass pre-MS population alone. Furthermore, to be consistent with the ages derived in this thesis for the high-mass SFRs, the data must be in the well-calibrated INT photometric system. The obvious goals of this project are as follows. i) Recalculate the IMF for Taurus and the high-mass SFRs to look for systematic differences. ii) Compare the disc fractions of SFRs at similar ages to establish whether discs survive longer in the low-density environment of Taurus. iii) Investigate whether there is evidence of differences in the rotational evolution of young pre-MS stars due to their environment. iv) Investigate whether there are age differences between different regions in Taurus, which may help differentiate between a star formation model that suggests it occurs in a tight cluster, later fragmenting into an expanding group of sub-clusters and a filamentary, gravitationally-driven collapse model.

7.2.2 Long-Term Calibration of Pre-Main-Sequence Evolutionary Models

The main uncertainties in deriving pre-MS ages from evolutionary models are; i) that pre-MS models do not currently match the observed shape of empirical isochrones (especially for masses $\lesssim 0.5\,\mathrm{M}_\odot$), ii) uncertainties in the assumed distance, and iii) uncertainties in the composition of the stars. Each of these issues can be addressed in the coming years as a result of large-scale surveys, supplemented with additional observational information.

The upcoming *Gaia* mission will provide astrometric and space motion data with which to identify all members of the known, nearby OB associations/moving groups (as

well as possibly determining new groups; cf. de Zeeuw et al. 1999). Kinematic traceback ages can then be derived for several groups – assuming a Galactic potential – with ages $\gtrsim 10\,\mathrm{Myr}$. Well-calibrated and homogeneous photometric measurements of these members stars are then required to create empirical isochrones for these groups (e.g. Mayne et al. 2007). These empirical isochrones can then be used to recalibrate the contemporary pre-MS evolutionary models of the day, which in turn, can be used to derive ages for young SFRs in conjunction with robust distances from *Gaia* and well-calibrated photometric observations.

The pre-MS evolutionary models tested in this thesis have been in public use for over a decade and are based on, at the time, contemporary estimates of the solar abundances ($Z \simeq 0.02$; e.g. Grevesse & Anders 1989; Grevesse & Sauval 1998). In recent years, these estimates have been revised ($Z \simeq 0.016$; e.g. Asplund et al. 2005, 2009) and it would be interesting to investigate what effects a change in the underlying composition of the evolutionary models would have on the computed L_{bol} and T_{eff}. Theorists are therefore encouraged to recalculate their models for the revised solar abundance of $Z = 0.016$, but also for sub- and super-solar compositions. The on-going *Gaia*-ESO survey, which is a project to obtain multi-object spectroscopic measurements of many of the stars that *Gaia* will observe, will provide invaluable data which can be used to determine the metallicity of many young moving groups/SFRs. Hence, using a similar method to that described above, this can then be used to recalibrate pre-MS evolutionary models over a range of metallicities.

This combination of precise photometry and spectroscopy for young stars spanning a range of ages further offers the possibility to observationally constrain the dependence of the BC-T_{eff} relation on $\log g$ as a function of age (as opposed to relying on the dependence as derived using atmospheric models). Due to intrinsic variability in the pre-MS phase (see Section 1.2.3.2) it is imperative that stars of a given age meet several criteria so that they can be used to derive bolometric corrections in several photometric bandpasses. Such stars should; i) be non-accreting (use Hα excess to establish this), ii) have very low reddening (which may otherwise complicate photospheric emission estimates), iii) have no associated circumstellar disc, iv) be bona fide members of a SFR with a well-determined age, and v) have small associated photometric uncertainties.

Bibliography

Abt, H. A. 1977, PASP, 89, 646

Adams, F. C., Hollenbach, D., Laughlin, G., & Gorti, U. 2004, ApJ, 611, 360

Adams, F. C., Lada, C. J., & Shu, F. H. 1987, ApJ, 312, 788

Alcalá, J. M., Krautter, J., Schmitt, J. H. M. M., et al. 1995, A&AS, 114, 109

Alexander, D. R., Augason, G. C., & Johnson, H. R. 1989, ApJ, 345, 1014

Alexander, D. R. & Ferguson, J. W. 1994, ApJ, 437, 879

Alexander, R. D., Clarke, C. J., & Pringle, J. E. 2006a, MNRAS, 369, 216

Alexander, R. D., Clarke, C. J., & Pringle, J. E. 2006b, MNRAS, 369, 229

Allain, S. 1998, A&A, 333, 629

Allard, F., Guillot, T., Ludwig, H.-G., et al. 2003, in IAU Symposium, Vol. 211, Brown
   Dwarfs, ed. E. Martín, 325

Allard, F. & Hauschildt, P. H. 1995, ApJ, 445, 433

Allard, F., Hauschildt, P. H., Alexander, D. R., & Starrfield, S. 1997, ARA&A, 35, 137

Allard, F., Hauschildt, P. H., Alexander, D. R., Tamanai, A., & Schweitzer, A. 2001, ApJ,
   556, 357

Allard, F., Hauschildt, P. H., & Schweitzer, A. 2000, ApJ, 539, 366

Allard, F., Homeier, D., & Freytag, B. 2011, in Astronomical Society of the Pacific Confer-
   ence Series, Vol. 448, Astronomical Society of the Pacific Conference Series, ed. C. Johns-
   Krull, M. K. Browning, & A. A. West, 91

Allard, N. F., Drira, I., Gerbaldi, M., Kielkopf, J., & Spielfiedel, A. 1998, A&A, 335, 1124

Allen, C. W. 1963, Astrophysical Quantities, ed. Allen, C. W.

Allen, L. E., Calvet, N., D'Alessio, P., et al. 2004, ApJS, 154, 363

Allen, T. S., Gutermuth, R. A., Kryukova, E., et al. 2012, ApJ, 750, 125

Alvarez, R. & Plez, B. 1998, A&A, 330, 1109

Aly, J. J. & Kuijpers, J. 1990, A&A, 227, 473

Ambartsumian, V. A. 1947, Stellar Evolution and Astrophysics, Armenian Acad. of Sci.

Ambartsumian, V. A. 1949, Dokl. Akad. Nauk SSR, 68, 22

An, D., Terndrup, D. M., Pinsonneault, M. H., et al. 2007, ApJ, 655, 233

Anders, E. & Grevesse, N. 1989, Geochim. Cosmochim. Acta, 53, 197

Andersen, J., Nordstrom, B., Garcia, J. M., & Gimenez, A. 1987, A&A, 174, 107

André, P. & Montmerle, T. 1994, ApJ, 420, 837

André, P., Ward-Thompson, D., & Barsony, M. 1993, ApJ, 406, 122

André, P., Ward-Thompson, D., & Barsony, M. 2000, Protostars and Planets IV, 59

Andrews, S. M. & Williams, J. P. 2005, ApJ, 631, 1134

Appenzeller, I. & Mundt, R. 1989, A&A Rev., 1, 291

Appenzeller, I., Oestreicher, R., & Jankovics, I. 1984, A&A, 141, 108

Ardila, D. R. & Basri, G. 2000, ApJ, 539, 834

Arias, J. I., Barbá, R. H., Maíz Apellániz, J., Morrell, N. I., & Rubio, M. 2006, MNRAS, 366, 739

Armitage, P. J. & Clarke, C. J. 1996, MNRAS, 280, 458

Asplund, M., Grevesse, N., & Sauval, A. J. 2005, in Astronomical Society of the Pacific Conference Series, Vol. 336, Cosmic Abundances as Records of Stellar Evolution and Nucleosynthesis, ed. T. G. Barnes, III & F. N. Bash, 25

Asplund, M., Grevesse, N., Sauval, A. J., & Scott, P. 2009, ARA&A, 47, 481

Ayliffe, B. A. & Bate, M. R. 2009, MNRAS, 393, 49

Bacciotti, F., Ray, T. P., Mundt, R., Eislöffel, J., & Solf, J. 2002, ApJ, 576, 222

Bachiller, R. 1996, ARA&A, 34, 111

Bacmann, A., André, P., Puget, J., et al. 2000, A&A, 361, 555

Bahcall, J. N., Basu, S., Pinsonneault, M., & Serenelli, A. M. 2005, ApJ, 618, 1049

Bailer-Jones, C. A. L. & Mundt, R. 2001, A&A, 367, 218

Balazs, L. G. & Kun, M. 1989, Astronomische Nachrichten, 310, 385

Baliunas, S. L. & Vaughan, A. H. 1985, ARA&A, 23, 379

Ballesteros-Paredes, J. & Hartmann, L. 2007, RMxAA, 43, 123

Ballesteros-Paredes, J., Hartmann, L., & Vázquez-Semadeni, E. 1999a, ApJ, 527, 285

Ballesteros-Paredes, J., Klessen, R. S., Mac Low, M., & Vázquez-Semadeni, E. 2007, Protostars and Planets V, 63

Ballesteros-Paredes, J., Vázquez-Semadeni, E., & Scalo, J. 1999b, ApJ, 515, 286

Balog, Z., Muzerolle, J., Rieke, G. H., et al. 2007, ApJ, 660, 1532

Balona, L. A. & Laney, C. D. 1996, MNRAS, 281, 1341

Balona, L. A. & Shobbrook, R. R. 1984, MNRAS, 211, 375

Banerjee, R. & Pudritz, R. E. 2006, ApJ, 641, 949

Baraffe, I., Chabrier, G., Allard, F., & Hauschildt, P. 2001, in Astronomical Society of the Pacific Conference Series, Vol. 243, From Darkness to Light: Origin and Evolution of Young Stellar Clusters, ed. T. Montmerle & P. André, 571

Baraffe, I., Chabrier, G., Allard, F., & Hauschildt, P. H. 1995, ApJL, 446, L35

Baraffe, I., Chabrier, G., Allard, F., & Hauschildt, P. H. 1998, A&A, 337, 403

Baraffe, I., Chabrier, G., Allard, F., & Hauschildt, P. H. 2002, A&A, 382, 563

Baraffe, I., Chabrier, G., Barman, T. S., Allard, F., & Hauschildt, P. H. 2003, A&A, 402, 701

Baraffe, I., Chabrier, G., & Gallardo, J. 2009, ApJL, 702, L27

Baraffe, I., Vorobyov, E., & Chabrier, G. 2012, ApJ, 756, 118

Barber, R. J., Tennyson, J., Harris, G. J., & Tolchenov, R. N. 2006, MNRAS, 368, 1087

Barkhatova, K. A., Zakharova, P. E., Shashkina, L. P., & Orekhova, L. K. 1985, AZh, 62, 854

Barnard, E. E. 1927, Carnegie Inst. Washington Pub., 247

Barnes, S. A. 2003a, ApJL, 586, L145

Barnes, S. A. 2003b, ApJ, 586, 464

Barrado, D., Stelzer, B., Morales-Calderón, M., et al. 2011, A&A, 526, A21

Barrado y Navascués, D., Stauffer, J. R., Bouvier, J., Jayawardhana, R., & Cuillandre, J.-C. 2004a, ApJ, 610, 1064

Barrado y Navascués, D., Stauffer, J. R., & Jayawardhana, R. 2004b, ApJ, 614, 386

Barrado y Navascués, D., Stauffer, J. R., Morales-Calderón, M., et al. 2007, ApJ, 664, 481

Barsony, M., Ressler, M. E., & Marsh, K. A. 2005, ApJ, 630, 381

Bary, J. S., Weintraub, D. A., & Kastner, J. H. 2002, ApJL, 576, L73

Basri, G. & Batalha, C. 1990, ApJ, 363, 654

Basri, G., Marcy, G. W., & Graham, J. R. 1996, ApJ, 458, 600

Basri, G., Marcy, G. W., & Valenti, J. A. 1992, ApJ, 390, 622

Bayo, A., Barrado, D., Stauffer, J., et al. 2011, A&A, 536, A63

Becker, W. & Stock, J. 1954, ZAp, 34, 1

Beckwith, S. V. W., Sargent, A. I., Chini, R. S., & Guesten, R. 1990, AJ, 99, 924

Beichman, C. A., Myers, P. C., Emerson, J. P., et al. 1986, ApJ, 307, 337

Béjar, V. J. S., Caballero, J. A., Rebolo, R., Zapatero Osorio, M. R., & Barrado y Navascués, D. 2004, Ap&SS, 292, 339

Béjar, V. J. S., Martín, E. L., Zapatero Osorio, M. R., et al. 2001, ApJ, 556, 830

Béjar, V. J. S., Zapatero Osorio, M. R., & Rebolo, R. 1999, ApJ, 521, 671

Belikov, A. N., Kharchenko, N. V., Piskunov, A. E., & Schilbach, E. 1999, A&AS, 134, 525

Belikov, A. N., Kharchenko, N. V., Piskunov, A. E., Schilbach, E., & Scholz, R.-D. 2002, A&A, 387, 117

Bell, C. P. M., Naylor, T., Mayne, N. J., Jeffries, R. D., & Littlefair, S. P. 2012, MNRAS, 424, 3178

Berghöfer, T. W. & Christian, D. J. 2002, A&A, 384, 890

Berghöfer, T. W. & Schmitt, J. H. M. M. 1998, in Astronomical Society of the Pacific Conference Series, Vol. 154, Cool Stars, Stellar Systems, and the Sun, ed. R. A. Donahue & J. A. Bookbinder, 2091

Bergin, E. A. & Tafalla, M. 2007, ARA&A, 45, 339

Bertout, C., Basri, G., & Bouvier, J. 1988, ApJ, 330, 350

Bertout, C., Siess, L., & Cabrit, S. 2007, A&A, 473, L21

Bessell, M. S. 1979, PASP, 91, 589

Bessell, M. S. 1990, PASP, 102, 1181

Bessell, M. S., Castelli, F., & Plez, B. 1998, A&A, 333, 231

Bessell, M. S. & Weis, E. W. 1987, PASP, 99, 642

Bethe, H. A. 1939, Physical Review, 55, 434

Bildsten, L., Brown, E. F., Matzner, C. D., & Ushomirsky, G. 1997, ApJ, 482, 442

Bjork, S. R. & Chaboyer, B. 2006, ApJ, 641, 1102

Blaauw, A. 1952, Bull. Astron. Inst. Netherlands, 11, 405

Blaauw, A. 1964, ARA&A, 2, 213

Blaauw, A. 1991, in NATO ASIC Proc. 342: The Physics of Star Formation and Early Stellar Evolution, ed. C. J. Lada & N. D. Kylafis, 125

Blaauw, A., Hiltner, W. A., & Johnson, H. L. 1959, ApJ, 130, 69

Blanco, V. M. 1956, ApJ, 123, 64

Blandford, R. D. & Payne, D. G. 1982, MNRAS, 199, 883

Blitz, L. 1993, in Protostars and Planets III, ed. E. H. Levy & J. I. Lunine, 125

Blitz, L. & Shu, F. H. 1980, ApJ, 238, 148

Boden, E. 1951, Uppsala Astron. Obs. Ann., 3, 1

Bodenheimer, P. 1965, ApJ, 142, 451

Bodenheimer, P. 1995, ARA&A, 33, 199

Böhm-Vitense, E. 1958, ZAp, 46, 108

Bok, B. J. 1934, Harvard College Observatory Circular, 384, 1

Bok, B. J. & Reilly, E. F. 1947, ApJ, 105, 255

Bolton, C. T. 1974, ApJL, 192, L7

Bonatto, C., Santos, Jr., J. F. C., & Bica, E. 2006, A&A, 445, 567

Bonnor, W. B. 1956, MNRAS, 116, 351

Bono, G., Caputo, F., Cassisi, S., Castellani, V., & Marconi, M. 1997, ApJ, 479, 279

Bonsack, W. K. & Greenstein, J. L. 1960, ApJ, 131, 83

Boss, A. P. 1997, Science, 276, 1836

Bouvier, J. 1990, AJ, 99, 946

Bouvier, J., Alencar, S. H. P., Harries, T. J., Johns-Krull, C. M., & Romanova, M. M. 2007, Protostars and Planets V, 479

Bouvier, J., Cabrit, S., Fernandez, M., Martin, E. L., & Matthews, J. M. 1993, A&A, 272, 176

Bouvier, J., Covino, E., Kovo, O., et al. 1995, A&A, 299, 89

Bouvier, J., Dougados, C., & Alencar, S. H. P. 2004, Ap&SS, 292, 659

Bouvier, J., Forestini, M., & Allain, S. 1997, A&A, 326, 1023

Bouvier, J., Grankin, K. N., Alencar, S. H. P., et al. 2003, A&A, 409, 169

Bouwman, J., Lawson, W. A., Dominik, C., et al. 2006, ApJL, 653, L57

Bouy, H., Huélamo, N., Martín, E. L., et al. 2007, A&A, 463, 641

Brandner, W., Zinnecker, H., Alcalá, J. M., et al. 2000, AJ, 120, 950

Bressert, E., Bastian, N., Gutermuth, R., et al. 2010, MNRAS, 409, L54

Briceño, C. 2009, in Revista Mexicana de Astronomia y Astrofisica Conference Series, Vol. 35, 12th IAU Regional Latin American Meeting of Astronomy, ed. G. Magris, G. Bruzual, & L. Carigi, 27

Briceño, C., Hartmann, L. W., Stauffer, J. R., et al. 1997, AJ, 113, 740

Briceño, C., Preibisch, T., Sherry, W. H., et al. 2007, Protostars and Planets V, 345

Brott, I., de Mink, S. E., Cantiello, M., et al. 2011, A&A, 530, A115

Brott, I. & Hauschildt, P. H. 2005, in ESA Special Publication, Vol. 576, The Three-Dimensional Universe with Gaia, ed. C. Turon, K. S. O'Flaherty, & M. A. C. Perryman, 565

Brown, A. G. A., de Geus, E. J., & de Zeeuw, P. T. 1994, A&A, 289, 101

Browning, M. K. 2011, in IAU Symposium, Vol. 271, Astrophysical Dynamics: From Stars to Galaxies, ed. N. H. Brummell, A. S. Brun, M. S. Miesch, & Y. Ponty, 69

Bubar, E. J., King, J. R., Soderblom, D. R., Deliyannis, C. P., & Boesgaard, A. M. 2007, AJ, 134, 2328

Burningham, B., Naylor, T., Jeffries, R. D., & Devey, C. R. 2003, MNRAS, 346, 1143

Burningham, B., Naylor, T., Littlefair, S. P., & Jeffries, R. D. 2005a, MNRAS, 363, 1389

Burningham, B., Naylor, T., Littlefair, S. P., & Jeffries, R. D. 2005b, MNRAS, 356, 1583

Burton, M. G., Lawrence, J. S., Ashley, M. C. B., et al. 2005, PASA, 22, 199

Caballero, J. A. 2008, MNRAS, 383, 750

Caballero, J. A., Béjar, V. J. S., Rebolo, R., et al. 2007, A&A, 470, 903

Cabrit, S., Edwards, S., Strom, S. E., & Strom, K. M. 1990, ApJ, 354, 687

Calvet, N., Basri, G., & Kuhi, L. V. 1984, ApJ, 277, 725

Calvet, N. & Gullbring, E. 1998, ApJ, 509, 802

Camenzind, M. 1990, in Reviews in Modern Astronomy, Vol. 3, Reviews in Modern Astronomy, ed. G. Klare, 234

Canuto, V. M. & Mazzitelli, I. 1991, ApJ, 370, 295

Canuto, V. M. & Mazzitelli, I. 1992, ApJ, 389, 724

Cardelli, J. A. & Clayton, G. C. 1988, AJ, 95, 516

Cardelli, J. A., Clayton, G. C., & Mathis, J. S. 1989, ApJ, 345, 245

Cargile, P. A. & James, D. J. 2010, AJ, 140, 677

Cargile, P. A., Stassun, K. G., & Mathieu, R. D. 2008, ApJ, 674, 329

Carkner, III, A. L. 1998, PhD thesis, Pennsylvania State University

Carpenter, J. M., Hillenbrand, L. A., & Skrutskie, M. F. 2001, AJ, 121, 3160

Carpenter, J. M., Mamajek, E. E., Hillenbrand, L. A., & Meyer, M. R. 2006, ApJL, 651, L49

Carpenter, J. M., Mamajek, E. E., Hillenbrand, L. A., & Meyer, M. R. 2009, ApJ, 705, 1646

Casagrande, L., Portinari, L., & Flynn, C. 2006, MNRAS, 373, 13

Casagrande, L., Ramírez, I., Meléndez, J., Bessell, M., & Asplund, M. 2010, A&A, 512, A54

Caselli, P., Benson, P. J., Myers, P. C., & Tafalla, M. 2002, ApJ, 572, 238

Castelli, F., Gratton, R. G., & Kurucz, R. L. 1997, A&A, 318, 841

Castelli, F. & Kurucz, R. L. 2004, in IAU Symposium, Vol. 210, Modelling of Stellar Atmospheres, ed. N. E. Piskunov, W. W. Weiss, & D. F. Gray, A20

Caughlan, G. R. & Fowler, W. A. 1988, Atomic Data and Nuclear Data Tables, 40, 283

Cavadore, C. & Dorn, R. J. 2000, in Astrophysics and Space Science Library, Vol. 252, Astrophysics and Space Science Library, ed. P. Amico & J. W. Beletic, 25

Ceccarelli, C., Castets, A., Caux, E., et al. 2000, A&A, 355, 1129

Cernicharo, J. 1991, in NATO ASIC Proc. 342: The Physics of Star Formation and Early Stellar Evolution, ed. C. J. Lada & N. D. Kylafis, 287

Chaboyer, B., Fenton, W. H., Nelan, J. E., Patnaude, D. J., & Simon, F. E. 2001, ApJ, 562, 521

Chaboyer, B., Green, E. M., & Liebert, J. 1999, AJ, 117, 1360

Chabrier, G. & Baraffe, I. 1997, A&A, 327, 1039

Chabrier, G. & Baraffe, I. 2000, ARA&A, 38, 337

Chabrier, G., Baraffe, I., Allard, F., & Hauschildt, P. 2000, ApJ, 542, 464

Chabrier, G., Gallardo, J., & Baraffe, I. 2007, A&A, 472, L17

Chamberlin, T. C. 1901, ApJ, 14, 17

Charbonnel, C., Däppen, W., Schaerer, D., et al. 1999, A&AS, 135, 405

Chen, L., de Grijs, R., & Zhao, J. L. 2007, AJ, 134, 1368

Chen, L., Hou, J. L., & Wang, J. J. 2003, AJ, 125, 1397

Chen, W. P., Chiang, P. S., & Li, J. Z. 2004, CJAA, 4, 153

Chian, B. T. & Zhu, G. L. 1966, Shanghai Observ. Ann., 26, 63

Chini, R., Hoffmeister, V. H., Nasseri, A., Stahl, O., & Zinnecker, H. 2012, MNRAS, 424, 1925

Chini, R. & Kruegel, E. 1983, A&A, 117, 289

Choi, P. I. & Herbst, W. 1996, AJ, 111, 283

Cieza, L. & Baliber, N. 2006, ApJ, 649, 862

Cieza, L. & Baliber, N. 2007, ApJ, 671, 605

Ciolek, G. E. & Mouschovias, T. C. 1995, ApJ, 454, 194

Clark, P. C., Bonnell, I. A., Zinnecker, H., & Bate, M. R. 2005, MNRAS, 359, 809

Clausen, J. V., Bruntt, H., Claret, A., et al. 2009, A&A, 502, 253

Clausen, J. V., Torres, G., Bruntt, H., et al. 2008, A&A, 487, 1095

Clemens, D. P., Yun, J. L., & Heyer, M. H. 1991, ApJS, 75, 877

Clement, R., Garcia, M., Reglero, V., Suso, J., & Fabregat, J. 1997a, A&AS, 125, 529

Clement, R., Reglero, V., Garcia, M., Fabregat, J., & Suso, J. 1997b, A&AS, 124, 499

Cody, A. M. & Hillenbrand, L. A. 2010, ApJS, 191, 389

Cohen, M. & Kuhi, L. V. 1979, ApJS, 41, 743

Cohen, M., Wheaton, W. A., & Megeath, S. T. 2003, AJ, 126, 1090

Cohen, R. E., Herbst, W., & Williams, E. C. 2004, AJ, 127, 1602

Collier Cameron, A. & Campbell, C. G. 1993, A&A, 274, 309

Collier Cameron, A., Campbell, C. G., & Quaintrell, H. 1995, A&A, 298, 133

Collier Cameron, A., Davidson, V. A., Hebb, L., et al. 2009, MNRAS, 400, 451

Collier Cameron, A., Donati, J., & Semel, M. 2002, MNRAS, 330, 699

Conti, P. S. & van den Heuvel, E. P. J. 1970, A&A, 9, 466

Contreras, M. E., Sicilia-Aguilar, A., Muzerolle, J., et al. 2002, AJ, 124, 1585

Costero, R. & Peimbert, M. 1970, Boletin de los Observatorios Tonantzintla y Tacubaya, 5, 229

Cousins, A. W. J. & Caldwell, J. A. R. 2001, MNRAS, 323, 380

Covino, E., Alcalá, J. M., Allain, S., et al. 1997, A&A, 328, 187

Covino, E., Catalano, S., Frasca, A., et al. 2000, A&A, 361, L49

Crampton, D. & Fisher, W. A. 1974, Publications of the Dominion Astrophysical Observatory Victoria, 14, 283

Crawford, D. L., Glaspey, J. W., & Perry, C. L. 1970, AJ, 75, 822

Crutcher, R. M. 1999, ApJ, 520, 706

Cuffey, J. & McCuskey, S. W. 1956, ApJ, 123, 59

Cunha, K., Smith, V. V., & Lambert, D. L. 1998, ApJ, 493, 195

Currie, T., Balog, Z., Kenyon, S. J., et al. 2007, ApJ, 659, 599

Currie, T., Evans, N. R., Spitzbart, B. D., et al. 2009a, AJ, 137, 3210

Currie, T., Hernandez, J., Irwin, J., et al. 2010, ApJS, 186, 191

Currie, T. & Kenyon, S. J. 2009, AJ, 138, 703

Currie, T., Kenyon, S. J., Balog, Z., et al. 2008, ApJ, 672, 558

Currie, T., Lada, C. J., Plavchan, P., et al. 2009b, ApJ, 698, 1

Cutri, R. M., Skrutskie, M. F., van Dyk, S., & et al. 2003, 2MASS Point Source Catalogue. Available at `http://www.ipac.caltech.edu/2mass/`, ed. Cutri, R. M., et al.

Da Rio, N., Gouliermis, D. A., & Gennaro, M. 2010a, ApJ, 723, 166

Da Rio, N., Robberto, M., Soderblom, D. R., et al. 2009, ApJS, 183, 261

Da Rio, N., Robberto, M., Soderblom, D. R., et al. 2010b, ApJ, 722, 1092

Daflon, S., Cunha, K., & Becker, S. R. 1999, ApJ, 522, 950

Dahm, S. E. 2005, AJ, 130, 1805

Dahm, S. E. & Hillenbrand, L. A. 2007, AJ, 133, 2072

Dahm, S. E. & Simon, T. 2005, AJ, 129, 829

D'Alessio, P., Hartmann, L., Calvet, N., et al. 2005, ApJ, 621, 461

Dame, T. M., Elmegreen, B. G., Cohen, R. S., & Thaddeus, P. 1986, ApJ, 305, 892

Damiani, F., Flaccomio, E., Micela, G., et al. 2004, ApJ, 608, 781

Damiani, F., Micela, G., Sciortino, S., et al. 2006a, A&A, 460, 133

Damiani, F., Prisinzano, L., Micela, G., & Sciortino, S. 2006b, A&A, 459, 477

Damjanov, I., Jayawardhana, R., Scholz, A., et al. 2007, ApJ, 670, 1337

D'Antona, F. & Mazzitelli, I. 1994, ApJS, 90, 467

D'Antona, F. & Mazzitelli, I. 1997, Mem. Soc. Astron. Italiana, 68, 807

de Winter, D., Koulis, C., The, P. S., et al. 1997, A&AS, 121, 223

de Zeeuw, P. T., Hoogerwerf, R., de Bruijne, J. H. J., Brown, A. G. A., & Blaauw, A. 1999, AJ, 117, 354

Deacon, N. R., Groot, P. J., Drew, J. E., et al. 2009, MNRAS, 397, 1685

Delfosse, X., Forveille, T., Ségransan, D., et al. 2000, A&A, 364, 217

Demarque, P., Woo, J.-H., Kim, Y.-C., & Yi, S. K. 2004, ApJS, 155, 667

Dobbie, P. D., Lodieu, N., & Sharp, R. G. 2010, MNRAS, 409, 1002

Dobbs, C. L. & Bonnell, I. A. 2007, MNRAS, 376, 1747

Dobbs, C. L., Bonnell, I. A., & Pringle, J. E. 2006, MNRAS, 371, 1663

Doi, M., Tanaka, M., Fukugita, M., et al. 2010, AJ, 139, 1628

Dolan, C. J. & Mathieu, R. D. 1999, AJ, 118, 2409

Dolan, C. J. & Mathieu, R. D. 2001, AJ, 121, 2124

Dolan, C. J. & Mathieu, R. D. 2002, AJ, 123, 387

Donati, J., Skelly, M. B., Bouvier, J., et al. 2010, MNRAS, 402, 1426

Dopita, M. A., Evans, I., & Schwartz, R. D. 1982, ApJL, 263, L73

Doppmann, G. W., Greene, T. P., Covey, K. R., & Lada, C. J. 2005, AJ, 130, 1145

Dormand, J. R. & Woolfson, M. M. 1989, The Origin of the Solar System: The Capture Theory, ed. Dormand, J. R. & Woolfson, M. M.

Dotter, A., Chaboyer, B., Jevremović, D., et al. 2008, ApJS, 178, 89

Draper, J. W. 1874, History of the Conflict Between Religion and Science, ed. Appleton, D., Harvard University

Drew, J. E., Greimel, R., Irwin, M. J., & et al. 2005, MNRAS, 362, 753

Dreyer, J. L. E. 1895, MmRAS, 51, 185

Duerr, R., Imhoff, C. L., & Lada, C. J. 1982, ApJ, 261, 135

Dufton, P. L., Brown, P. J. F., Fitzsimmons, A., & Lennon, D. J. 1990, A&A, 232, 431

Dufton, P. L., Smartt, S. J., Lee, J. K., et al. 2006, A&A, 457, 265

Dumont, S., Heidmann, N., Kuhi, L. V., & Thomas, R. N. 1973, A&A, 29, 199

Duncan, D. K. 1981, ApJ, 248, 651

Duncan, J. C. 1920, ApJ, 51, 4

Dutrey, A., Guilloteau, S., Duvert, G., et al. 1996, A&A, 309, 493

Dutrey, A., Guilloteau, S., Piétu, V., et al. 2008, A&A, 490, L15

Duvert, G., Cernicharo, J., Bachiller, R., & Gomez-Gonzalez, J. 1990, A&A, 233, 190

Eaton, N. L., Herbst, W., & Hillenbrand, L. A. 1995, AJ, 110, 1735

Ebert, R. 1955, ZAp, 37, 217

Eddington, A. S. 1917, MNRAS, 77, 596

Eddington, A. S. 1926, The Internal Constitution of the Stars

Edwards, S. 1995, in Revista Mexicana de Astronomia y Astrofisica Conference Series, Vol. 1, Circumstellar Disks, Outflows, and Star Formation, ed. S. Lizano & J. M. Torrelles, 309

Edwards, S. 1997, in IAU Symposium, Vol. 182, Herbig-Haro Flows and the Birth of Stars, ed. B. Reipurth & C. Bertout, 433

Edwards, S., Cabrit, S., Strom, S. E., et al. 1987, ApJ, 321, 473

Edwards, S., Strom, S. E., Hartigan, P., et al. 1993, AJ, 106, 372

Egan, M. P., Shipman, R. F., Price, S. D., et al. 1998, ApJL, 494, L199

Eiroa, C., Oudmaijer, R. D., Davies, J. K., et al. 2002, A&A, 384, 1038

Ekström, S., Georgy, C., Eggenberger, P., et al. 2012, A&A, 537, A146

Elias, J. H. 1978, ApJ, 223, 859

Elmegreen, B. G. 1993, ApJL, 419, L29

Elmegreen, B. G. 2000, ApJ, 530, 277

Elmegreen, B. G. 2007, ApJ, 668, 1064

Enoch, M. L., Evans, II, N. J., Sargent, A. I., & Glenn, J. 2009, ApJ, 692, 973

Enoch, M. L., Young, K. E., Glenn, J., et al. 2006, ApJ, 638, 293

Evans, II, N. J., Dunham, M. M., Jørgensen, J. K., et al. 2009, ApJS, 181, 321

Feigelson, E. D. 1996, ApJ, 468, 306

Feigelson, E. D. & Decampli, W. M. 1981, ApJL, 243, L89

Feigelson, E. D., Gaffney, III, J. A., Garmire, G., Hillenbrand, L. A., & Townsley, L. 2003, ApJ, 584, 911

Feigelson, E. D. & Montmerle, T. 1999, ARA&A, 37, 363

Ferguson, J. W., Alexander, D. R., Allard, F., et al. 2005, ApJ, 623, 585

Ferreira, J., Pelletier, G., & Appl, S. 2000, MNRAS, 312, 387

Ferrière, K. M. 2001, Reviews of Modern Physics, 73, 1031

Fleck, R. C. & Hunter, J. H. 1976, MNRAS, 175, 335

Fleck, Jr., R. C. 1981, ApJL, 246, L151

Flynn, F. H. 1965, MNRAS, 130, 9

Folha, D. F. M. & Emerson, J. P. 1999, A&A, 352, 517

Forbrich, J., Preibisch, T., Menten, K. M., et al. 2007, A&A, 464, 1003

Forestini, M. 1994, A&A, 285, 473

Fortier, A., Benvenuto, O. G., & Brunini, A. 2007, A&A, 473, 311

Fowler, W. A., Caughlan, G. R., & Zimmerman, B. A. 1975, ARA&A, 13, 69

Franciosini, E., Pallavicini, R., & Sanz-Forcada, J. 2006, A&A, 446, 501

Franco, J. & Cox, D. P. 1983, ApJ, 273, 243

Freedman, R. S., Marley, M. S., & Lodders, K. 2008, ApJS, 174, 504

Freytag, B., Allard, F., Ludwig, H.-G., Homeier, D., & Steffen, M. 2010, A&A, 513, A19

Fukugita, M., Ichikawa, T., Gunn, J. E., et al. 1996, AJ, 111, 1748

Gagné, M., Caillault, J.-P., & Stauffer, J. R. 1995, ApJ, 445, 280

Gahm, G. F. 1990, in IAU Symposium, Vol. 137, Flare Stars in Star Clusters, Associations and the Solar Vicinity, ed. L. V. Mirzoian, B. R. Pettersen, & M. K. Tsvetkov, 193

Galli, D. & Shu, F. H. 1993a, ApJ, 417, 220

Galli, D. & Shu, F. H. 1993b, ApJ, 417, 243

Gamow, G. 1939, Nature, 144, 575

Garmany, C. D. & Stencel, R. E. 1992, A&AS, 94, 211

Garrison, R. F. 1967, PASP, 79, 433

Gauvin, L. S. & Strom, K. M. 1992, ApJ, 385, 217

Genzel, R. & Stutzki, J. 1989, ARA&A, 27, 41

Georgelin, Y. M. & Georgelin, Y. P. 1976, A&A, 49, 57

Getman, K. V., Feigelson, E. D., Grosso, N., et al. 2005, ApJS, 160, 353

Getman, K. V., Feigelson, E. D., Townsley, L., et al. 2006, ApJS, 163, 306

Ghosh, P. & Lamb, F. K. 1978, ApJL, 223, L83

Ghosh, P. & Lamb, F. K. 1979, ApJ, 232, 259

Giampapa, M. S., Basri, G. S., Johns, C. M., & Imhoff, C. 1993, ApJS, 89, 321

Gieles, M., Moeckel, N., & Clarke, C. J. 2012, MNRAS, L501

Girardi, L., Bertelli, G., Bressan, A., et al. 2002, A&A, 391, 195

Gomez, M., Jones, B. F., Hartmann, L., et al. 1992, AJ, 104, 762

González-Solares, E. A., Walton, N. A., Greimel, R., et al. 2008, MNRAS, 388, 89

Goodman, A. A., Benson, P. J., Fuller, G. A., & Myers, P. C. 1993, ApJ, 406, 528

Goodson, A. P., Winglee, R. M., & Böhm, K. 1997, ApJ, 489, 199

Gorlova, N., Balog, Z., Rieke, G. H., et al. 2007, ApJ, 670, 516

Gorti, U. & Hollenbach, D. 2009, ApJ, 690, 1539

Gould, A. & Kollmeier, J. A. 2004, ApJS, 152, 103

Grankin, K. N., Melnikov, S. Y., Bouvier, J., Herbst, W., & Shevchenko, V. S. 2007, A&A, 461, 183

Greenstein, J. L. & Wallerstein, G. 1958, ApJ, 127, 237

Gregorio-Hetem, J. & Hetem, A. 2002, MNRAS, 336, 197

Gregory, S. G., Donati, J.-F., Morin, J., et al. 2012, ApJ, 755, 97

Gregory, S. G., Matt, S. P., Donati, J., & Jardine, M. 2008, MNRAS, 389, 1839

Grevesse, N. & Anders, E. 1989, in American Institute of Physics Conference Series, Vol. 183, Cosmic Abundances of Matter, ed. C. J. Waddington, 1

Grevesse, N. & Sauval, A. J. 1998, Space Sci. Rev., 85, 161

Groot, P. J., Verbeek, K., Greimel, R., & et al. 2009, MNRAS, 399, 323

Grubissich, C. 1959, ZAp, 47, 24

Guarcello, M. G., Micela, G., Damiani, F., et al. 2009, A&A, 496, 453

Guarcello, M. G., Prisinzano, L., Micela, G., et al. 2007, A&A, 462, 245

Guenther, D. B., Demarque, P., Kim, Y.-C., & Pinsonneault, M. H. 1992, ApJ, 387, 372

Guenther, E. & Ball, M. 1998, in Astronomical Society of the Pacific Conference Series, Vol. 154, Cool Stars, Stellar Systems, and the Sun, ed. R. A. Donahue & J. A. Bookbinder, 1701

Guenther, E. W. & Ball, M. 1999, A&A, 347, 508

Guetter, H. H. 1979, AJ, 84, 1846

Gullbring, E., Calvet, N., Muzerolle, J., & Hartmann, L. 2000, ApJ, 544, 927

Gullbring, E., Hartmann, L., Briceño, C., & Calvet, N. 1998a, ApJ, 492, 323

Gullbring, E., Hartmann, L., Briceño, C., Calvet, N., & Muzerolle, J. 1998b, in Astronomical Society of the Pacific Conference Series, Vol. 154, Cool Stars, Stellar Systems, and the Sun, ed. R. A. Donahue & J. A. Bookbinder, 1709

Gum, C. S. 1955, MmRAS, 67, 155

Gutermuth, R. A., Myers, P. C., Megeath, S. T., et al. 2008, ApJ, 674, 336

Haisch, Jr., K. E., Lada, E. A., & Lada, C. J. 2001a, AJ, 121, 2065

Haisch, Jr., K. E., Lada, E. A., & Lada, C. J. 2001b, ApJL, 553, L153

Hardie, R. H., Heiser, A. M., & Tolbert, C. R. 1964, ApJ, 140, 1472

Haro, G. 1953, ApJ, 117, 73

Haro, G., Iriarte, B., & Chavira, E. 1953, Boletin de los Observatorios Tonantzintla y Tacubaya, 1, 3

Harris, D. L., Morgan, W. W., & Roman, N. G. 1954, ApJ, 119, 622

Harris, G. L. H. 1976, ApJS, 30, 451

Hartigan, P., Hartmann, L., Kenyon, S. J., Strom, S. E., & Skrutskie, M. F. 1990, ApJL, 354, L25

Hartigan, P., Kenyon, S. J., Hartmann, L., et al. 1991, ApJ, 382, 617

Hartigan, P., Strom, K. M., & Strom, S. E. 1994, ApJ, 427, 961

Hartman, J. D., Bakos, G. Á., Kovács, G., & Noyes, R. W. 2010, MNRAS, 408, 475

Hartman, J. D., Gaudi, B. S., Pinsonneault, M. H., et al. 2009, ApJ, 691, 342

Hartmann, L. 1998, Accretion Processes in Star Formation, ed. Hartmann, L., Cambridge University Press

Hartmann, L. 2001, AJ, 121, 1030

Hartmann, L. 2003, ApJ, 585, 398

Hartmann, L., Ballesteros-Paredes, J., & Bergin, E. A. 2001, ApJ, 562, 852

Hartmann, L., Ballesteros-Paredes, J., & Heitsch, F. 2012, MNRAS, 420, 1457

Hartmann, L., Cassen, P., & Kenyon, S. J. 1997, ApJ, 475, 770

Hartmann, L., Zhu, Z., & Calvet, N. 2011, arXiv:astro-ph/1106.3343

Harvey, P. M., Huard, T. L., Jørgensen, J. K., et al. 2008, ApJ, 680, 495

Hasan, P., Kilambi, G. C., & Hasan, S. N. 2008, Ap&SS, 313, 363

Hauschildt, P. H., Allard, F., & Baron, E. 1999a, ApJ, 512, 377

Hauschildt, P. H., Allard, F., Ferguson, J., Baron, E., & Alexander, D. R. 1999b, ApJ, 525, 871

Hauschildt, P. H., Baron, E., Starrfield, S., & Allard, F. 1996, ApJ, 462, 386

Hayashi, C. 1961, PASJ, 13, 450

Hayashi, C. 1966, ARA&A, 4, 171

Hayashi, M. 1965, PASJ, 17, 177

Hebb, L., Stempels, H. C., Aigrain, S., et al. 2010, A&A, 522, A37

Heger, A., Langer, N., & Woosley, S. E. 2000, ApJ, 528, 368

Heintze, J. R. W. 1973, in IAU Symposium, Vol. 54, Problems of Calibration of Absolute Magnitudes and Temperature of Stars, ed. B. Hauck & B. E. Westerlund, 231

Heiter, U., Kupka, F., van't Veer-Menneret, C., et al. 2002, A&A, 392, 619

Heitsch, F., Burkert, A., Hartmann, L. W., Slyz, A. D., & Devriendt, J. E. G. 2005, ApJL, 633, L113

Heitsch, F., Slyz, A. D., Devriendt, J. E. G., Hartmann, L. W., & Burkert, A. 2006, ApJ, 648, 1052

Henderson, C. B. & Stassun, K. G. 2012, ApJ, 747, 51

Henize, K. G. 1976, ApJS, 30, 491

Hensberge, H., Pavlovski, K., & Verschueren, W. 2000, A&A, 358, 553

Henyey, L. G., Lelevier, R., & Levée, R. D. 1955, PASP, 67, 154

Herbig, G. H. 1954, PASP, 66, 19

Herbig, G. H. 1957, ApJ, 125, 654

Herbig, G. H. 1960a, ApJ, 131, 516

Herbig, G. H. 1960b, ApJS, 4, 337

Herbig, G. H. 1962, Advances in Astronomy and Astrophysics, 1, 47

Herbig, G. H. 1978, Can Post-T Tauri Stars Be Found?, ed. Mirzoyan, L. V., 171

Herbig, G. H. 1998, ApJ, 497, 736

Herbig, G. H. & Bell, K. R. 1988, Third Catalog of Emission-Line Stars of the Orion Population : 3 : 1988, ed. Herbig, G. H. & Bell, K. R.

Herbig, G. H. & Dahm, S. E. 2001, PASP, 113, 195

Herbig, G. H. & Dahm, S. E. 2002, AJ, 123, 304

Herbig, G. H., Vrba, F. J., & Rydgren, A. E. 1986, AJ, 91, 575

Herbst, W. 2001, in IAU Colloq. 183, Vol. 246, Small Telescope Astronomy on Global Scales, ed. B. Paczynski, W.-P. Chen, & C. Lemme, 177

Herbst, W., Bailer-Jones, C. A. L., Mundt, R., Meisenheimer, K., & Wackermann, R. 2002a, A&A, 396, 513

Herbst, W., Eislöffel, J., Mundt, R., & Scholz, A. 2007, Protostars and Planets V, 297

Herbst, W., Hamilton, C. M., Vrba, F. J., et al. 2002b, PASP, 114, 1167

Herbst, W., Herbst, D. K., Grossman, E. J., & Weinstein, D. 1994, AJ, 108, 1906

Herbst, W. & Mundt, R. 2005, ApJ, 633, 967

Herczeg, G. J. & Hillenbrand, L. A. 2008, ApJ, 681, 594

Hernández, J., Calvet, N., Hartmann, L., et al. 2005, AJ, 129, 856

Hernández, J., Calvet, N., Hartmann, L., et al. 2009, ApJ, 707, 705

Hernández, J., Hartmann, L., Megeath, T., et al. 2007, ApJ, 662, 1067

Hernández, J., Morales-Calderon, M., Calvet, N., et al. 2010, ApJ, 722, 1226

Herrero, A., Kudritzki, R. P., Vilchez, J. M., et al. 1992, A&A, 261, 209

Hertzsprung, E. 1911, Publikationen des Astrophysikalischen Observatoriums zu Potsdam, 63

Hester, J. J., Scowen, P. A., Sankrit, R., et al. 1996, AJ, 111, 2349

Hillenbrand, L. A. 1997, AJ, 113, 1733

Hillenbrand, L. A. 2005, in STSci Symposium Series, Vol. 19, A Decade of Discovery: Planets Around Other Stars, ed. M. Livio

Hillenbrand, L. A. 2009, in IAU Symposium, Vol. 258, The Ages of Stars, ed. E. E. Mamajek, D. R. Soderblom, & R. F. G. Wyse, 81

Hillenbrand, L. A., Massey, P., Strom, S. E., & Merrill, K. M. 1993, AJ, 106, 1906

Hillenbrand, L. A., Strom, S. E., Calvet, N., et al. 1998, AJ, 116, 1816

Hillenbrand, L. A., Strom, S. E., Vrba, F. J., & Keene, J. 1992, ApJ, 397, 613

Hillenbrand, L. A. & White, R. J. 2004, ApJ, 604, 741

Hiltner, W. A. & Johnson, H. L. 1956, ApJ, 124, 367

Hiltner, W. A. & Morgan, W. W. 1969, AJ, 74, 1152

Hirota, T., Bushimata, T., Choi, Y. K., et al. 2007, PASJ, 59, 897

Hoag, A. A., Johnson, H. L., Iriarte, B., et al. 1961, Publications of the U.S. Naval Observatory Second Series, 17, 1

Hohle, M. M., Neuhäuser, R., & Schutz, B. F. 2010, Astronomische Nachrichten, 331, 349

Hollenbach, D. & Adams, F. C. 2004, in Astronomical Society of the Pacific Conference Series, Vol. 323, Star Formation in the Interstellar Medium: In Honor of David Hollenbach, ed. D. Johnstone, F. C. Adams, D. N. C. Lin, D. A. Neufeeld, & E. C. Ostriker , 3

Homeier, D., Hauschildt, P. H., & Allard, F. 2003, in Astronomical Society of the Pacific Conference Series, Vol. 288, Stellar Atmosphere Modeling, ed. I. Hubeny, D. Mihalas, & K. Werner, 357

Hopmann, J. 1924, Veröff. Astron. Inst. Bonn, 19, 1

Hoyle, F. & Schwarzschild, M. 1955, ApJS, 2, 1

Huang, W., Gies, D. R., & McSwain, M. V. 2010, ApJ, 722, 605

Hubble, E. P. 1922, ApJ, 56, 162

Hubeny, I. & Lanz, T. 1995, ApJ, 439, 875

Hubeny, I., Mihalas, D., & Werner, K., eds. 2003, Astronomical Society of the Pacific Conference Series, Vol. 288, Stellar Atmosphere Modeling

Humphreys, R. M. 1978, ApJS, 38, 309

Hunter, C. 1962, ApJ, 136, 594

Hunter, Jr., J. H., Sandford, II, M. T., Whitaker, R. W., & Klein, R. I. 1986, ApJ, 305, 309

Iglesias, C. A. & Rogers, F. J. 1996, ApJ, 464, 943

Iglesias, C. A., Rogers, F. J., & Wilson, B. G. 1992, RMxAA, 23, 9

Irwin, J., Aigrain, S., Hodgkin, S., et al. 2007, MNRAS, 380, 541

Irwin, J. & Bouvier, J. 2009, in IAU Symposium, Vol. 258, The Ages of Stars, ed. E. E. Mamajek, D. R. Soderblom, & R. F. G. Wyse, 363

Isella, A. & Natta, A. 2005, A&A, 438, 899

Ivezić, Ž., Smith, J. A., Miknaitis, G., & et al. 2007, AJ, 134, 973

James, D. J., Melo, C., Santos, N. C., & Bouvier, J. 2006, A&A, 446, 971

Janes, K. & Adler, D. 1982, ApJS, 49, 425

Jaschek, C. & Gomez, A. E. 1998, A&A, 330, 619

Jayawardhana, R., Coffey, J., Scholz, A., Brandeker, A., & van Kerkwijk, M. H. 2006, ApJ, 648, 1206

Jeans, J. H. 1902, Royal Society of London Philosophical Transactions Series A, 199, 1

Jeans, J. H. 1917, MNRAS, 77, 186

Jeans, J. H. 1919, Problems of Cosmogony and Stellar Dynamics, ed. Jeans, J. H., Cambridge University Press

Jeffries, R. D. 2004, in Chemical Abundances and Mixing in Stars in the Milky Way and its Satellites, ed. S. Randich & L. Pasquini, ESO Astrophysics Symposium

Jeffries, R. D. 2007, MNRAS, 376, 1109

Jeffries, R. D., James, D. J., & Thurston, M. R. 1998, MNRAS, 300, 550

Jeffries, R. D., Maxted, P. F. L., Oliveira, J. M., & Naylor, T. 2006, MNRAS, 371, L6

Jeffries, R. D., Naylor, T., Devey, C. R., & Totten, E. J. 2004, MNRAS, 351, 1401

Jeffries, R. D., Naylor, T., Walter, F. M., Pozzo, M. P., & Devey, C. R. 2009, MNRAS, 393, 538

Jeffries, R. D. & Oliveira, J. M. 2005, MNRAS, 358, 13

Jeffries, R. D., Oliveira, J. M., Naylor, T., Mayne, N. J., & Littlefair, S. P. 2007, MNRAS, 376, 580

Jeffries, R. D., Thurston, M. R., & Hambly, N. C. 2001, A&A, 375, 863

Jensen, E. L. N. 2001, in Astronomical Society of the Pacific Conference Series, Vol. 244, Young Stars Near Earth: Progress and Prospects, ed. R. Jayawardhana & T. Greene, 3

Johns, C. M. & Basri, G. 1995a, AJ, 109, 2800

Johns, C. M. & Basri, G. 1995b, ApJ, 449, 341

Johns-Krull, C. M., Valenti, J. A., & Koresko, C. 1999, ApJ, 516, 900

Johns-Krull, C. M., Valenti, J. A., & Linsky, J. L. 2000, ApJ, 539, 815

Johnson, H. L. 1957a, ApJ, 126, 121

Johnson, H. L. 1957b, ApJ, 126, 134

Johnson, H. L. 1958, Lowell Observatory Bulletin, 4, 37

Johnson, H. L. 1962, ApJ, 136, 1135

Johnson, H. L. 1965, Communications of the Lunar and Planetary Laboratory, 53, 73

Johnson, H. L. 1966, ARA&A, 4, 193

Johnson, H. L. & Morgan, W. W. 1953, ApJ, 117, 313

Johnson, H. L. & Morgan, W. W. 1955, ApJ, 122, 429

Jones, B. F. & Herbig, G. H. 1979, AJ, 84, 1872

Jordi, C., Trullols, E., & Galadi-Enriquez, D. 1996, A&A, 312, 499

Jordi, K., Grebel, E. K., & Ammon, K. 2006, A&A, 460, 339

Jørgensen, J. K., Bourke, T. L., Myers, P. C., et al. 2005a, ApJ, 632, 973

Jørgensen, J. K., Schöier, F. L., & van Dishoeck, E. F. 2005b, A&A, 437, 501

Joy, A. H. 1945, ApJ, 102, 168

Joy, A. H. 1949, ApJ, 110, 424

Kawaler, S. D. 1988, ApJ, 333, 236

Kenyon, M. J., Jeffries, R. D., Naylor, T., Oliveira, J. M., & Maxted, P. F. L. 2005, MNRAS, 356, 89

Kenyon, S. J. & Gómez, M. 2001, AJ, 121, 2673

Kenyon, S. J. & Hartmann, L. 1987, ApJ, 323, 714

Kenyon, S. J. & Hartmann, L. 1995, ApJS, 101, 117

Kenyon, S. J., Hartmann, L., Hewett, R., et al. 1994, AJ, 107, 2153

Keppens, R., MacGregor, K. B., & Charbonneau, P. 1995, A&A, 294, 469

Kharchenko, N. V., Piskunov, A. E., Röser, S., Schilbach, E., & Scholz, R.-D. 2005, A&A, 438, 1163

Kholopov, P. N. 1959, Soviet Ast., 3, 425

Kilambi, G. C. 1977, MNRAS, 178, 423

King, D. L. 1985, RGO/La Palma Technical Note 31, 1

Kirk, H., Johnstone, D., & Di Francesco, J. 2006, ApJ, 646, 1009

Kitamura, Y., Momose, M., Yokogawa, S., et al. 2002, ApJ, 581, 357

Königl, A. 1991, ApJL, 370, L39

Königl, A. & Pudritz, R. E. 2000, Protostars and Planets IV, 759

Kraus, A. L., Tucker, R. A., Thompson, M. I., Craine, E. R., & Hillenbrand, L. A. 2011, ApJ, 728, 48

Kraus, S., Balega, Y. Y., Berger, J.-P., et al. 2007, A&A, 466, 649

Kuker, M. & Rudiger, G. 1997, A&A, 328, 253

Kurosawa, R., Harries, T. J., & Symington, N. H. 2006, MNRAS, 370, 580

Kurucz, R. L. 1979, ApJS, 40, 1

Kurucz, R. L. 1991, in NATO ASIC Proc. 341: Stellar Atmospheres - Beyond Classical Models, 441

Kurucz, R. L. 1992, in IAU Symposium, Vol. 149, The Stellar Populations of Galaxies, ed. B. Barbuy & A. Renzini, 225

Lacy, C. H. S., Torres, G., Claret, A., & Vaz, L. P. R. 2005, AJ, 130, 2838

Lacy, C. H. S., Torres, G., Latham, D. W., Zakirov, M. M., & Arzumanyants, G. C. 1997, AJ, 114, 1206

Lada, C. J. 1987, in IAU Symposium, Vol. 115, Star Forming Regions, ed. M. Peimbert & J. Jugaku, 1

Lada, C. J. 1991, in NATO ASIC Proc. 342: The Physics of Star Formation and Early Stellar Evolution, ed. C. J. Lada & N. D. Kylafis, 329

Lada, C. J. & Adams, F. C. 1992, ApJ, 393, 278

Lada, C. J. & Lada, E. A. 2003, ARA&A, 41, 57

Lada, C. J., Muench, A. A., Lada, E. A., & Alves, J. F. 2004, AJ, 128, 1254

Lada, C. J., Muench, A. A., Luhman, K. L., et al. 2006, AJ, 131, 1574

Lada, C. J. & Wilking, B. A. 1984, ApJ, 287, 610

Lamm, M. H., Bailer-Jones, C. A. L., Mundt, R., Herbst, W., & Scholz, A. 2004, A&A, 417, 557

Lamm, M. H., Mundt, R., Bailer-Jones, C. A. L., & Herbst, W. 2005, A&A, 430, 1005

Landolt, A. U. 1992, AJ, 104, 340

Langer, W. D., van Dishoeck, E. F., Bergin, E. A., et al. 2000, Protostars and Planets IV, 29

Lanz, T. & Hubeny, I. 2003, ApJS, 146, 417

Lanz, T. & Hubeny, I. 2007, ApJS, 169, 83

Larson, R. B. 1969, MNRAS, 145, 271

Larson, R. B. 1973, ARA&A, 11, 219

Larson, R. B. 1981, MNRAS, 194, 809

Larson, R. B. 1986, MNRAS, 218, 409

Lee, Y., Stark, A. A., Kim, H., & Moon, D. 2001, ApJS, 136, 137

Leggett, S. K. 1992, ApJS, 82, 351

Leggett, S. K., Allard, F., Berriman, G., Dahn, C. C., & Hauschildt, P. H. 1996, ApJS, 104, 117

Lejeune, T. & Schaerer, D. 2001, A&A, 366, 538

Lindholm, E. H. 1957, ApJ, 126, 588

Linsky, J. L., Gagné, M., Mytyk, A., McCaughrean, M., & Andersen, M. 2007, ApJ, 654, 347

Littlefair, S. P., Naylor, T., Burningham, B., & Jeffries, R. D. 2005, MNRAS, 358, 341

Littlefair, S. P., Naylor, T., Harries, T. J., Retter, A., & O'Toole, S. 2004, MNRAS, 347, 937

Littlefair, S. P., Naylor, T., Mayne, N. J., Saunders, E. S., & Jeffries, R. D. 2010, MNRAS, 403, 545

Lodieu, N., Deacon, N. R., & Hambly, N. C. 2012, MNRAS, 422, 1495

Lodieu, N., Dobbie, P. D., & Hambly, N. C. 2011, A&A, 527, A24

Lodieu, N., Zapatero Osorio, M. R., Rebolo, R., Martín, E. L., & Hambly, N. C. 2009, A&A, 505, 1115

Lohmann, W. 1957, ZAp, 42, 114

Looney, L. W., Tobin, J. J., & Kwon, W. 2007, ApJL, 670, L131

Looney, L. W., Wang, S., Hamidouche, M., Safier, P. N., & Klein, R. 2006, ApJ, 642, 330

López-Morales, M. & Ribas, I. 2005, ApJ, 631, 1120

Lucy, L. B. 2006, A&A, 457, 629

Ludwig, H.-G., Allard, F., & Hauschildt, P. H. 2006, A&A, 459, 599

Ludwig, H.-G., Caffau, E., & Kučinskas, A. 2008, in IAU Symposium, Vol. 252, The Art of Modelling Stars in the 21st Century, ed. L. Deng & K. L. Chan, 75

Ludwig, H.-G., Freytag, B., & Steffen, M. 1999, A&A, 346, 111

Luhman, K. L. 1999, ApJ, 525, 466

Luhman, K. L., Allen, P. R., Espaillat, C., Hartmann, L., & Calvet, N. 2010, ApJS, 186, 111

Luhman, K. L., Lada, E. A., Muench, A. A., & Elston, R. J. 2005a, ApJ, 618, 810

Luhman, K. L., Mamajek, E. E., Allen, P. R., & Cruz, K. L. 2009, ApJ, 703, 399

Luhman, K. L., McLeod, K. K., & Goldenson, N. 2005b, ApJ, 623, 1141

Luhman, K. L., Stauffer, J. R., Muench, A. A., et al. 2003, ApJ, 593, 1093

Lutz, T. E. & Kelker, D. H. 1973, PASP, 85, 573

Lynden-Bell, D. & Pringle, J. E. 1974, MNRAS, 168, 603

Lynds, B. T. 1962, ApJS, 7, 1

Lyo, A., Lawson, W. A., Mamajek, E. E., et al. 2003, MNRAS, 338, 616

Lyra, W., Moitinho, A., van der Bliek, N. S., & Alves, J. 2006, A&A, 453, 101

Lyttleton, R. A. 1961, MNRAS, 122, 399

Mac Low, M. & Klessen, R. S. 2004, Reviews of Modern Physics, 76, 125

Magakian, T. Y., Movsessian, T. A., & Nikogossian, E. H. 2004, Astrophysics, 47, 162

Magni, G. & Mazzitelli, I. 1979, A&A, 72, 134

Makidon, R. B., Rebull, L. M., Strom, S. E., Adams, M. T., & Patten, B. M. 2004, AJ, 127, 2228

Mamajek, E. E., Meyer, M. R., Hinz, P. M., et al. 2004, ApJ, 612, 496

Mamajek, E. E., Meyer, M. R., & Liebert, J. 2002, AJ, 124, 1670

Manova, G. A. 1959, Soviet Ast., 3, 188

Markarian, B. E. 1952, Dokl. Akad. Nauk SSR, 15, 11

Martín, E. L., Brandner, W., Bouvier, J., et al. 2000, ApJ, 543, 299

Martín, E. L., Rebolo, R., & Magazzù, A. 1994, ApJ, 436, 262

Mason, B. D., Gies, D. R., Hartkopf, W. I., et al. 1998, AJ, 115, 821

Masunaga, H. & Inutsuka, S. 2000, ApJ, 531, 350

Mathieu, R. D. 1986, Highlights of Astronomy, 7, 481

Mathieu, R. D. 2004, in IAU Symposium, Vol. 215, Stellar Rotation, ed. A. Maeder & P. Eenens, 113

Matt, S. & Pudritz, R. E. 2005a, ApJL, 632, L135

Matt, S. & Pudritz, R. E. 2005b, MNRAS, 356, 167

Matt, S. & Pudritz, R. E. 2007, in IAU Symposium, Vol. 243, Star-Disk Interaction in Young Stars, ed. J. Bouvier & I. Appenzeller, 299

Matt, S. P., Pinzón, G., de la Reza, R., & Greene, T. P. 2010, ApJ, 714, 989

Maxted, P. F. L., Jeffries, R. D., Oliveira, J. M., Naylor, T., & Jackson, R. J. 2008, MNRAS, 385, 2210

Mayne, N. J. & Harries, T. J. 2010, MNRAS, 409, 1307

Mayne, N. J., Harries, T. J., Rowe, J., & Acreman, D. M. 2012, MNRAS, 423, 1775

Mayne, N. J. & Naylor, T. 2008, MNRAS, 386, 261

Mayne, N. J., Naylor, T., Littlefair, S. P., Saunders, E. S., & Jeffries, R. D. 2007, MNRAS, 375, 1220

McCaughrean, M. J. & O'Dell, C. R. 1996, AJ, 111, 1977

McCray, R. & Snow, Jr., T. P. 1979, ARA&A, 17, 213

McCrea, W. H. 1960, Royal Society of London Proceedings Series A, 256, 245

McKee, C. F. 1989, ApJ, 345, 782

McKee, C. F. 1995, in Astronomical Society of the Pacific Conference Series, Vol. 80, The Physics of the Interstellar Medium and Intergalactic Medium, ed. A. Ferrara, C. F. McKee, C. Heiles, & P. R. Shapiro, 292

McKee, C. F. & Ostriker, E. C. 2007, ARA&A, 45, 565

McKee, C. F., Zweibel, E. G., Goodman, A. A., & Heiles, C. 1993, in Protostars and Planets III, ed. E. H. Levy & J. I. Lunine, 327

McSwain, M. V. & Gies, D. R. 2005, in Astronomical Society of the Pacific Conference Series, Vol. 337, The Nature and Evolution of Disks Around Hot Stars, ed. R. Ignace & K. G. Gayley, 270

Meibom, S., Barnes, S. A., Latham, D. W., et al. 2011a, ApJL, 733, L9

Meibom, S., Mathieu, R. D., Stassun, K. G., Liebesny, P., & Saar, S. H. 2011b, ApJ, 733, 115

Mendoza V., E. E. 1966, ApJ, 143, 1010

Mendoza V., E. E. 1968, ApJ, 151, 977

Menten, K. M., Reid, M. J., Forbrich, J., & Brunthaler, A. 2007, A&A, 474, 515

Mercer-Smith, J. A., Cameron, A. G. W., & Epstein, R. I. 1984, ApJ, 279, 363

Meyer, M. R. & Beckwith, S. V. W. 2000, in Lecture Notes in Physics, Berlin Springer Verlag, Vol. 548, ISO Survey of a Dusty Universe, ed. D. Lemke, M. Stickel, & K. Wilke, 341

Meyer, M. R., Calvet, N., & Hillenbrand, L. A. 1997, AJ, 114, 288

Mihalas, D. 1978, Stellar atmospheres, ed. Mihalas, D., W. H. Freeman & Co.

Mihalas, D., Dappen, W., & Hummer, D. G. 1988, ApJ, 331, 815

Miller, K. A. & Stone, J. M. 1997, ApJ, 489, 890

Minkowski, R. 1947, PASP, 59, 257

Mitchell, R. I. & Johnson, H. L. 1957, ApJ, 125, 414

Moitinho, A., Alves, J., Huélamo, N., & Lada, C. J. 2001, ApJL, 563, L73

Montalbán, J., D'Antona, F., Kupka, F., & Heiter, U. 2004, A&A, 416, 1081

Montes, D., López-Santiago, J., Martínez-Arnáiz, R. M., et al. 2009, in American Institute of Physics Conference Series, Vol. 1094, American Institute of Physics Conference Series, ed. E. Stempels, 943

Montmerle, T., Feigelson, E. D., Bouvier, J., & André, P. 1993, in Protostars and Planets III, ed. E. H. Levy & J. I. Lunine, 689

Montmerle, T., Koch-Miramond, L., Falgarone, E., & Grindlay, J. E. 1983, ApJ, 269, 182

Morales-Calderón, M., Stauffer, J. R., Stassun, K. G., et al. 2012, ApJ, 753, 149

Moreno-Corral, M. A., Chavarria, K. C., de Lara, E., & Wagner, S. 1993, A&A, 273, 619

Morgan, W. W., Whitford, A. E., & Code, A. D. 1953, ApJ, 118, 318

Moscadelli, L., Reid, M. J., Menten, K. M., et al. 2009, ApJ, 693, 406

Moulton, F. R. 1905, ApJ, 22, 165

Mouschovias, T. C. 1976, ApJ, 207, 141

Mullan, D. J. & MacDonald, J. 2001, ApJ, 559, 353

Murdin, P. & Penston, M. V. 1977, MNRAS, 181, 657

Muzerolle, J., Calvet, N., Briceño, C., Hartmann, L., & Hillenbrand, L. 2000, ApJL, 535, L47

Muzerolle, J., Calvet, N., & Hartmann, L. 1998, ApJ, 492, 743

Myers, P. C. & Khersonsky, V. K. 1995, ApJ, 442, 186

Najita, J., Carr, J. S., & Mathieu, R. D. 2003, ApJ, 589, 931

Najita, J. R., Carr, J. S., Glassgold, A. E., & Valenti, J. A. 2007, Protostars and Planets V, 507

Nakamura, F. & Li, Z. 2005, ApJ, 631, 411

Nakano, T. 1998, ApJ, 494, 587

Natta, A., Prusti, T., Neri, R., et al. 2001, A&A, 371, 186

Naylor, T. 1998, MNRAS, 296, 339

Naylor, T. 2009, MNRAS, 399, 432

Naylor, T. & Fabian, A. C. 1999, MNRAS, 302, 714

Naylor, T. & Jeffries, R. D. 2006, MNRAS, 373, 1251

Naylor, T. & Mayne, N. J. 2010, Highlights of Astronomy, 15, 763

Naylor, T., Totten, E. J., Jeffries, R. D., et al. 2002, MNRAS, 335, 291

Neuhäuser, R. 1997, Science, 276, 1363

Neuhäuser, R., Sterzik, M. F., Schmitt, J. H. M. M., Wichmann, R., & Krautter, J. 1995, A&A, 297, 391

Nishiyama, S., Nagata, T., Kusakabe, N., et al. 2006, ApJ, 638, 839

Nordhagen, S., Herbst, W., Rhode, K. L., & Williams, E. C. 2006, AJ, 132, 1555

Norman, C. & Silk, J. 1980, ApJ, 238, 158

O'Dell, C. R., Muench, A., Smith, N., & Zapata, L. 2008, Star Formation in the Orion Nebula II: Gas, Dust, Proplyds and Outflows, ed. Reipurth, B., 544

O'Dell, C. R., Wen, Z., & Hu, X. 1993, ApJ, 410, 696

Ogura, K. & Ishida, K. 1981, PASJ, 33, 149

Ogura, K., Sugitani, K., & Pickles, A. 2002, AJ, 123, 2597

Oke, J. B. 1965, ARA&A, 3, 23

Oke, J. B. & Gunn, J. E. 1983, ApJ, 266, 713

Oliveira, J. M., Jeffries, R. D., & van Loon, J. T. 2009, MNRAS, 392, 1034

Oliveira, J. M., Jeffries, R. D., van Loon, J. T., Littlefair, S. P., & Naylor, T. 2005, MNRAS, 358, L21

Oosterhoff, P. T. 1937, Annal. Sterre. Leiden, 17, A1

Orsatti, A. M., Vega, E. I., & Marraco, H. G. 2000, A&AS, 144, 195

Orsatti, A. M., Vega, E. I., & Marraco, H. G. 2006, AJ, 132, 1783

Palla, F. & Stahler, S. W. 1990, ApJL, 360, L47

Palla, F. & Stahler, S. W. 1999, ApJ, 525, 772

Palla, F. & Stahler, S. W. 2002, ApJ, 581, 1194

Park, B.-G. & Sung, H. 2002, AJ, 123, 892

Park, B.-G., Sung, H., Bessell, M. S., & Kang, Y. H. 2000, AJ, 120, 894

Parker, R. J. & Meyer, M. R. 2012, MNRAS, 427, 637

Parsamian, E. S. & Chavira, E. 1982, Bol. Inst. Tonantzintla, 3, 69

Partridge, H. & Schwenke, D. W. 1997, J. Chem. Phys., 106, 4618

Patel, N. A., Goldsmith, P. F., Heyer, M. H., Snell, R. L., & Pratap, P. 1998, ApJ, 507, 241

Pecaut, M. J., Mamajek, E. E., & Bubar, E. J. 2012, ApJ, 746, 154

Penston, M. V., Hunter, J. K., & O'Neill, A. 1975, MNRAS, 171, 219

Pérez, M. R., Joner, M. D., Thé, P. S., & Westerlund, B. E. 1989, PASP, 101, 195

Pérez, M. R., Thé, P. S., & Westerlund, B. E. 1987, PASP, 99, 1050

Perri, F. & Cameron, A. G. W. 1974, Icarus, 22, 416

Perryman, M. A. C., Lindegren, L., Kovalevsky, J., et al. 1997, A&A, 323, L49

Petrov, P. P., Gahm, G. F., Gameiro, J. F., et al. 2001, A&A, 369, 993

Pickles, A. J. 1998, PASP, 110, 863

Pinsonneault, M. H., Deliyannis, C. P., & Demarque, P. 1992, ApJS, 78, 179

Pinsonneault, M. H., Stauffer, J., Soderblom, D. R., King, J. R., & Hanson, R. B. 1998, ApJ, 504, 170

Piskunov, A. E., Belikov, A. N., Kharchenko, N. V., Sagar, R., & Subramaniam, A. 2004, MNRAS, 349, 1449

Plez, B. 1992, A&AS, 94, 527

Pollack, J. B. 1984, ARA&A, 22, 389

Pollack, J. B., Hubickyj, O., Bodenheimer, P., et al. 1996, Icarus, 124, 62

Pols, O. R., Tout, C. A., Eggleton, P. P., & Han, Z. 1995, MNRAS, 274, 964

Popper, D. M. 1994, AJ, 108, 1091

Popper, D. M. 1997, AJ, 113, 1457

Popper, D. M., Lacy, C. H., Frueh, M. L., & Turner, A. E. 1986, AJ, 91, 383

Porras, A., Christopher, M., Allen, L., et al. 2003, AJ, 126, 1916

Pozzo, M. 2001, PhD thesis, Keele University

Pozzo, M., Jeffries, R. D., Naylor, T., et al. 2000, MNRAS, 313, L23

Pozzo, M., Naylor, T., Jeffries, R. D., & Drew, J. E. 2003, MNRAS, 341, 805

Prato, L., Greene, T. P., & Simon, M. 2003, ApJ, 584, 853

Preibisch, T., Brown, A. G. A., Bridges, T., Guenther, E., & Zinnecker, H. 2002, AJ, 124, 404

Preibisch, T. & Feigelson, E. D. 2005, ApJS, 160, 390

Preibisch, T., Guenther, E., Zinnecker, H., et al. 1998, A&A, 333, 619

Preibisch, T., Kim, Y.-C., Favata, F., et al. 2005a, ApJS, 160, 401

Preibisch, T., McCaughrean, M. J., Grosso, N., et al. 2005b, ApJS, 160, 582

Preibisch, T. & Zinnecker, H. 1999, AJ, 117, 2381

Preibisch, T. & Zinnecker, H. 2002, AJ, 123, 1613

Preibisch, T. & Zinnecker, H. 2004, A&A, 422, 1001

Preibisch, T., Zinnecker, H., & Herbig, G. H. 1996, A&A, 310, 456

Preibisch, T., Zinnecker, H., & Schmitt, J. H. M. M. 1993, A&A, 279, L33

Prentice, A. J. R. 1978, Moon and Planets, 19, 341

Pringle, J. E., Allen, R. J., & Lubow, S. H. 2001, MNRAS, 327, 663

Prisinzano, L., Damiani, F., Micela, G., & Pillitteri, I. 2007, A&A, 462, 123

Prisinzano, L., Damiani, F., Micela, G., & Sciortino, S. 2005, A&A, 430, 941

Prisinzano, L., Micela, G., Flaccomio, E., et al. 2008, ApJ, 677, 401

Prosser, C. F., Stauffer, J. R., Hartmann, L., et al. 1994, ApJ, 421, 517

Randich, S., Aharpour, N., Pallavicini, R., Prosser, C. F., & Stauffer, J. R. 1997, A&A, 323, 86

Randich, S., Pallavicini, R., Meola, G., Stauffer, J. R., & Balachandran, S. C. 2001, A&A, 372, 862

Rauw, G., Nazé, Y., Gosset, E., et al. 2002, A&A, 395, 499

Rebolo, R., Martin, E. L., & Magazzu, A. 1992, ApJL, 389, L83

Rebull, L. M. 2001, AJ, 121, 1676

Rebull, L. M., Makidon, R. B., Strom, S. E., et al. 2002, AJ, 123, 1528

Rebull, L. M., Stauffer, J. R., Megeath, S. T., Hora, J. L., & Hartmann, L. 2006a, ApJ, 646, 297

Rebull, L. M., Stauffer, J. R., Ramirez, S. V., et al. 2006b, AJ, 131, 2934

Rebull, L. M., Wolff, S. C., & Strom, S. E. 2004, AJ, 127, 1029

Reggiani, M., Robberto, M., Da Rio, N., et al. 2011, A&A, 534, A83

Reipurth, B. 1999, A General Catalogue of Herbig-Haro Objects. VizieR On-line Data Catalog: V/104

Roccatagliata, V., Bouwman, J., Henning, T., et al. 2011, ApJ, 733, 113

Rodgers, C. T., Canterna, R., Smith, J. A., Pierce, M. J., & Tucker, D. L. 2006, AJ, 132, 989

Roeser, S., Demleitner, M., & Schilbach, E. 2010, AJ, 139, 2440

Rogers, F. J. 1994, in IAU Colloq. 147: The Equation of State in Astrophysics, ed. G. Chabrier & E. Schatzman, 16

Rogers, F. J. & Iglesias, C. A. 1992, ApJS, 79, 507

Rogers, F. J. & Iglesias, C. A. 1993, in Astronomical Society of the Pacific Conference Series, Vol. 42, GONG 1992. Seismic Investigation of the Sun and Stars, ed. T. M. Brown, 155

Rogers, F. J., Swenson, F. J., & Iglesias, C. A. 1996, ApJ, 456, 902

Román-Zúñiga, C. G., Elston, R., Ferreira, B., & Lada, E. A. 2008, ApJ, 672, 861

Romanova, M. M., Ustyugova, G. V., Koldoba, A. V., & Lovelace, R. V. E. 2002, ApJ, 578, 420

Rucinski, S. M. 1985, AJ, 90, 2321

Rucinski, S. M. & Krautter, J. 1983, A&A, 121, 217

Ruprecht, J. 1966, Bull. Astron. Inst. Czechoslovakia, 17, 33

Russell, H. N. 1910, AJ, 26, 147

Russell, H. N. 1913, The Observatory, 36, 324

Rydgren, A. E., Strom, S. E., & Strom, K. M. 1976, ApJS, 30, 307

Rydgren, A. E. & Vrba, F. J. 1983, ApJ, 267, 191

Sacco, G. G., Franciosini, E., Randich, S., & Pallavicini, R. 2008, A&A, 488, 167

Safronov, V. S. 1972, Evolution of the Protoplanetary Cloud and Formation of the Earth and Planets., ed. Safronov, V. S., Israel Program for Scientific Translations

Sagar, R. 1976, Ap&SS, 40, 447

Sagar, R. & Joshi, U. C. 1978, MNRAS, 184, 467

Sagar, R. & Joshi, U. C. 1979, Ap&SS, 66, 3

Sana, H., Gosset, E., & Evans, C. J. 2009, MNRAS, 400, 1479

Sana, H., Gosset, E., Nazé, Y., Rauw, G., & Linder, N. 2008, MNRAS, 386, 447

Sandstrom, K. M., Peek, J. E. G., Bower, G. C., Bolatto, A. D., & Plambeck, R. L. 2007, ApJ, 667, 1161

Sanner, J., Altmann, M., Brunzendorf, J., & Geffert, M. 2000, A&A, 357, 471

Santos, N. C., Melo, C., James, D. J., et al. 2008, A&A, 480, 889

Sanz-Forcada, J., Franciosini, E., & Pallavicini, R. 2004, A&A, 421, 715

Sargent, A. I., van Duinen, R. J., Aalders, J. W. G., Fridlund, C. V. M., & Nordh, H. L. 1981, ApJ, 249, 607

Saumon, D., Chabrier, G., & van Horn, H. M. 1995, ApJS, 99, 713

Saumon, D. & Guillot, T. 2004, ApJ, 609, 1170

Saunders, E. S., Naylor, T., Mayne, N., & Littlefair, S. P. 2009, MNRAS, 397, 405

Savage, B. D. & Mathis, J. S. 1979, ARA&A, 17, 73

Schaller, G., Schaerer, D., Meynet, G., & Maeder, A. 1992, A&AS, 96, 269

Schmidt, O. Y. 1944, Dokl. Akad. Nauk SSR, 6

Schmidt-Kaler, T. 1982, in Landolt-Börnstein, Neue Serie VI/2b, 453, 15

Schneps, M. H., Ho, P. T. P., & Barrett, A. H. 1980, ApJ, 240, 84

Scholz, A. 2009, in American Institute of Physics Conference Series, Vol. 1094, American Institute of Physics Conference Series, ed. E. Stempels, 61

Scholz, A., Coffey, J., Brandeker, A., & Jayawardhana, R. 2007, ApJ, 662, 1254

Schönberg, M. & Chandrasekhar, S. 1942, ApJ, 96, 161

Schwartz, R. D., Wilking, B. A., & Giulbudagian, A. L. 1991, ApJ, 370, 263

Schwenke, D. W. 1998, Faraday Discussions, 109, 321

Ségransan, D., Delfosse, X., Forveille, T., et al. 2000, A&A, 364, 665

Shahbaz, T., Smale, A. P., Naylor, T., et al. 1996, MNRAS, 282, 1437

Sharma, S., Pandey, A. K., Ogura, K., et al. 2006, AJ, 132, 1669

Sharp, C. M. & Burrows, A. 2007, ApJS, 168, 140

Sharpless, S. 1952, ApJ, 116, 251

Sharpless, S. 1954, ApJ, 119, 200

Sharpless, S. 1959, ApJS, 4, 257

Sherry, W. H., Walter, F. M., & Wolk, S. J. 2004, AJ, 128, 2316

Sherry, W. H., Walter, F. M., Wolk, S. J., & Adams, N. R. 2008, AJ, 135, 1616

Shu, F., Najita, J., Ostriker, E., et al. 1994, ApJ, 429, 781

Shu, F. H. 1977, ApJ, 214, 488

Shu, F. H., Adams, F. C., & Lizano, S. 1987, ARA&A, 25, 23

Sicilia-Aguilar, A., Hartmann, L., Calvet, N., et al. 2006a, ApJ, 638, 897

Sicilia-Aguilar, A., Hartmann, L. W., Briceño, C., Muzerolle, J., & Calvet, N. 2004, AJ, 128, 805

Sicilia-Aguilar, A., Hartmann, L. W., Fürész, G., et al. 2006b, AJ, 132, 2135

Sicilia-Aguilar, A., Hartmann, L. W., Hernández, J., Briceño, C., & Calvet, N. 2005, AJ, 130, 188

Sicilia-Aguilar, A., Henning, T., Juhász, A., et al. 2008, ApJ, 687, 1145

Siess, L., Dufour, E., & Forestini, M. 2000, A&A, 358, 593

Siess, L., Forestini, M., & Bertout, C. 1999, A&A, 342, 480

Siess, L., Forestini, M., & Dougados, C. 1997, A&A, 324, 556

Sills, A., Pinsonneault, M. H., & Terndrup, D. M. 2000, ApJ, 534, 335

Simon, M., Dutrey, A., & Guilloteau, S. 2000, ApJ, 545, 1034

Simon, M., Ghez, A. M., & Leinert, C. 1993, ApJL, 408, L33

Simon, T., Vrba, F. J., & Herbst, W. 1990, AJ, 100, 1957

Simonson, III, S. C. & van Someren Greve, H. W. 1976, A&A, 49, 343

Skumanich, A. 1972, ApJ, 171, 565

Slesnick, C. L., Hillenbrand, L. A., & Massey, P. 2002, ApJ, 576, 880

Smartt, S. J. & Rolleston, W. R. J. 1997, ApJL, 481, L47

Smith, M. D. 1994, A&A, 287, 523

Smith, M. G. 1968, Ap&SS, 1, 68

Smith, R. & Jeffries, R. D. 2012, MNRAS, 420, 2884

Snell, R. L., Loren, R. B., & Plambeck, R. L. 1980, ApJL, 239, L17

Soderblom, D. R. 1996, in Astronomical Society of the Pacific Conference Series, Vol. 109,
    Cool Stars, Stellar Systems, and the Sun, ed. R. Pallavicini & A. K. Dupree, 315

Soderblom, D. R., Nelan, E., Benedict, G. F., et al. 2005, AJ, 129, 1616

Solomon, P. M., Sanders, D. B., & Scoville, N. Z. 1979, in IAU Symposium, Vol. 84, The
    Large-Scale Characteristics of the Galaxy, ed. W. B. Burton, 35

Southworth, J., Zucker, S., Maxted, P. F. L., & Smalley, B. 2004, MNRAS, 355, 986

Stahler, S. W. 1983, ApJ, 274, 822

Stahler, S. W. & Palla, F. 2005, The Formation of Stars, ed. Stahler, S. W. & Palla, F.,
    Wiley-VCH

Stassun, K. G., Ardila, D. R., Barsony, M., Basri, G., & Mathieu, R. D. 2004a, AJ, 127,
    3537

Stassun, K. G., Mathieu, R. D., Mazeh, T., & Vrba, F. J. 1999, AJ, 117, 2941

Stassun, K. G., Mathieu, R. D., & Valenti, J. A. 2007, ApJ, 664, 1154

Stassun, K. G., Mathieu, R. D., Vaz, L. P. R., Stroud, N., & Vrba, F. J. 2004b, ApJS,
    151, 357

Stauffer, J. R., Hartmann, L. W., Fazio, G. G., et al. 2007, ApJS, 172, 663

Stauffer, J. R., Hartmann, L. W., Prosser, C. F., et al. 1997, ApJ, 479, 776

Stauffer, J. R., Jones, B. F., Backman, D., et al. 2003, AJ, 126, 833

Stauffer, J. R., Rebull, L. M., Carpenter, J., et al. 2005, AJ, 130, 1834

Stauffer, J. R., Schild, R., Barrado y Navascues, D., et al. 1998, ApJ, 504, 805

Stead, J. J. & Hoare, M. G. 2009, MNRAS, 400, 731

Steffen, A. T., Mathieu, R. D., Lattanzi, M. G., et al. 2001, AJ, 122, 997

Stempels, H. C., Hebb, L., Stassun, K. G., et al. 2008, A&A, 481, 747

Sterzik, M. F., Alcalá, J. M., Neuhaeuser, R., & Schmitt, J. H. M. M. 1995, A&A, 297, 418

Stolte, A., Brandner, W., Brandl, B., Zinnecker, H., & Grebel, E. K. 2004, AJ, 128, 765

Straižys, V. 1977, Multicolor Stellar Photometry. Photometric Systems and Methods, ed. Gartsev, V. T.

Strassmeier, K. G., Welty, A. D., & Rice, J. B. 1994, A&A, 285, L17

Strom, K. M. & Strom, S. E. 1994, ApJ, 424, 237

Strom, K. M., Strom, S. E., Edwards, S., Cabrit, S., & Skrutskie, M. F. 1989a, AJ, 97, 1451

Strom, K. M., Wilkin, F. P., Strom, S. E., & Seaman, R. L. 1989b, AJ, 98, 1444

Strom, S. E., Strom, K. M., & Edwards, S. 1988, in NATO ASIC Proc. 232: Galactic and Extragalactic Star Formation, ed. R. E. Pudritz & M. Fich, 53

Strom, S. E., Strom, K. M., & Grasdalen, G. L. 1975, ARA&A, 13, 187

Struve, O. 1927, Astronomische Nachrichten, 231, 17

Sukhbold, T. & Howell, S. B. 2009, PASP, 121, 1188

Sung, H. & Bessell, M. S. 1999, MNRAS, 306, 361

Sung, H., Chun, M., & Bessell, M. S. 2000, AJ, 120, 333

Swenson, F. J., Faulkner, J., Rogers, F. J., & Iglesias, C. A. 1994, ApJ, 425, 286

Tan, J. C., Krumholz, M. R., & McKee, C. F. 2006, ApJL, 641, L121

Tassis, K. & Mouschovias, T. C. 2004, ApJ, 616, 283

Terebey, S., Shu, F. H., & Cassen, P. 1984, ApJ, 286, 529

Terndrup, D. M., Stauffer, J. R., Pinsonneault, M. H., et al. 2000, AJ, 119, 1303

Thé, P.-S. 1960, ApJ, 132, 40

Thé, P. S., de Winter, D., Feinstein, A., & Westerlund, B. E. 1990, A&AS, 82, 319

Tian, K. P., van Leeuwen, F., Zhao, J. L., & Su, C. G. 1996, A&AS, 118, 503

Tognelli, E., Prada Moroni, P. G., & Degl'Innocenti, S. 2011, A&A, 533, A109

Torres, G., Sandberg Lacy, C. H., & Claret, A. 2009, AJ, 138, 1622

Torres, G., Stefanik, R. P., Andersen, J., et al. 1997, AJ, 114, 2764

Tout, C. A., Livio, M., & Bonnell, I. A. 1999, MNRAS, 310, 360

Townsley, L. K., Feigelson, E. D., Montmerle, T., et al. 2003, ApJ, 593, 874

Trullols, E. & Jordi, C. 1997, A&A, 324, 549

Trumpler, R. J. 1930, PASP, 42, 214

Turner, D. G. 1976, AJ, 81, 97

Turner, D. G. 1979, PASP, 91, 642

Uribe, A., García-Varela, J.-A., Sabogal-Martínez, B.-E., Higuera G., M. A., & Brieva, E. 2002, PASP, 114, 233

Černis, K. & Straižys, V. 2003, Baltic Astronomy, 12, 301

Valenti, J. A. & Johns-Krull, C. M. 2004, Ap&SS, 292, 619

van Altena, W. F. & Jones, B. F. 1972, A&A, 20, 425

van Altena, W. F., Lee, J. T., & Hoffleit, E. D. 1995, The General Catalogue of Trigonometric Stellar Parallaxes. 4th Ed., Yale University Observatory, ed. van Altena, W. F., Lee, J. T., & Hoffleit, E. D.

van Ballegooijen, A. A. 1994, Space Sci. Rev., 68, 299

van den Ancker, M. E., The, P. S., Feinstein, A., et al. 1997, A&AS, 123, 63

Vázquez-Semadeni, E., Kim, J., Shadmehri, M., & Ballesteros-Paredes, J. 2005, ApJ, 618, 344

Vázquez-Semadeni, E., Passot, T., & Pouquet, A. 1995, in Revista Mexicana de Astronomia y Astrofisica, vol. 27, Vol. 3, The Fifth Mexico-Texas Conference on Astrophysics: Gaseous Nebulae and Star Formation, ed. M. Pena & S. Kurtz, 61

Verbeek, K., de Groot, E., Groot, P. J., et al. 2012, MNRAS, 420, 1115

Vink, J. S., Brott, I., Gräfener, G., et al. 2010, A&A, 512, L7

Vink, J. S., de Koter, A., & Lamers, H. J. G. L. M. 2001, A&A, 369, 574

von Hoerner, S. 1957, ZAp, 42, 273

von Weizsäcker, C. F. 1938, Physikalische Zeitschrift, 39, 633

Vorobyov, E. I. & Basu, S. 2006, ApJ, 650, 956

Voss, R., Diehl, R., Vink, J. S., & Hartmann, D. H. 2010, A&A, 520, A51

Vrba, F. J., Rydgren, A. E., Chugainov, P. F., Shakovskaia, N. I., & Zak, D. S. 1986, ApJ, 306, 199

Walborn, N. R. 1971, ApJS, 23, 257

Walker, M. F. 1957, ApJ, 125, 636

Walker, M. F. 1959, ApJ, 130, 57

Walker, M. F. 1961, ApJ, 133, 438

Walker, M. F. 1969, ApJ, 155, 447

Walker, M. F. 1972, ApJ, 175, 89

Wallerstein, G., Herbig, G. H., & Conti, P. S. 1965, ApJ, 141, 610

Walter, F. M. 1986, ApJ, 306, 573

Walter, F. M., Brown, A., Mathieu, R. D., Myers, P. C., & Vrba, F. J. 1988, AJ, 96, 297

Walter, F. M. & Kuhi, L. V. 1981, ApJ, 250, 254

Walter, F. M., Wolk, S. J., & Sherry, W. 1998, in Astronomical Society of the Pacific Conference Series, Vol. 154, Cool Stars, Stellar Systems, and the Sun, ed. R. A. Donahue & J. A. Bookbinder, 1793

Wang, J., Townsley, L. K., Feigelson, E. D., et al. 2008, ApJ, 675, 464

Wang, Y. 1995, ApJL, 449, L153

Ward-Thompson, D., André, P., Crutcher, R., et al. 2007, Protostars and Planets V, 33

Ward-Thompson, D., Scott, P. F., Hills, R. E., & André, P. 1994, MNRAS, 268, 276

Weidner, C. & Vink, J. S. 2010, A&A, 524, A98

West, A. A., Walkowicz, L. M., & Hawley, S. L. 2005, PASP, 117, 706

Wetherill, G. W. 1989, in The Formation and Evolution of Planetary Systems, ed. H. A. Weaver & L. Danly, 1, Cambridge University Press

White, G. J., Lefloch, B., Fridlund, C. V. M., et al. 1997, A&A, 323, 931

White, R. J. & Basri, G. 2003, ApJ, 582, 1109

White, R. J., Ghez, A. M., Reid, I. N., & Schultz, G. 1999, ApJ, 520, 811

White, R. J., Greene, T. P., Doppmann, G. W., Covey, K. R., & Hillenbrand, L. A. 2007, Protostars and Planets V, 117

Wichmann, R., Krautter, J., Covino, E., et al. 1997, A&A, 320, 185

Wichmann, R., Krautter, J., Schmitt, J. H. M. M., et al. 1996, A&A, 312, 439

Wildey, R. L. 1963, AJ, 68, 190

Wildey, R. L. 1964, ApJS, 8, 439

Wilking, B. A., Harvey, P. M., & Joy, M. 1984, AJ, 89, 496

Wilking, B. A., Lada, C. J., & Young, E. T. 1989, ApJ, 340, 823

Wolf, M. 1904, MNRAS, 64, 838

Wolk, S. J. 1996, PhD thesis, Harvard-Smithsonian Center for Astrophysics

Wood, D. O. S. & Churchwell, E. 1989, ApJ, 340, 265

Woolfson, M. M. 1964, Royal Society of London Proceedings Series A, 282, 485

Woolfson, M. M. 1993, QJRAS, 34, 1

Yee, J. C. & Jensen, E. L. N. 2010, ApJ, 711, 303

Yi, I. 1994, ApJ, 428, 760

Yorke, H. W., Bodenheimer, P., & Laughlin, G. 1993, ApJ, 411, 274

Young, C. H., Jørgensen, J. K., Shirley, Y. L., et al. 2004, ApJS, 154, 396

Zapatero Osorio, M. R., Béjar, V. J. S., Pavlenko, Y., et al. 2002, A&A, 384, 937

Zappala, R. R. 1972, ApJ, 172, 57

Zuckerman, B. & Palmer, P. 1974, ARA&A, 12, 279

Appendix A

Photometric Observations: Exposure Times

Table A.1: The central coordinates for each field-of-view and exposure times in the INT-WFC $(UgriZ)_{\mathrm{WFC}}$ bandpasses for the sample of SFRs.

Field	R.A.	Dec.	Filter	Exposure time
	(J2000.0)			(sec; $\times 1$ unless stated)
Cep OB3b	$22^{\mathrm{h}}\,55^{\mathrm{m}}\,43.3^{\mathrm{s}}$	$+62°\,40'\,13.6''$	U_{WFC}	$1(\times 2)$, $10(\times 3)$, $100(\times 2)$
			g_{WFC}	$1(\times 2)$, $10(\times 3)$, 100, $200(\times 2)$, 500
			r_{WFC}	$1(\times 2)$, $10(\times 2)$, 100, $200(\times 2)$, 500
			i_{WFC}	$1(\times 2)$, $10(\times 2)$, 100, $200(\times 2)$, 500
			Z_{WFC}	$1(\times 2)$, $10(\times 2)$, 100, $200(\times 2)$, 500
χ Per	$02^{\mathrm{h}}\,22^{\mathrm{m}}\,48.7^{\mathrm{s}}$	$+57°\,07'\,30.0''$	U_{WFC}	$1(\times 2)$, $10(\times 2)$, $100(\times 2)$
			g_{WFC}	$1(\times 2)$, $10(\times 2)$, 100, 200, 300, 500
			r_{WFC}	$1(\times 2)$, $10(\times 2)$, 100, 200, 300, 500
			i_{WFC}	$1(\times 2)$, $10(\times 2)$, 100, 200, 300, 500
			Z_{WFC}	$1(\times 2)$, $10(\times 2)$, 100, 200, 300, 500
IC 348	$03^{\mathrm{h}}\,44^{\mathrm{m}}\,30.0^{\mathrm{s}}$	$+32°\,00'\,00.0''$	U_{WFC}	$1(\times 2)$, $10(\times 2)$, 100
			g_{WFC}	$1(\times 2)$, $10(\times 2)$, 100, $500(\times 2)$
			r_{WFC}	$1(\times 2)$, $10(\times 2)$, 100, $500(\times 2)$
			i_{WFC}	$1(\times 2)$, $10(\times 2)$, 100, $500(\times 2)$
			Z_{WFC}	$1(\times 2)$, $10(\times 2)$, 100, $500(\times 2)$
IC 5146	$21^{\mathrm{h}}\,53^{\mathrm{m}}\,24.0^{\mathrm{s}}$	$+47°\,15'\,36.0''$	U_{WFC}	1, 10, $100(\times 2)$
			g_{WFC}	1, 10, 100, $200(\times 3)$, 500
			r_{WFC}	1, 10, 100, $200(\times 3)$, 500
			i_{WFC}	1, 10, 100, $200(\times 3)$, 500
			Z_{WFC}	1, 10, 100, $200(\times 3)$, 500

Table A.1: *continued*

Field	R.A.	Dec.	Filter	Exposure time
	(J2000.0)			(sec; $\times 1$ unless stated)
			U_{WFC}	$1(\times 2)$, $10(\times 2)$, 100
			g_{WFC}	$1(\times 2)$, $10(\times 2)$, 100, $200(\times 2)$, 500
λ Ori A	$05^{\mathrm{h}}\,36^{\mathrm{m}}\,25.0^{\mathrm{s}}$	$+09°\,38'\,25.8''$	r_{WFC}	$1(\times 2)$, $10(\times 2)$, 100, $200(\times 2)$, 500
			i_{WFC}	$1(\times 2)$, $10(\times 2)$, 100, $200(\times 2)$, 500
			Z_{WFC}	$1(\times 2)$, $10(\times 2)$, 100, $200(\times 2)$, 500
			g_{WFC}	$200(\times 2)$, 500
λ Ori B	$05^{\mathrm{h}}\,34^{\mathrm{m}}\,58.5^{\mathrm{s}}$	$+09°\,38'\,25.8''$	r_{WFC}	$200(\times 2)$, 500
			i_{WFC}	$200(\times 2)$, 500
			Z_{WFC}	$200(\times 2)$, 500
			g_{WFC}	$200(\times 3)$, 500
λ Ori C	$05^{\mathrm{h}}\,36^{\mathrm{m}}\,25.0^{\mathrm{s}}$	$+10°\,02'\,25.6''$	r_{WFC}	$200(\times 3)$, 500
			i_{WFC}	$200(\times 3)$, 500
			Z_{WFC}	$200(\times 3)$, 500
			U_{WFC}	1, 10, 100
			g_{WFC}	1, 10, 100, $500(\times 2)$
λ Ori D	$05^{\mathrm{h}}\,34^{\mathrm{m}}\,48.6.0^{\mathrm{s}}$	$+10°\,02'\,25.6''$	r_{WFC}	1, 10, 100, $500(\times 2)$
			i_{WFC}	1, 10, 100, $500(\times 2)$
			Z_{WFC}	1, 10, 100, $500(\times 2)$
			U_{WFC}	$1(\times 2)$, $10(\times 2)$, 100
			g_{WFC}	$1(\times 2)$, $10(\times 2)$, 100, $200(\times 2)$, 500
NGC 1960	$05^{\mathrm{h}}\,36^{\mathrm{m}}\,18.0^{\mathrm{s}}$	$+34°\,08'\,24.1''$	r_{WFC}	$1(\times 2)$, $10(\times 2)$, 100, $200(\times 2)$, 500
			i_{WFC}	$1(\times 2)$, $10(\times 2)$, 100, $200(\times 2)$, 500
			Z_{WFC}	$1(\times 2)$, $10(\times 2)$, 100, $200(\times 2)$, 500
			U_{WFC}	1, 10, 100
			g_{WFC}	1, 10, 100, $500(\times 2)$
NGC 2169	$06^{\mathrm{h}}\,08^{\mathrm{m}}\,24.0^{\mathrm{s}}$	$+13°\,57'\,54.0''$	r_{WFC}	1, 10, 100, $500(\times 2)$
			i_{WFC}	1, 10, 100, $500(\times 2)$
			Z_{WFC}	1, 10, 100, $500(\times 2)$
			U_{WFC}	1, 10, 100
			g_{WFC}	1, 10, 100, $500(\times 2)$
NGC 2244	$06^{\mathrm{h}}\,31^{\mathrm{m}}\,55.5^{\mathrm{s}}$	$+04°\,56'\,34.3''$	r_{WFC}	1, 10, 100, $500(\times 2)$
			i_{WFC}	1, 10, 100, $500(\times 2)$
			Z_{WFC}	1, 10, 100, $500(\times 2)$

Table A.1: *continued*

Field	R.A.	Dec.	Filter	Exposure time
	(J2000.0)			(sec; $\times 1$ unless stated)
NGC 2362	$07^{\rm h}\,18^{\rm m}\,39.6^{\rm s}$	$-24°\,57'\,00.0''$	$U_{\rm WFC}$	1, 10, 100
			$g_{\rm WFC}$	1, 10, 100, 500($\times 2$)
			$r_{\rm WFC}$	1, 10, 100, 500($\times 2$)
			$i_{\rm WFC}$	1, 10, 100, 500($\times 2$)
			$Z_{\rm WFC}$	1, 10, 100, 500($\times 2$)
NGC 6530	$18^{\rm h}\,04^{\rm m}\,05.0^{\rm s}$	$-24°\,22'\,00.0''$	$U_{\rm WFC}$	1, 10
			$g_{\rm WFC}$	1, 10, 500($\times 2$)
			$r_{\rm WFC}$	1, 10, 500
			$i_{\rm WFC}$	1, 10, 500
			$Z_{\rm WFC}$	1, 10, 500
NGC 6611	$18^{\rm h}\,18^{\rm m}\,48.0^{\rm s}$	$-13°\,47'\,00.0''$	$U_{\rm WFC}$	1($\times 2$), 10($\times 2$), 100
			$g_{\rm WFC}$	1($\times 2$), 10($\times 2$), 100, 500($\times 2$)
			$r_{\rm WFC}$	1($\times 2$), 10($\times 2$), 100, 500($\times 2$)
			$i_{\rm WFC}$	1($\times 2$), 10($\times 2$), 100, 500($\times 2$)
			$Z_{\rm WFC}$	1($\times 2$), 10($\times 2$), 100, 500($\times 2$)
NGC 7160	$21^{\rm h}\,53^{\rm m}\,40.0^{\rm s}$	$+62°\,36'\,12.0''$	$U_{\rm WFC}$	1($\times 2$), 10($\times 2$), 100
			$g_{\rm WFC}$	1($\times 2$), 10($\times 2$), 100, 200($\times 2$), 500
			$r_{\rm WFC}$	1($\times 2$), 10($\times 2$), 100, 200($\times 2$), 500
			$i_{\rm WFC}$	1($\times 2$), 10($\times 2$), 100, 200($\times 2$), 500
			$Z_{\rm WFC}$	1($\times 2$), 10($\times 2$), 100, 200($\times 2$), 500
ONC	$05^{\rm h}\,35^{\rm m}\,13.7^{\rm s}$	$-05°\,27'\,03.6''$	$U_{\rm WFC}$	1($\times 2$), 10($\times 2$), 100
			$g_{\rm WFC}$	1($\times 2$), 10($\times 2$), 100, 200, 300, 500
			$r_{\rm WFC}$	1($\times 2$), 10($\times 2$), 100, 200, 300, 500
			$i_{\rm WFC}$	1($\times 2$), 10($\times 2$), 100, 200, 300, 500
			$Z_{\rm WFC}$	1($\times 2$), 10($\times 2$), 100, 200, 300, 500
σ Ori A	$05^{\rm h}\,40^{\rm m}\,14.2^{\rm s}$	$-02°\,20'\,18.0''$	$g_{\rm WFC}$	200, 300, 500
			$r_{\rm WFC}$	200, 300, 500
			$i_{\rm WFC}$	200, 300, 500
			$Z_{\rm WFC}$	200, 300, 500
σ Ori B	$05^{\rm h}\,40^{\rm m}\,13.1^{\rm s}$	$-02°\,51'\,47.7''$	$U_{\rm WFC}$	1, 10, 100
			$g_{\rm WFC}$	1, 10, 100, 200, 300, 500
			$r_{\rm WFC}$	1, 10, 100, 200, 300, 500
			$i_{\rm WFC}$	1, 10, 100, 200, 300, 500
			$Z_{\rm WFC}$	1, 10, 100, 200, 300, 500

Table A.1: *continued*

Field	R.A.	Dec.	Filter	Exposure time
	(J2000.0)			(sec; $\times 1$ unless stated)
			U_{WFC}	1, 10, 100
			g_{WFC}	1, 10, 100, 200, 300, 500
σ Ori C	$05^{\mathrm{h}}\,38^{\mathrm{m}}\,07.7^{\mathrm{s}}$	$-02°\,20'\,18.0''$	r_{WFC}	1, 10, 100, 200, 300, 500
			i_{WFC}	1, 10, 100, 200, 300, 500
			Z_{WFC}	1, 10, 100, 200, 300, 500
			g_{WFC}	500
σ Ori D	$05^{\mathrm{h}}\,38^{\mathrm{m}}\,07.7^{\mathrm{s}}$	$-02°\,51'\,51.0''$	r_{WFC}	500
			i_{WFC}	500
			Z_{WFC}	500

Table A.2: The central coordinates for each field-of-view and exposure times in the INT-WFC $(UgriZ)_{\mathrm{WFC}}$ bandpasses for the Pleiades fields.

Field	R.A.	Dec.	Filter	Exposure time
	(J2000.0)			(sec; $\times 1$ unless stated)
Pleiades A	$03^{\mathrm{h}}\,46^{\mathrm{m}}\,19.2^{\mathrm{s}}$	$+23°\,38'\,02.4''$	U_{WFC}	1, 10
			g_{WFC}	1, 10, 100, 500($\times 2$)
			r_{WFC}	1, 7, 50, 250
			i_{WFC}	1, 10, 100($\times 2$)
			Z_{WFC}	1, 7, 50, 250
Pleiades B	$03^{\mathrm{h}}\,45^{\mathrm{m}}\,00.0^{\mathrm{s}}$	$+23°\,44'\,45.6''$	U_{WFC}	1, 10
			g_{WFC}	1, 10, 100, 500($\times 2$)
			r_{WFC}	1, 7, 50, 250
			i_{WFC}	1, 10, 100($\times 2$)
			Z_{WFC}	1, 7, 50, 250
Pleiades C	$03^{\mathrm{h}}\,43^{\mathrm{m}}\,44.4^{\mathrm{s}}$	$+23°\,58'\,08.4''$	U_{WFC}	1, 10
			g_{WFC}	1, 10, 100, 500($\times 2$)
			r_{WFC}	1, 7, 50, 250
			i_{WFC}	1, 10, 100($\times 2$)
			Z_{WFC}	1, 7, 50, 250
Pleiades D	$03^{\mathrm{h}}\,42^{\mathrm{m}}\,36.0^{\mathrm{s}}$	$+23°\,58'\,08.4''$	U_{WFC}	1, 10
			g_{WFC}	1, 10, 100, 500($\times 2$)
			r_{WFC}	1, 7, 50, 250
			i_{WFC}	1, 10, 100($\times 2$)
			Z_{WFC}	1, 7, 50, 250
Pleiades E	$03^{\mathrm{h}}\,43^{\mathrm{m}}\,44.4^{\mathrm{s}}$	$+24°\,24'\,28.8''$	U_{WFC}	1, 10
			g_{WFC}	1, 10, 100, 500($\times 2$)
			r_{WFC}	1, 7, 50, 250
			i_{WFC}	1, 10, 100($\times 2$)
			Z_{WFC}	1, 7, 50, 250

Table A.3: The central coordinates for each field-of-view and exposure times in the INT-WFC $(UgriZ)_{\mathrm{WFC}}$ bandpasses for the SDSS Stripe 82 standard fields.

Field	R.A.	Dec.	Filter	Exposure time
	(J2000.0)			(sec; $\times 1$ unless stated)
SDSS Stripe 82 A	$20^{\mathrm{h}}\,48^{\mathrm{m}}\,57.2^{\mathrm{s}}$	$-00°\,53'\,47.7''$	U_{WFC}	5, 50
			g_{WFC}	5, 50
			r_{WFC}	5, 50
			i_{WFC}	5, 50
			Z_{WFC}	5, 50
SDSS Stripe 82 B	$23^{\mathrm{h}}\,00^{\mathrm{m}}\,00.0^{\mathrm{s}}$	$+00°\,00'\,00.0''$	U_{WFC}	5, 50
			g_{WFC}	5, 50
			r_{WFC}	5, 50
			i_{WFC}	5, 50
			Z_{WFC}	5, 50
SDSS Stripe 82 C	$01^{\mathrm{h}}\,31^{\mathrm{m}}\,45.0^{\mathrm{s}}$	$-00°\,40'\,00.0''$	U_{WFC}	5, 50
			g_{WFC}	5, 50
			r_{WFC}	5, 50
			i_{WFC}	5, 50
			Z_{WFC}	5, 50
SDSS Stripe 82 D	$03^{\mathrm{h}}\,55^{\mathrm{m}}\,00.0^{\mathrm{s}}$	$+00°\,00'\,00.0''$	U_{WFC}	5, 50
			g_{WFC}	5, 50
			r_{WFC}	5, 50
			i_{WFC}	5, 50
			Z_{WFC}	5, 50

Appendix B

Pleiades Single-Star Sequence

Table B.1: The Pleiades single-star sequence in the INT-WFC $(griZ)_{\mathrm{WFC}}$ and 2MASS JHK_{s} bandpasses.

g_{WFC}	r_{WFC}	i_{WFC}	Z_{WFC}	J	H	K_{s}
9.099				8.231	8.085	8.016
9.276				8.351	8.191	8.119
9.450				8.467	8.293	8.220
9.623				8.578	8.390	8.319
9.794				8.688	8.486	8.416
9.964				8.797	8.582	8.513
10.133				8.906	8.678	8.608
10.303				9.018	8.775	8.704
10.471				9.132	8.875	8.799
10.640				9.251	8.979	8.894
10.807	10.377	10.270	10.251	9.370	9.082	8.987
10.972	10.505	10.389	10.364	9.484	9.181	9.078
11.133	10.645	10.516	10.481	9.594	9.275	9.166
11.292	10.783	10.640	10.596	9.699	9.364	9.251
11.445	10.914	10.758	10.704	9.796	9.445	9.330
11.593	11.040	10.871	10.809	9.887	9.520	9.405
11.735	11.161	10.979	10.908	9.970	9.588	9.473
11.870	11.273	11.079	11.000	10.043	9.646	9.534
11.998	11.378	11.172	11.086	10.110	9.699	9.589
12.120	11.478	11.261	11.168	10.169	9.745	9.637
12.237	11.569	11.342	11.243	10.223	9.788	9.680
12.350	11.661	11.422	11.317	10.273	9.826	9.720
12.461	11.749	11.500	11.389	10.320	9.863	9.757
12.572	11.837	11.577	11.460	10.367	9.899	9.794
12.683	11.926	11.654	11.529	10.418	9.938	9.832

Table B.1: *continued*

g_{WFC}	r_{WFC}	i_{WFC}	Z_{WFC}	J	H	K_{s}
12.797	12.018	11.734	11.604	10.473	9.980	9.872
12.913	12.107	11.811	11.675	10.534	10.025	9.914
13.030	12.203	11.893	11.750	10.600	10.069	9.958
13.150	12.299	11.974	11.824	10.667	10.112	10.004
13.271	12.396	12.057	11.900	10.731	10.161	10.051
13.393	12.493	12.138	11.973	10.794	10.213	10.099
13.515	12.589	12.218	12.046	10.857	10.268	10.148
13.639	12.687	12.298	12.118	10.921	10.325	10.198
13.763	12.782	12.375	12.187	10.984	10.381	10.248
13.885	12.874	12.449	12.251	11.044	10.435	10.297
14.009	12.972	12.527	12.319	11.107	10.492	10.347
14.132	13.067	12.602	12.384	11.170	10.550	10.396
14.253	13.165	12.678	12.447	11.231	10.607	10.444
14.373	13.262	12.752	12.508	11.289	10.660	10.490
14.493	13.363	12.829	12.569	11.347	10.713	10.536
14.609	13.458	12.901	12.624	11.399	10.761	10.579
14.725	13.554	12.973	12.676	11.450	10.808	10.621
14.838	13.650	13.046	12.729	11.496	10.849	10.660
14.948	13.742	13.115	12.778	11.538	10.888	10.697
15.056	13.835	13.184	12.829	11.578	10.925	10.731
15.161	13.926	13.252	12.881	11.613	10.957	10.762
15.264	14.015	13.318	12.934	11.646	10.987	10.791
15.366	14.103	13.382	12.985	11.679	11.017	10.820
15.469	14.187	13.444	13.037	11.711	11.048	10.849
15.574	14.273	13.505	13.088	11.746	11.081	10.880
15.679	14.360	13.567	13.141	11.782	11.115	10.912
15.789	14.449	13.629	13.193	11.824	11.155	10.948
15.903	14.543	13.694	13.249	11.869	11.200	10.988
16.021	14.648	13.763	13.309	11.916	11.248	11.033
16.146	14.764	13.838	13.374	11.970	11.304	11.084
16.279	14.904	13.922	13.446	12.032	11.368	11.143
16.418	15.066	14.015	13.527	12.101	11.438	11.209
16.568	15.239	14.118	13.615	12.178	11.521	11.285
16.727	15.418	14.233	13.714	12.264	11.613	11.370
16.896	15.598	14.358	13.820	12.360	11.715	11.466
17.072	15.783	14.493	13.934	12.462	11.821	11.568
17.246	15.961	14.627	14.049	12.562	11.925	11.668
17.426	16.144	14.768	14.169	12.670	12.037	11.775

Table B.1: *continued*

g_{WFC}	r_{WFC}	i_{WFC}	Z_{WFC}	J	H	K_{s}
17.627	16.345	14.926	14.307	12.797	12.168	11.902
17.864	16.580	15.114	14.471	12.960	12.339	12.065
18.145	16.855	15.338	14.671	13.167	12.553	12.272
18.450	17.153	15.583	14.890	13.399	12.785	12.504
18.748	17.440	15.821	15.104	13.623	13.016	12.728
19.005	17.687	16.025	15.287	13.807	13.206	12.911
19.207	17.882	16.185	15.431	13.936	13.335	13.040
19.375	18.046	16.317	15.550	14.032	13.433	13.134
19.534	18.200	16.440	15.659	14.120	13.523	13.219
19.691	18.355	16.561	15.766	14.205	13.608	13.303
19.849	18.514	16.684	15.876	14.290	13.690	13.387
20.005	18.668	16.801	15.979	14.377	13.774	13.469
20.160	18.824	16.918	16.081	14.459	13.853	13.551
20.313	18.976	17.033	16.179	14.542	13.934	13.630
20.464	19.126	17.146	16.277	14.619	14.008	13.707
20.611	19.271	17.256	16.372	14.695	14.082	13.781
20.756	19.409	17.362	16.463	14.769	14.153	13.852
20.898	19.545	17.465	16.551	14.839	14.222	13.920
21.035	19.680	17.567	16.637	14.904	14.284	13.984
21.171	19.812	17.665	16.720	14.970	14.347	14.046
21.303	19.941	17.761	16.801	15.032	14.407	14.104
21.433	20.070	17.856	16.881	15.090	14.463	14.160
21.559	20.195	17.947	16.958	15.145	14.515	14.213
21.683	20.320	18.036	17.030	15.198	14.564	14.263
21.804	20.443	18.123	17.100	15.247	14.611	14.310
21.921	20.564	18.207	17.166	15.293	14.653	14.354
22.037	20.688	18.292	17.232	15.337	14.695	14.396
22.149	20.802	18.368	17.290	15.379	14.734	14.434
22.258	20.922	18.446	17.348	15.417	14.770	14.470
22.366	21.041	18.522	17.406	15.453	14.803	14.504
22.470	21.160	18.595	17.462	15.485	14.834	14.534
22.571	21.282	18.666	17.516	15.515	14.862	14.562
22.671	21.405	18.736	17.571	15.543	14.889	14.588
22.767	21.533	18.803	17.623	15.567	14.912	14.610
22.861	21.667	18.867	17.673	15.590	14.933	14.631
22.952	21.818	18.929	17.723	15.608	14.950	14.648
23.042		18.991	17.772	15.625	14.966	14.664
23.119		19.042	17.814	15.638	14.978	14.675

Table B.1: *continued*

g_{WFC}	r_{WFC}	i_{WFC}	Z_{WFC}	J	H	K_{s}
		19.135	17.888			
		19.223	17.959			
		19.310	18.029			
		19.397	18.100			
		19.481	18.168			
		19.565	18.236			
		19.648	18.303			
		19.729	18.369			
		19.809	18.434			
		19.888	18.499			
		19.965	18.562			
		20.041	18.623			
		20.116	18.685			
		20.189	18.744			
		20.261	18.804			
		20.331	18.861			
		20.400	18.918			
		20.467	18.973			
		20.533	19.027			
		20.597	19.080			
		20.660	19.132			
		20.721	19.183			
		20.780	19.232			
		20.838	19.280			
		20.894	19.326			
		20.943	19.367			